SUMMERTIME SURFACE MASS BALANCE AND ATMOSPHERIC PROCESSES ON THE MCMURDO ICE SHELF, ANTARCTICA.

A thesis submitted in partial fulfilment of the

requirements for the Degree

of Doctor of Philosophy

in the Department of Geography

by Penelope Catherine Clendon

University of Canterbury

2009

Abstract

The aim of this research was to demonstrate the relationship between variations in summertime surface mass balance of the McMurdo Ice Shelf and atmospheric processes. The approach encompassed a broad range of techniques. An existing energy balance mass balance model was adapted to deal with debris-covered ice surfaces and modified to produce distributed output. Point based surface energy and mass balance for two key surfaces of the ice shelf were linked to different synoptic types that were identified using a manual synoptic classification. The distributed model was initialised with distributed parameters derived from satellite remote sensing and forced with data from a regional climate model. Patterns of summertime surface mass balance produced by the distributed model were assessed against stake measurements and with respect to atmospheric processes.

During the summers of 2003-2004 and 2004-2005 an automatic weather station (AWS) was operated on bare and debris-covered ice surfaces of the McMurdo Ice shelf, Antarctica. Surface mass balance was calculated using the energy balance model driven by the data from the AWS and additional data from permanent climate stations. Net mass balance for the measurement period was reproduced reasonably well when validated against directly measured turbulent fluxes, stake measurements, and continuously measured surface height at the AWS.

For the bare ice surface net radiation provided the major energy input for ablation, whereas sensible heat flux was a second heat source. Ablation was by both melt (70%) and sublimation (30%). At the debris-covered ice site investigated, it is inferred that the debris cover is sufficient to insulate the underlying ice from ablation.

Synoptic weather situations were analysed based on AVHRR composite images and surface pressure charts. Three distinct synoptic situations were found to occur during the summers, these were defined as Type A, low pressure system residing in the Ross Sea Embayment; Type B, anticyclonic conditions across region; and Type C, a trough of low pressure extending into the Ross Sea Embayment. A dependence of surface energy fluxes and mass balance on synoptic situation was identified for the bare ice surface.

The distributed model was found to produce spatial patterns of mass balance which compared well with stake measurements. Mass balance patterns show that the McMurdo Ice Shelf was generally ablating in the west, and accumulating in the east during summer. Areas of enhanced ablation were found which were likely to be caused by the surface conditions and topographic effects on the wind field. The mean summertime surface mass balance across the entire ice shelf for the 2003-2004 and 2004-2005 summers were –2.5 mm w.e. and –6.7 mm w.e. respectively. The differences between the two summers are inferred to be a result of more frequent type A conditions occurring during the summer of 2004-2005.

Acknowledgements

First and foremost, many thanks to my supervising team Wendy Lawson and Ian Owens. They have provided guidance, support and patience throughout the whole process. I would also like to express my appreciation to other my other supervisors: Rachel Spronken-Smith and Bryan Storey.

Logistical support for this research has been provided by Antarctica New Zealand, Gateway Antarctica, and the Deparment of Geography. Personal funding was provided through Antarctica New Zealand, New Zealand Federation of Graduate Women, Ministry of Foreign Affairs and Trade, and the good old Student Loan.

Data were supplied by Matthew Lazzara, Antarctic Meteorological Research Center (AMRC), University of Wisconsin; National Institute of Water and Atmospheric Science (NIWA); and NASA Land Processes Distributed Active Archive Center. Also many thanks to W. Greuell for making the SOMARS model available.

Extra special thanks to Gillian Blackler for her prompt and thorough editing, and also for her never ending patience and personal support.

Also thanks for support from the following: Justin Harrison, Luke Copland, Ian Hawes, Nick Keye, Walter Gallagher, John Thyne, Burn Hockey, Andy Sturman, Andrew Oliphant, Becky Goodsall, and the staff of Scott Base.

The people I love are the ones that kept me sane so thanks to Mum and Dad for believing in me, Blene for distracting me, Emma for the funnies, and Meg for the yummies. And finally, I would like to thank Dan. He has believed in me, endured all my problems, given me “the little things” and been patient to the very end.

Table of contents

List of figures

List of tables

List of symbols

Symbol	Description	Units	Value if constant
$C_{a,}$	volumetric heat capacity of substance (by volume)	J m^{-3} K^{-1}	C_a=0.0012 x 10^6
c_d	specific heat capacity of debris	J $kg^{-1}K^{-1}$	-
c_p	specific heat of a air at constant pressure (by mass)	J kg^{-1} K^{-1}	1005.7 ± 2.5
c_{pi}	specific heat capacity of ice	J $kg^{-1}K^{-1}$	-
e_s	saturation vapour pressure	Pa	-
F	freezing rate	J kg^{-1}	
g	acceleration due to gravity	m s^{-2}	9.81
$h_{1,2}$	relative humidity	-	-
k	effective conductivity	W m-^{1} K^{-1}	-
K↓	incoming shortwave radiation	W m^{-2}	-
K↑	outgoing shortwave radiation	W m^{-2}	-
k_0	von Kármán's constant	-	0.4
k_d	thermal conductivity of debris	W m-^{1} K^{-1}	-
L	Obukhov length	m	-
L↓	incoming longwave radiation	W m^{-2}	-
L↑	outgoing longwave radiation	W m^{-2}	-
$L\downarrow_{raw}$	raw incoming longwave radiation	W m^{-2}	-
$L\uparrow_{raw}$	raw outgoing longwave radiation	W m^{-2}	-
L_f	latent heat of fusion	J kg^{-1}	3.337 x 10^5 at 0°C
L_S	latent heat of sublimation	J kg^{-1}	2.834 x 10^6 at 0°C
L_V	latent heat of vaporisation	J kg^{-1}	2.501 x 10^6 at 0°C
m	mass	kg	-
M	melt rate (mass per unit area)	kg m^{-2} s^{-1}	-
M_a	Molecular weight of air	g mol^{-1}	29
M_{di}	melt rate at debris-ice interface	m s^{-1}	-
Me	total melt	mm w.e.	-

Symbol	Description	Units	Value if constant
M_W	molecular weight of water	g mol^{-1}	18
O	other mass balance terms (erosion/deposition by wind and snowdrift sublimation)	mm w.e.	-
Pr	precipitation	mm w.e.	-
p	atmospheric pressure	Pa	-
q	specific humidity	kg kg^{-1}	-
*q**	humidity scale		
*Q**	net radiation	W m^{-2}	-
Q_{di}	downward energy flux at the debris-ice interface	W m^{-2}	-
Q_E	latent heat flux	W m^{-2}	-
Q_G	subsurface conductive flux	W m^{-2}	-
Q_H	sensible heat flux	W m^{-2}	-
Q_M	surface melt energy	W m^{-2}	-
Q_P	energy from precipitation	W m^{-2}	-
Q_{sd}	downward flux of energy from a layer of snow over debris	W m^{-2}	-
Q_t	total energy flux from the atmosphere toward the glacier surface	W m^{-2}	-
R	universal gas constant	J mol^{-1} K^{-1}	8.314
Re	Reynolds number	-	-
Ri	Richardson number	-	-
R_v	gas constant for water vapour	J kg^{-1} K^{-1}	461.5
SMB	surface mass balance	mm w.e.	-
Su	sublimation	mm w.e.	-
t	time	s	-
T	air temperature	°C	-
T_0, T_1, T_2	temperature at surface (0), and heights 1, 2	°C	-
T_{di}	temperature at debris-ice interface	°C	-
u	wind speed	m s^{-1}	-

Symbol	Description	Units	Value if constant
u_*	friction velocity	m s^{-1}	-
v	kinematic viscosity of air	m^2 s^{-1}	1.461 x 10^{-5}
v	proportion of voids in debris	-	-
w	vertical wind speed	m s^{-1}	-
z_0, z_{0h}, z_{0e}	roughness length of momentum, heat and vapour	m	-
$z_{1,2}$	instrument height at points 1,2	m	-
z_{di}	depth of the debris-ice interface	m	-
ε	emissivity	-	-
ζ	absorptivity	-	-
θ*	temperature scale	-	-
φ	porosity	-	-
Ψ	stability correction term	-	-
Ψ	transmissivity	-	-
κ	thermal diffusivity of the debris	m^2 s^{-1}	-
Δm	ablation	mm w.e.	-
σ	Stefan-Boltzmann constant	W m^{-2} K^{-4}	5.67 x 10^{-8}
θ	potential temperature	K	-
α	albedo	-	-
ρ	density of a substance	kg m^{-3}	1.292 at SPA
ρ_a	density of dry air	kg m^{-3}	1.292 at SPA
ρ_d	density of debris	kg m^{-3}	917
ρ_i	density of ice	kg m^{-3}	917
ρ_v	vapour density (absolute humidity)	kg m^{-3}	1.292 at SPA
ρ_w	density of water	kg m^{-3}	1000
Φ_m, Φ_h	stability functions for temperature and humidity	-	-

Common subscripts

a	air
d	debris
i	ice
v	voids
w	water
z	height/depth
λ	wavelength

1 Introduction and aims

1.1 Introduction

Complex numerical models of the atmosphere and oceans are now being used to predict the response of the Earth's systems to increased levels of greenhouse gases in the atmosphere. However, estimates of changes in surface accumulation and ablation in polar regions under changing climate conditions are subject to high uncertainty (van der Veen, 2002; Lemke *et al.*, 2007). Most of the models used in the prediction of mass balance are based on direct temperature forcing, and do not include other factors such as atmospheric circulation patterns which may be equally as important. Energy balance models are a means by which changes brought about by atmospheric circulation may be incorporated into the assessment of surface mass balance. There are few studies in which ablation is calculated explicitly from the surface energy balance in polar regions and more realistic models for estimating surface ablation are required (van de Veen, 2002; Hock, 2005). To improve current understanding of ice-atmosphere linkages, it is necessary to develop methods by which distributed surface mass balance can be assessed in response to changes in atmospheric conditions.

Ice shelves provide a good platform to investigate ice-atmosphere interactions as they encompass several surface types found in polar regions. Furthermore, almost half of the Antarctic coastline is comprised of floating ice shelves that account for 11% of Antarctica's total surface area (King and Turner, 1997). Additionally, ice shelves are sensitive indicators of climatic change (Vaughan and Doake, 1996) yet ice shelf-climate interactions have received surprisingly little attention.

Because ice shelves are floating bodies of ice, their movement is not driven by gravity. Pushed by glaciers from behind, ice shelves move seaward and are unconstricted at their front. Consequently, the mass balance of an ice shelf is made up of different components than that for other glaciers. Accumulation of an ice shelf can be from precipitation on its surface, snow redistribution, flux of ice from the

surrounding glaciers, or basal freezing. Ablation can be from the calving of icebergs, surface melt and subsequent runoff, sublimation, or basal melting.

Surface ablation is driven by the exchange of energy between the surface and the atmosphere, which in turn is influenced by variations in climate and surface conditions. The primary controls on the surface energy balance (SEB) and hence ablation are the surface nature and meteorological variables, both of which change in time and space. As well as being an important component in global mass balance, ablation may also exert a control on other mass balance processes. For example, it is thought that ice shelf collapse is affected by surface melting (Scambos *et al.,* 2000).

The McMurdo Ice Shelf, in the Ross Sea Region (Figure 1.1), provides an important and opportune site for the investigation of ice-shelf atmosphere energy linkages. The ice shelf is adjacent to two research bases: McMurdo Station, (USA) and Scott Base (NZ) and is important in the ongoing logistics for research programs supported by the bases. Its proximity to these bases, as well as its small size (approximately 5000 km^2), and a history of research (Section 1.5) makes the McMurdo Ice Shelf an ideal location for this type of study. The ice shelf also has variable surface characteristics and therefore presents an opportunity to investigate how surface types affect mass balance. Furthermore, recent research has suggested that it is currently in a state of dynamic equilibrium with its environment (Lawson *et al.*, *submitted*).

This chapter firstly introduces the reader to the three research themes that this work draws on - those concerning surface energy and surface mass balance, ice-atmospheric circulation linkages, and debris on ice. The McMurdo Ice Shelf is then described, followed by a description of the thesis aims and objectives. The chapter finishes with an outline of the thesis structure.

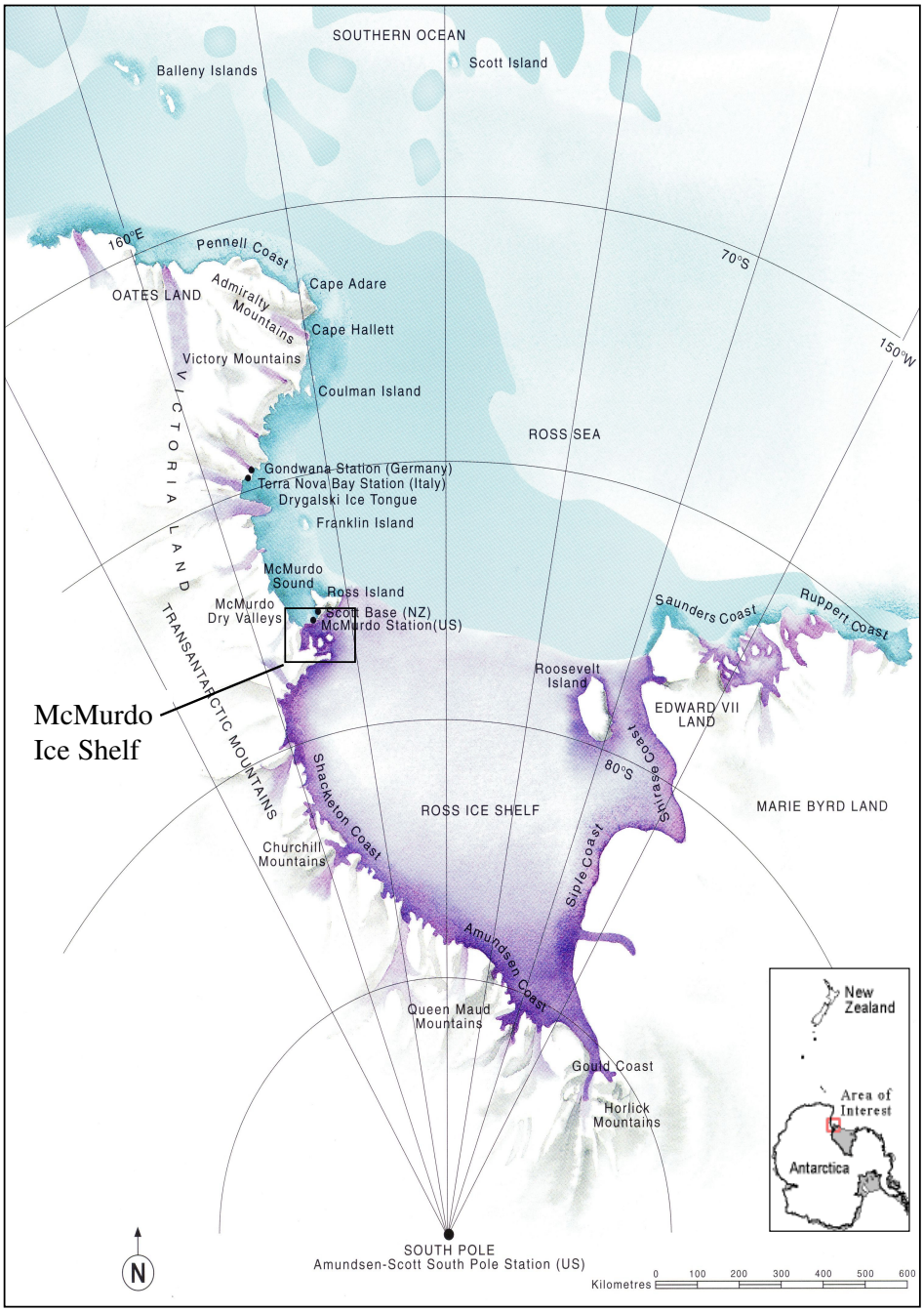

Figure 1.1. The Ross Sea Region, showing the Ross Sea Embayment and approximate location of McMurdo Ice Shelf (Waterhouse, 2001 p.4).

1.2 Surface energy and surface mass balance

This section firstly outlines the physical principles of atmosphere-surface energy exchange. Then a review of recent research concerning energy and mass balance in polar regions is given.

1.2.1 Surface mass and energy exchange

The surface mass balance (mm w.e.) at a point on a glacier is the balance of the components of accumulation and ablation for a given time period:

$$SMB = Pr + Su + Me + O \qquad 1.1$$

where *SMB* is the surface mass balance, *Pr* is precipitation, *Su* is sublimation, *Me* is melt followed by evaporation or runoff, and *O* accounts for other terms such as erosion/deposition by wind and snowdrift sublimation (terms that remove mass from the surface are defined as negative). The amount of energy available for melt and sublimation is determined by the surface energy balance, which is the sum of the net fluxes of energy exchanged at the surface and is now described.

Radiant energy received at a surface may be reflected, absorbed, or transmitted. The radiation budget describes the gains and losses of this radiant energy. The balance of the radiation budget, net radiation, is the basic input into the surface energy balance, which is used to examine how the energy is partitioned. The surface energy balance determines how much energy is available for ablation.

During clear sky days, radiant energy received at the earth's surface can be calculated with a high degree of certainty given the latitude and time of year. Outgoing radiant energy in all wavelengths, however, varies significantly as a function of the nature of the surface. Radiant energy, for a given wavelength (λ), received at the surface may be reflected (α_λ), absorbed (ζ_λ), or transmitted (Ψ_λ) through the medium: so that

$$\alpha_\lambda + \zeta_\lambda + \psi_\lambda = 1 \qquad 1.2$$

However, according to Oke (1987), these properties can be considered constant for a wavelength band, such as short-wave (solar) radiation (0.15 - 3.00 μm), or long-wave radiation (3.00 - 100.00 μm).

As short-wave radiation is considered the primary source of energy for ice ablation (Paterson, 1994), reflectivity of short-wave radiation (albedo) is of great importance.

Short-wave albedo of an ice mass surface is a function of the age of the ice or snow, sun angle, grain size, presence of air bubbles, impurities, surface water, and the presence and nature of supra-glacial debris. The surface is defined here as the active surface where the primary atmosphere-ice mass energy exchange occurs and may consist of ice, snow, debris, or a combination of these.

Surface albedo can range from 0.10 to 0.97 across differing glacier surfaces (Paterson, 1994). Reflection of long-wave radiation is significantly less, with long-wave reflectivity generally less than 0.10 for all surface types (Oke, 1987). The term albedo is used in this thesis to refer specifically to the short-wave albedo. Albedo of ice is high compared with other natural surfaces and studies have shown it to have both a diurnal and seasonal variability (Paige, 1968; Braithwaite and Olesen, 1989; Bintanja *et al.*, 1997; Lewis *et al.*, 1998; Arendt, 1999). The albedo of supra-glacial debris is much lower, ranging from 0.10 (Paterson, 1994) to 0.21 (Takeuchi *et al.*, 2000).

All substances at temperatures above absolute zero (0 K, -273.2º C) emit energy. A perfect radiator (black body) emits exactly the same amount of energy as it receives at a given temperature. Any substance that is not a black body emits energy at a rate (I) according to its emissivity (ε_λ), as follows:

$$I = \varepsilon_\lambda \sigma T_0^{\,4} \qquad 1.3$$

in W m^{-2} where σ is the Stefan-Boltzmann constant (5.67 x 10^{-8} J K^{-4} m^{-2} s^{-1}) and T_0 is the surface temperature (K). According to Kirchoff's Law, emissivity is equal to the absorptivity (ζ_λ) for the same wavelength:

$$\varepsilon_\lambda = \zeta_\lambda \qquad 1.4$$

Snow and ice are near perfect black body radiators in the infrared (ε_λ close to unity). In contrast, supra-glacial debris has a lower emissivity, and accordingly will absorb a lower proportion of energy.

Ice and snow are unusual in that they transmit solar radiation. Thus, it is necessary to view the energetics as relating to a volume as opposed to a surface (Henneken *et al.,* 1994; Oke, 1994). This transmitting characteristic has been recognized as the cause of subsurface melting, or 'solid state greenhouse' (Paige, 1968; Ishikawa and Kobayashi, 1985; Brandt and Warren, 1993).

The radiation budget is defined by:

$$Q^* = K\downarrow - K\uparrow + L\downarrow - L\uparrow \quad (1.5)$$

or

$$Q^* = K^* + L^* \quad (1.6)$$

where Q^* is net all-wave radiation of a surface, K↓ and L↓ are the incident short-wave and long-wave radiation fluxes respectively, K↑ is reflected short-wave radiation and L↑ is emitted long-wave radiation. Net parameters are denoted by an asterisk.

Energy can be transported to and from the active surface via turbulent fluxes as well as the radiant fluxes outlined above. Turbulent transfer is achieved by eddies conducting sensible and latent heat to or from the glacier surface. If the air immediately above the glacier is warmer than the surface, sensible heat is transferred to the surface. If the air is colder than the surface, sensible heat is transferred from the surface to the air. Similarly, when the vapour pressure of the air above the surface is higher than that of the surface, vapour condenses on the surface and the surface gains latent heat. When the vapour pressure of the air is lower than the surface, evaporation or sublimation occurs and the surface loses latent heat. The degree of turbulence in the near surface atmosphere dictates the amount of energy transferred via these processes. Furthermore, heat may also be exchanged vertically downwards into the underlying snow, ice or debris by means of conduction.

The total surface energy flux (Q_t) is represented by:

$$Q_t = Q^* + Q_H + Q_E + Q_P \quad (1.7)$$

where Q_H is turbulent sensible heat flux, Q_E is the turbulent latent heat flux, and Q_P is the heat flux due to precipitation (Fluxes towards the surface are taken as positive). Q_t can be further subdivided into conductive heat flux Q_G and a penetrating part of the short-wave radiation which are discussed in detail in chapter three (Sections 3.2.2 and 3.2.3).

1.2.2 Research on surface energy and surface mass balance in polar regions

Work on surface energy and surface mass balance in polar regions has been mainly limited to point based investigations but distributed models are becoming more prevalent.

There have been numerous recent studies on energy and mass balance of snow surfaces in Antarctica (van den Broeke 2004a,b; van As et al., 2005a,b), and on ice surfaces in other environments such as Greenland (van de Wall *et al.*, 2005) and Norway (Andreassen *et al.,* 2008). However, energy and mass balance measurements over Antarctic ice surfaces are still rare. van den Broeke (1997) emphasized the need for more energy balance measurements over ice and suggested that the combination of models that are empirically validated with data from automated weather stations would be a powerful tool to assess the Antarctic energy balance.

A comprehensive point based study has been conducted on the SEB of blue ice areas (BIA) of Dronning Maud Land, Antarctica (Bintanja and van den Broeke, 1995; Bintanja *et al.,*1997; Bintanja, 2000; Bintanja and Reijmer, 2001). These studies indicated that the largest flux was net radiation, followed by sensible heat. Sensible heat was the only source during the winter. Most of the available heat was used for sublimation, with a total energy flux small for blue ice and slightly larger for snow indicating that ice gains more heat than snow during summer. Spatial variability of the fluxes was significant (Bintanja and van den Broeke, 1995). For example, Bintanja and van den Broeke (1995) found a net flux of -29 W m^{-2} in a BIA of Dronning Maud Land, whilst on the snow surface nearby, the flux was between -15 and -22 W m^{-2}. This variability was attributed to differences in albedo across the different surfaces, and to the prevailing weather conditions (Bintanja and Reijmer, 2001).

Research on Antarctic SEB has often concentrated on sublimation and disregarded melt processes (e.g. Stearns and Weidner, 1993; Bintanja and van den Broeke, 1995; Schneider, 1999). However, Das and Alley (2005) and Liston and Winther (2005) showed that melt in Antarctica is widespread and should therefore be included in considerations of mass balance.

Surface mass balance models fall into two main categories: surface energy balance and temperature-index methods. Energy balance models compute energy fluxes between the atmosphere and the ice surface, and are driven by atmospheric variables such as temperature, wind speed, humidity, radiative fluxes, cloud, and precipitation. To date most surface energy balance models have either been point based or along glacier centre lines, with distributed models only recently being attempted (Hock, 2005). In contrast, temperature-index models are simplified by relating ablation directly to atmospheric temperature and, less frequently, to incoming solar radiation. For this research only the energy balance approach is considered because it is better able to adapt to changes in atmospheric circulation (van der Veen, 2002; Greuell and Genthon, 2003; Bougamont *et al.,* 2005).

Energy balance models often use internally-generated components (not parameterised or specified) such as incoming short-wave and long-wave radiation. These components have been addressed thoroughly in the literature and are relatively well understood (Hock, 2005). Although models have been shown to be sensitive to variations in albedo, aerodynamic roughness length and surface temperature, these parameters are often assumed constant, or have been used as tuning parameters (e.g. Reijmer *et al.,* 2001; Greuell and Genthon, 2003; Hock, 2005).

In order to address such sensitivities, a number of studies have emphasised the need to internally-generate albedo (Braithwaite and Oleson, 1989; Zuo and Oerlemans; 1996; Lewis *et al.,* 1998; Arendt, 1999). The ability to incorporate changes in snow albedo in energy balance models is well established. However, for simplicity, the ice albedo is often considered static in time and space in energy balance models (Greuell and Genthon 2004; Hock, 2005). While temporal variations of ice albedo are smaller than that of snow (Cutler and Munro, 1996), spatial variation can be considerable (Paterson, 1994). Some models incorporate a linear change in ice albedo with elevation (Oerlemans, 1992), while others consider snow and ice albedo separately (e.g. Greuell and Konzelmann, 1994; Arnold *et al.,* 1996; Brock *et al.,* 2000b).

Turbulent fluxes are highly sensitive to the aerodynamic roughness length (z_0) (Braithwaite, 1995; Brock *et al.,* 2000b). Despite this sensitivity, z_0 is often

approximated (Greuell and Genthon, 2004) or used as a tuning parameter (e.g. Braun and Hock, 2004; Hock, 2005). Brock *et al*. (2000b) incorporated a modelled z_0 for snow but were unable to establish any method for modelling z_0 for ice. This gap in the knowledge base means that the z_0 used must be considered carefully when modelling turbulent fluxes.

Surface temperature is a factor that has received little attention in mass balance modelling, despite the fact that it is an important consideration in energy flux calculation (De Ridder and Mensink, 2003; Reijmer *et al*., 2001). Often energy balance models assume a melting surface, and thus a fixed surface temperature, which can lead to an overestimation of melt (Hock, 2005). Furthermore, both sublimation and subsurface melt can occur when the surface is below freezing point (Liston, *et al.*, 1999), highlighting the importance of allowing for variable surface temperatures in SEB modelling.

The climate variables used to drive SEB mass balance models are generally taken from one climate station, located away from the glacier itself (e.g. Greuell and Konzelmann, 1994). These data are either assumed spatially invariant or interpolated with altitude using an assumed lapse rate (Hock, 2005). Recently some work has coupled SEB mass balance models with distributed input (discussed below).

SOMARS (Simulation of glacier surface Mass balance And Related Sub-surface processes) is a readily available glacier centre line mass balance model that addresses most of the concerns outlined above. It was tested successfully at the ETH-Camp, West Greenland (Greuell and Konzelmann, 1994), and has since had several adaptations (e.g. Bougamont *et al.,* 2005).

Many broad-scale surface mass balance studies have been conducted across the Antarctic, including the Ross Sea Region, but distributed energy balance based analyses are uncommon (van der Veen, 2002). A general circulation model was created by van den Broeke (1997) to examine sublimation over the whole Antarctic Continent. However, when compared with ground based measurements, the model only produced fair results (van den Broeke, 1997).

Recent research has attempted to couple energy balance models with spatially distributed climate variables. Bougamont *et al.* (2005) coupled an energy balance model with spatially distributed climate variables to assess the surface mass balance of the Greenland Ice Sheet. They used output from the European Centre for Medium-range Weather Forecast (ECMWF) reanalysis (ERA-40) coupled with an energy balance model in order to assess its ability to identify inter-annual variability. They found that modelled spatial and temporal wet zone compared well with that identified with remote sensing (Bougamont *et al*., 2005).

Liston and Winther (2005) used broad scale data from a meteorological distribution model (MicroMet) combined with the distribution of blue ice determined with AVHRR and a customised energy balance model for blue ice to determine broad scale surface and subsurface melt. Their results suggest that a large amount of surface and subsurface melt is occurring across Antarctica.

1.3 Ice-atmospheric circulation linkages

In a comprehensive review of energy balance modeling, Hock (2005) suggested that research needs to focus on the links between energy fluxes and synoptic scale processes. It is clear that, although not well understood, these relationships are important for understanding the controls on temporal variability of melting, prediction of the effects of climatic change, and for validation of climate models in polar regions.

Surface energy fluxes and mass balance are intimately coupled with atmospheric circulation and therefore with synoptic conditions. However, this link has been only been examined by a few researchers. Of the limited number of studies, most have identified that different air masses exert strong controls on the surface energy or mass balance (Yarnal, 1984; Neale and Fitzharris, 1997; Petrone and Rouse, 2000; Leathers *et al*., 2004). Even less attention has been paid to this relationship in the polar regions. This knowledge is however very important when down scaling global and regional climate models and for climate change research.

Neale and Fitzharris (1997) found that different synoptic conditions generated distinctive energy budgets in melting snowpack in the Southern Alps of New Zealand. They found that net radiation was most important during anticyclonic systems, but that most melting occurred when sensible heat was an important source of energy (Neale and Fitzharris, 1997). Leathers *et al.* (2004) used a snowpack model, and an airmass identification scheme to identify large ablation events in the Appalachian Mountains of North America. They identified five air mass types causing large ablation events, some of which were "moist" and some of which were "dry" (Leathers *et al.,* 2004 p.1898). They also found significant energy input from condensation and accounted for extreme melt conditions by the combination of high sensible and latent heat (Leathers *et al.*, 2004). Petrone and Rouse (2000) examined in detail the synoptic conditions in sub-arctic regions of Canada. Although their study was not focussed on melt, they found that the synoptic regimes exerted strong controls on the energy balance, and that evaporation was highest during high pressure conditions.

Alt (1987) developed synoptic analogs for extreme mass balance conditions on the Queen Elizabeth Island Ice Caps, High Arctic, Canada. A ridge at all levels was associated with summertime melt maxima, while suppression of melt was associated with a deep trough causing maritime winds. Accumulation maxima were linked to lower and upper atmospheric low pressure systems (Alt, 1987). They found that during anticyclonic conditions, with a ridge over the Queen Elizabeth Islands, high rates of melting occurred. These synoptic analogs were developed specifically for paleoclimatic reconstructions (Alt, 1987).

In the southern high latitudes, very limited research has been done at the temporal scale that captures air mass characteristics. One notable exception is the work by Braun *et al.* (2001) who also found strong linkages between large scale circulation and mass balance. Their study examined the effects of large-scale atmospheric circulation on energy balance terms of the King George Island Ice Cap, on the South Shetland Islands. The maximum melt rate found was associated with advection of warm, moist air masses. During these conditions the contribution of turbulent fluxes exceeded that of radiation balance. Periods found to not contribute to ablation were associated with dry, cold continental air masses (Braun *et al.,* 2001).

Some work has been done by Bintanja and Reijmer (2001b) and Liston *et al.* (1999) who have investigated surface energy balance components of blue ice areas with specific reference to atmospheric conditions such as cloud and moisture. These however, have not been related to synoptic scale circulation.

1.4 Debris on ice

Debris-cover affects the SEB through more than just its albedo (Brock *et al.*, 2000a). Debris can both enhance and inhibit melt depending on its depth and thermal properties. Debris on the surface of a temperate glacier has been shown to augment melting until it is approximately 1-2 cm thick (Nakawo and Rana, 1999). As the debris layer gets thicker, the effect decreases until a critical thickness is reached, at which point the ablation beneath the debris equals that on debris free areas (Nicholson, 2005). The critical thickness varies depending on thermal properties of debris and the location. When the debris is thick enough to insulate the underlying ice, energy received at the surface is stored temporarily within the debris and returned to the atmosphere as long-wave radiation and sensible heat.

Measurement of ablation beneath debris is difficult (Nakawo and Rana, 1999; Purdie and Fitzharris, 1999; Nicholson, 2005). Although it has been shown that it is possible to estimate rates of ablation beneath supraglacial debris using surface temperature (Nakawo and Young, 1982; Nakawo and Rana, 1999), the technique is based on assumptions that cannot necessarily be used for polar regions.

It has been suggested that for debris-covered glaciers in temperate environments, the temperature gradient can be assumed to be linear with depth on a 24 hour timescale (Nicholson and Benn, 2006). This assumption is only valid if the debris is in thermal equilibrium, meaning that there is negligible change in heat storage from day to day (Farouki, 1981; Williams and Smith, 1989; Nicholson and Benn, 2006). Furthermore, past research of this nature has been performed primarily on temperate glaciers, and has assumed that the temperature at the debris-ice interface is equal to 0ºC (Nakawo and Young 1981; Purdie and Fitzharris, 1999; Conway and Rasmussen, 2000; Nicholson and Benn, 2006). However, this cannot be assumed in a polar environment (Nicholson and Benn, 2006).

The effect of debris on ice in polar regions has been the focus of very few studies. The recent discovery of ice below sediment in the Dry Valleys (Antarctica) has prompted a recent research effort into the sublimation of ice through sediment. These recent

works are mostly theoretical and hotly debated (e.g. Hindmarsh *et al.*, 1998), or involve controlled field experiments (e.g. van Dijk and Law, 2003).

Knowledge of debris processes in polar environments is also important for paleoclimatic reconstructions as the presence of debris on ice in polar regions has been linked to the preservation of relic ice (Hindmarsh *et al.,* 1998), to ice rafted debris (Hindmarsh and Jenkins, 2001) and to Heinrich events (Glasser *et al.,* 2006).

1.5 The McMurdo Ice Shelf

The McMurdo Ice Shelf is an approximately 5000 km^2 floating ice shelf in the Ross Sea Region, Antarctica (Figure 1.1). It is bounded by Minna Bluff (up to 920 m.a.s.l.), Mt Discovery (2681 m.a.s.l.), and the Koettlitz Glacier to the south, Ross Island to the north, Ross Ice Shelf to the east and Scott Coast to the west (Figure 1.2). Ross Island is of volcanic origins and is dominated by the active volcano Mt Erebus at 3794 m.a.s.l. To the west, aligned north-south, the Trans Antarctic Mountains rise to over 3000 m.a.s.l. The adjacent and upstream Ross Ice Shelf extends to 85º south (Figure 1.1). The McMurdo Ice Shelf itself is punctuated by the relatively low-lying Brown

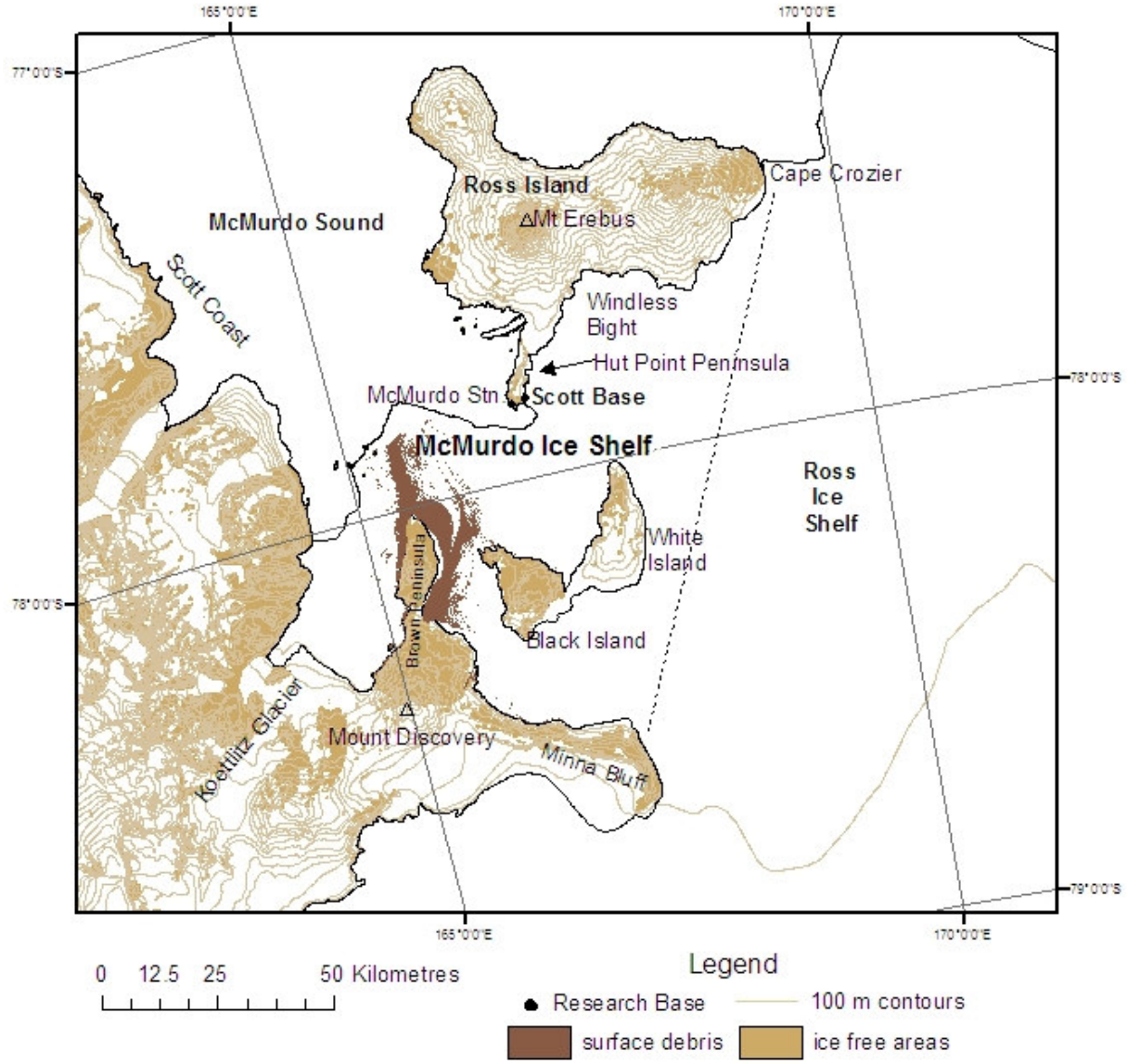

Figure 1.2 McMurdo Region. The approximate eastern boundary of the ice shelf is indicated with a dashed line.(adapted from Scientific Committee for Antarctic Research, 2000).

Peninsula, Black Island, and White Island. The ice shelf is between 20 and 300 m thick, with the thickest sections near Windless Bight, and the Koetlittz Glacier.

The flow regime of the ice shelf is complex, partially due to the numerous processes of accumulation and ablation as outlined above. Ice flows into the McMurdo Ice Shelf from the Ross Ice Shelf to the east, which renders the eastern boundary between the ice shelves arbitrary. For the purposes of this research, the eastern boundary of the McMurdo Ice Shelf is taken to be along a straight line between Minna Bluff and Cape Crozier (Figure 1.2). The ice shelf movements in the eastern regions have been established as travelling from north and south, converging, and then flowing westward (Swithinbank, 1970; McCrae, 1984). To the west, the flow is generally to the northeast at 1.5 - 18.3 m annually (Glasser *et al.*, 2006). The flow regime in the southern part of the ice shelf and area to the north of the Koettlitz Glacier are not well known (McCrae, 1984).

Ross Island has been the base for exploration of Antarctica for more than a century. In the 1950s Scott Base (New Zealand) and McMurdo Station (U.S.) were established on Hut Point Peninsula, Ross Island, as part of the International Geophysical Year. Accordingly, the region has been relatively well documented. The McMurdo Ice Shelf has been the subject of a wide variety of glaciological research due to its proximity to the bases. Relevant aspects of this research are summarised below.

1.5.1 Mass balance

The McMurdo Ice Shelf is fed by ice flow from Ross Ice Shelf, the southern slopes of Ross Island, Koettlitz Glacier and the smaller glaciers on White Island. Direct surface accumulation from precipitation and blowing snow occurs throughout the year (Sinclair, 1988). Furthermore, water freezes in tide-cracks and basal freezing occurs on the underside of the ice shelf. Precipitation in the region varies considerably in space, with the mean at McMurdo Station approximately 180-190 mm per annum (Monaghan *et al.*, 2006). There is a strong east-west gradient of surface accumulation (Figure 1.3) with a maximum annual accumulation of around 508 mm w.e. in the Windless Bight area (density of ice was assumed to be 400 kg m^{-3}) which reduces to between 52 and 172 mm w.e. near to McMurdo Station.

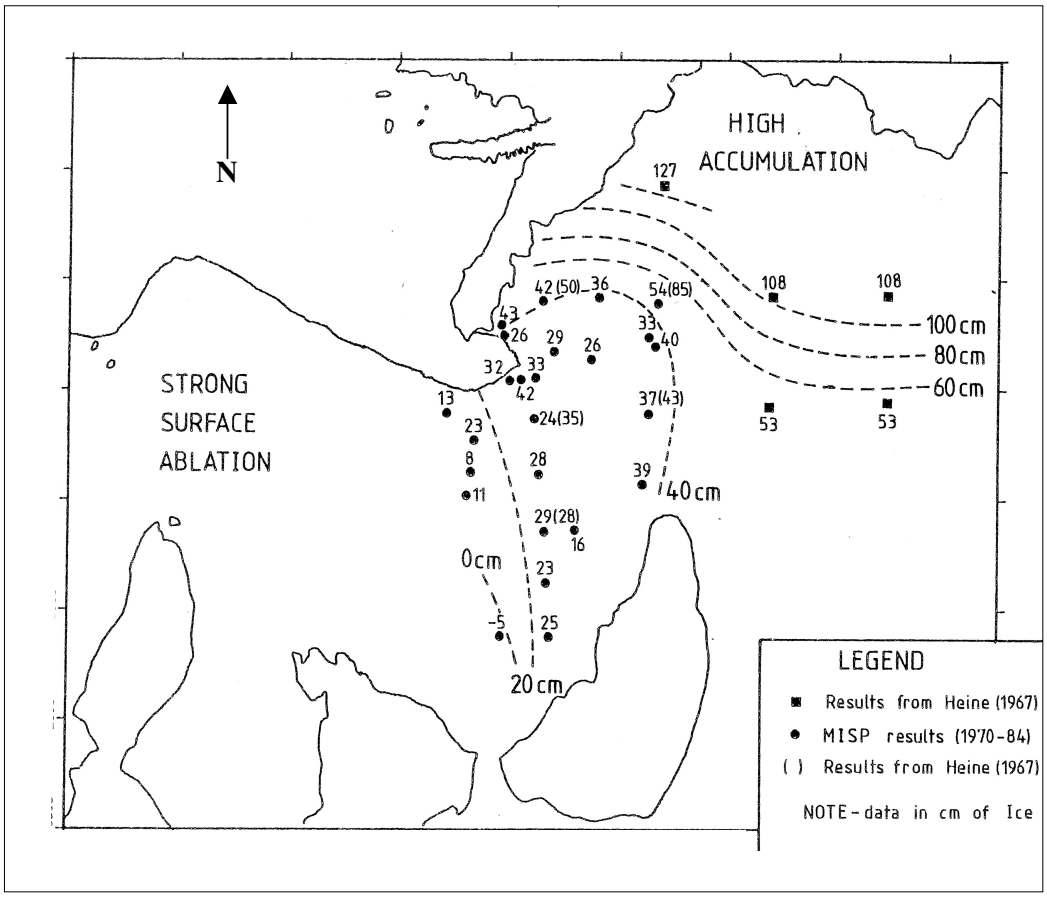

Figure 1.3 Summary of surface mass balance research performed on the McMurdo Ice Shelf up to 1984. Note values shown are from stakes measurements, and are given in cm of ice (McCrae, 1984, p.39).

Ablation of the McMurdo Ice Shelf is by means of surface sublimation and melt, occasional calving, and bottom melting (McCrae, 1984). The western part of the ice shelf experiences strong surface ablation with values of net mass loss of up to 4.41 m over a summer (Glasser *et al.,* 2006). A transition zone between accumulation and ablation runs between White Island and the ice shelf front. The location of this transitional area has been reported by several researchers (Stuart and Bull 1963; Paige, 1968; Swithinbank, 1970). No work on the Southern McMurdo Ice Shelf mass balance has been published to date.

1.5.2 Surface characteristics

Two surface types dominate the ablation area of the McMurdo Ice Shelf: bare glacier ice and debris-covered ice. The bare glacier ice surface has a mottled appearance comprising patches of white bubbly ice, and areas of clear blue glacier ice. The two types of ice alternate in a linear fashion (Figure 1.4). These linear features are the result of the prevailing southwesterly winds, as they descend from Minna Bluff and Mount Discovery (Swithinbank, 1970). Small patches of debris and snowdrifts are also typically found on the bare ice.

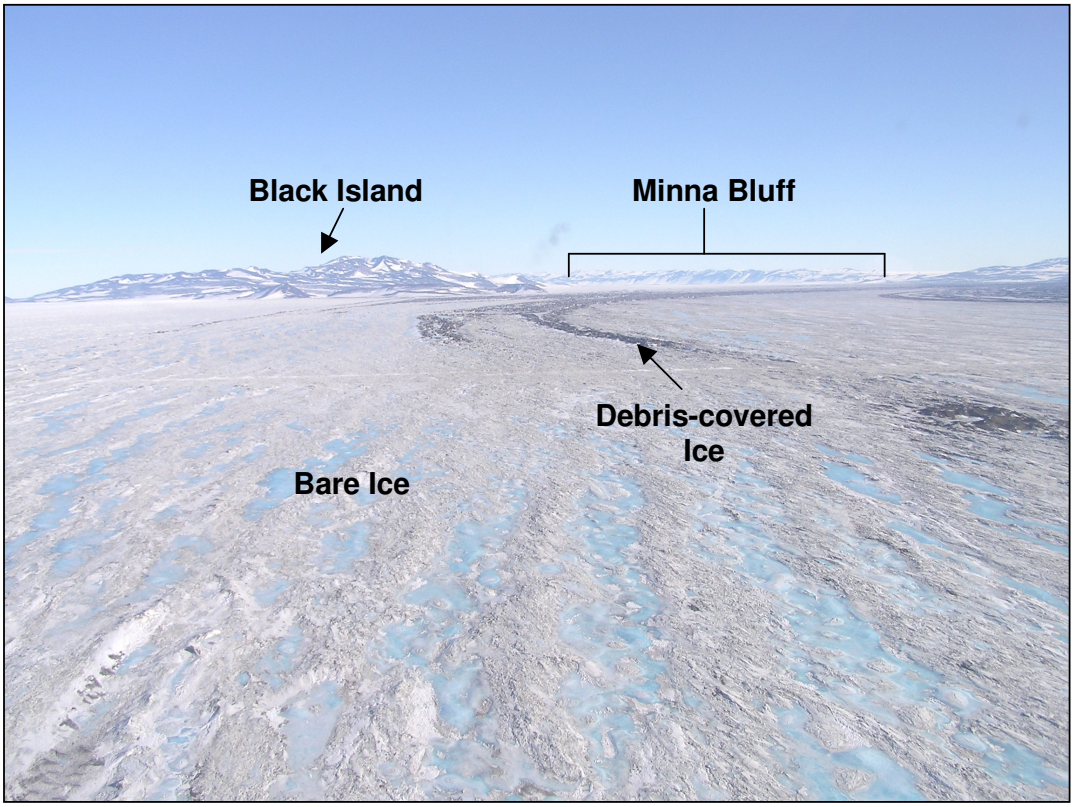

Figure 1.4. The ablation area of the McMurdo Ice Shelf. Photograph is facing south from near the ice shelf front. The bare ice is comprised of both white bubbly ice and blue coloured ice. See Figure 1.2 for relevant map coverage.

In the debris-covered ice areas, bands of marine-derived debris up to ~1 m thick mantle the ice. This type of surface accounts for approximately 6% of the McMurdo Ice Shelf surface area and is primarily in the vicinity of Brown Peninsula (Figure 1.2). The mechanism proposed for the accumulation of such sediment is by a combination of basal freezing and surface ablation (Debenham, 1919, *in* Whitehead, 1989). Extensive research has been conducted on the debris and has confirmed its marine

origins (Swithinbank, 1970; Kellogg and Kellogg, 1987; Whitehead, 1989). The debris is continuously reworked and redistributed across the ice shelf surface (Glasser *et al.*, 2006).

Approximately 20% of the ice shelf surface is covered in meltwater during summertime (Pridmore *et al.,* 1995). The meltwater is in the form of streams, ponds and lakes of up to 10^4 m^2. The melting that occurs during the summer is beneath the surface in the western part of the ice shelf, with a progression to open pools in the east (Paige 1968). According to Paige (1968), this subsurface melt occurs exclusively beneath the surface of the blue glacier ice. Subsurface melt pools are usually 0.5 to 1.0 m deep and 10.0 to 15.0 m in diameter. These pools are covered by a layer of ice that decreases in thickness from around 0.30 to 0.40 m in mid December to as little as 0.07 m in mid January (McCrae 1984).

1.6 Thesis objectives and approach

To improve current understanding of ice-atmosphere linkages, the overall aim of this research is to demonstrate the relationship between variations in summertime surface mass balance of the McMurdo Ice Shelf and atmospheric processes. In order to achieve this overall aim, the following specific objectives will be addressed:

- Characterize the McMurdo Ice Shelf climate for the summers of 2003-2004 and 2004-2005.
- Identify distinct synoptic situations that occur during the summer.
- Determine surface energy and surface mass balance of two key surfaces of the McMurdo Ice Shelf and link these with the distinct synoptic types.
- Detect surface characteristics used for distributed mass balance modelling.
- Determine the pattern of summertime surface mass balance over the entire McMurdo Ice Shelf and associate this with the climate characteristics.

The approach encompasses a broad range of techniques. These include: analysis of data from specific field measurements and permanent climate stations, application of a manual synoptic classification, application of a energy balance mass balance model, adapting the model to include debris-covered ice processes, manipulation of remote sensing imagery, as well as modification of the model to run in a distributed fashion.

1.7 Thesis structure

This thesis comprises six chapters. As the thesis involves a diverse range of methods, the structure is such that results are placed as close as possible to the relevant methodology. This chapter introduces the physical principles of the ice-atmosphere energy exchanges, discusses the key themes which have emerged in previous studies, and describes the general character of the study area. Chapter two introduces the reader to the regional weather and climate and examines distinct synoptic situations for the area. Chapter three adapts a surface energy balance model and uses it to investigate the SEB for two surface types found in the ablation area of the McMurdo Ice Shelf. Chapter four uses remote sensing and ground-based methods to explore spatial characteristics of the ice shelf used for distributed mass balance modelling. The fifth chapter draws together the key strands of the previous chapters and examines spatial patterns of surface mass balance over two summers using a distributed energy balance model. Chapter six comprises a summary of the research findings, followed by a discussion of the significance and implications.

2 Climatological setting

2.1 Introduction

In order to provide a climatological context for this research and to help understand how the atmosphere interacts with the surface of the McMurdo Ice Shelf, this chapter considers the climate of the McMurdo Ice Shelf by addressing the following specific objectives:

- Describe and compare climate characteristics during the summers of 2003-2004 and 2004-2005, and place them into a longer-term context.
- Identify distinct synoptic situations that occurred during the two summers.
- Determine the microclimate of two key surfaces at the McMurdo Ice shelf, and the key differences between them.
- Associate the microclimate of the two key surfaces with the distinct synoptic types.

The chapter begins with a description of the regional climate. Next, using data from permanent weather stations, the two summers used in the rest of this research are compared and a discussion on how representative they are in a longer-term context is provided. A synoptic classification is then presented. Next, the microclimate of the McMurdo Ice Shelf surface is examined for a bare and a debris-covered ice site. The microclimate section includes a description of field instrumentation and sampling regime as well as demonstrating how the surface microclimate is dependent on synoptic situation. The chapter concludes with a summary of the main findings.

2.2 Regional Overview

The McMurdo Ice Shelf is the site of convergence of several different air masses: dry, very cold air from the high East Antarctic continental plateau; cold, moister air from the Ross Ice Shelf; and relatively warm, moist air from the Ross Sea (Monaghan *et al.,* 2005). As with other coastal regions of Antarctica, the synoptic scale circulation is characterised by east-moving low pressure systems (King and Turner, 1997 p.189). These large depressions are generally mature, dissipating, and have a general meridional movement, but due to the topographical contrast between the oceans and the Antarctic mainland they are deflected to the east.

The Ross Sea Embayment and Ice Shelf is a location of annually average low pressure (Simmonds *et al.*, 2003). Occasionally, low-pressure systems forming the circumpolar trough travel around Cape Adare (Figure 1.1) and situate themselves in the Ross Sea Embayment. On the eastern side of these low pressure systems, relatively warm, moist air is advected towards the coast whilst on the western side, the colder, drier air of the continent is drawn seaward (King and Turner, 1997). This situation allows for moist warm air to be drawn across the Ross Ice Shelf and into the McMurdo Sound area for extended periods. These southerly winds are associated with an influx of warm, moist air (O'Connor and Bromwich, 1988).

Winds in the region have been the subject of numerous studies. Katabatic winds in the Ross Ice Shelf area propagate over the Ross Ice Shelf and extend to the Ross Sea (Bromwich *et al.,* 1992). They are most common in winter, and are enhanced by the positioning of a synoptic scale low-pressure system over the Amunsden Sea causing southeasterly flow over the ice shelf. The regional air has high stability, especially in winter, as a result a strong inversion that develops over the Ross Ice Shelf (O'Connor and Bromwich, 1988). Barrier winds are also a characteristic of the area, O'Connor and Bromwich (1988) found barrier winds in the vicinity of Ross Island, created by the blocking effect of the TransAntarctic Mountains on the wind flowing from the east, and then being deflected to the north. At a localised scale, features such as Minna Bluff and Ross Island (Figure 2.1) further affect the wind, causing flow splitting and stagnation (Sinclair, 1988; Monaghan *et al.,* 2005). Windless Bight (Figure 1.2) is an area of anomalous calm as a result of this stagnation.

Temperature also varies over small spatial scales: the 1977-2004 mean average annual temperature for McMurdo Station (Figure 1.2) was -16.7ºC, while for the same time period the mean annual temperature reported at Scott Base (Figure 1.2) was -19.4 ºC. This difference is the result of flow splitting around Hut Point Peninsula, further emphasising the importance of local topographical effects (King and Turner, 1997). Fog occurrence is common in the area during the summer months and can often result in surface deposits (Lazzara, 2006).

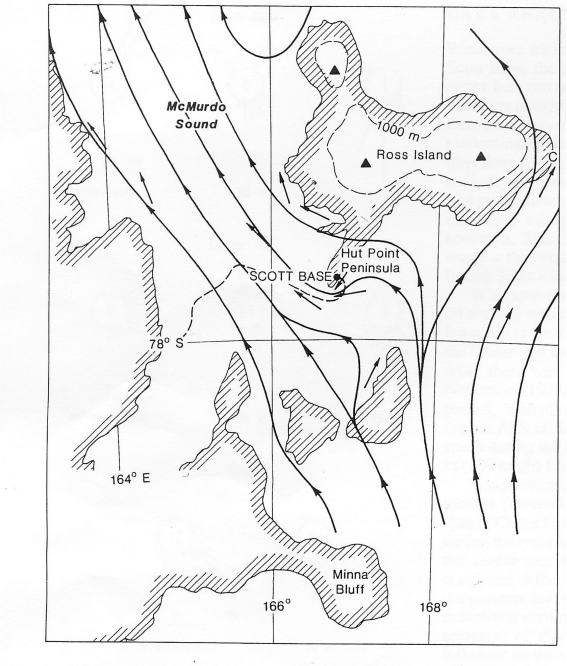

Figure 2.1 The McMurdo Ice Shelf area indicating streamlines of prevailing winds at the sites located at the heads of the arrow (Sinclair 1988 p238).

Precipitation in the region varies considerably in space, with the mean at McMurdo Station approximately 180-190 mm per annum (Monaghan *et al.*, 2006). Complicating this picture is the redistribution of snow by wind, as blowing snow is commonly observed in the area (Monaghan *et al.*, 2006). However, maximum wind speed and precipitation are reported to occur in the winter months (Bromwich, 1988; King and Turner, 1997; Monaghan *et al.*, 2006) suggesting that redistribution is not as important during the summer.

2.3 Seasonal Setting

Using standard climate observations from Scott Base and McMurdo Station, it is possible to compare and contrast the general climate conditions during the summers investigated in this research (2003-2004 and 2004-2005). At these sites, observations have been made since as early as 1957, making it possible to place these two summers in a longer-term context and to assess how representative they are.

Long-term observations were obtained from NIWA (National Institute of Water and Atmospheric Science) for the manual and automatic weather stations located at Scott Base. These data include air temperature, pressure, global radiation, wind speed, and wind direction. Additionally, observations of precipitation, cloud cover, wind speed and direction for McMurdo Station were obtained from the AMRC (Antarctic Meteorological Research Center) archives. While the data from these two locations are considered generally representative of the climate in the area, both stations are not located on the ice shelf, and, as discussed in section 2.2, exhibit different wind dynamics to elsewhere in the region. Therefore, in order to assess the wind environment during the summers of interest, summer data were also obtained from archives at the University of Wisconsin for several automatic weather stations located in the McMurdo region (Figure 2.2).

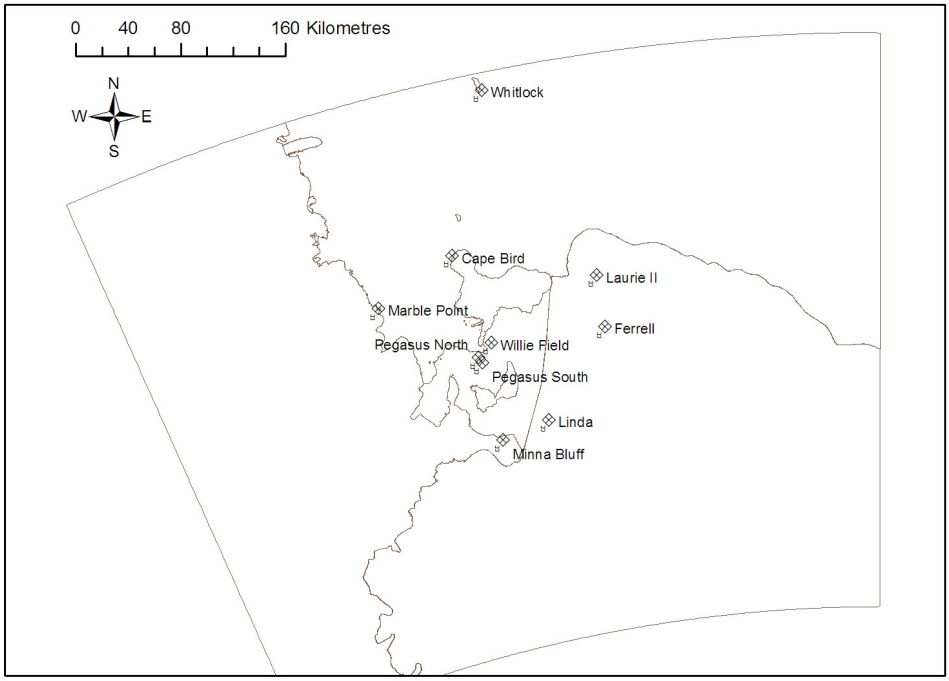

Figure 2.2 Locations of Automatic Weather Stations (AWS) in the McMurdo Region. Data from stations Whitlock, Minna Bluff, Linda, Ferrell, Marble Point, and Pegasus North and South were used in this research.

The distinction of four seasons in Antarctica is difficult to make as most locations exhibit a classic 'coreless' winter during which temperatures vary only a small amount followed by a short peaked summer (Figure 2.3). This cycle makes climatological analysis using a standard three-month definition of summer inappropriate (King and Turner, 1997). In an attempt to provide an objective definition of the seasons, Périard and Pettré (1993) defined summer as beginning in late November to the end of February for Dumont d'Urville. The melt season is also difficult to define, as, while most coastal Antarctic melting occurs in December and January (Zwally and Fiegles, 1994), the length of the melt season has been shown to vary considerably. For example, Fahnestock *et al*. (2002) found that melt season on Antarctic Peninsula ice shelves varied between 0 and ~124 days between 1978 and 2000. Therefore, in order to encompass the melt season, the rest of this research will define the summer period as that being November through February, inclusive.

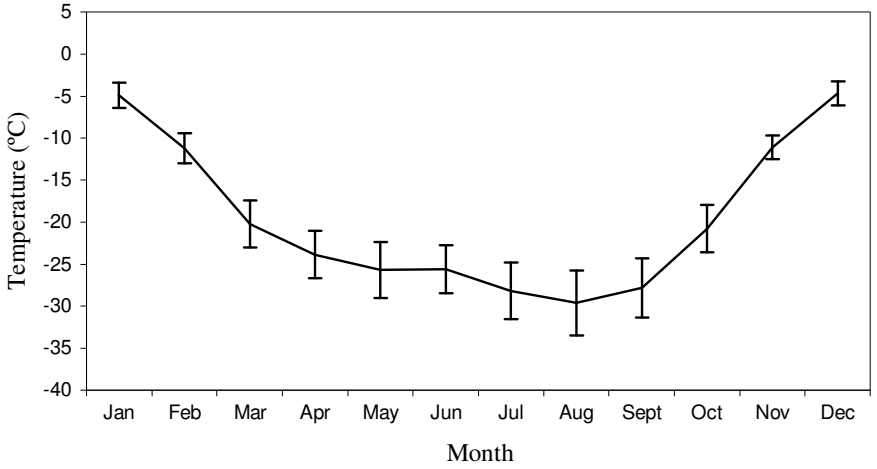

Figure 2.3 Mean monthly air temperature at 2100(UTC) recorded at Scott Base for 1964 – 2005. Error bars shown are the standard deviation.

The summers of 2003-2004 and 2004-2005 were distinctly different (Table 2.1). Notably the 2004-2005 summer had higher air temperatures, and more precipitation, while 2003-2004 had higher relative humidity and pressure (Table 2.1). All mean monthly temperatures were lower during the 2003-2004 summer, with the exception of December 2003, which was 1.4 ºC higher. Monthly maximum temperatures were consistently lower for 2003-2004. Overall, these temperatures equated to the 2003-2004 summer being 1.5 ºC lower at McMurdo Station and 2.0 ºC at Scott Base than during the 2004-2005 summer. It was determined that the summertime temperatures recorded at Scott Base for 2003-2004 were

statistically distinct from 2004-2005 and that 2004-2005 were statistically distinct from the long-term mean (Appendix A, Table A.1).

Table 2.1 Climate variables from Scott Base and McMurdo Station for a) the 2003-2004 summer period, and b) 2004-2005 summer period.

a) 2003-2004	November	December	January	February	Nov-Feb combined
McMurdo Station					
Mean temperature (ºC)	-9.6	-2.4	-3.4	-8.8	-6.1
Maximum temperature (ºC)	0.6	7.0	5.4	1.2	7.0
Minimum temperature (ºC)	-21.1	-10.0	-15.9	-22.2	-22.2
Wind speed (m s^{-1})	8.7	8.8	7.7	7.0	8.0
Wind Direction	71	85	73	64	
Total Precipitation (mm w.e.)	0.7	37.3	5.3	1.3	51.6
Sky cover (8ths)	5.7	5.5	4.8	5.0	5.2
Scott Base					
Mean temperature (ºC)	-12.5	-4.8	-7.0	-12.6	-9.2
Pressure (hPa)	989.1	1000.3	991.3	1000.7	995.3
Relative humidity (%)	64	72	80	71	72

b) 2004-2005	November	December	January	February	Nov-Feb combined
McMurdo Station					
Mean temperature (ºC)	-6.6	-1.0	-2.3	-8.7	-4.6
Maximum temperature (ºC)	2.7	6.0	5.7	3.5	6.0
Minimum temperature (ºC)	-19.4	-8.8	-8.9	-22.7	-22.7
Wind speed (m s^{-1})	8.4	7.7	8.9	8.9	8.5
Wind Direction	99	55	99	79	
Total Precipitation (mm w.e.)	9.4	9.9	46.0	4.3	69.6
Sky cover (8ths)	5.3	4.6	5.8	5.1	5.2
Scott Base					
Mean temperature (ºC)	-9.5	-3.3	-4.6	-11.2	-7.2
Pressure (hPa)	984.1	997	993.4	985.9	990.1
Relative humidity (%)	68	71	80	63	71

Pressure was highest during the 2003-2004 summer, with all but January being higher than in 2004-2005, giving a mean difference of 5 hPa. More precipitation was recorded during all summer months of 2004-2005 with the exception of December (Table 2.1). December 2003 and January 2005 had a particularly high amount of precipitation (Table 2.1). Relative humidity varied for each month, with the most exceptional being a 21% decrease between

January and February 2005 (Table 2.1). For both summers, the mean wind was from the eastnortheast sector with 2004-2005 having the strongest overall winds (Table 2.1).

Both summers exhibited typical climatic patterns as shown in long-term records (Table 2.2), with an increase in temperature and relative humidity during January and February and a decrease in wind speed compared with the winter months yet some features in terms of the long-term record can be observed, especially in the air temperature records.

Table 2.2 Long-term mean variables recorded at Scott Base. The long-term mean of temperature and pressure are based on daily 2100 (UTC) observations made from 1957 – 2005. Relative humidity data are from automated weather station data daily means from 1988-2005.

	November	December	January	February	Nov-Feb combined
Mean temperature (ºC)	-11.1	-4.6	-4.9	-11.2	-6.1
Pressure (hPa)	987.0	992.5	994.2	993.1	995.3
Relative humidity (%)	69	74	77	71	72

The air temperature was consistently lower during the summer of 2003-2004 than the long-term mean (Figure 2.4). In addition, during this summer, pressure was higher than the long-term record with the exception of February (Table 2.2). Over the four-month summer, relative humidity was similar to the long-term mean, with it being slightly low during the first two months and then slightly high for the second two.

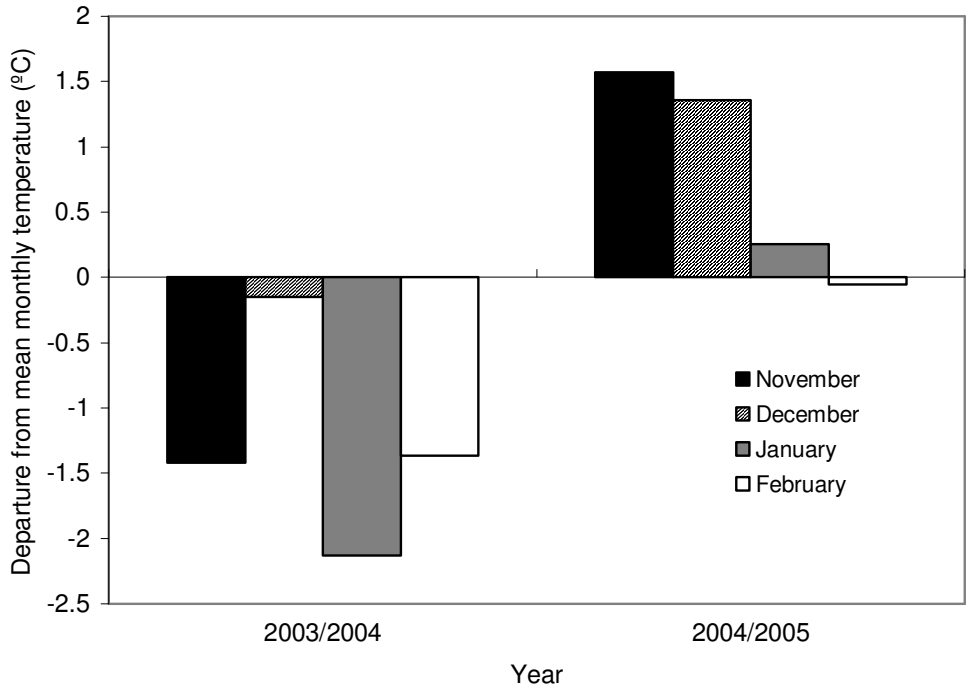

Figure 2.4 Departures from the Scott Base monthly mean temperature recorded at Scott Base based on daily 2100 (UTC) observations made from 1957 – 2005.

The 2004-2005 summer was also distinctive in terms of temperature. During this summer, the temperatures were higher than the long term mean for all months except February, when the temperature was very similar to the long-term record (Figure 2.4, Table 2.2). Pressure recorded during the period was less consistent, with both lower and higher values reported, and overall pressure being lower by 1.6 hPa. Relative humidity was overall lower than the long-term mean by 2.2 hPa for the summer, although this value was influenced by February, which was 7.3 hPa lower the long-term mean for that month. Of note is a relatively high mean humidity value (80.2%) reported during January 2005.

In summary, the summers of 2003-2004 and 2004-2005 were dissimilar. The summer of 2003-2004 was cooler and had higher pressures than the long-term records. Conversely, 2004-2005 summer was warmer than usual.

2.4 Synoptic conditions

To further explore differences between the two summer periods - and to link atmospheric circulation with the microclimate - distinct synoptic conditions were identified using synoptic classification.

The only southern high latitude synoptic classification found in the literature was that by Braun *et al.* (2001) for the King George Ice Cap, South Shetland Islands. Unfortunately, because their work was based on direction of air mass advection and very site specific it could not be used for this research. Therefore, as no pre-existing standard synoptic classification which applied to the McMurdo Ice Shelf region was available, a new synoptic classification was carried out.

While much recent work has used automated classification systems (Yarnal *et al.*, 2001), manual synoptic typing is still a commonly used procedure and allows identification of synoptic types that may not be identified using automated processes (Barry and Carleton, 2001; Yarnal *et al.,* 2001). Misclassification may occur during both manual and automated analysis due to the dynamic nature of the atmosphere. In this study, a manual synoptic classification was performed. As it is a subjective procedure, manual classification is difficult to replicate, so in order to create as an objective approach as possible, the following procedure was used.

Composite satellite images focused on the McMurdo Region were obtained from the Antarctic Meteorological Research Centre (AMRC), at the University of Wisconsin. The composite image consists of a mosaic of infrared imagery from geostationary and polar orbiting satellite data, superimposed with surface mean sea level pressure charts (Figure 2.5). Images are centred over Ross Island, and were compiled for every 12-hour time period for November 2003 to February 2004 and November 2004 to February 2005.

Pressure and flow parameters were identified using printed images and a predefined window (~800 x 600 km) centered on the McMurdo Ice Shelf (Figure 2.5). For each 12-hr composite image, isobar curvature within this window was recorded as either cyclonic, anticylconic or indistinguishable. Spacing of isobars was measured as a proxy for intensity of the gradient wind, and the direction of the gradient wind for each image was recorded as

a compass coordinate. Using these data, a simple classification was performed by splitting the images into groups of cyclonic/anticyclonic curvature and by further splitting the cyclonic group based on the isobar gradient and wind direction. This process identified three distinct classes: a) Cyclonic, isobaric spacing < 4 mb/200 km, wind direction from Southern sector; b) Anticyclonic, isobaric spacing > 4 mb/500 km, no discernable wind direction; c) Cyclonic, isobaric spacing >4 mb/200 km. Each image was then assigned to a class. If all of an image's parameters did not lie within any of the defined classes' thresholds, the image was assigned to a fourth, undefined class. 91% of the 12-hr composite images could be classified into the three distinct classes.

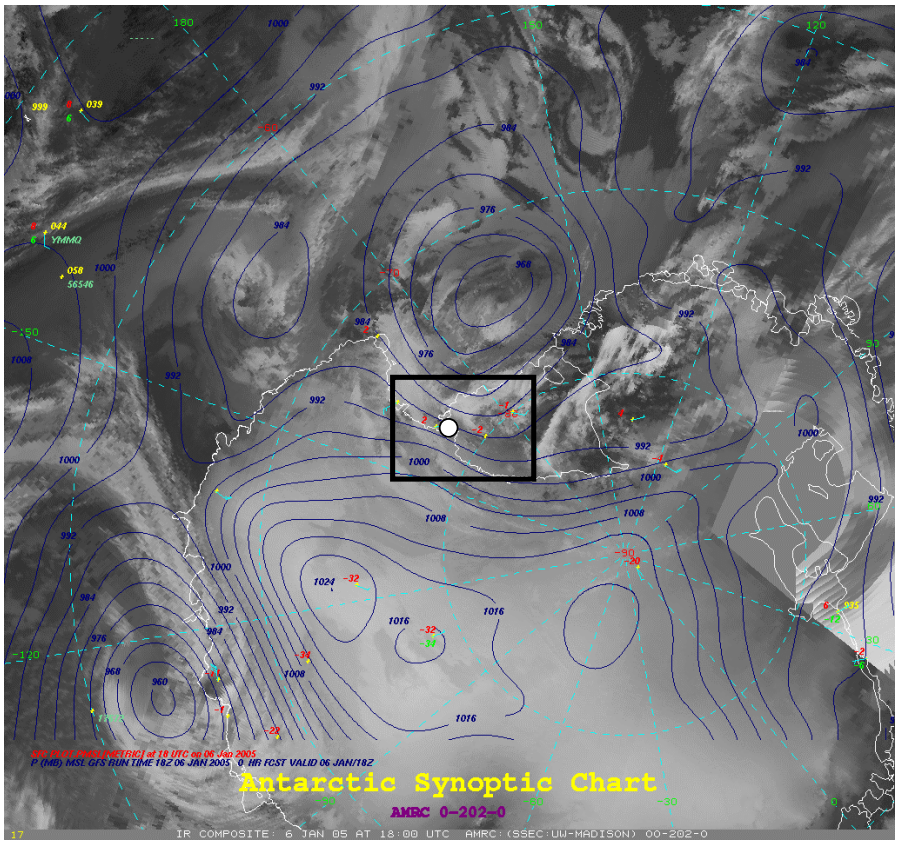

Figure 2.5 Example of a composite image with mean sea level pressure superimposed, used for this research. The black rectangle represents the window used in the initial synoptic classification. The white dot is the location of the McMurdo Ice Shelf.

In order to describe the synoptic types that each of these classes represented, the images for each class were scrutinised at a larger scale (~1500 km), taking into consideration pressure center locations and cloud configuration. A general pattern was identified for each of the classes. The three distinct classes were found to represent:

- Type A: Low pressure system residing in the Ross Sea Embayment.
- Type B: Anticyclonic conditions across region.
- Type C: A trough of low pressure extending into the Ross Sea Embayment.

To further demonstrate that these synoptic types represent differing conditions, meteorological data from McMurdo Station and Scott Base were also compiled for each type and a Welch t-test was applied for each variable and the synoptic types paired. The Welch t-test was used here as the samples had unequal variances. In several cases the meteorological data were significantly different between the three synoptic types (Table 2.3). As each synoptic type is significantly different from the others in at least two climatic variables (Table 2.3), it is considered that each type is distinct.

Table 2.3 Pairs of synoptic types showing significant differences in meteorological variables recorded at McMurdo Station and Scott Base. Bold pairs are significantly different.

Variable	Level of significance	Synoptic type pairs
McMurdo Station		
Windspeed	<0.05	**A & B, A & C**
	not significant	B & C
Pressure	<0.05	**A & B, B & C**
	not significant	A & C
Precipitation	not significant	A & B, A & C, B & C
Cloud cover	< 0.05	**A & B, A & C**
	not significant	B & C
Air temperature	not significant	A & B, A & C, B & C
Scott Base		
Air temperature	not significant	A & B, A & C, B & C
Relative humidity	<0.05	**B & C**
	not significant	A & B, A & C
Global radiation	< 0.05	**A & B, A & C**
	not significant	B & C

To allow for future analysis on a daily basis (Sections 2.6.1, 2.7.1, 3.6.4, 3.7.4), each day needed to be assigned a single synoptic type. Because 12-hour images were used in the above analysis, further classification was necessary. To perform this reclassification, each day was assigned a synoptic type from Table 2.4. Thus, if both of the 12-hour images for a given day were originally assigned the same type, the day was defined as having that type.

This reclassification reduced the total number of days able to be classified to 200 (83 %). No days had the combination of type A and B, further supporting the suggestion that these two types are distinct.

Table 2.4 Synoptic types used to classify each of the 2003-2004 and 2004-2005 summer. Each day assigned one of these synoptic types based on the two 12-hour images for that day.

Type	Description	No. images	Proportion
A	Both 12-hour images Type A as defined in text	66	14%
B	Both 12-hour images Type B as defined in text	122	25%
C	Both 12-hour images Type C as defined in text	98	20%
AB	One image type A, one type B	0	0
AC	One image type A, one type C	59	12%
BC	One image type B, one type C	56	12%
D	One image undefined and one as A,B, or C. Or both images undefined.	81	17%

As it was important to assign each day to a distinct synoptic type, only Types A through C are used for further analysis as the other types are considered transitional and, by definition, not distinct. The following describes each of the three distinct synoptic types.

2.4.1 Type A: Low pressure system residing in the Ross Sea Embayment

This type is characterised by a deep low-pressure system located within the Ross Sea Embayment. The low-pressure systems originate in the circumpolar trough, and migrate into the Ross Sea Embayment, where they remain for several days (King and Turner, 1997). Because of the positioning of these systems (Figure 2.6a), air is drawn from the Ross Sea, across the Ross Ice Shelf and towards the study site from the south. Type A conditions occurred more frequently in 2004-2005 summer with a 5% difference between the summers (Table 2.5).

McMurdo Station received its strongest winds during this type of situation (Figure 2.9), these were from the southeast sector. Winds in the wider region were strong and predominantly from the south and southwest (Figure 2.6b). Mean atmospheric pressure at Scott Base was relatively low during Type A conditions especially in comparison to those during Type B conditions (Table 2.6). The mean temperature during Type A conditions at Scott Base was higher than during the other conditions (Table 2.6). Relative humidity was not higher than during Type B conditions, which would be expected, but it was higher than

during Type C conditions. Cloud fraction was the highest during Type A conditions, and global radiation at Scott Base was lower than during other situations (Table 2.6).

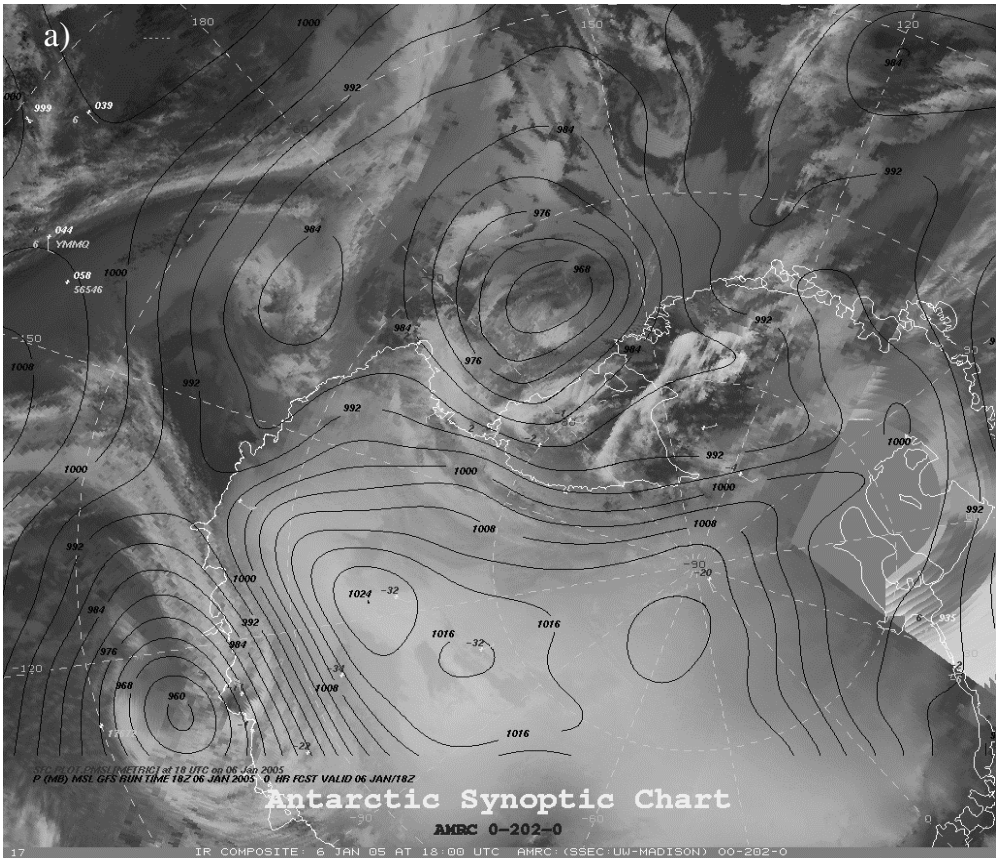

Figure 2.6 Synoptic Type A, Low pressure system residing in the Ross Sea Embayment a) typical synoptic chart, b) mean daily winds at surrounding automatic weather stations (AWS).

2.4.2 Type B: Anticyclonic conditions across region

The second situation was typified by anticyclonic conditions over the Ross Ice Shelf (Figure 2.7a). Regional pressures are high (Table 2.6), and gradient winds were minimal. These situations usually coincided with low-pressure systems tracking to the north of the Ross Sea Embayment, but not encroaching into it. Winds were lighter and more variable than during Type A conditions (Figure 2.7b), although some stronger winds were received from the southeast. Winds were variable in the vicinity of Ross Island AWS in the immediate vicinity of McMurdo Ice Shelf are variable but generally are low strength with a southeast to southwest origin (Figure 2.7b). Type B conditions were recorded more than twice as often during the 2003-2004 summer compared with 2004-2005 (Table 2.5).

Mean air temperature at McMurdo Station was over 1ºC higher during Type B conditions than Type A (Table 2.6), which may be accounted for by the surrounding land and overlying air warming up during lower wind speeds and high insolation. Relative humidity was also higher during these conditions. Pressure, on average, was 8 hPa greater than during for Type A conditions (Table 2.6). Global radiation received at Scott Base was the maximum during these conditions and cloud fraction the lowest (Table 2.6) which would be expected during anticylonic systems.

2.4.3 Type C: Trough of low pressure extending into the Ross Sea Embayment

While most synoptic scale low-pressure systems do not track into the Ross Sea Embayment, there are periods when the pressure in the area is reduced by a trough extending into the embayment (Figure 2.8a). This occurs when a low-pressure system is situated to the north of the embayment and travelling eastward.

Type C conditions were the most frequent during 2004-2005, accounting for 26% of of this summer (Table 2.5). The winds recorded at McMurdo Station were variable but most coming from the east and northeast (Figure 2.9). Winds were variable across the region with an apparent northeasterly showing at three AWS in agreement with the winds from McMurdo (Figure 2.8b).

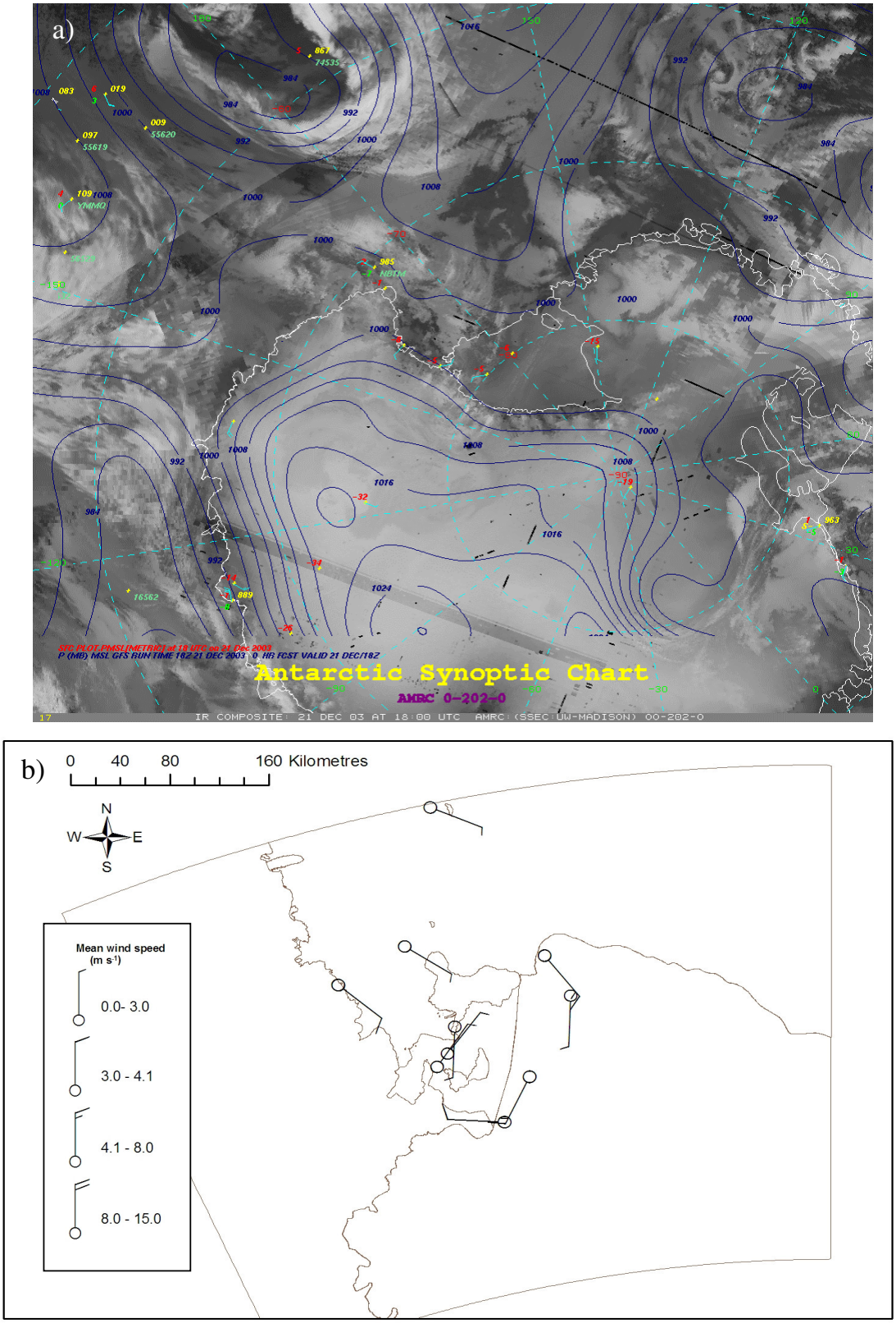

Figure 2.7 Synoptic Type B, anticyclonic conditions across region a) typical synoptic chart, b) mean daily winds at surrounding automatic weather stations (AWS).

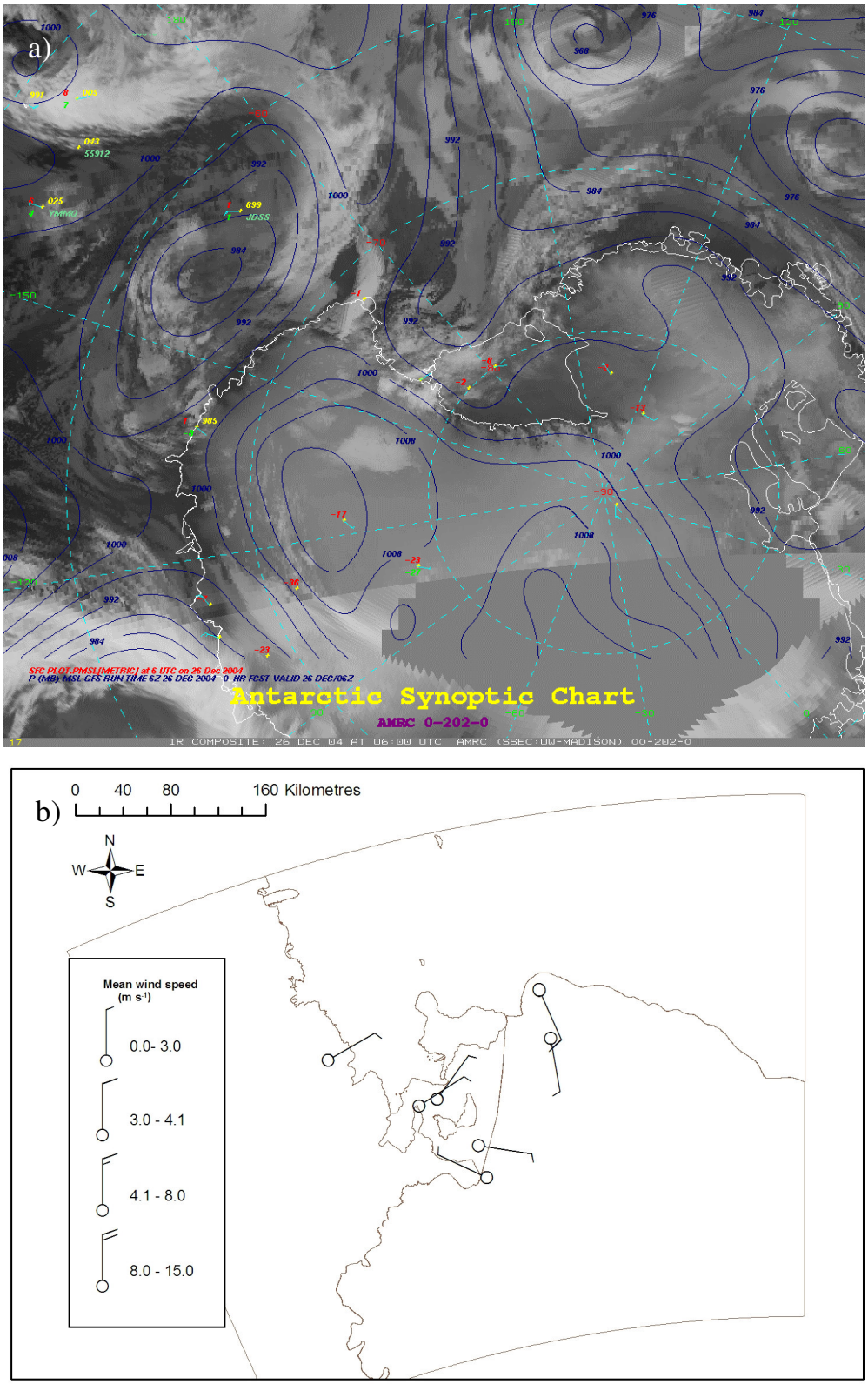

Figure 2.8 Synoptic Type C, Low pressure extending into the Ross Sea Embayment a) typical synoptic chart, b) mean daily winds at surrounding automatic weather stations (AWS).

The mean temperature during this situation was in-between the other two types, yet the coldest for Scott Base (Table 2.6). Mean atmospheric pressure was also intermediate between Type A and Type B pressures, but closer to that experienced during Type A. (Table 2.6). The most outstanding feature of Type C conditions was the low relative humidity (Table 2.6). These conditions dominated February 2005, and explain the apparently low humidity then. One possible explanation is that during these conditions the drier air of the continent is drawn towards Scott Base, as low temperatures accompany the low humidity.

Table 2.5 Frequency of classified synoptic types during November 2003 – February 2004 and November 2004 – February 2005.

Type	Description	03/04	04/05
A	Low pressure system residing in the Ross Sea Embayment	11%	16%
B	Anticyclonic conditions across region	34%	15%
C	Trough of low pressure extending into the Ross Sea Embayment	13%	26%

Table 2.6 Mean daily surface climatic conditions during the three synoptic classes defined in text taken from Scott Base and McMurdo Station. Note of the periods analysed November 2003 – February 2004 and November 2004 – February 2005.

	Type A	Type B	Type C
McMurdo Station			
Mean temperature (ºC)	-6.4	-5.0	-5.3
Wind speed (m s^{-1})	12.6	7.4	7.6
Wind Direction (º)	106	46	62
Mean precipitation (mm w.e.)	1.33	0.17	0.26
Sky cover (8ths)	6.8	5.0	4.7
Scott Base			
Mean temperature (ºC)	-7.3	-7.6	-7.7
Pressure (hPa)	990	998	992
Relative humidity (%)	72	75	67
Global radiation (MJ $m^{-2}d^{-1}$)	19.4	23.7	23.5

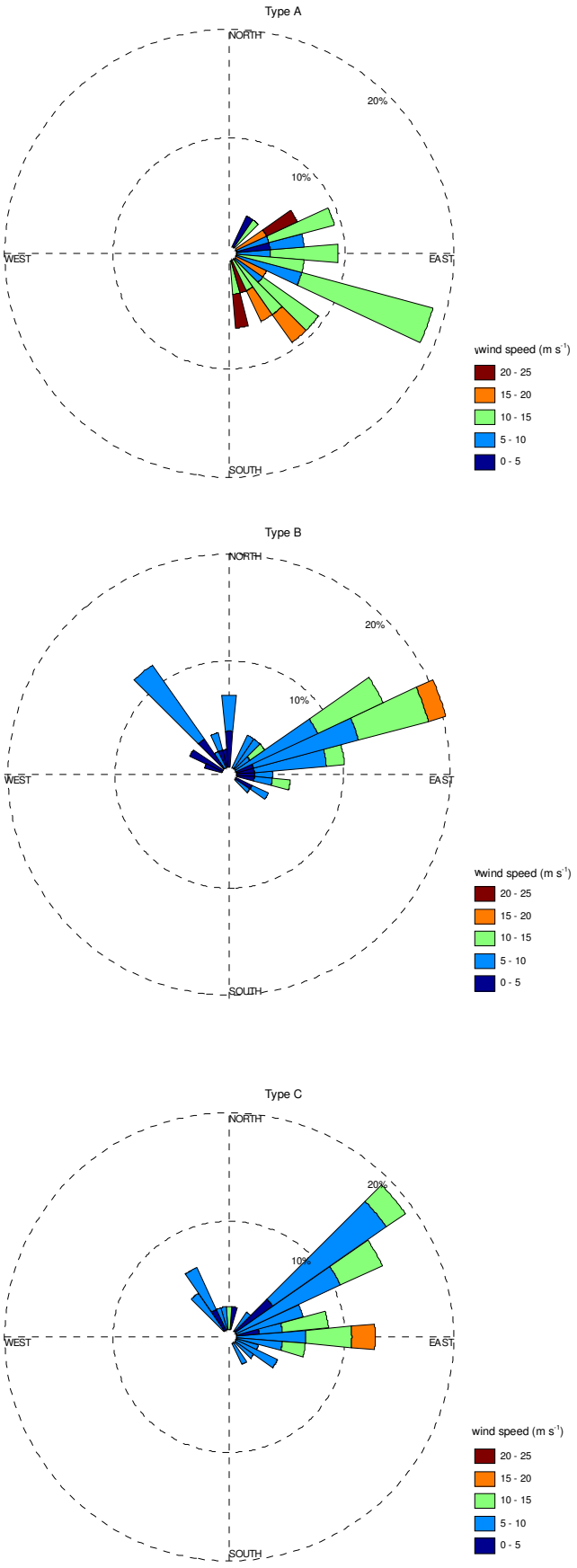

Figure 2.9 Wind speed and direction recorded at McMurdo Station during the summers of 2003-2004 and 2004-2005 according to synoptic type as defined in text.

2.5 Field instrumentation and deployment

In order to explore the microclimate of the surface of the McMurdo Ice Shelf (Sections 2.6, 2.7) and to calculate surface energy balance (Chapter 3), a customised automatic weather station (AWS) was deployed on the ice shelf during the summers of 2003-2004 and 2004-2005. Additionally, direct measurements were made of turbulent fluxes using an eddy covariance system and of net ablation using stakes.

2.5.1 Sites and sampling regime

The AWS was located on an area of debris-covered ice for a period during the summer of 2003-2004 and on a bare ice site during 2004-2005. The positioning of the instrumentation was carefully chosen so that measurements were representative of the bare ice and debris-covered ice sites. Energy balance measurements require an extensive fetch of the surface type so that advective effects can be assumed negligible. In the case of the bare ice site, this positioning was simple as the surface is similar in all directions for many kilometres. At the debris-covered ice site, the instruments were located for the largest possible homogenous fetch.

The debris-covered ice site was located in an area of ice covered by a layer of debris, near the end of Brown Peninsula (Figure 2.11). The area had low, rolling topography with frozen ponds in the hollows. The AWS was located on a level site, such that it was surrounded by as much level ground as possible. In order to account for the high variation in topography, the AWS was also sited with respect to the predominant wind direction. The AWS was placed in a relatively wide and elongated hollow, oriented in the direction of the reported prevailing wind direction (See Figure 2.1). Upwind (southeast) there was approximately 90 m of level debris-covered ice, while downwind (northwest) there was approximately 75 m of level debris-covered ice and then a frozen pond. To either side of the basin were small rolling mounds up to 3 m. The debris layer here was approximately 0.60 - 1.00 m thick, and consisted of sand and gravel with occasional coarser material. This site was instrumented for 87 days during the summer of 2003-2004, and for 11 days in early summer of 2004-2005 (Figure 2.10). Although the observations at the two sites cover different periods, they are both sufficiently long to provide a broad indication of the conditions and allow comparisons.

The bare ice site was located on an exposed ice surface to the east of Brown Peninsula (Figure 2.11). The ice in the area consisted of both white bubbly ice and blue glacier ice and was free of debris. The topography was level in all directions (Figure 2.12). The bare ice site was instrumented for 48 days during the 2004-2005 summer (Figure 2.10).

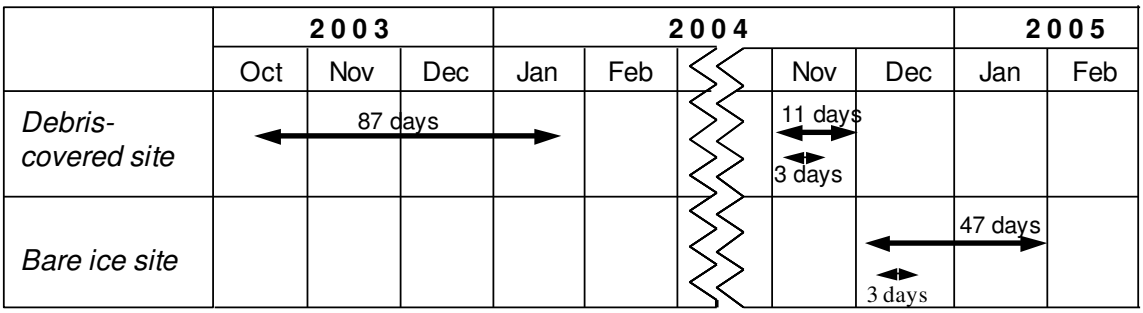

Figure 2.10 Overview of automatic weather station (AWS) sampling period. The 3-day periods indicate eddy covariance measurement.

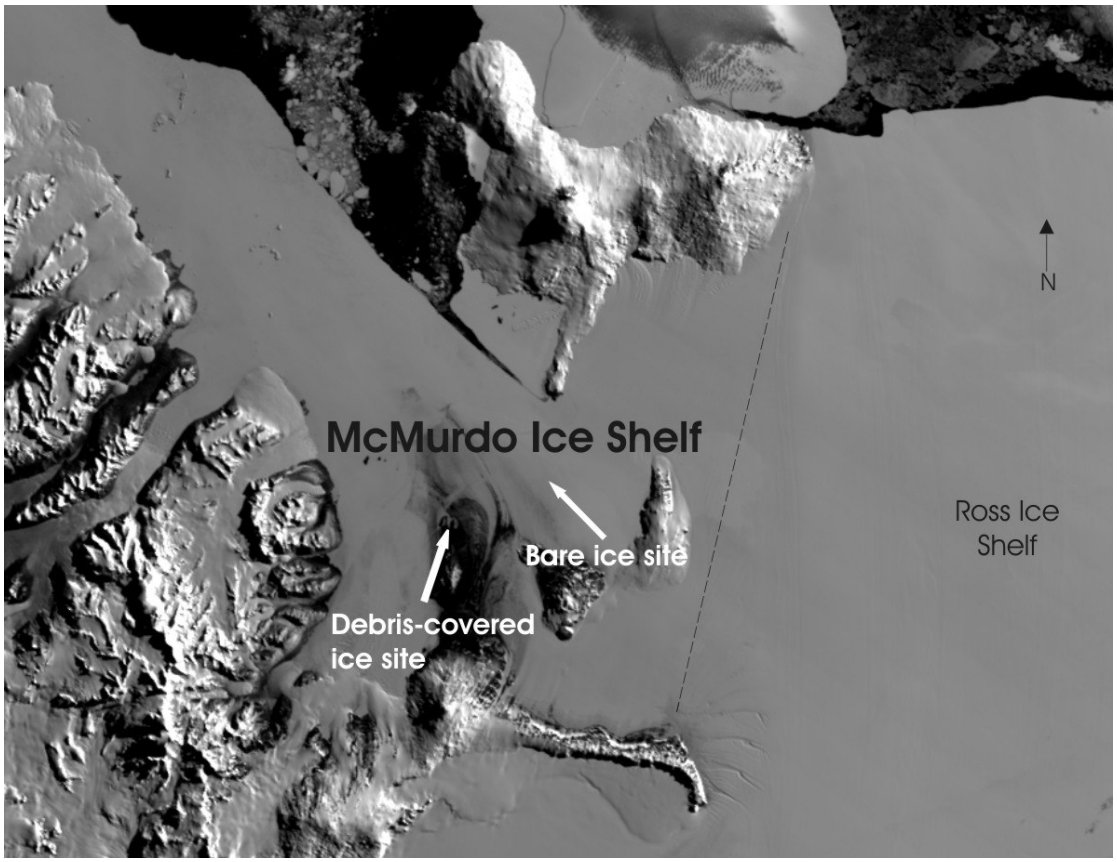

Figure 2.11 Location of surface energy balance measurements bare ice, and debris-covered ice. For topographical feature names, please refer to Figure 1.2.

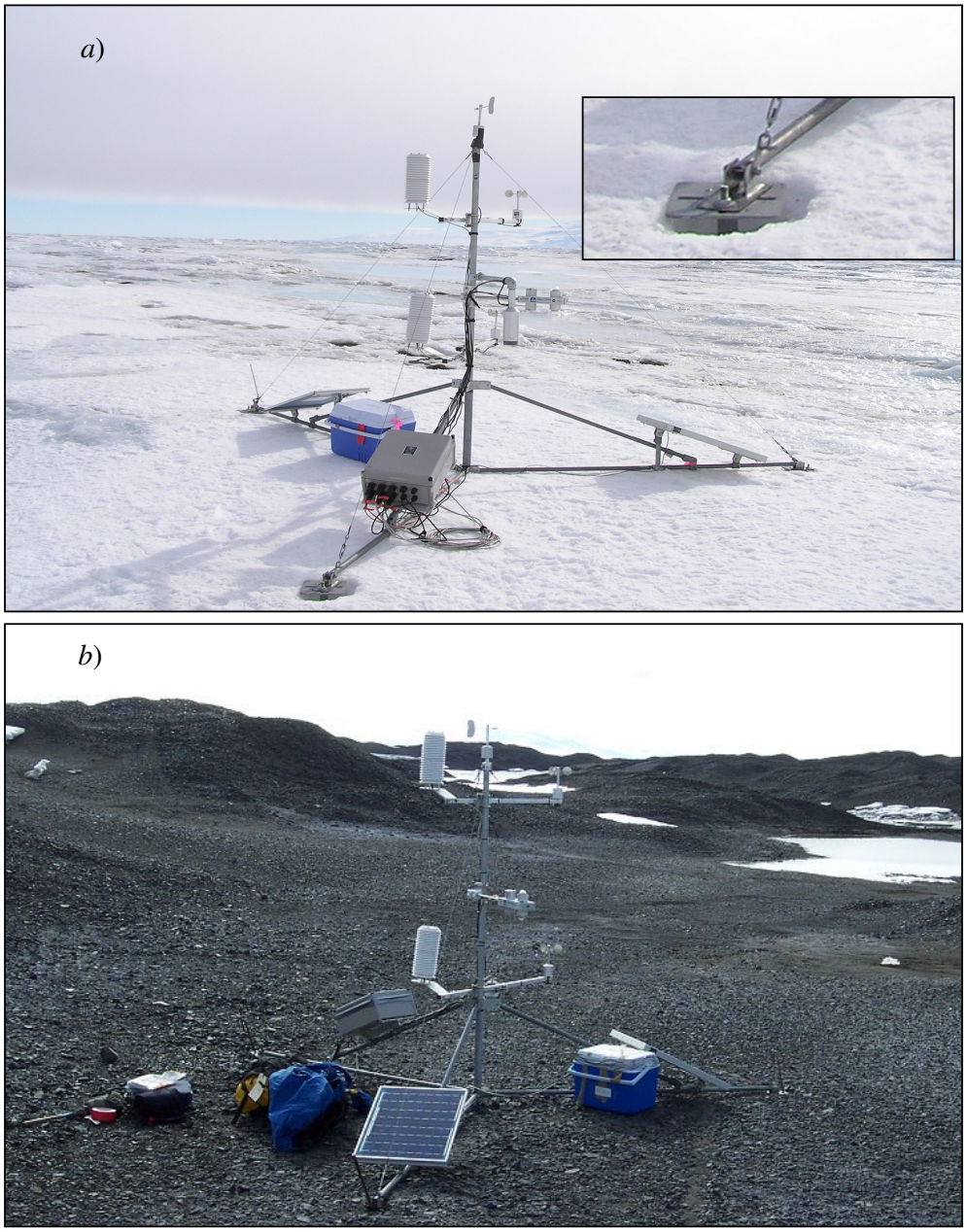

Figure 2.12 Sampling sites used to measure the microclimate and radiation budget in the ablation area of the McMurdo Ice Shelf, showing the automatic weather station (AWS) customised for this research a) Bare ice surface, with inset showing specially made legs. b) Debris-covered ice.

2.5.2 Instrumentation and data treatment

Automatic weather station

The automatic weather station was designed for easy installation and transportability by helicopter (all components < 2 m). Sensors were mounted on a pole (Figure 2.13) supported by a fully adjustable tripod, which allows the pole to be installed vertically on uneven ground. At the debris-covered ice site, the AWS was free standing, with the tripod resting directly on the debris surface (Figure 2.12b). At the bare-ice site, in order to prevent any tilting due to differential ablation, each of the tripod legs was attached to a custom-made ice screw (~ 1 m), which was drilled vertically into the ice (Figure 2.12a & inset).

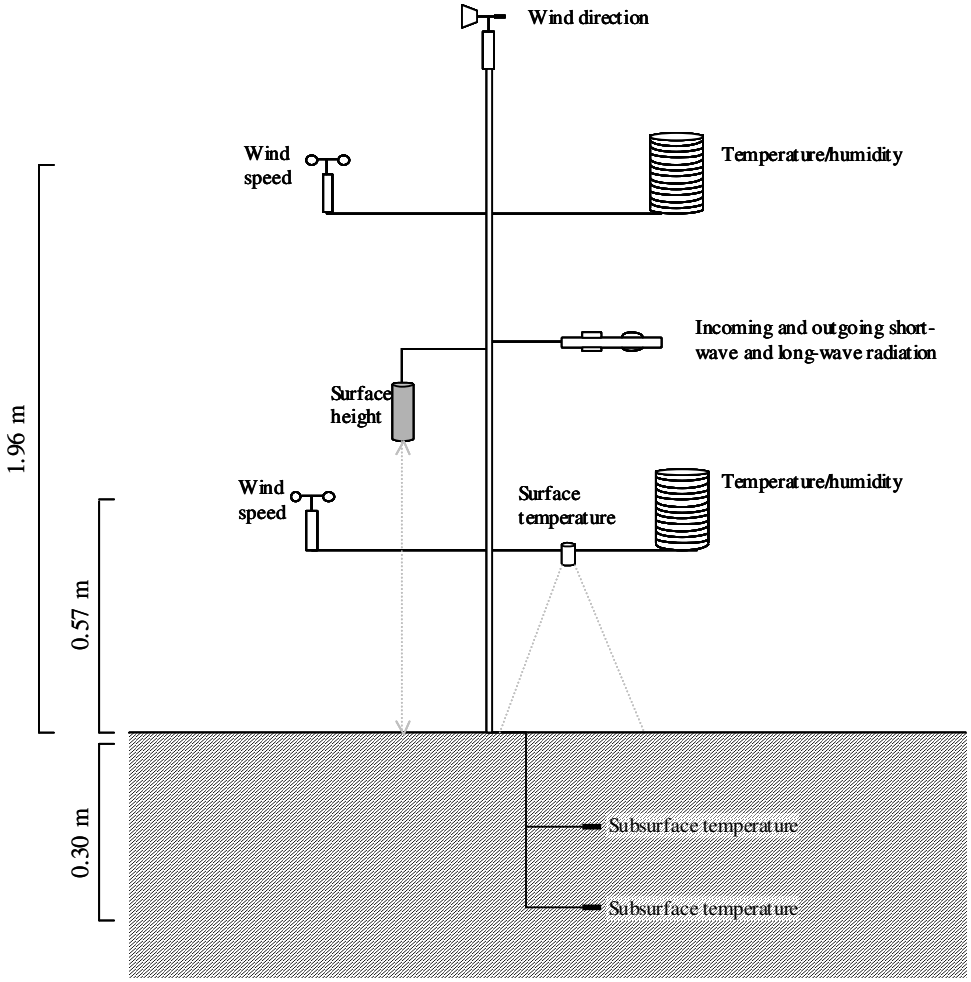

Figure 2.13 Configuration of automatic weather station (AWS) used in measurement of the radiation budget and surface energy balance. Subsurface measurements were only used for debris-covered ice site. Surface height only used for bare ice site. Heights indicated are those for the initial conditions at the debris-covered ice site.

Power was supplied to the AWS system using gel cell batteries, recharged with solar panels (Figure 2.12). Data were recorded using a Campbell Scientific CR23X data logger. All the sensors were sampled at one-second intervals and averaged half hourly. Sensors were chosen to be suited to the environment; model numbers and accuracies of all the sensors are outlined in Table 2.7.

Table 2.7 Sensors used on the AWS with manufacturers specifications.

Sensor	Temperature Range	Reported accuracies
Vaisala HMP45C	-40 to +60 °C	± 0.4ºC (-20ºC) ±2 %RH (0...90 %RH) ±3 %RH (90...100 %RH)
Vector A100LM	-30 to +70 °C	1% of reading between 20Kts and 110Kts (up to 2% above 110Kts, 0.2Kts below 20Kts)
Vector W200P	-50 to +70 °C	± 3° in steady winds over 5m/s (6m/s /WR, 3.5m/s /LV), with +/-2° obtainable following calibration.
Everest I.R. Surface Temperature Sensor (4000.4GL)	-40 C to 100 °C	+/- 0.5 deg C
VAISALA PTB100B	-40 to +60 °C	-20...+45 °C PT100B: ±3 hPa -40...+60 °C PT100B ±4 hPa
Campbell Scientific SR50 Sonic ranging sensor	-30 to +50 °C	± 1 cm or 0.4% of target height (whichever is greater)
Kipp & Zonen CNR1	-40 - +70 °C	Daily totals ± 10%

Radiative fluxes were measured directly using a Kipp and Zonen CNR1 system mounted on the AWS (Figure 2.12, 2.13). This system has both upward and downward facing pyranometers (short-wave) and pyrgeometers (long-wave), as well as an internal thermistor (pt100), which was used to adjust long-wave fluxes with reference to sensor temperature, as measurements of long-wave radiation are sensitive to the sensor heating and cooling. The following temperature correction was applied:

$$L\uparrow = L\uparrow_{measured} + \sigma T_{sensor}^{4} \qquad 2.1$$

$$L\downarrow = L\downarrow_{measured} + \sigma T_{sensor}^{4} \qquad 2.2$$

where σ is the Stefan-Boltzmann constant (5.67×10^{-8} W m^{-2} K^{-4}), T_{sensor} is the temperature measured by the internal thermistor and the $_{measured}$ subscript refers to the raw measured radiative fluxes.

The CNR1 system is also reported to have a poor cosine response when used during large solar zenith angles (Campbell Scientific Inc., 2003a; van den Broeke *et al.*, 2004b; van As *et al.*, 2005a). Although not an issue when the sky is overcast, during clear-sky days this response can cause considerable problems, including albedo values greater than unity. Following a similar method to other researchers (cf. van den Broeke *et al.*, 2004b; van As *et al.*, 2005b), this issue was overcome by determining an accumulated albedo value and adjusting the incoming short-wave radiation accordingly.

Temperature of the ice shelf surface was measured using an Everest infrared surface temperature sensor (4000.4GL). This sensor was mounted facing towards the surface, pointing to an area between the tripod legs. Observations of pressure were made with a Vaisala PTB100B positioned in the box containing the data logger (Figure 2.12). Wind direction was recorded using a Vector W200P mounted at the top of the AWS pole (Figures 2.12, 2.13).

Vertical profiles of temperature, wind speed and humidity were measured using sensors at two heights (Figure 2.13). At the debris-covered ice site, these heights were 0.57 and 1.96 m, and at the bare ice site, they were 1.04 and 1.99 m. At both levels, temperature and humidity were measured using a Vaisala sensor (HMP45C) and wind speed with a Vector anemometer (A100LM). The HMP45C was housed in a radiation shield (Figure 2.12) which allows for natural ventilation, and stops direct heating from the sun. Despite being housed in a shield, due to the lack of artificial ventilation, temperatures could be overestimated during periods of low wind speed and strong insolation.

As the HMP45C measures relative humidity with respect to water rather than ice, readings below freezing are likely to be unrealistically low. Here, the method by Anderson (1994) is used to rescale the relative humidity with respect to ice (e.g. Box and Steffen, 2001; van den Broeke et al., 2004a; van As *et al.*, 2005a; and Cullen *et al.*, 2007b). In order to do this rescaling, the measured relative humidity is first multiplied by the ratio of saturated vapour pressure with respect to water over saturation vapour pressure with respect to ice for the given temperature. Saturation vapour pressures were determined using Goff Gratch type formula from WMO (2000). The second stage of the rescaling is based on the original sensor temperature scaling (a quadratic). However, this stage was not applied here, because

the temperature range was too small to allow fitting a realistic, plausible, quadratic equation to the data. Additionally, the temperature values were well within the sensor's range (–10 to 0 ºC), further suggesting that the data are centred around the turning point of the original quadratic temperature correction curve, where the correction factor would be close to unity anyway. Super-saturation is not accounted for as the instrumentation is unable to measure such values (Box and Steffen, 2001) and its occurrence was found to be infrequent on an AWS located on Halley Ice Shelf (Anderson, 1996). The sensor was brand new when first deployed to the study site, and factory calibrated, but calibration was not performed prior to the second field season or subsequently.

At the debris-covered site, subsurface debris temperature was determined using temperature probes (Campbell Scientific 107) placed within the debris, at depths of 0.15 m and 0.30 m (Figure 2.13). Also, at the bare ice site, surface ablation was determined using an ultrasonic depth gauge (Campbell Scientific SD50). Treatment of the ablation data will be discussed in chapter three (Section 3.4.2).

Ablation stakes

To validate modelled surface mass balance (Chapter three), during the 2004-2005 summer, ablation stakes were placed on similar surfaces in the vicinity of the bare ice site (one approximately 5 m away, and two approximately 2 km away). These ablation stakes consisted of hollow white PVC poles drilled into the ice. The net surface mass balance was determined by measurement of the length of exposed pole at the start and the end of the sampling period indicated in Figure 2.10.

Eddy covariance system

In order to validate turbulent fluxes modelled in chapter three and to enable determination of atmospheric roughness lengths, turbulent fluxes were directly measured at each site for a short period with a fast-response eddy covariance system (Figure 2.14). This system comprised a 3D sonic anemometer (Campbell Scientific CSAT3) and a Krypton Hygrometer (KH20) connected to a CR10X data logger, and mounted on a small tripod. The eddy covariance system was installed approximately 5 m from the AWS at the debris-covered ice site from Day 314 to Day 318 2004 and approximately 4 m from the bare ice site for four days from Day 338 to Day 342, 2004 (Figure 2.10). The height of the midpoint

of the sonic anemometer was 1.11 m from the surface at the bare ice site and 1.31 m at the debris-covered ice site. Sampling was at 10 Hz and vertical velocity, air temperature and humidity covariances were determined for 30 minute periods. No specific de-spiking or detrending was applied as the raw, high resolution data were not stored.

During installation and measurement using eddy covariance systems, it is difficult to align sensors so that the mean crosswind component is equal to zero (Finnigan *et al.*, 2003). This problem is usually overcome by applying a post processing coordinate rotation. As no high frequency data were recorded, coordinate rotation was not performed here. In order to reduce this problem, during installation the CSAT sonic anemometer was pointed into the predominant wind direction, as well as being levelled regularly. This levelling combined with a near flat surface should minimise the influence of non-horizontal wind flow.

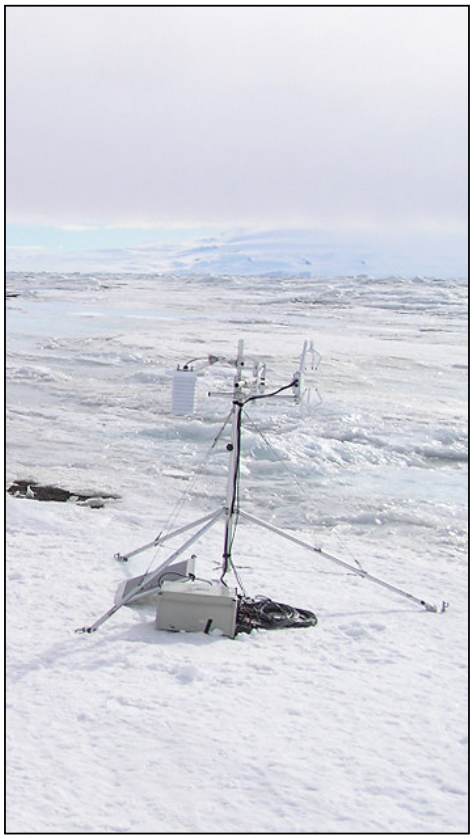

Figure 2.14 Eddy covariance system used for validation of the surface energy balance modelled in chapter three - shown at the bare ice site, December 2004.

Due to difficulties using fine-wire thermocouples in this environment, the sonic anemometer was also used to record the air temperature. During the measurement period no blowing snow was observed. In addition, several corrections are often made to eddy covariance datasets, these are discussed in section 3.4.1.

2.6 Debris-covered ice microclimate

The debris-covered ice site was characterized by large variability in most climate variables. Of particular note is a large range of air and surface temperatures (Table 2.8), with a span of 28.4 ºC and 46.4 ºC respectively.

Table 2.8 Climate variables recorded at the Debris-covered ice site for the period Day 299, 2003 – Day 16, 2004. Temperature and relative humidity are taken from 1.99 m.

	Mean	Minimum	Maximum
Air temperature (ºC)	-5.8	-22.5	5.9
Surface temperature (ºC)	0.3	-21.2	25.2
0.15 m Subsurface temperature (ºC) *	2.5	-0.1	7.1
0.30 m Subsurface temperature (ºC)	-4.9	-16.5	2.0
Wind Speed (m s^{-1})	3.5	0.1	14.4
Wind direction (º)	87	-	-
Relative humidity (%)	63	30	97
Pressure (hPa)	1004.7	989.1	1022.8
Net radiation (W m^{-2})	145.9	-74.9	560.1
Mean albedo	0.20	0.04	0.92

** Due to sensor problems the 0.15 m subsurface temperature was only available from the later part of the measurement period (Day 353, 2003 – Day 16, 2004).*

While some excessive air temperatures may be recorded due to the lack of artificial aspiration of the sensors (Section 2.5.2), some of the variability can be partly explained by the measurement period capturing seasonal change - with a sharp increase in temperatures for the region during December (Figure 2.3). Large surface temperature variations are to be expected given the nature of the surface.

The surface at the debris-covered ice site changed throughout the measurement period. At the beginning of the measurement period, the debris was blanketed in snow from the winter approximately 0.30 m deep. Over time, as this snow ablated, the albedo decayed and the debris became fully exposed at approximately Day 341. This snow maintained a high albedo and therefore restricted the total amount of net radiation (Figure 2.15). Over the entire measurement period, the mean daily albedo of the debris-covered site was 0.20, but during the periods when no snow was present (after Day 341), the mean albedo was 0.12. Fresh snowfall after this date also increased the albedo (Figure 2.15). The minimum albedo

recorded is very low (0.04) and is likely to be a result of a wet surface and/or problems with instrumentation when the solar zenith angle is large (see section 2.5.2). Throughout the period of measurement, the surface temperature was consistently higher than the air (Figure 2.16) indicative of instability.

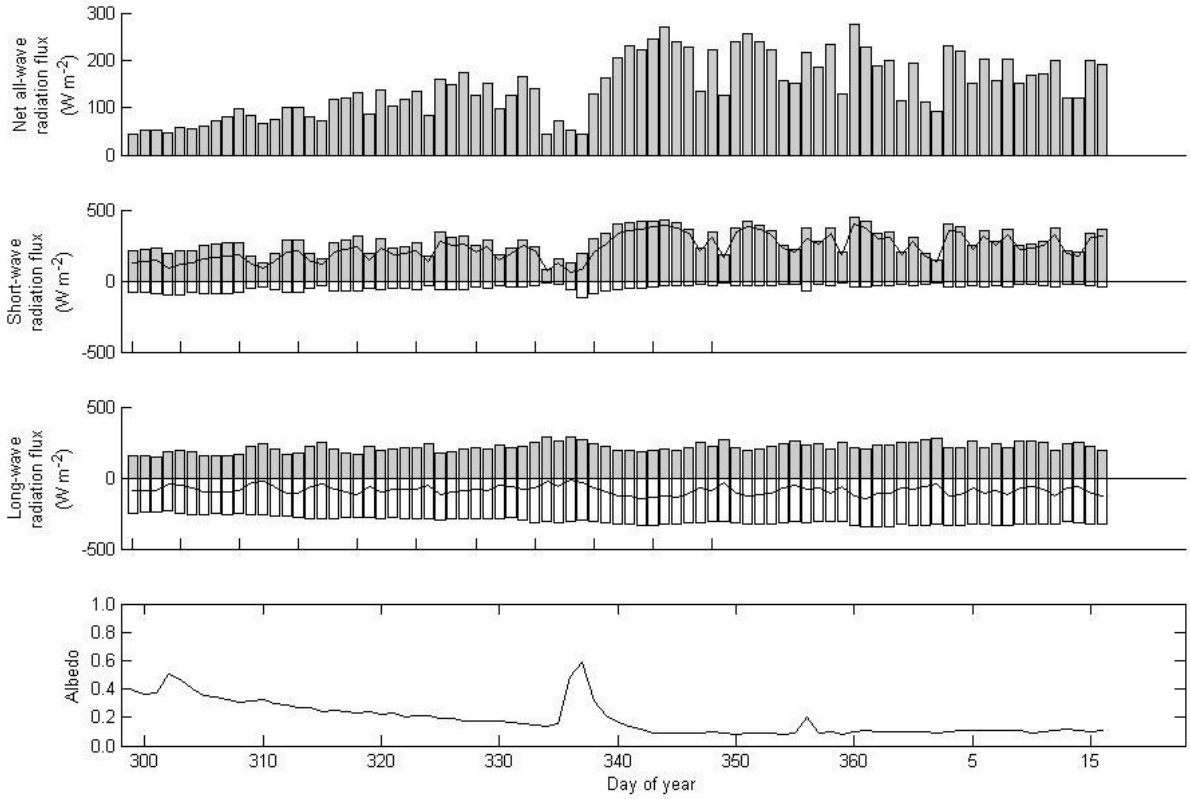

Figure 2.15 Mean daily radiation budget measured at the debris-covered ice site on the McMurdo Ice Shelf, Day 299 2003 – Day, 16, 2004. a) Net radiation, b) Short-wave radiation showing positive incoming (grey bars) and negative outgoing (white bars) and net (black line) c) Long-wave radiation, presented as for short-wave, and d) albedo.

Albedo of the surface had a large effect on the radiation budget. At the beginning of the measurement period, all components of the radiation budget were low (Figure 2.15). After the initial snow ablated, all the components of the radiation budget increased (Figure 2.15). Over the period, the mean net short-wave radiation was 231 W m^{-2} with a range of 64 to 404 W m^{-2}. Net long-wave radiation had a mean of -86 W m^{-2}, ranging from –13 to –147 W m^{-2}.

Wind at the debris-covered ice site was variable during the measurement period, with the mean wind coming from the eastern sector (Figure 2.19). Also frequent were winds from the southeast and northwest, which is aligned with the topography (described in section 2.5.1). The majority of the 30 minute mean winds during the measurement period were relatively low speed (< 5 m s^{-1}). The strongest wind speeds observed were from the southeast (Figure 2.19). Relative humidity and pressure also varied considerably throughout the measurement period (Figure 2.16). Relative humidity increased in the second half of the measurement period, when the debris surface was free of snow (Figure 2.16). Absolute humidity also increased because temperatures were higher at this time as well.

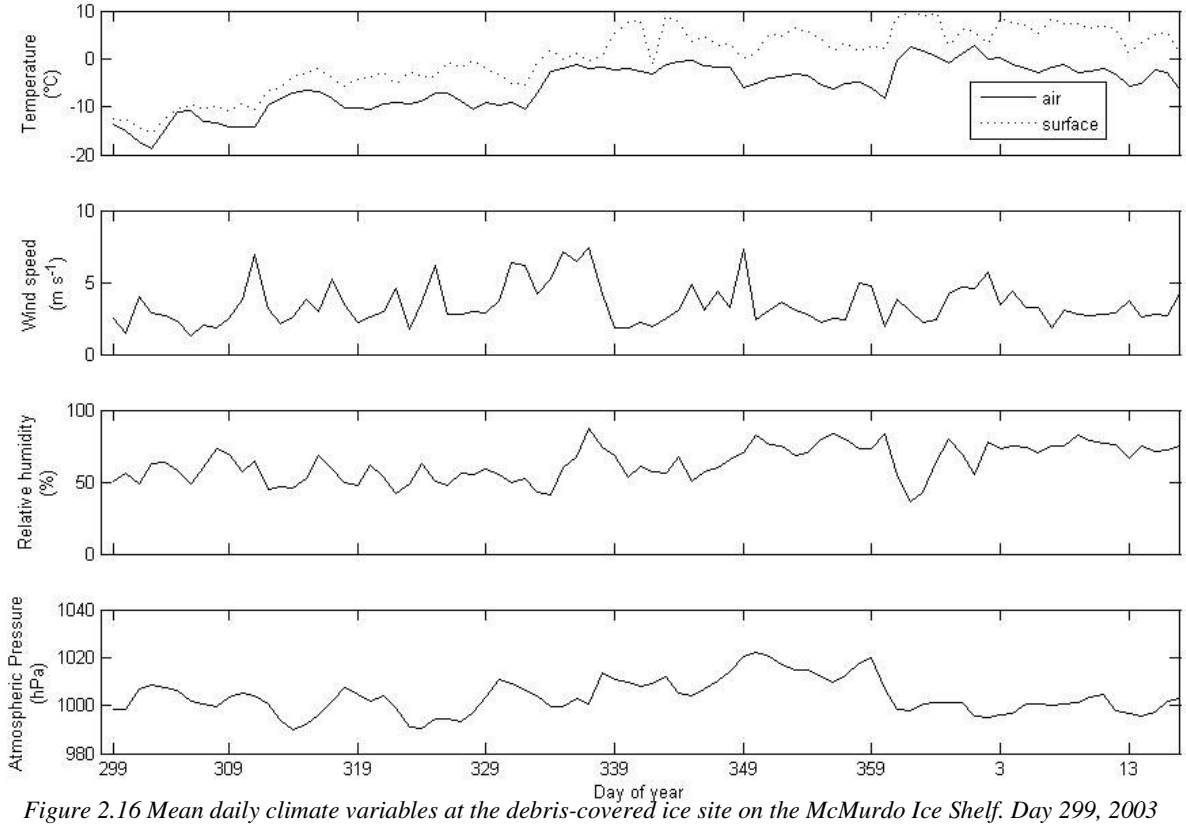

Figure 2.16 Mean daily climate variables at the debris-covered ice site on the McMurdo Ice Shelf. Day 299, 2003 – Day 16, 2004.

During the measurement period several snowfall events were recorded at McMurdo Station. The most notable of these events occurred around Day 335, 2003 and resulted in precipitation of 11.9 mm w.e. Although no precipitation observations were made at the debris-covered ice measurement site, snowfall is apparent as evidenced by changes in albedo (Figure 2.15). High relative humidity, wind speed and increased temperatures accompanied this event, as well as increased long-wave radiation and decreased short-wave (Figure 2.15, 2.16). During the precipitation event the net short-wave radiation, net long-wave radiation, and net radiation were all reduced significantly (Figure 2.15). These climatic situations are typical of a large cyclonic system entering the Ross Sea Embayment, such as during Type A conditions.

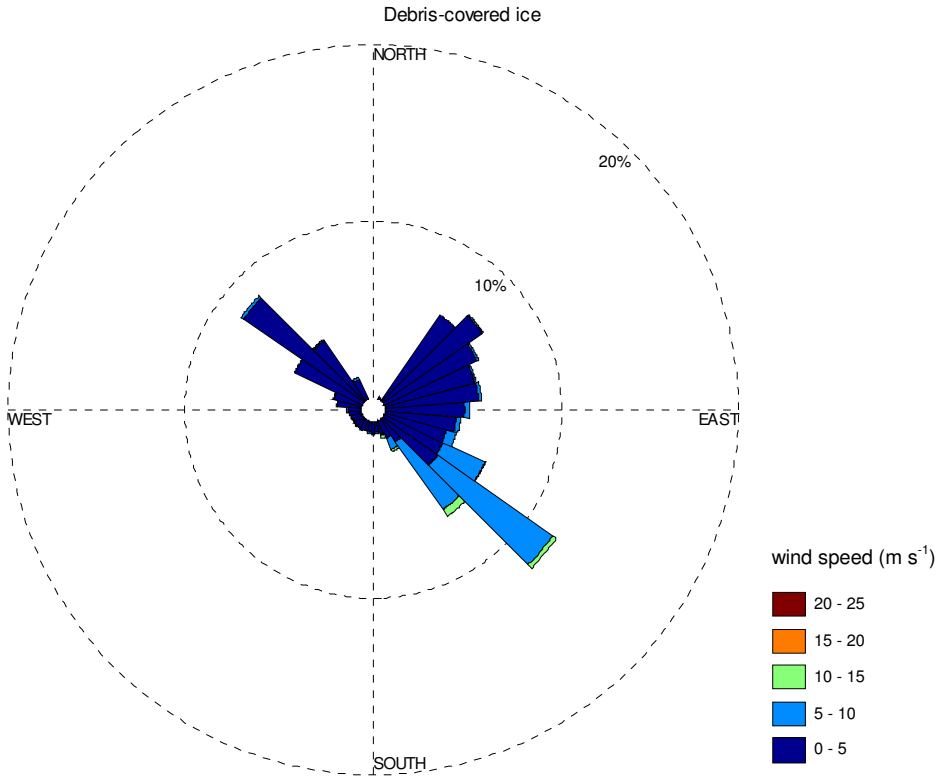

Figure 2.17 Wind speed and direction recorded at the Debris-covered ice site during the measurement period (Day 299, 2003 – Day 16, 2004).

2.6.1 Synoptic conditions and debris-covered ice microclimate

During Type A conditions the debris-covered ice site meteorological conditions were distinctive. Noticeably, the wind speed was higher, while temperature and relative humidity were lower than during other synoptic conditions (Table 2.9). Winds during these

conditions were strong and from the southeast (Figure 2.18). A lower temperature during these conditions is probably due to the cooler air being brought across the debris surface. Supporting the synoptic classification, Type A had the least short-wave and highest long-wave radiation receipts (Table 2.9), indicative of cloudy conditions.

High pressure was the principal characteristic of Type B conditions (Table 2.9). These conditions also had associated lower wind speed than during other synoptic types, especially compared with Type A. The winds were from varying directions, but predominantly from the northeast (Figure 2.17). Such wind conditions are to be expected during this synoptic conditon as there is no gradient wind, and localized effects can occur. Temperatures are higher during these conditions, due to high net radiation, low wind speeds, and the heating of the surface and thus the overlying air. As is common during periods of high pressure, Type B had clear skies, shown by having the highest incoming short-wave radiation and lowest long-wave radiation for the site (Table 2.9). The measurement period (Day 299, 2003 to Day 16, 2004) was dominated by Type B conditions.

Type C conditions appear to be between Type A and B in all meteorological variables with the exception of pressure, which was only 0.5 hPa less that during Type A conditions. The winds were variable, with a the strongest (5 –10 m s^{-1}) coming from the northwest.

Table 2.9 Mean daily surface climatic conditions experienced at the debris-covered ice site during the three synoptic classes defined in text.

	Type A	Type B	Type C
Temperature (ºC)	-5.8	-4.7	-4.9
Wind speed (m s^{-1})	4.9	3.0	3.5
Wind direction (º)	120	64	88
Relative Humidity (%)	57	69	62
Pressure (hPa)	1001.5	1010.7	1001.0
Incoming short-wave radiation (W m^{-2})	198.9	329.4	276.3
Incoming long-wave radiation (W m^{-2})	238.9	212.9	222.6

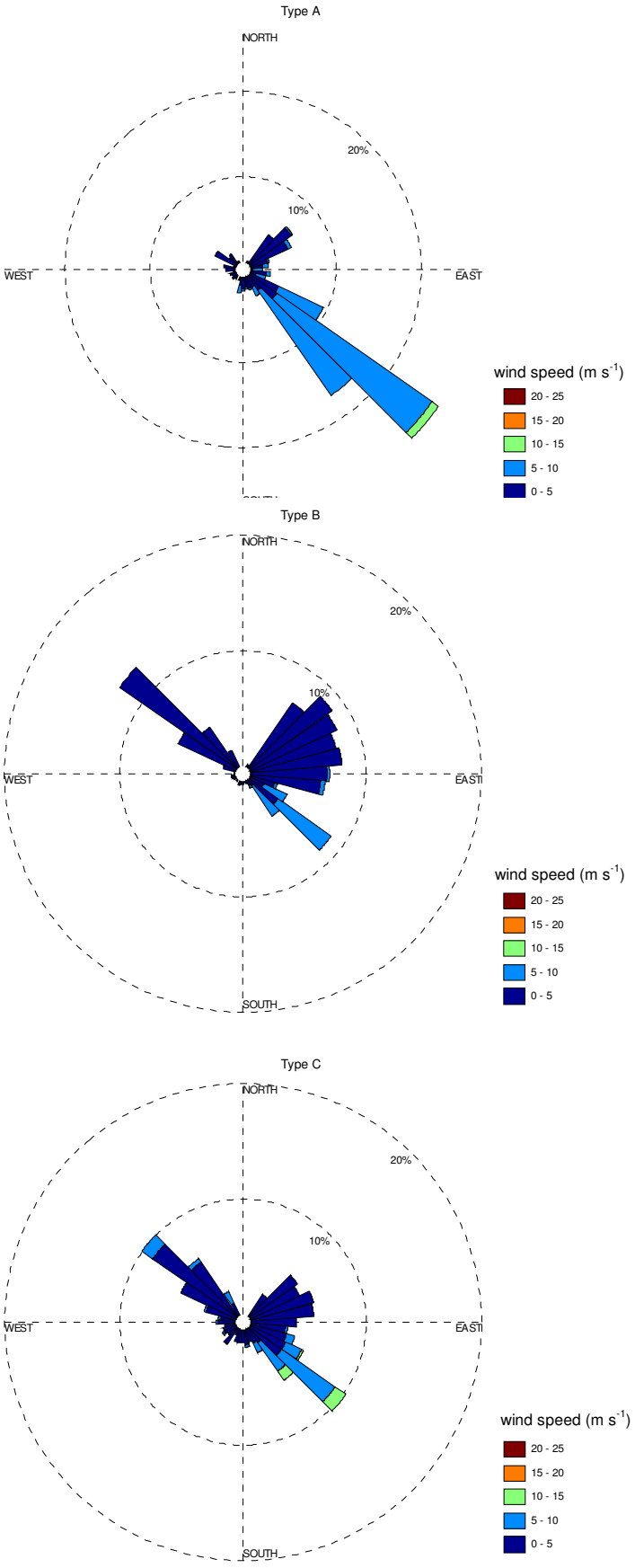

Figure 2.18 Wind speed and direction recorded at the debris-covered ice site during the summers of 2003-2004 according to synoptic types as defined in text.

2.7 Bare ice microclimate

In contrast to the debris-covered ice site, the bare ice site is characterised by low temperatures and high humidity (Table 2.10). The mean air temperature was –2.3 ºC, with a range of 12.6 ºC. Compared to the debris-covered ice site, this range is small. On the whole, the air temperature was higher than the surface (Figure 2.19), which suggests stability (common over ice bodies). This inversion occurs primarily at the beginning and end of the measurement period but is variable and can change throughout the day. The bare ice site surface temperature varied throughout the measurement period with a net cooling effect (Figure 2.19). The mean daily surface temperature was raised to melting point during Days 4, 5 and 7, 2005. The surface also reaches melting point for shorter intervals during the measurement period (not shown).

Table 2.10 Climate variables recorded at the bare ice site for the period Day 342, 2004 – Day 21, 2005. Temperature and Humidity are from 1.96 m.

	Mean	Minimum	Maximum
Air temperature (ºC)	-2.3	-9.1	3.5
Surface temperature (ºC)	-3.4	-13.8	1.1
Wind Speed (m s^{-1})	3.0	0.1	16.2
Wind direction (º)	64	-	-
Relative humidity (%)	79	35	97
Pressure (hPa)	1005.1	993.7	1021.4
Net radiation (W m^{-2})	51.8	-63.8	237.8
Mean albedo	0.64	0.44	0.97

While the mean wind speed at the bare-ice site was lower than that measured at the debris-covered ice site, the maximum measured wind speed of both sites was at the bare ice site (Table 2.8, 2.10). Most of the high winds occurred between day 3 and day 9, 2005, and for a short time at the beginning of the measurement period (Figure 2.19). Over the measurement period, the mean wind direction was from the eastnortheast, but as the winds were variable (Figure 2.21), the mean is not a good representation. Strong winds during the measurement period were from the southern sector, while the majority of winds came from the northeast. Lighter winds are shown to come from the northwest (Figure 2.21). The majority of the half hour mean wind speeds were between 0 and 5 m s^{-1}.

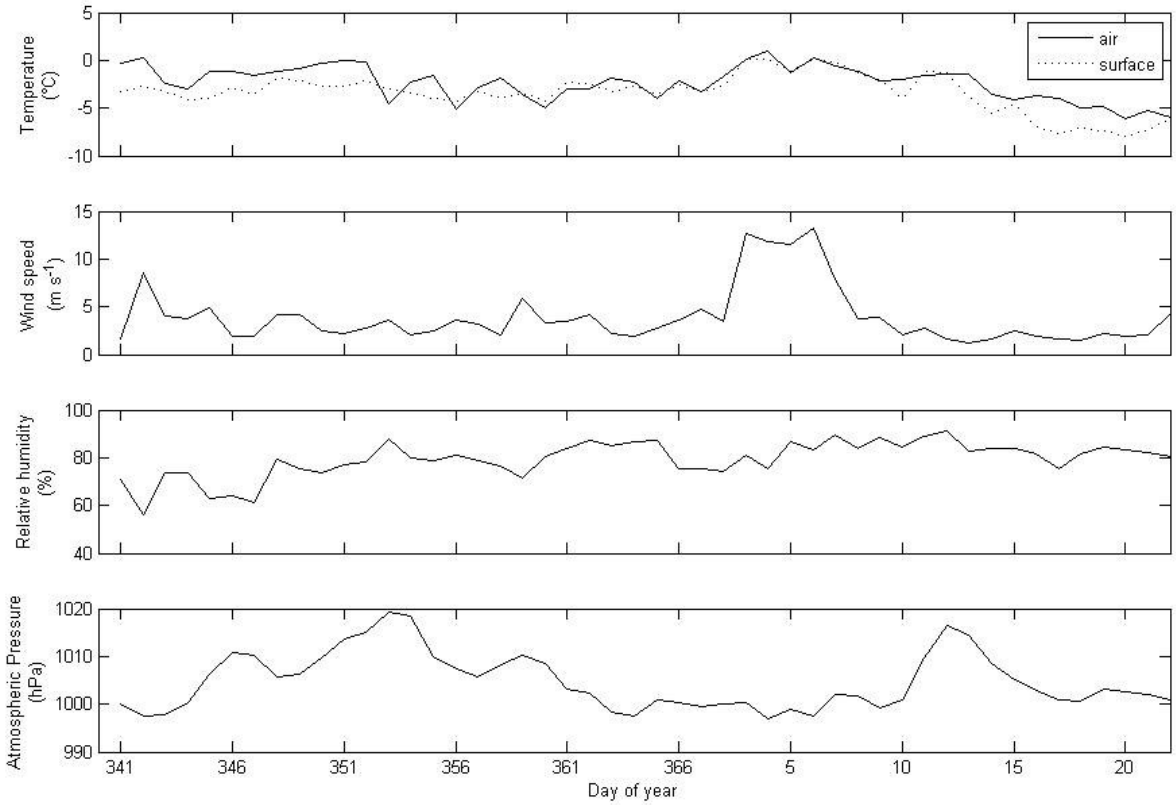

Figure 2.19 Mean daily climate variables at the bare ice site on the McMurdo Ice Shelf. Day 341, 2004 – Day 22, 2005.

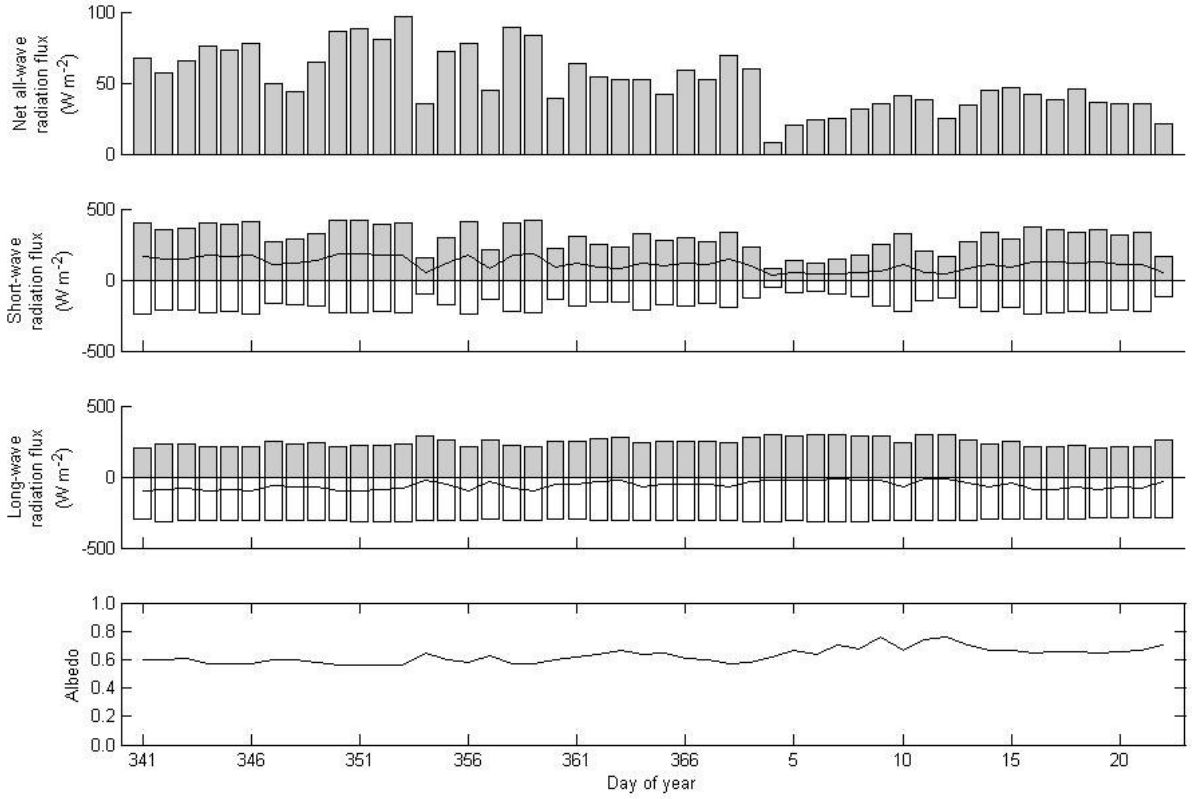

Figure 2.20 Mean daily radiation budget measured at the bare ice site on the McMurdo Ice Shelf, Day 341, 2004 – Day, 22, 2005. a) Net radiation, b) Short-wave radiation showing positive incoming (grey bars) and negative outgoing (white bars) and net (black line) c) Long-wave radiation, presented as for short-wave, and d) albedo.

Net Radiation varies considerably, from 8 to 96 W m^{-2}, with a mean of 52 W m^{-2} (Figure 2.20). Net short-wave radiation is positive throughout the measurement period representing a net source of energy ranging from 31 to 185 W m^{-2}, while net long-wave radiation is negative, indicative of a loss, and ranges from -15 to -99 W m^{-2}. All components were considerably decreased during the period Day 3 – 9, 2005 (Figure 2.20).

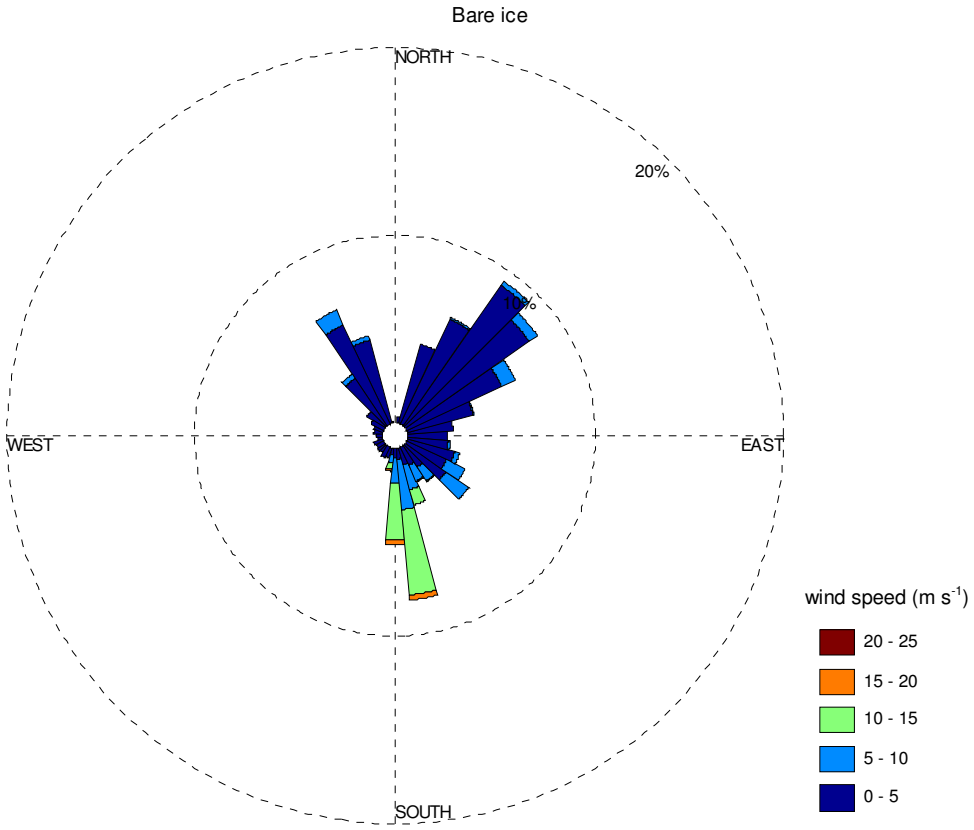

Figure 2.21 Wind speed and direction recorded at the bare ice site during the measurement period (Day 341, 2004 – Day 23, 2005).

The reduction in the radiation budget during the event of Day 3-9 can be partly attributed to changes at the surface. For example, the snow cover causes an increase in albedo (Figure 2.20). The effect of a change in albedo is primarily on net short-wave radiation and consequently on net radiation (Figure 2.20). Also, between Day 3 and Day 9 2005, the surface temperature increased (Figure 2.19). As highlighted earlier (Section 2.1.1), the surface temperature directly controls the emitted long-wave radiation. Although the incoming long-wave radiation may be increased due to cloud cover, the emitted long-wave

radiation associated with a higher surface temperature offsets this increase, resulting in a small net long-wave radiation. These conditions are likely to occur during a Type A situation (discussed below).

The albedo of the bare ice site changes throughout the measurement period (Figure 2.20), with the mean daily range varying between 0.57 and 0.76 and an overall mean of 0.63. The albedo increases appreciably on Day 4 in conjunction with the considerable snowfall recorded at McMurdo Station. Other snowfall events recorded at McMurdo Station appear to be region-wide, as they affect the albedo at the bare ice site, although these are more subtle.

2.7.1 Synoptic conditions and bare ice microclimate

Links between the distinct synoptic types and the microclimate at the bare ice site were varied. The most obvious effects were shown in the wind data.

During Type A conditions, wind speed, temperature and relative humidity were all increased, while pressure was low (Table 2.11). Wind measured during these conditions at the bare ice site was strong (10 – 15 m s^{-1}), and from the south (Figure 2.22). The mean temperature during Type A conditions at the bare ice site was higher than during the other conditions (Table 2.11) as would be expected if the air is being drawn in to the site from the Ross Sea as described in section 2.2. Similar to what occurred at the debris-covered ice, incoming short-wave radiation was reduced and incoming long-wave radiation increased during Type A conditions (Figure 2.21). A relatively high humidity (80%) supports the theory of warm, moist air being transported to the area (Section 2.2).

During Type B conditions, at the bare ice site, winds were light and came from the northeast sector (Figure 2.22). Low wind speeds (0 - 5 m s^{-1}) occurred more often for Type B conditions than for Type A with the mean being 2.7 m s^{-1}. The bare ice site had a mean air temperature of -1.6 ºC during Type B conditions, 1 ºC lower than during Type A conditions (Table 2.11). Relative humidity at the bare ice site is slightly lower than during Type A conditions (Table 2.11), Pressure, on average, is 20 hPa greater than during for Type A conditions (Table 2.11). Mean daily incoming short-wave radiation is considerably

higher (by 155 W m^{-2}) than during Type A conditions, showing that Type B had much clearer skies.

Table 2.11 Mean daily surface climatic conditions experienced at the bare ice site during the three synoptic classes defined in text.

	Type A	Type B	Type C
Temperature (ºC)	-0.6	-1.6	-2.7
Wind speed (m s^{-1})	9.3	2.7	3.6
Wind direction (º)	167	38	32
Relative Humidity (%)	82	77	77
Pressure (hPa)	999.3	1009.3	1003.1
Incoming short-wave radiation (W m^{-2})	177.9	333.4	324.9
Incoming long-wave radiation (W m^{-2})	281.7	237.0	234.6

Type C was the most common situation during the measurement period of 2004-2005, occurring on 45% of days able to be classified. As experienced at the debris-covered ice site, Type C microclimate conditions are generally in-between Type A and Type B. The mean temperature during this situation (-2.7 ºC) was considerably lower than for Types A and B (Table 2.11). Mean atmospheric pressure at the bare ice site, 1003 hPa, which is intermediate between Type A and Type B pressures (Table 2.11). Mean daily incoming short-wave radiation was much higher than for Type A, and close to Type B conditions, suggesting reasonably clear skies. Supporting this assumption is the fact that the minimum mean incoming long-wave radiation occurred during these conditions (Table 2.11).

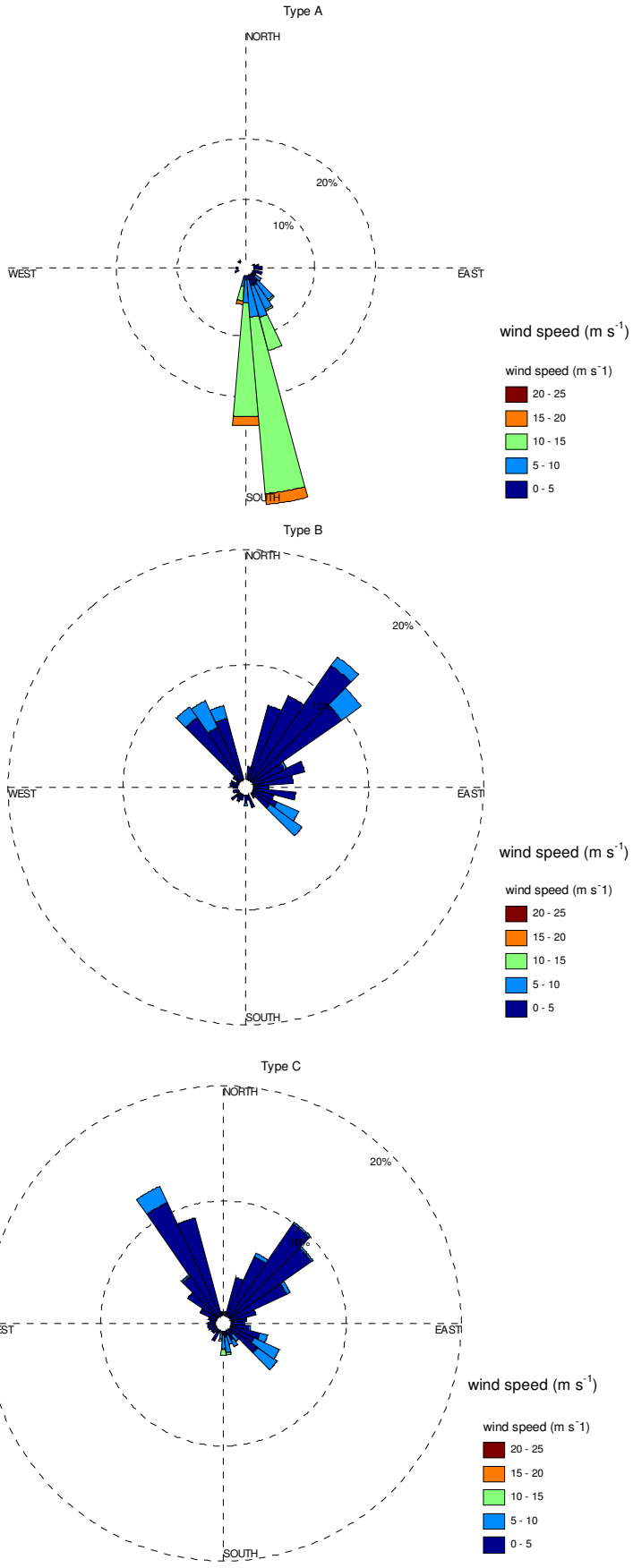

Figure 2.22 Wind speed and direction recorded at the bare ice site during the summer of 2004-2005 according to synoptic types as defined in text.

2.8 Summary

The climate of the McMurdo Ice Shelf area is complex with several different air masses drawn into the area and winds strongly affected by local topography. The summers investigated for this research had similar meteorological conditions to the long term mean. However, the summer of 2003-2004 was slightly cooler than the long term mean and had higher than normal pressure. The summer of 2004-2005 was warmer than usual.

Three distinct synoptic types were found to occur during the summer, these were:

- Type A: Low pressure system residing in the Ross Sea Embayment.
- Type B: Anticyclonic conditions across region.
- Type C: A trough of low pressure extending into the Ross Sea Embayment.

Differences between the two summers can be explained by the frequency of different synoptic situations occurring. During the 2003-2004 summer, conditions were often anticyclonic (Type B), with low wind speeds and clear skies. During the 2004-2005 summer, there were more Type C conditions, causing increased cloudiness and wind speeds. During 2004-2005 Type A conditions occurred more frequently than in 2003-2004 which resulted in high wind speeds and precipitation.

The microclimate of the McMurdo Ice Shelf is strongly affected by the surface type in summer. Debris-covered ice has an extremely large temperature range and conditions are affected considerably by snow. Bare ice, was cooler, and had less range in temperatures. The debris-covered ice and bare ice are affected differently during the various synoptic conditions. During Type A conditions at the debris-covered ice site temperature was reduced. Conversely, the temperature was increased at a bare ice site during type A conditions. The microclimate has an important influence on the surface energy and surface mass balance at the sites, which is explored in chapter three.

3 Surface energy and surface mass balance

3.1 Introduction

The surface energy balance (SEB) helps determine how much energy is available for ablation. Examining the distinctive characteristics of the surface energy balance enables an understanding of sources and sinks of energy. In order to identify the distinctive characteristics of surface energy and surface mass balance of an ice shelf ablation area point based surface energy balances are determined by adapting an existing surface energy balance model and running it for the two dominant surfaces found in the ablation area of the McMurdo Ice Shelf: bare and debris-covered ice. Specifically the following questions are addressed:

- What is the relative importance of the sources of energy at the ice shelf surface?
- How and when does ablation occur?
- Are there characteristic surface energy or surface mass balances for different synoptic situations?

The first section of this chapter introduces the energy balance model used in this research; it then describes the adaptations that are made to the model in order to run it for debris-covered ice. The next section describes how the model is run for the McMurdo Ice Shelf including descriptions of the run periods, specific variables and assumptions made. Then the performance of the adapted model is validated against measured variables. Ensemble runs are then used to test and determine the sensitivity of the model. The surface energy and surface mass balance is then presented for both surface types for the measurement periods, then with respect to the synoptic conditions, and the previous research. The chapter concludes with a summary of the main findings.

3.2 Model description

SOMARS (Simulation of glacier surface Mass balance And Related Sub-surface processes) is a glacier surface mass balance model and is used as a foundation for this research. This model was originally developed and tested successfully for the ETH-Camp, West Greenland (Greuell and Oerlemans, 1986; Greuell and Konzelmann, 1994). Since then, it has been used in several applications and been adapted for the treatment of capillary water and runoff (Zuo and Oerlemans, 1996; Greuell and Smeets, 2001; Reijmer and Oerlemans, 2002; Bougamont *et al.*, 2005; Erath, 2005). The model has been made freely available and is supplied with the Fortran source code so that it can be easily customised.

The model computes surface mass balance at several points along a glacier centre line. It can be considered as having two main parts: a surface energy balance component (Section 3.2.1) and a sub-surface component (Section 3.2.2). The surface energy balance component calculates the energy exchange between the atmosphere and the surface, while the englacial component determines sub-surface processes including conduction, downward percolation of water, penetration of short-wave radiation, densification, and runoff of meltwater. The surface mass balance for each point is then computed as the sum of precipitation, condensation, sublimation/evaporation and runoff (Bougamont *et al.,* 2005). With the exception of precipitation (which is an input into the model), all of these variables are computed within the model. Other processes of ablation/accumulation (O in Equation 1.1) are not considered in the SOMARS model.

The model can be forced by daily means of temperature, relative humidity, wind speed, and cloud cover from a climate station located outside the thermal influence of the glacier, or by a set of more comprehensive measurements recorded more frequently at an AWS situated on the glacier. Temporal resolution of the model is not constrained, and can be specified by the user.

In order to allow comparisons of surface energy balance between debris-covered and clean ice, SOMARS is adapted in this study by modifying latent heat flux for debris-covered ice and by creating a separate debris sub-surface component (Section 3.2.3).

3.2.1 Surface energy balance calculation

Components of the surface energy balance (Equation 1.7) are either taken from measurements or calculated as follows.

Turbulent flux calculations are based on the Monin-Obukhov similarity theory and are given by:

$$Q_H = \rho_a c_p u_* \theta * \quad 3.1$$

$$Q_E = \rho_a L\, u_* q * \quad 3.2$$

where ρ_a is the air density (kg m^{-3}), c_p is the specific heat capacity of air (J kg^{-1} K^{-1}), L is the latent heat of sublimation or evaporation (2.8 x 10^6 or 2.5 x10^6 J kg^{-1} respectively), u_* the friction velocity (m s^{-1}), θ* the temperature scale, and q* the humidity scale. The friction velocity (u_*) is determined using:

$$u_* = k_0 z \frac{\partial u}{\partial z} \Big/ \Phi_m \quad 3.3$$

where u is the wind speed (m s^{-1}) at height z (m), k_0 is the von Karman constant (0.4), and Φ_m is a stability function according to Dyer (1974).

The temperature scale (θ*) is:

$$\theta * = \frac{k_0 z}{\Phi_h} \frac{\partial \theta}{\partial z} \quad 3.4$$

where θ is potential temperature (K) at height z. The humidity scale (q*) is:

$$q * = \frac{k_0 z}{\Phi_h} \frac{\partial q}{\partial z} \quad 3.5$$

where Φ_m and Φ_h are the stability functions for the momentum and scalar quantities of temperature and humidity according to Dyer (1974).

In the atmospheric surface layer, the scalar quantities are assumed to be constant with height, so equations 3.5 – 3.6 can be integrated between two heights (Bintanja and van den Broeke, 1995; Bougamont *et al.*, 2005). In the case of the bulk method (which uses the glacier surface as one level) these heights are the height of the observations and the height at which the certain measured variables reach their surface values (the roughness lengths of momentum, heat and vapour). At the surface, it is assumed the wind speed is zero and the air is considered saturated with respect to ice.

In this study, a prescribed value for the roughness length of momentum (z_0) is used to determine the roughness lengths for heat (z_{0h}) and vapour (z_{0e}). The assumption that roughness lengths are equal is often made over snow and ice surfaces (Bintanja and van den Broeke 1995; Braun and Hock, 2004) where:

$$z_0 = z_{0h} = z_{0e} \quad 3.6$$

However, there is evidence to suggest that this assumption is not valid over ice (Braithwaite, 1995; Brock and Arnold, 2000). In a review on parameterising roughness lengths Andreas (2002) suggests that using the roughness Reynolds number to estimate z_{0h} is suitable for most conditions over snow and ice (Andreas (2002) also suggests that the parameterisation of z_{0e} requires further data analysis). The scheme by Andreas (1987) uses the Reynolds roughness number, and is the only scheme known to the author that is specifically adapted to predict z_{0e} over snow and ice. Therefore, this scheme is used in this research to determine the values for roughness lengths of vapour and heat, where:

$$\ln\left(\frac{z_{0h}}{z_0}\right) = 0.317 - 0.565\ln(\mathrm{Re}^*) - 0.183\ln(\mathrm{Re}^*)^2 \quad 3.7$$

$$\ln\left(\frac{z_{0e}}{z_0}\right) = 0.396 - 0.512\ln(\mathrm{Re}^*) - 0.180\ln(\mathrm{Re}^*)^2 \quad 3.8$$

Re* is the roughness Reynolds number defined by:

$$\mathrm{Re}^* = u_* \frac{z_0}{v} \quad 3.9$$

where v is the kinematic viscosity of air (1.461 x 10^{-5} m^2 s^{-1}).

Within SOMARS the z_0 used to calculate turbulent fluxes is a function of density of the uppermost grid based on prescribed z_0 for dry snow, wet snow and bare ice. The prescribed value of z_0 for the ice and debris surfaces were determined using eddy covariance measurements as described in section 3.3.1.

As discussed in chapters one and two, the processes involved in ablation of debris-covered ice are quite different to that of bare ice. In this situation, turbulent fluxes are computed using the same method as for bare ice, but since the specific humidity of the debris surface was not recorded and is dependent on wetness as well as temperature (Tsengdar and Pielke, 1992), the surface energy balance was determined for two extremes: saturated and

completely dry debris (cf. Nicholson and Benn, 2006). As the saturated situation is an extreme upper limit it is likely to lead to an overestimation of the latent heat flux.

For saturated conditions the surface vapour pressure is taken as the saturation vapour pressure for the debris surface temperature. If the debris surface is below freezing vapour pressure is calculated with respect to ice as is appropriate for frozen soils (Williams and Smith, 1989). When the debris is considered fully saturated the saturation vapour pressure gradient will act to transport vapour towards colder regions where there is lower vapour pressure (Hindmarsh *et al.,* 1998). In the case of dry debris, the surface vapour pressure is taken to be the same as the atmospheric vapour pressure, implying that there is no latent heat exchange occurring between the atmosphere and the ice beneath the debris (e.g. Nakawo and Young, 1981; Nicholson and Benn, 2006).

3.2.2 Ice/snow sub-surface component

The sub-surface component of the SOMARS model incorporates conduction, downward percolation of water, penetration of short-wave radiation, densification, and runoff of meltwater. Albedo and surface temperature are also derived using variables determined within this sub-surface component. Horizontal advection and conduction, and heat due to ice deformation are all considered negligible and therefore neglected (Greuell and Konzelmann, 1994).

The sub-surface component of the model uses a non-uniform grid extending vertically downwards from the surface, with grid boxes increasing in size with depth. The grid extends down to a pre-defined depth, usually 25 m, to ensure annual temperature oscillations are dampened. The size of the uppermost grid box is altered as a result of accumulation, condensation, and evaporation while the dimensions of the rest of the grid boxes change according to densification. For the arithmetic midpoint of each grid box, hereinafter referred to as the grid point, the temperature, water content and density are calculated. These are calculated by solving the thermodynamic equation:

$$\rho c_{pi} \frac{dT}{dt} = \frac{\partial}{\partial z}\left(k \frac{\partial T}{\partial z}\right) + \frac{\partial Qt}{\partial z} - \frac{\partial}{\partial z}(ML_f) + \frac{\partial}{\partial FL_f} \qquad 3.10$$

where ρ is the snow or ice density (kg m^{-3}), c_{pi} is the specific heat capacity of ice (J kg^{-1}K^{-1}), k is the effective conductivity (W m^{-1}K^{-1}), $\frac{\partial Qt}{\partial z}$ is energy from the atmosphere,

M is the melt rate (kg m^{-2} s^{-1}), L_f is the latent heat of fusion (0.334 x10^6 J kg^{-1}) and F is the freezing rate (J kg^{-1}). The grid size, density of the uppermost and lowest grid boxes, and a temperature profile are initially prescribed.

Densification of the snow is determined by empirical relations from Herron and Lagway (1980) which are described in detail by Greuell and Konzelmann (1994). The effective conductivity is assumed to be a function of the density:

$$k = 2.1\times10^{-2} + 4.2\times10^{-4}\rho + 2.2\times10^{-9}\rho^3 \qquad 3.11$$

and is calculated for each grid point.

The amount of melting is determined as a function of the grid point temperature. If the temperature is positive, melting occurs and the temperature is set to 0 ºC (Bougamont *et al.*, 2005). Properties of each grid point determine what happens to the meltwater. For each grid point a maximum retention capacity is calculated based on the irreducible water saturation (Coleou and Lesaffre, 1998). Water that exceeds this maximum percolates downwards until an impermeable layer ($\rho \geq 910$ kg m^{-3}) is reached. The remaining water fills up the pore spaces and forms a slush layer (Bougamont *et al.*, 2005). Runoff is calculated both inside the snowpack and on the surface and can either be set to runoff immediately or tuned using a scheme which defines the length of time for runoff on different slopes (Zuo and Oerlemans, 1996).

The surface temperature is determined using a linear extrapolation of the temperatures of the top two grid cells. Albedo is calculated by using the density of, and the amount of water in the uppermost grid point (Zuo and Oerlemans, 1996).

3.2.3 Debris sub-surface component

Since energy and mass transfer processes within debris are different from those of within ice, a sub-surface component was developed specifically for debris-covered ice. This was then incorporated into SOMARS.

Following Nicholson and Benn (2006) and Conway and Rasmussen (2000), it is assumed that energy is transported through the debris purely by conduction. Other fluxes are ignored. This assumption may be made as other forms of transport such as energy from infiltrated

water and from sublimation through debris have been shown to be negligible (Hindmarsh *et al.*, 1998; Sakai *et al.*, 2004). For the purposes of this research, it is assumed that:

- lateral heat flux is negligible,
- energy flux associated with precipitation is negligible,
- heat transfer within the debris layer occurs only by conduction,
- there is no penetration of short-wave radiation into the debris,
- sublimation occurring at the debris-ice interface is negligible,
- debris thermal properties do not change in space or time,
- the change from debris to debris-free ice is abrupt,
- all melt at the debris-ice interface is an instant loss to the system.

Sub-debris ice melt rate in m s^{-1} (M_{di}) can be approximated using the downward energy flux at the debris-ice interface (Q_{di}) where:

$$M_{di} = \frac{Q_{di}}{\rho_i L_f} \qquad 3.12$$

A proportion of Q_{di} is also conducted into the ice as in the snow and ice subsurface component. For simplification, until the debris-ice interface temperature reaches 0ºC it is assumed that the $M_{di} = 0$ and all Q_{di} is used to heat the body of ice.

Within the debris, heat flux by conduction (Q_G) is the product of the thermal conductivity of the debris and the temperature gradient within the debris, and can be approximated as:

$$Q_G = k_d \frac{\partial T}{\partial z} \qquad 3.13$$

where k_d is the thermal conductivity of debris (W m^{-1} K^{-1}).

If the temperature gradient can be assumed linear with depth, the conductive flux at the debris-ice interface can be calculated using:

$$Q_{di} \cong Q_G \cong k_d \frac{\partial T}{\partial z} \cong k_d \frac{(T_0 - T_{di})}{z_{di}} \qquad 3.14$$

where z_{di} is the depth of debris at the debris-ice interface (m); T_0 and T_{di} are the temperature (ºC) at the surface and the debris-ice interface respectively. Past research of this nature has assumed that the gradient is linear on a 24hr basis, or no storage change is occurring, or that T_{di} is equal to 0 ºC (Nakawo and Young, 1981; Purdie and Fitzharris, 1999; Conway and Rasmussen, 2000; Nicholson and Benn, 2006). Measurements made at the research site

show that T_{di} is likely to be well below 0ºC at times, and also that heat storage change occurs. This change is indicated by a marked increase in debris temperature over the measurement period (Figure 3.1). Furthermore, inspection of measured $\frac{\partial T}{\partial z}$ in the first 0.3 m of debris suggests that the temperature gradient, while close to linear for 24-hour periods (Figure 3.2), is not likely to be linear to greater depths, or on other time scales.

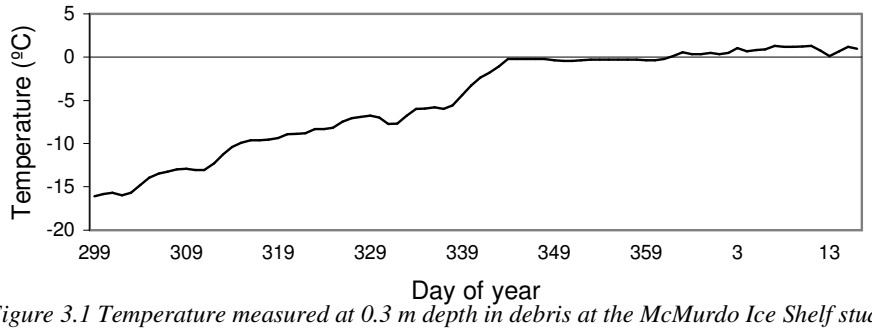

Figure 3.1 Temperature measured at 0.3 m depth in debris at the McMurdo Ice Shelf study site, Day 299 2003 to 16, 2004. The debris is approximately 0.6 m deep at this site. Increase in temperature over the period indicates that significant heat storage change is occurring.

If the thermal diffusivity is considered uniform throughout the debris it is possible to assume that there is a periodic temperature variation, which decreases in amplitude with depth (Farouki, 1981; Stull, 1988; Williams and Smith, 1989). This cycle present at the site to at least a depth of 0.30 m (Figure 3.3).

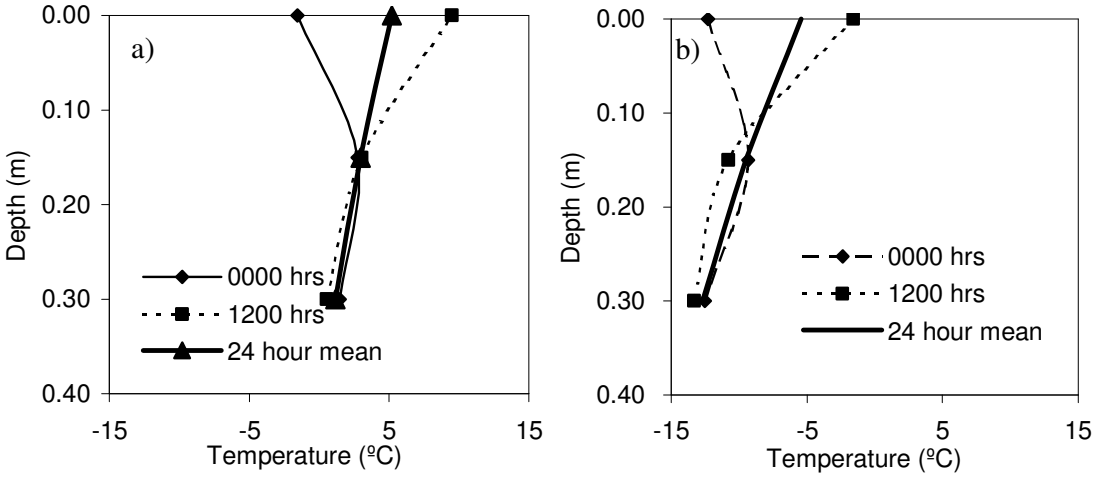

Figure 3.2 Examples of measured debris temperature profiles on the McMurdo Ice Shelf for a) Day 16, 2004 and b) Day 315, 2004. 0.30 m was maximum depth of measurement.

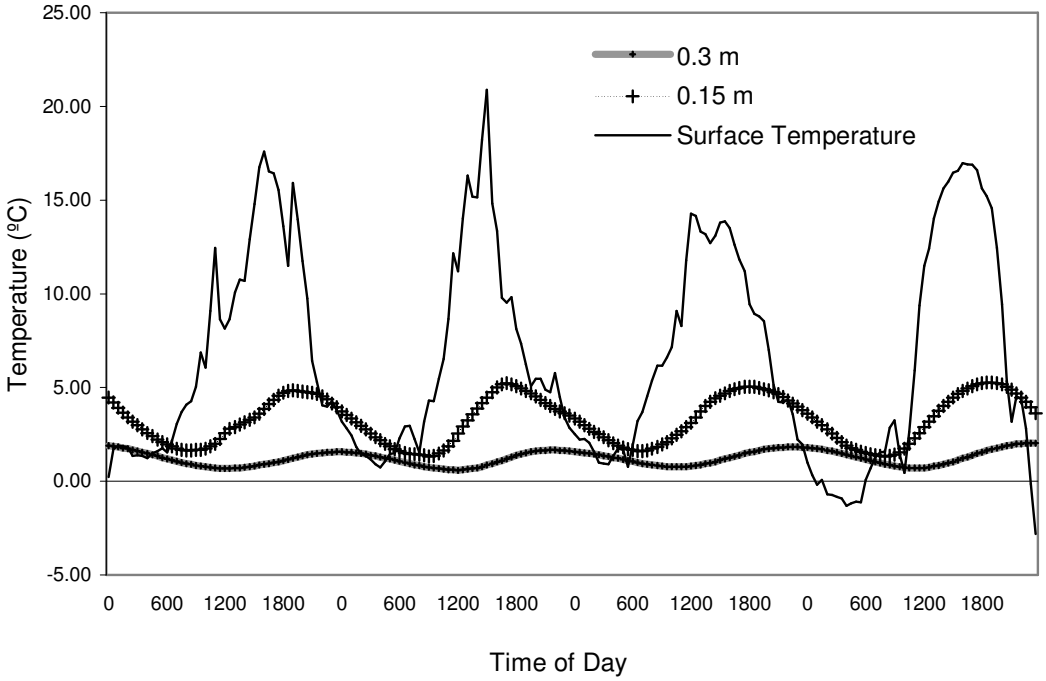

Figure 3.3 Surface and sub-surface temperatures at the debris-covered ice site for Day 9-12, 2004.

Despite being unable to assume a linear gradient, the conductive flux at each grid point can be approximated. This process requires an initial sub-surface temperature profile, the debris thermal conductivity, and the energy flux from atmosphere. The conductive flux can then be calculated using the thermodynamic equation as follows.

For each time step, for each grid point within the debris (i), the amount of energy conducted downwards ($Q_{G(i)}$) is calculated using the temperature profile. The heat conducted to the next level is determined as a function of the (linear) temperature gradient at that point:

$$Q_{G(i)} \cong k_d \frac{\partial T}{\partial z} \cong k_d \frac{(T_{(i)} - T_{(i-1)})}{z_{(i+1)} - z_{(i)}} \qquad 3.15$$

A new temperature profile is then determined, based on the balance of energy received from above, and that energy conducted downwards. For the uppermost grid point (i=1) the energy from above is that supplied from the atmosphere Q_t,

$$T_{(i,j+t)} \cong T_{(i,j)} + \frac{(Q_{t(j)} - Q_{G(i,j)})t}{(c_d m_{(i,j)})} \qquad 3.16$$

where i is the grid point, j is the time, t is the time step used, c_d is the heat capacity of the debris (J kg^{-1}K^{-1}), and m is mass per unit area (kg m^{-2}). For each of the remaining grid points the energy from above is that conducted from grid point directly above it ($Q_{G(i\text{-}1)}$) and the new grid point temperature is calculated using:

$$T_{(i,j+t)} \cong T_{(i,j)} + \frac{(Q_{G(i-1,j)} - Q_{G(i,j)})t}{(c_d m_{(i,j)})} \qquad 3.17$$

this process is iterated for each grid point within the debris, until the debris-ice interface grid point is reached.

Below the debris, the ice thermal conductivity (k_i) and heat capacity (c_i) of ice are used in place of that for the debris. In addition, the first ice grid box is set to the same size as the uppermost debris grid box with the grid continuing to extend downwards into the ice and grid boxes increasing in size to a predefined depth. The uppermost ice grid box is used to determine if any sub-debris melt has occurred. If the temperature of the uppermost ice grid point is determined to be > 0 ºC then it is set to 0 ºC and melting is initiated.

A complication is that of new snow on the debris surface. If there is precipitation the top of the grid is extended by one or more grid boxes. The size of the new grid boxes is defined by the amount of precipitation. These extra grid boxes are removed when all the snow has ablated. When there is snow on the surface, the debris sub-surface component continues in the same manner as above, but the energy transferred to the uppermost debris grid point (Q_{sd}) is comprised of energy conducted from the snow layer as well as Q_t, which includes any penetrated short-wave radiation. The snow will densify and melt as per the normal SOMARS calculations outlined above (Section 3.2.2). The snow layer will also receive energy from below if it is colder than the debris, which is represented by a negative Q_{sd}. The albedo of the snow surface is adjusted from the fresh snow value to the debris value. The rate of change in the albedo was used as a means of tuning the model. As the debris sub-surface component does not allow for infiltration of moisture it is assumed that all the snowmelt above the debris runs off immediately.

Similar to the snow/ice subsurface component, the debris sub-surface component must be initialized with a temperature profile. As the debris-ice interface position does not change, a prescribed depth of debris is used and is held constant for the entire model run. The depth and density of any snow that is already overlying the debris must also be prescribed.

Because no ablation data at the debris-ice interface are available, melt beneath the debris calculated with the debris sub-surface component is regarded as only approximate. However, since the energy balance components at the active surface are calculated using the SOMARS model, they provide a good basis for comparison with the bare ice site.

3.3 Running the model for the McMurdo Ice Shelf

The adapted model was run as a point surface energy balance model for both sites using measured incoming radiative fluxes, air temperature, relative humidity and wind speed recorded at the AWS described in chapter two as input. In addition, precipitation records from McMurdo Station were used as a proxy for precipitation occurring at the sites. The model was run using the air temperature, relative humidity and wind speed from the highest level on the AWS (Section 2.5.2). The time step used in all model runs was 30 minutes. The model was run over several periods based on the data available (Table 3.1).

Table 3.1 Model run periods used for validation, sensitivity, and for presenting the surface energy and surface mass balance on the McMurdo Ice Shelf in this chapter.

Site	Model run period
Bare ice	Day 338 – Day 342, 2004
	Day 341, 2004 – Day 22, 2005
Debris-covered ice	Day 299, 2003 – Day 16, 2004
	Day 315 – Day 318, 2004
	Day 317 – Day 339, 2004

Due to power supply issues, AWS data were not obtained for the period between 2100, Day 339 and 0900 Day 340, 2004. For the duration of this gap the model was provided with temperature, relative humidity, and wind speed derived from the eddy covariance system, and incoming solar radiation was interpolated. This period was not used to test the performance of the model.

The success of the adapted SOMARS model was examined by validating the model output against directly measured surface temperature, turbulent fluxes, and specific surface mass balance. In addition the sensitivity of the model was determined by running it with a variety of initial parameters and conditions.

The model may be run for any ice or debris-covered ice surfaces, but several parameters are site-specific. The following assumptions were made specifically for the McMurdo Ice Shelf:

- heat conducted upwards from the base of the ice shelf is negligible,
- densification of snow by Greuell and Konzelmann (1994) is appropriate for this site,
- all melt is an instant loss to the system.

In addition, several parameters specific to the McMurdo Ice Shelf needed to be prescribed. The determination of these parameters is outlined in the following sections (Sections 3.3.1 – 3.3.4).

3.3.1 Roughness length of momentum

Modelled turbulent fluxes over snow and ice have been shown to be sensitive to roughness lengths (Denby and Smeets 2000; Calanca, 2001; Reijmer and Oerlemans, 2002; van den Broeke *et al.*, 2004a; Cullen *et al.*, 2007a). Roughness length for momentum (z_0) can be determined from wind profile measurements (Stull 1988; Munro, 1989), eddy covariance data (Sun, 1999), or the height of the roughness elements (Lettau, 1969). In this study z_0 was determined using the profile and eddy covariance methods and is discussed with respect to published values.

The profile method uses observations of velocity at two heights and can be calculated as follows:

$$\ln z_0 = \left(\frac{u_1 \ln z_2 - u_2 \ln z_1}{u_1 - u_2} \right) \qquad 3.18$$

using wind speed u_1 and u_2 (m s^{-1}) at heights z_1 and z_2 (m) above the surface. While this method is commonly used (Bintanja, 1995; Takeuchi *et al.*, 1999; Klok *et al.,* 2005) it is subject to problems due to sensor sensitivity, and the eddy covariance method is now more frequently used (e.g. van den Broeke, 2004a; van As, 2005a; Cullen *et al.*, 2007b).

Eddy-covariance measurements of friction velocity (u_*) can be used to determine z_0 using:

$$\ln\left(\frac{z_0}{z} \right) = -k_0 \frac{u}{u_*} - \psi(z/L), \qquad 3.19$$

where k_0 is the von Karman constant (0.4), u is the wind speed (m s^{-1}), Ψ is a stability correction term, which is a function of the dimensionless stability parameter (z/L), and is based on the Businger-Dyer relationships presented in Stull (1988). L is the Obukhov length (Stull, 1988, p.181):

$$L = -\frac{-\overline{\theta_v} u_*^{\,3}}{k_0 g (\overline{w'\theta_v'})} \qquad 3.20$$

where g is acceleration due to gravity (m s^{-2}), $\overline{\theta_v}$ is the mean potential temperature (K), $\overline{w'\theta_v'}$ is the buoyancy flux in the vertical (K m s^{-1}), k_0 is the von Karman constant (0.4), z the height (m), and u_* the friction velocity (m s^{-1}), defined as

$$u_*^2 = \left(\overline{u'w'}^2 + \overline{v'w'}^2\right)^{1/2} \quad 3.21$$

where $\overline{u'w'}$ and $\overline{v'w'}$ are the kinematic flux of east and west momentum in the vertical. According to Stull (1988), in the special case where the coordinate system is aligned in the direction of the surface stress,

$$u_*^2 = \left(\overline{u'w'}\right) \quad 3.22$$

Calculated roughness lengths for momentum (z_0) using wind profile and eddy covariance methods were found to be in the range of 10^{-4} to 10^{-2} m for bare ice and 10^{-3} to 10^{-1} m for snow-free debris-covered ice (Table 3.2). Research on turbulent transfers over snow and ice (King and Anderson 1994; Bintanja, 1995; Bintanja, 2000; Calanca, 2001; Klok and Oerlemans, 2002; van den Broeke, 2004a; van As 2005a,b; Cullen *et al.* 2007a) report a large variation in values of z_0 ranging from 10^{-5} to 10^{-2} m. The values calculated in this research for the bare ice site (Table 3.2) lie within the bounds of these published values.

Using eddy covariance data during near-neutral stability ($-0.2 < z/L < 0.2$) and non-snowdrift ($u_* < 0.3$ m s^{-1}) conditions (cf. van den Broeke, 2004a) the median z_0 value was found to be 2.5 x 10^{-3} m (Table 3.2). This value is of a similar magnitude to the mean value determined using the profile method (1.6 x 10^{-3} m), although an order of magnitude different to the median using the profile method (4.7 x 10^{-4} m). This value is also less than reported on ice surfaces of non-polar glaciers (Klok *et al.* 2005; Cullen *et al*. 2007a), but larger than that found on polar snow and blue ice surfaces (Bintanja, 2000).

Few researchers have investigated turbulent fluxes over debris-covered ice, and z_0 has therefore rarely been considered in this context. Takeuchi *et al.* (2000) reported a value of 6.3 x 10^{-3} m for the debris-covered sections of the Khumbu Glacier in Nepal using the profile method. They also mention that Inoue and Yoshida (1980) had similar values (3.5 x 10^{-3} m). Nicholson and Benn (2006) used a value of 1 x 10^{-2} m based on values reported for rough ice and sastrugi and values calculated by Takeuchi *et al*. (2000). Roughness lengths of other relevant surfaces are: coarse snow with sastrugi, 1 x 10^{-2} m (Paterson 1994), and soils, 1 x 10^{-3} to 1 x 10^{-2} m (Oke, 1987). Values of z_0 calculated at the debris-coved ice site (using

profile and eddy covariance methods) are of similar magnitude to published values (1 x 10^{-1} to 1 x10^{-3} m).

Table 3.2 Roughness lengths of momentum (z_0) during periods when the eddy covariance system was in place alongside the AWS. Values were determined using either wind profile or eddy covariance methods.

	Bare ice				Debris-covered ice			
Method	Mean (m)	Median (m)	Std dev (m)	Number of profiles	Mean (m)	Median (m)	Std dev (m)	Number of profiles
Eddy covariance	1.6 x 10^{-2}	3.5 x 10^{-3}	5.4 x 10^{-2}	1101	1.2 x10^{-1}	4.6 x 10^{-2}	1.5 x10^{-1}	1028
Eddy covariance*	3.5 x 10^{-3}	2.5 x 10^{-3}	3.8 x 10^{-3}	342	9.3 x 10^{-2}	4.2 x 10^{-2}	1.2 x 10^{-2}	147
Profile method*	1.6 x 10^{-3}	4.7 x 10^{-4}	6.4 x 10^{-2}	1311	3.9 x 10^{-2}	5.0 x 10^{-3}	1.0 x 10^{-1}	1785

**During periods of neutral atmospheric stability (-0.2 < z/L < 0.2) and no snowdrift ($u_* < 0.3$ m s^{-1})*

In SOMARS, z_0 is determined as a function of density of the uppermost grid box, based on the prescribed z_0 for dry snow, wet snow and bare ice. Greuell and Konzelmann (1994) and Bougamont *et al.* (2005) used 1.2 x 10^{-4} m for dry snow, 1.3 x 10^{-3} m for wet snow and 3.2 x 10^{-3} m for ice successfully on the Greenland Ice Sheet.

Roughness length of momentum (z_0) for the bare ice site is set to 2.5 x 10^{-3} m based on the eddy covariance measurements, and the dry and wet snow values are as used by Greuell and Konzelmann (1994). For the debris-covered surface z_0 is set to 3.9 x10^{-2} m, which was derived from the largest set of profiles (Table 3.2). The debris-covered surface is only altered when there is a layer of snow on the surface – in which case the density function above is used.

The z_0 values used for the model here are subject to several issues including adequate ventilation, instrument height measurement (Brock *et al.*, 2006), using an arithmetic mean over geometric mean, and the lack of homogenous ground surrounding the debris-covered ice site. Whilst more accurate values may have been obtained by addressing these issues, the z_0 values calculated here are considered superior to using published values and are in keeping with other studies.

3.3.2 Debris thermal properties

Thermal conductivity (k) varies as a function of particle size, porosity and moisture content (Oke, 1987). For this research thermal conductivity is estimated following the method of

Conway and Rasmussen (2000) and Nicholson and Benn (2006) using heat capacity and diffusivity. Firstly, thermal diffusivity of the debris (κ) is determined using a one-dimensional thermal diffusion equation:

$$\frac{\partial T}{\partial t} = \kappa \frac{\partial^2 T}{\partial z^2} \qquad 3.23$$

where T is debris temperature (K), t is time, and z is the depth (m). A value of κ at each measurement point is taken as the gradient of the line of best fit of the first derivative of temperature with time, versus the second derivative of temperature with depth (Nicholson and Benn, 2006). High κ values imply that temperature changes will be large and rapid. Deviations from the best-fit line imply non-conductive behaviour, possibly caused by phase changes (Conway and Rasmussen, 2000).

The thermal conductivity (k) can then be determined using the volumetric heat and the diffusivity according to Farouki (1981) where:

$$k = \left[x_d c_d \rho_d + x_w c_w \rho_w + x\ c_a \rho_a\right]\kappa \qquad 3.24$$

where x is the volume fraction, c the specific heat capacity (J kg^{-1} K^{-1}), and ρ the density (kg m^{-3}), of the debris ($_d$), water ($_w$) and air ($_a$).

Nicholson and Benn (2006) assumed that the debris was either fully saturated or dry and determined the thermal conductivity (k) using:

$$k = \left[c_d \rho_d (1-\varphi) + c_v \rho_v \varphi\right]\kappa \qquad 3.25$$

where φ is the porosity and v denotes voids. In order to calculate a maximum and minimum thermal conductivity, conditions of fully saturated (voids filled with water) and completely dry (voids filled with air) were used.

The depth-averaged κ for the debris was found to be: 0.37 ± 0.005 mm^2 s^{-1} and is comparable to those reported in the literature which range from 0.3 to 0.9 mm^2 s^{-1} (Table B.1 in Appendix B). This value was determined using data from days with no snow cover. This dataset consisted of 28 days of 30 minute data from 2003-2004 and 9 days of 10 minute data from the November 2004 measurement period.

The debris at the measurement site is described by Glasser *et al.* (2006), and consists of sandy gravel, gravelly sand, sandy pebble-gravel or diamicton of with some coarser

material. It has a mixed lithology, but is dominated by fine-grained volcanics (65%), and vesicular lava (33%) with a small proportion of granite (2%). Volumetric heat capacity was calculated using a specific heat capacity of 830 J kg^{-1} K^{-1} for volcanic rock (Nicholson, 2005), a density of 2700 kg m^{-3}, and 0.3 porosity for supraglacial debris (Conway and Rasmussen, 2000).

The thermal conductivity (k_d) determined for the debris-covered site was 0.59 W m^{-1} K^{-1} for dry debris and 1.53 W m^{-1} K^{-1} for saturated debris. These values are comparable with the values used in the literature for debris-covered ice ablation studies (Table B.1 in Appendix B). The dry debris value is of similar magnitude to those reported by Campbell *et al.* (1998) for soils in the dry valleys and at Scott Base, which ranged from 0.20 to 0.26 W m^{-1} K^{-1}. The *k* value is also at the low end for those reported in the literature by Clauser and Huegnes (1995) for volcanic rocks (1.5 – 3.5 W m^{-1} K^{-1}). Notably, the thermal conductivity values reported by Campbell *et al.* (1998) did not change significantly with moisture content. The dry value calculated here is also slightly higher than that reported for sandy soil, 0.3 W m^{-1} K^{-1} (Oke, 1987). Conversely, the saturated value is less than reported for a saturated sandy soil, which is 2.2 W m^{-1} K^{-1} (Oke, 1987).

The adapted SOMARs model was run twice for each period of measurements on the debris-covered ice site, using the dry debris thermal conductivity value (0.59 W m^{-1} K^{-1}), and then again for the saturated debris thermal conductivity value (1.53 W m^{-1} K^{-1}).

3.3.3 Initial temperature profile

At the bare ice site a theoretical initial temperature profile was used in the model. The profile used was based on the annual average air temperature recorded at various AWS on the ice shelf, and the surface temperature from the beginning of measurements. Using these values and the shape of a temperature profile published by McCrae (1984) an initial temperature profile was created.

For the debris-covered ice site the temperature profile within the top 0.3 m of debris was calculated using measured values, and the temperature profile for the underlying ice was based on that used for the bare ice site.

3.3.4 Other parameters

Specific parameters used in the running of the model for the McMurdo Ice Shelf are outlined in Table 3.3. The density of the snow at the debris-covered ice site was not measured, so a value of 400 kg m^{-3} was assumed. Density of the exposed ice shelf ice was set to 917 kg m^{-3}. All other values model parameters were set to the model default.

Table 3.3 Input parameters used in running of the model for the McMurdo Ice shelf.

Parameter	**Value**
Bare ice z_0	2.5 x 10^{-3} m
Frozen snow z_0	1.2 x 10^{-4} m
Melting snow z_0	1.3 x 10^{-3} m
Debris z_0	3.9 x10^{-2} m
Saturated debris k_d	1.53 W m^{-1} K^{-1}
Dry debris k_d	0.59 W m^{-1} K^{-1}
Density of initial snow cover on debris	400 kg m^{-3}
Density of ice	917 kg m^{-3}
Depth of grid	25 m
Size of uppermost grid cell	0.15 m
Size of lowermost gird cell	3.00 m
Time step	30 minutes
Density of debris	2700 kg m^{-3}
Cloud cover	Held constant at 0.5
Heat capacity of debris	830 J kg^{-1} K^{-1}
Depth of debris	0.60 m

3.4 Model validation

To ensure that all the significant processes are captured within the model, and to examine the extent to which the model is capable of reproducing reasonable mass and energy fluxes, model output was compared with several directly measured variables. Suitable measurements available included surface temperature, sensible heat flux and latent heat flux at both sites. Additionally, surface mass balance was measured at the bare ice site and subsurface temperatures at the debris-covered ice site.

In order to evaluate model performance, model output and measured data were compared. Using these two datasets, the mean, Pearson's Product-Moment Correlation Coefficient (r), root mean squared error (RMSE), and an index of agreement (d) were calculated. The index of agreement used here is that presented by Willmott (1981). It is similar to the Nash-Sutcliffe efficiency coefficient (Krause, *et al.* 2005), but ranges between 0 and 1, with an efficiency of 1 being a perfect match between observed and modelled values. Unlike the correlation coefficient r, d is sensitive to changes in proportionality (Willmott, 1982). Comparisons were performed at two resolutions: high resolution (half hourly) over the period that eddy covariance data were available, and low resolution (daily means) for longer periods that the AWS was installed.

Before comparisons between modelled and measured values were made some of the directly measured quantities needed correction. These corrections are now described.

3.4.1 Turbulent flux corrections

As described in section 2.5.2 an eddy covariance system was installed alongside the AWS for a short period. The eddy covariance method is theoretically the best method to determine turbulent fluxes as it measures them directly and few assumptions are made (Spronken-Smith *et al.*, 2006). Despite this, researchers have found that there are difficulties in obtaining closure of the energy balance when the turbulent fluxes have been determined by this method (Massman and Lee, 2002; Mauder *et al.,* 2007). Problems with eddy covariance result from either instrument limitations, or from obtaining measurements during meteorological conditions (particularly stable) for which the instruments are not well suited (Massman and Lee, 2002). Additionally, several corrections must be made to the raw data before the fluxes can be calculated and interpreted confidently.

When using sonic anemometer derived temperature for flux calculations, the sonic temperature flux must be corrected for the effect of moisture (Schotanus, 1983; Liu *et al.,* 2001). The corrected sensible heat flux $\left(\overline{w'T'_c}\right)$ is determined from the sonic temperature flux:

$$\left(\overline{\mathrm{w'\,T'_C}}\right) = \overline{w'T'_S} - 0.51\overline{w'q'}\overline{T} + \frac{2\overline{T}}{c^2}\overline{w'u'} \qquad 3.26$$

where T is the temperature (ºC), c is the sound velocity (m s^{-1}), u, v, w are the x, y, z wind velocity components (m s^{-1}), and q is the specific humidity (kg kg^{-1}). Acoustic temperature data are internally corrected for crosswind contamination by the sonic anemometer (CSAT3).

As the Krypton Hygrometer (KH20) measures the absorption of oxygen as well as water vapour, a correction was applied for the absorption of oxygen (Tanner and Greene, 1989; Massman *et al.,* 1990). Air density was accounted for in the flux calculations by applying the WPL (Webb-Pearman Leuning) correction from Webb *et al.* (1980). The mean percent change from the WPL correction was a gain of 7.7%.

Although a spatial separation and frequency response correction is often made (e.g. Moore, 1986; Horst 1997 & 2000; Cullen *et al.*, 2007a; Mauder, 2007) it has not been included here for a number of reasons. Firstly, in order to minimise spectral loss due to sensor separation, the KH20 was positioned at the same height as, and as close as possible to, the CSAT3 sonic anemometer. Due to the nature of the corrections, if $S/z << 1$, the correction will be small (Massman and Lee, 2002; Oncley *et al.,* 2007), where S is the sensor displacement and z the height. In this study S/z values were 0.09 and 0.08 for the clean and debris-covered ice sites respectively. Furthermore, to apply corrections from Moore (1986) or Horst (1997) a co spectral frequency analysis is necessary. As no raw data were recorded, a frequency analysis was not possible, and no suitable published analysis was available.

Oncley *et al.* (2007) found that the spatial separation correction was the largest of the series of corrections applied to their measured fluxes. Spatial corrections increased their latent heat flux by 7% and decreasing the sensible heat by 2%. Over the flat ice of Kilimanjaro, Cullen *et al.* (2007a) reported much larger losses, including up to 14% of latent heat flux loss in the stability range ($-0.1 < z/L < 0.25$) and larger for more stable conditions. Massman and Lee

(2002) suggest that difficulties experienced in flux measurements are largely meteorological in nature, particularly during stable conditions and that measured fluxes must be treated with caution.

3.4.2 Height data

Surface height measurements using the sonic ranger proved to be problematic. While the sonic ranger accuracy is ± 0.01 m, there was also a large amount of noise in the signal received (Figure 3.4a). A noisy signal may be a result of electromagnetic interference, low density snow, or an uneven surface (Campbell Scientific, 2003b). Reflections from drifting snow may also cause an increased surface height record. As an initial step to deal with any inaccurate readings, the quality signal from the sensor itself was used to filter bad readings

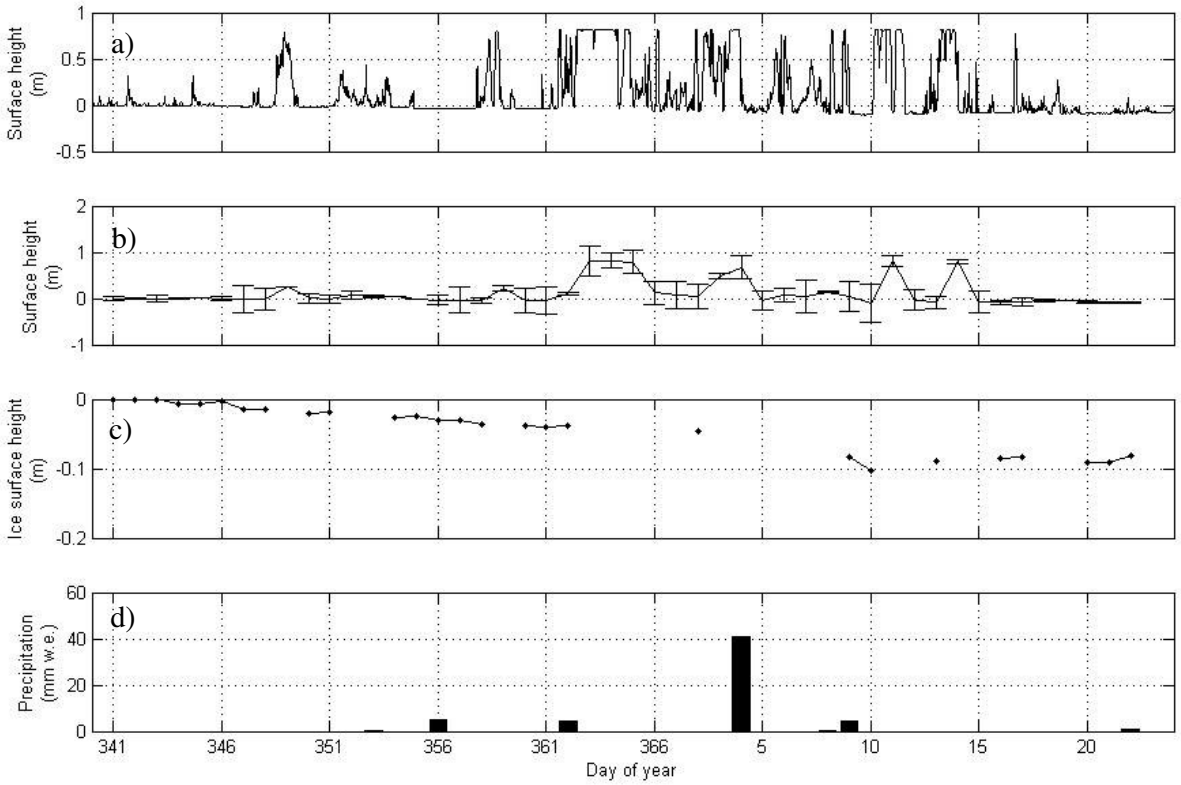

Figure 3.4 Surface height and precipitation recorded for (Day 341, 2004 – Day 22, 2005), a) raw sonic ranger data b) sonic ranger daily mean c) sonic ranger daily mode indicating the approximate ice surface height d) precipitation recorded at McMurdo Station.

within the datalogger program. However noise was still apparent in the dataset, requiring further treatment.

Regrettably, using the mean daily values of surface height incorporated the noise, providing unrealistic values (Figure 3.4b). There is no apparent correlation between the precipitation

records from McMurdo Station (Figure 3.4d) and the increases in surface height at the bare ice site (Figure 3.4a, b). It is likely that the high values are a result of the issues mentioned above and unlikely that meaningful accumulation data can be extracted from the sonic ranger record over these periods. It is evident that there is a definite baseline in the raw data that is likely to represent the ice surface height (Figure 3.4a). To determine the approximate baseline, the raw data was binned (by rounding to the nearest millimetre) and then the mode for each day was found (Figure 3.4c). Although incomplete, the trend in the mode time series is similar to the trend in the baseline in the raw data (Figure 3.4a) and was thus regarded as a realistic representation of the ice surface.

Ablation stake measurements can also be problematic due to the subjective nature of locating them and accuracy in measurements. Stakes were placed in white ice (not blue) and measured at the beginning and end of the measurement period to the nearest millimetre.

Given the above difficulties in collecting direct measurements of surface height the data must be examined with caution. However, since there are two different sources, and the measurements were taken over long periods there is still reasonable data with which to compare model output.

3.4.3 Bare ice site validation results

The bare ice modelled turbulent fluxes are in the correct direction and roughly of the same magnitude as the measured fluxes (Figure 3.5a,b). In the first part of the covariance measurement period (2100, Day 338 – 0600, Day 339, 2004), the atmosphere was stable (Figure 3.5d), and the sensible heat fluxes are reasonably modelled well (Figure 3.5a). The stability then became highly variable (Figure 3.5d) and there is an associated increase in modelling error.

In the latter part of the measurement period (from 1000, Day 340 onwards), the majority of the values of sensible heat flux were low ($< \pm$ 10 W m^{-2}) and conditions were near neutral (Figure 3.5d). A narrow range of values during this period (-11 to 34 W m^{-2}) and the fluctuation between positive and negative makes interpretation of the model performance difficult. Over the eddy covariance measurement period the correlation between the modelled and measured sensible heat (Figure 3.6a) at the bare ice site was only fair (r = 0.56, d = 0.71). The largest fluxes of sensible heat occurred during stable conditions and

were directed towards the ice (Figure 3.7a). As very few large sensible heat fluxes (>100 W m^{-2}) were recorded during this period, it is suggested that the model is likely to predict large fluxes as well as it does at the debris-covered ice site (Section 3.4.4) as the equipment and data treatment were identical.

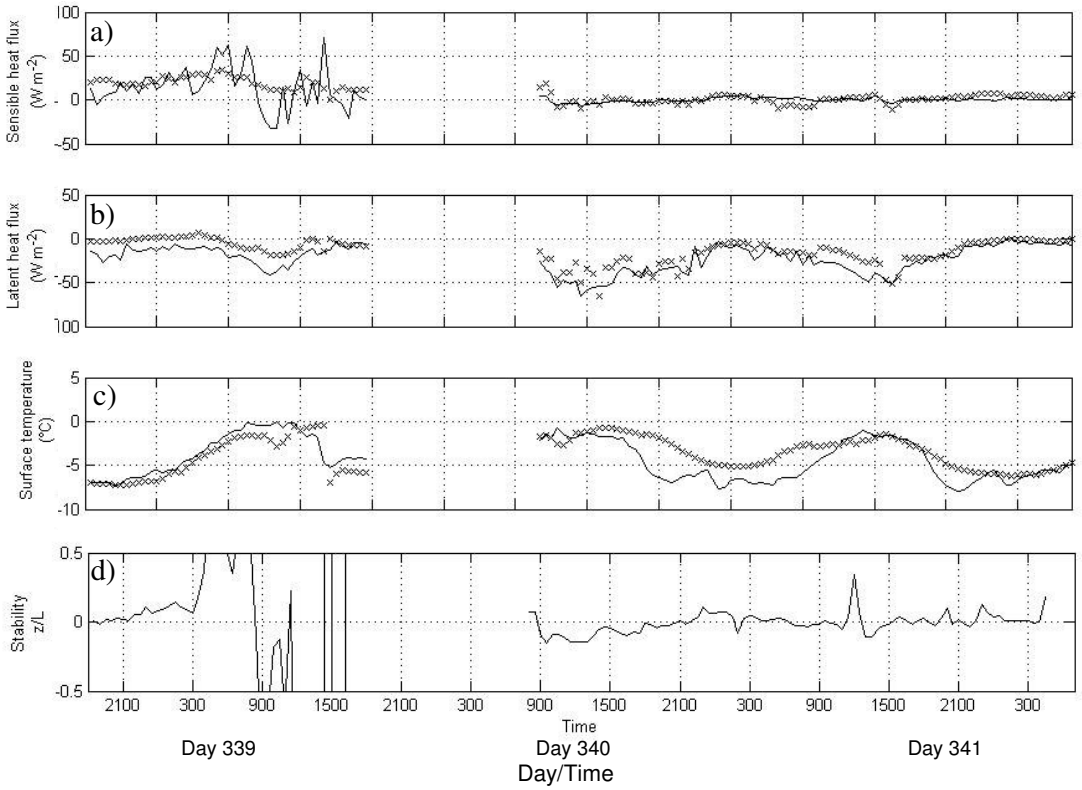

Figure 3.5 Time series of 30 minute SOMARS modelled output with variables directly measured at the bare ice site for the period that the eddy covariance system was in place (2100 Day 338 – 0700 Day 342, 2004). Measured variables are shown by a solid line, and modelled with x's. a) Sensible heat flux b) Latent heat flux c) Surface temperature d) Stability where positive values represent a stable environment. Missing data was due to power supply issues (Section 3.3).

Latent heat flux over the bare ice site was consistently negative during the eddy covariance measurement period (Figure 3.5b). The modelled latent heat fluxes follow the progress of the measured latent heat flux well (Figure 3.5b). Throughout the period there was a slight underestimation of magnitude of the latent heat flux (Figure 3.6b). Overall, the model was relatively good at predicting latent heat flux over the bare ice with a correlation coefficient of 0.86, and an index of agreement of 0.83.

Throughout the eddy covariance measurements at the bare ice site the atmosphere was mostly neutral (Figure 3.5d). The largest negative latent heat fluxes were reported when the atmosphere was unstable (Figure 3.7), although these were still small (< 70 W m^{-2}).

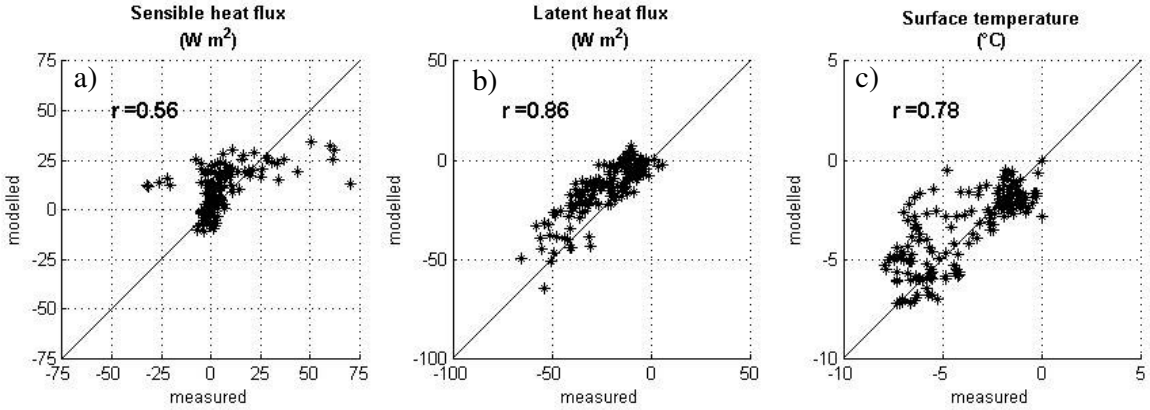

Figure 3.6 Correlation between 30 minute SOMARS modelled results with variables directly measured at the bare ice site for the period that the eddy covariance system was in place (0900 Day 338 – 0700 Day 342, 2004).

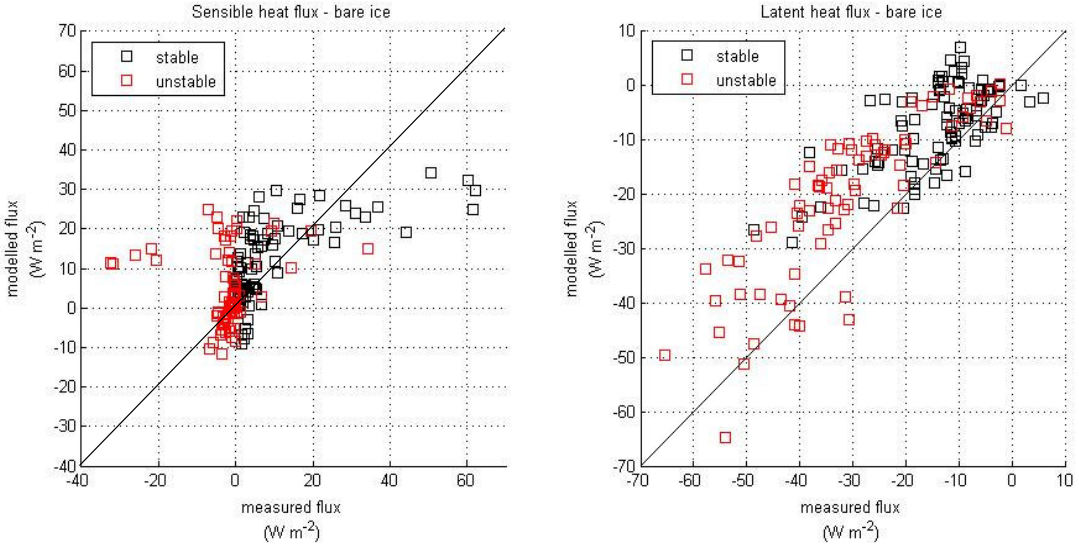

Figure 3.7 Comparison between 30 minute measured and modelled turbulent fluxes, a) Sensible heat flux, b) Latent heat flux, showing stable and unstable cases at the bare ice site (2100 Day 338 – 0700 Day 342).

The surface temperature is one of the key variables in the surface energy balance, yet one of the most difficult to measure or model (Section 1.2.2). Modelled surface temperature was compared with that independently measured using the Everest sensor (Section 2.5.2). For the bare ice, the model performed reasonably well at predicting the surface temperature, both at

a half hour resolution (Figure 3.5c), and in the calculated daily mean (Figure 3.8a). The diurnal cycle of surface temperature was captured very well (Figure 3.5c) with a correlation coefficient of 0.78 and index of agreement of 0.83 for the eddy covariance measurement period. However, during this period, the surface temperature was slightly overestimated (Figure 3.6c). Over the longer period that the model was run the mean daily surface temperature was also slightly overestimated (Figure 3.8) and the accuracy reduced (r=0.69). Despite this reduced correlation the trends are captured well, even during periods when the

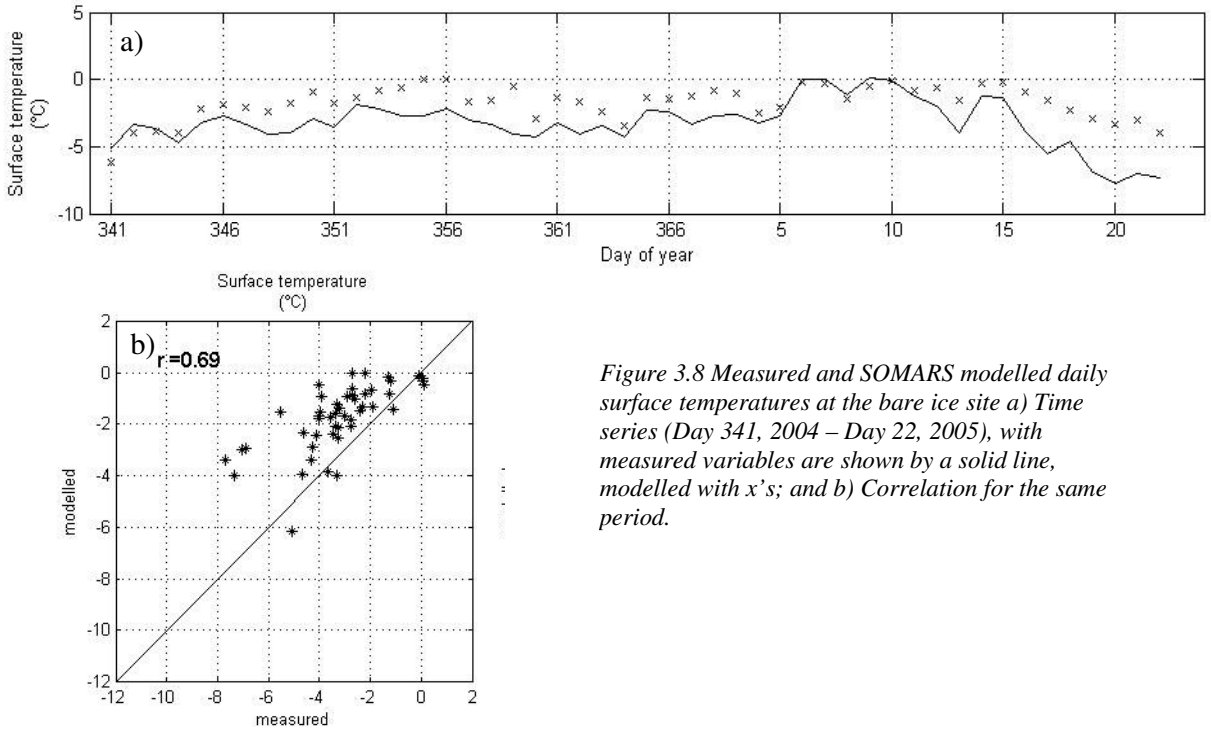

Figure 3.8 Measured and SOMARS modelled daily surface temperatures at the bare ice site a) Time series (Day 341, 2004 – Day 22, 2005), with measured variables are shown by a solid line, modelled with x's; and b) Correlation for the same period.

surface was around melt point (Figure 3.8a). There is a fair index of agreement (d=0.67) between measured and modeled daily surface temperatures.

The overall modelled net surface height change is modelled well when considered with respect to that measured at the closest ablation stakes (Table 3.4). In view of the uncertainties in the calculated and measured surface mass balance, the differences between them are considered acceptable.

Table 3.4 Modelled and measured total surface height change on bare ice in the McMurdo Ice Shelf ablation area, from Day 341, 2004 to day 22, 2005.

Source	Surface height (m)
Modelled	- 0.047
Mean stake measurements	-0.053
Stake 90	- 0.020
Stake 91	- 0.041
Stake 92	- 0.100
Sonic ranger (mode)	- 0.081

Over the entire period the model captures the general surface height change trend of gradual ablation (Figure 3.9), but there are some features that warrant discussion. Firstly, the model appears to overestimate the ablation rate between Day 351 and 361, 2004. This period is also around the time when the surface temperature is overestimated, which could result in an overall overestimate of ablation, especially by melting.

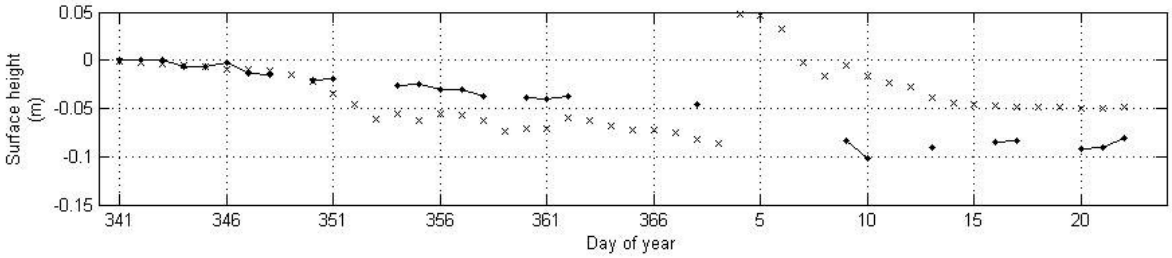

Figure 3.9 Time series of SOMARS modelled surface height with directly measured at the bare ice (Day 341, 2004 – Day 22, 2005). Measured variables are shown by points and a solid line, modelled with x's. The measured surface height represents the ice surface (See section 3.4.2)

The second major feature is on Day 4, 2005, where the modelled surface height shows a rapid increase. This increase is directly related to the large precipitation amount used to force the model (Figure 3.4d). There is no associated change apparent in the measured surface height (Figure 3.9) as it is only representative of the ice surface (Section 3.4.2). However, with such a large amount of precipitation recorded at McMurdo Station it is likely that there was a quantity of precipitation at the bare ice site. As the modelled surface height remains higher than that measured after this event, it may be that the precipitation recorded at McMurdo Station was considerably more than that at the bare ice site. In order to see how reduced precipitation would affect the modelled surface energy and surface mass balance, an extra run of the model was made with half the amount of precipitation for Day 4, 2004 (Appendix C). It was found that the relative proportions and directions of the energy balance

components were not significantly altered (Appendix C). Therefore, it was decided that analysis should be continued using the model forced with the true precipitation record from McMurdo Station.

In summary, the model performance at the bare ice site is considered realistic. The agreement between turbulent fluxes is reasonable taking into account the uncertainties in both measured and modelled values (Table 3.5). The model captures realistic variability, with the modeled standard deviations similar to those for the measured (Table 3.5). Importantly, the direction of the fluxes is largely correct, suggesting that the Monin-Obhukov similarity theory is applicable at the bare ice site. The model performs well at calculating surface temperatures (Table 3.5). Surface mass balance was modeled reasonably well although this success may have been somewhat affected by overestimated ablation being balanced by an excessive precipitation input. It was considered that the surface mass balance is modelled realistically, especially given that precipitation in the model is prescribed using data from a different site.

Table 3.5 Summary of comparison of SOMARS modelled results with variables directly measured at the bare ice site. The turbulent fluxes and surface temperature are compared at 30-minute intervals for the period that the eddy covariance system was in place (2100 Day 338 – 0700 Day 342, 2004). The remaining variables are daily means for the period the model was run (Day 341, 2004 – Day 22, 2005). Standard deviation is shown in brackets.

	Mean sensible heat flux ($W\ m^{-2}$)	Mean latent heat flux ($W\ m^{-2}$)	Mean surface Temperature (ºC)	Mean daily surface Temperature (ºC)
Observed	5.1 (15.4)	-22.6 (15.3)	-3.9 (2.4)	-3.5 (1.9)
Modelled	8.6 (10.3)	-13.4 (13.1)	-3.2 (2.1)	-1.8 (1.2)
Correlation coefficient	0.56	0.86	0.78	0.69
Root mean squared error	12.8	10.4	1.4	1.9
Index of Agreement	0.71	0.83	0.83	0.67

3.4.4 Debris-covered ice site validation results

It was found that the overall model performance at the debris covered ice site was typically better when the debris was considered saturated. Consequently, the majority of the results presented in this section are for saturated conditions.

Both turbulent fluxes and the surface temperatures are modelled well during the eddy covariance period over debris-covered ice (Figure 3.10). Sensible heat flux is primarily directed away from the surface during the eddy covariance measurement period with some large values (maximum, -252 W m^{-2}). Modelled sensible heat flux followed the same diurnal pattern as measured with largest negative fluxes during the afternoon (Figure 3.10a). During this period at the debris-covered ice site there was much more instability (Figure 3.10d) than at the bare ice site (Figure 3.5d) due to the warm debris surface. The sensible fluxes are also much higher at the debris-covered ice site (reaching >200 W m^{-2}) than at the bare ice site (maximum 70 W m^{-2}). This difference is due to the larger difference in temperature between the surface and the air. Sensible heat transfer in the range -50 to +50 Wm^{-2} were quite well modelled but the magnitudes less than -50 W m^{-2} were consistently underestimated (Figure 3.11a).

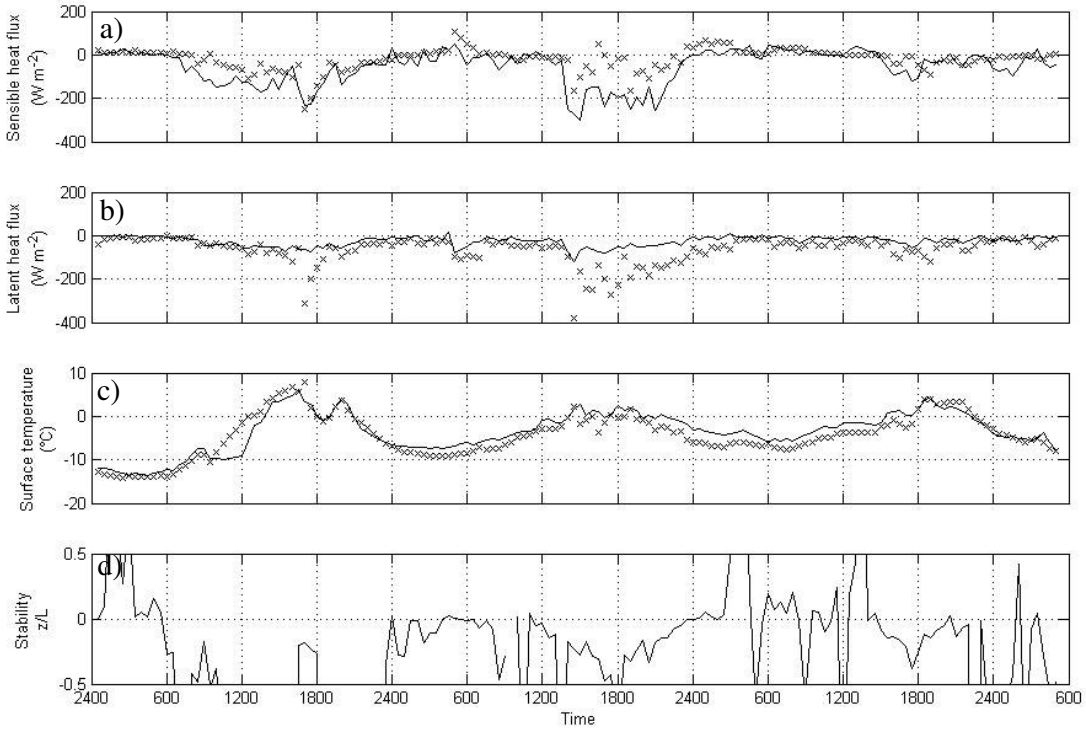

Figure 3.10 Time series of 30 minute SOMARS modelled results with variables directly measured at the debris-covered ice site for the period that the eddy covariance system was in place (0000, Day 315 – Day 0500 Day 318, 2004). Measured variables are shown by a solid line, modelled with x's. Note: these values are for the model run that assumes that the debris is saturated. a) Sensible heat flux b) Latent heat flux c) Surface temperature d) Stability - where positive values represent a stable environment.

The majority of the modelled and measured latent heat fluxes were negative at the debris-covered site. The modelled values were generally large in magnitude and in some cases quite significantly so (Figure 3.10b). This apparent overestimation may be partly attributed to the eddy covariance data being underestimated due to lack of sensor separation adjustment (Section 3.4.1). Although the loss can be the large (Section 3.4.1) the sensor separation adjustment could only account for some of the difference. It is also likely that the latent heat flux is overestimated due to the assumption of a saturated surface (Figure 3.12b), with the true value highly likely to lie somewhere in between the dry and saturated extremes. Furthermore, Krause *et al.* (2005) suggest that the correlation coefficient places too much emphasis on higher values and thus distorting the reported model efficiency. It is important to note that the modelled flux direction was consistent with that measured with the eddy covariance system (Figure 3.10b).

Throughout the eddy covariance measurements at the debris-coved ice site the atmosphere was predominantly unstable (Figure 3.10d). During stable conditions both of the turbulent fluxes were small (Figure 3.12a,b). When the conditions were unstable the fluxes were larger and more varied (Figure 3.12a,b).

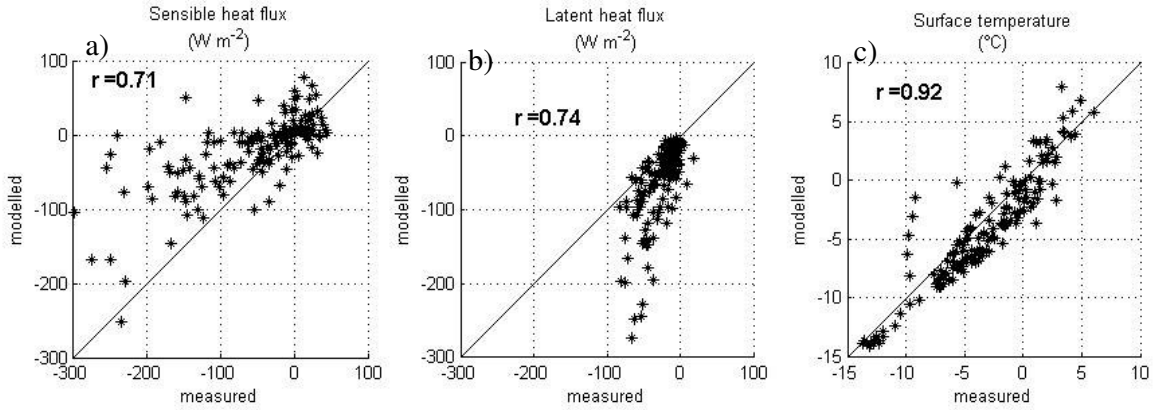

Figure 3.11 Correlation between 30 minute SOMARS modelled results with variables directly measured at the debris-covered ice site for the period that the eddy covariance system was in place (0000, Day 315 – Day 0500 Day 318, 2004). Note: these values are for the model run that assumes that the debris is saturated. Where a) is Sensible heat flux, b) Latent heat flux, c) Surface temperature.

The newly created debris subsurface component modelled the temperature conditions of the debris reasonably well. Temperatures tended to be underestimated during unstable conditions resulting in an underestimate of larger magnitude sensible heat fluxes (Figure 3.11a). During the eddy covariance period, half hourly surface temperatures (Figure 3.10c, 3.11c) show that the diurnal cycle is demonstrated well (r = 0.92, d = 0.95).

Modelled mean daily surface temperatures are in excellent agreement with the measured temperatures at the debris-covered ice for both longer run periods, both capturing trends well (Figure 3.13a, 3.15a). During the first long-term period the model performed well (Figure 3.14a) with both a correlation coefficient and index of agreement of 0.96. Although the second period was less competent at modelling the surface temperature (Figure 3.16a) it was still considered very good, with a correlation coefficient of 0.83 and an index of agreement of 0.90. The RMSE was reduced for this second period (Table 3.7). Given the accuracy of the sensor used to measure the surface temperature (±0.5 ºC) this result is very satisfactory. This performance is especially good as the bulk method (which relies on the surface temperature) is used to calculate the turbulent fluxes.

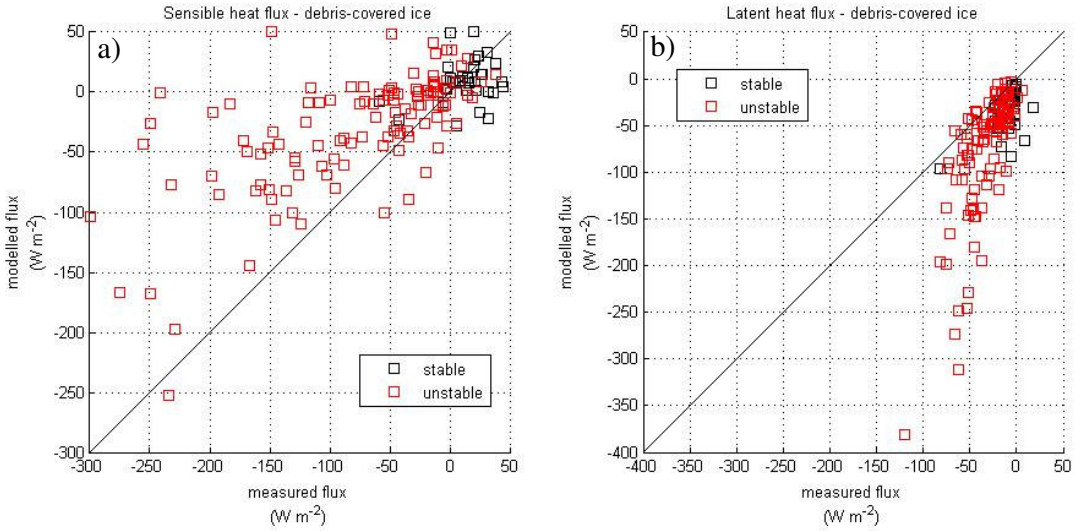

Figure 3.12 Comparison between 30 minute measured and modelled turbulent fluxes, a) Sensible heat flux, and b) Latent heat flux, showing stable and unstable cases at the debris-covered ice site (0000, Day 315 – Day 0500 Day 318, 2004).

Mean daily subsurface temperatures modelled using the new subsurface component were also very good (Figures 3.13, 3.15). At the beginning of the 2003-2004 period, the modelled mean daily surface and subsurface temperatures are underestimated (Figure 3.13). These underestimated values were all during the period when there was old snow overlying the debris, suggesting that the model may not capture all processes or that the snow density used was incorrect (density was not measured at this site). When the debris was free of snow (After Day 340, 2003 and Day 317 – 339, 2004) temperatures were modelled very well (Figures 3.13 and 3.14), demonstrating that the energy conduction process is captured

adequately within the model. Overall the correlation between modelled and measured subsurface temperatures was very good (Figure 3.14, 3.16).

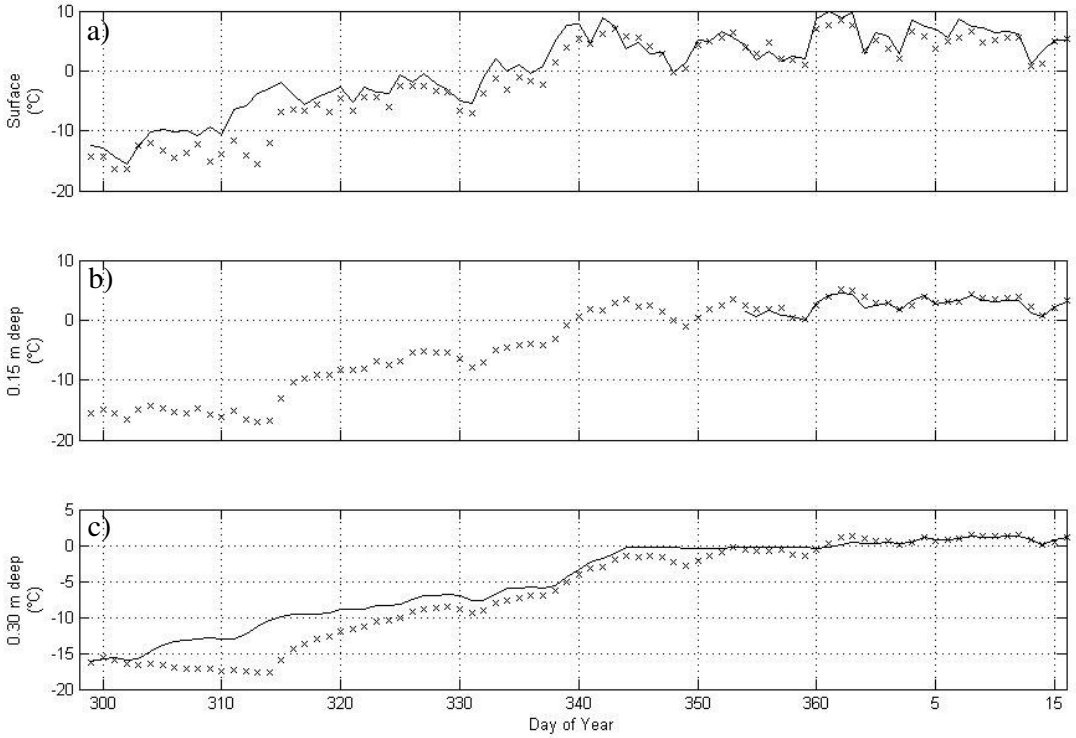

Figure 3.13 Time series of SOMARS modelled results with variables directly measured at the debris-covered ice site for the first "long term" period that the AWS was installed (Day 299, 2003 - Day 16, 2004). Measured variables are shown by a solid line, modelled with x's. Where a) Surface temperature b) 0.15 m deep temperature c) 0.30 m deep temperature.

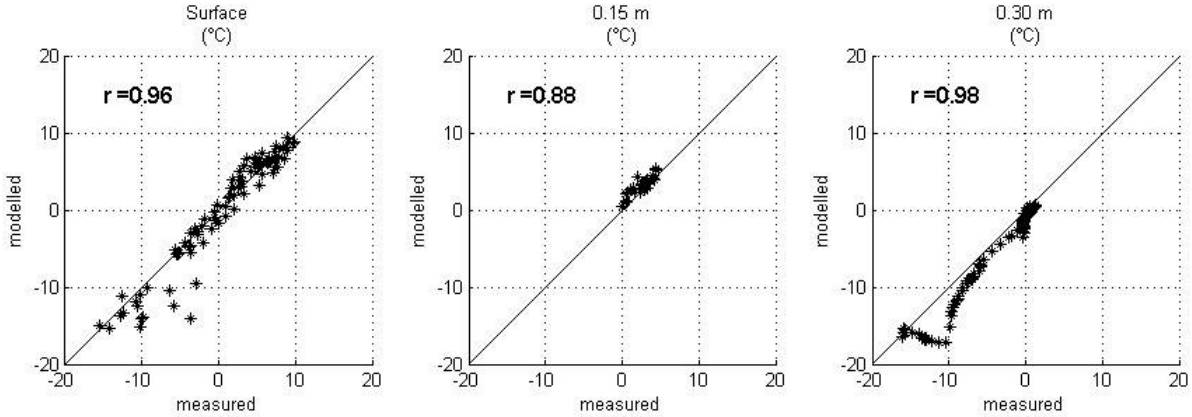

Figure 3.14 Correlation between SOMARS modelled results with variables directly measured at the debris-covered ice site for the first "long term" period that the AWS was installed (Day 299, 2003 - Day 16, 2004). Where a) Surface temperature b) 0.15 m deep temperature c) 0.30 m deep temperature.

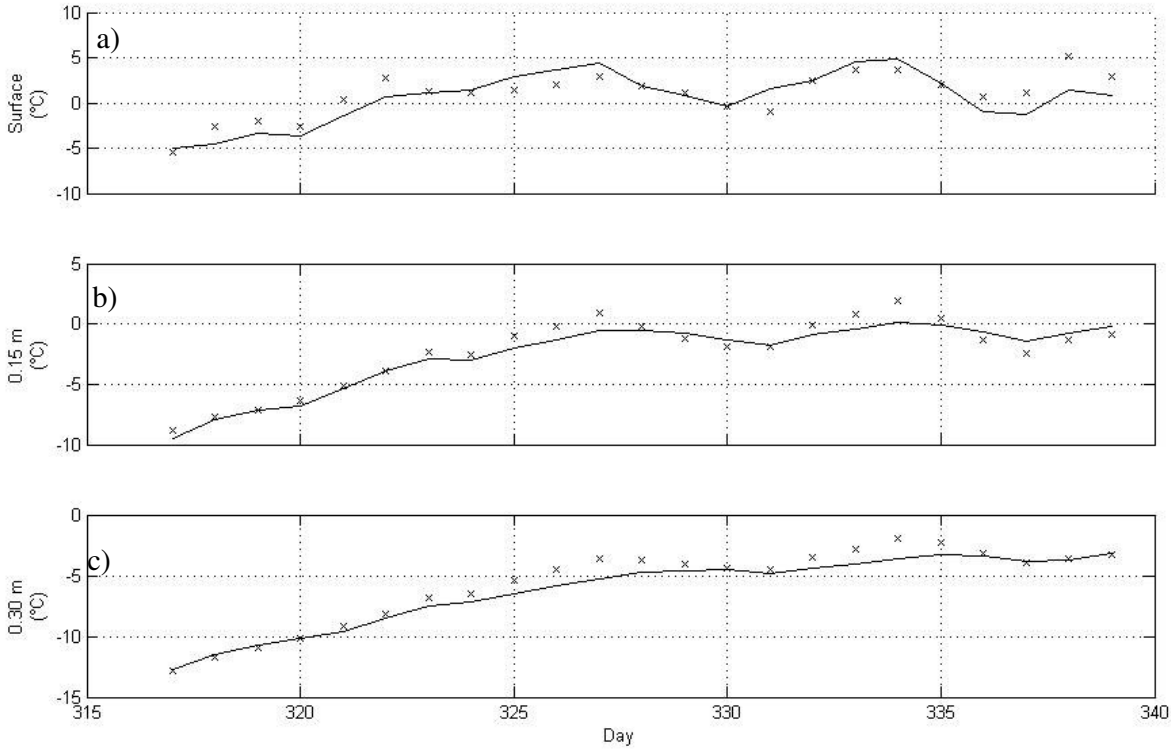

Figure 3.15 Time series of SOMARS modelled mean dailytemperatures with variables directly measured at the Debris-covered ice site for the second "long term" period that the AWS was installed (Day 317 - Day 339, 2004). Measured variables are shown by a solid line, modelled with x's. Where a) Surface temperature b) 0.15 m deep temperature c) 0.30 m deep temperature.

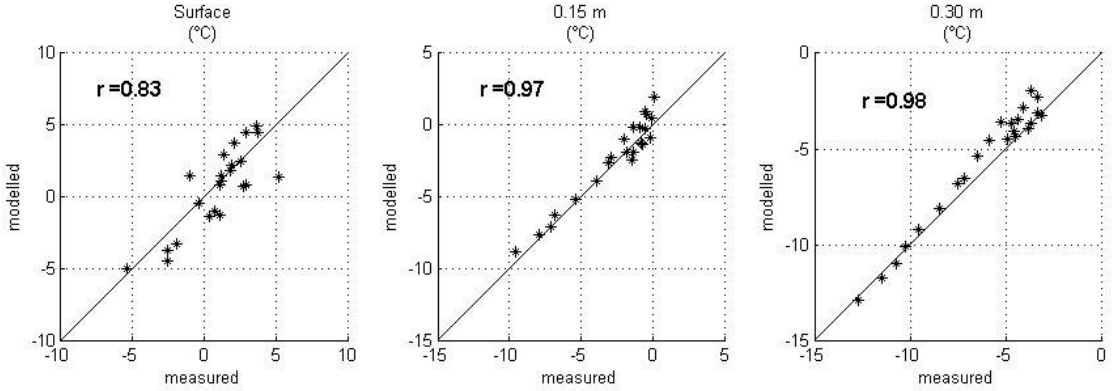

Figure 3.16 Correlation between SOMARS modelled temperature against variables directly measured at the Debris-covered ice site for the second "long term" period that the AWS was installed (Day 317 - Day 339, 2004). Where a) Surface temperature b) 0.15 m deep temperature c) 0.30 m deep temperature.

In summary, the turbulent fluxes were modelled well considering the issues in calculating z_0. The sensible heat flux was reasonably well modeled using the saturated debris situation (Figure 3.10a, 3.11a), with a slight improvement using the dry situation (Table 3.6). The model overestimated the latent heat flux over debris-covered ice in saturated conditions (Table 3.6). However, given that the debris is considered saturated, the measured latent heat flux is likely to be low (Section 3.4.1), and the modelled flux direction is correct, the model is considered to be performing satisfactorily. The latent heat flux direction was incorrect when a dry surface is considered dry (Table 3.6) this is likely due to the fact that the dry surface assumption is an extreme. Latent heat flux is likely to be occurring due to sublimation at depth in the debris layer. All temperatures (surface and sub-surface) were modelled very well at the debris-covered ice site when the debris is considered saturated (Table 3.7). Based on these validation results the model is considered adequate to assess the surface energy balance of the bare and debris-covered ice of the McMurdo Ice Shelf.

Table 3.6 Comparison of SOMARS modelled results with variables directly measured at the debris-covered ice site from 0000, Day 315 – Day 0500 Day 318, 2004 using a 30-minute averaging period. Standard deviation is shown in brackets. For saturated debris the thermal conductivity is held at 1.53 W m^{-1} K^{-1} and the surface vapour pressure is calculated with respect to the surface temperature. For the dry debris case the thermal conductivity is set to 0.59 W m^{-1} K^{-1} and the surface vapour pressure is equal to that of the atmosphere.

	Saturated debris			Dry Debris		
	Sensible heat flux (W m^{-2})	Latent heat flux (W m^{-2})	Surface temperature (ºC)	Sensible heat flux (W m^{-2})	Latent heat flux (W m^{-2})	Surface temperature (ºC)
Observed mean	-51.2(94.0)	-27.3(30.5)	-3.3(4.6)	-51.2(94)	-27.3 (30.5)	-3.30(4.6)
Modelled mean	-11.6 (40.9)	-60.0(52.5)	-5.1(3.9)	-34.5(73.0)	48.5(46.1)	-2.9(6.5)
Correlation coefficient	0.71	0.74	0.92	0.75	0.52	0.89
Root mean squared error	69.2	60.6	2.1	57.3	45.0	3.3
Index of Agreement	0.74	0.55	0.95	0.85	0.57	0.91

Table 3.7 Comparison of SOMARS modelled and directly measured temperatures at the debris-covered ice site during two measurement periods. At the beginning of the first measurement period there was approximately 0.3 m snow on the ground, while during the second period the debris was snow free. Standard deviation is shown in brackets. For both of the shown model runs the debris thermal conductivity is held at 1.00 W m^{-1} K^{-1} and the surface vapour pressure is calculated with respect to the surface temperature.

	Mean daily debris temperatures, Day 299, 2003 - Day 16, 2004.			Mean daily debris temperatures, Day 317 - Day 339, 2004.		
	Surface (ºC)	0.15 m * (ºC)	0.30 m (ºC)	Surface (ºC)	0.15 m (ºC)	0.30 m (ºC)
Observed mean	0.3(6.5)	2.5(1.3)	-4.9 (5.6)	1.0(2.4)	-2.6(2.8)	-6.2(2.9)
Modelled mean	-1.5 (7.4)	2.8 (1.2)	-6.4 (6.8)	0.6(2.8)	-2.3(2.9)	-5.7(3.2)
Correlation coefficient	0.96	0.89	0.98	0.83	0.97	0.98
Root mean squared error	2.8	0.7	2.3	1.6	0.8	0.8
Index of Agreement	0.96	0.93	0.97	0.90	0.98	0.98

** Temperatures at 0.15 m were only available from Day 326, 2003- Day, 17 2004.*

3.5 Sensitivity

In order to test the sensitivity of the modelled surface mass balance, several input parameters and calculation schemes were varied, the model run again, and the resulting surface mass balance compared. The model was run for the period Day 341, 2004 – Day 22, 2005 on bare ice and for the period Day 299, 2003 - Day 16, 2004 on debris-covered ice.

The value of roughness length of momentum reported in the literature varies considerably (Section 3.3.1). In order to test the sensitivity of the model to different roughness lengths, the upper and lower range used are those published for similar sites. Results suggest that although the model is not overly sensitive to the momentum roughness length, the method of calculating the heat and vapour roughness lengths is important (Table 3.8).

A few published surface energy studies have used the same value of z_0 for z_{0e} and z_{0h} (Section 3.3.1). In this study, when the roughness lengths were set to be equal, the offset was extremely large (Table 3.8). This result agrees with other research where the roughness lengths are shown to be important (e.g. Reijmer and Oerlemans, 2002; Cullen *et al.,* 2007a). Importantly, this sensitivity testing shows that calculation of roughness lengths of heat and vapour must be carefully considered. This is because, although the overall change may not be large, the changes in sublimation and melt can be significant and cancel each other thus giving the impression that the model is not overly sensitive to the change.

In order to test the response of the model to changes in air temperature, it was increased by 0.2 ºC, which is the reported accuracy of the sensor (Section 2.5.2, Table 2.5). Running the model using this temperature change for the bare ice site shows only a 5.7% increase in melting (+3.9 mm w.e.) which is only slightly offset by a decrease in sublimation (-0.7 mm w.e.).

The method used to correct for stability is also shown to be relatively important. For the bare ice site the correction for stability by Dyer (1974) is used whereas for the debris-covered ice site the correction used by Businger *et al.* (1971) was found to be most

appropriate. Changing the correction at the bare ice site to that proposed by Högström (1988) and by Beljaars and Holtslag (1991) resulted in small changes of 0.3% and –0.6% respectively. The largest difference was when the stability correction from Businger *et al.* (1971) was applied, which resulted in an overall increase in mass loss of 2.9%.

Table 3.8. Change in surface mass balance components over the period 341, 2004 – Day 22, 2005 over bare ice with regard to the reference sublimation of 29.0 mm w.e. melt/runoff of 69.4 mm w.e. and net surface mass balance of -43.0 mm w.e. Note: the default stability correction used was that of Dyer (1974) and the method of calculating roughness lengths of heat and vapour were those by Andreas (1987).

Parameter adjustment	Change in sublimation (mm w.e.)	Change in melt/runoff (mm w.e.)	Change in surface mass balance (mm w.e.)
Momentum roughness length 1 x 10^{-1}	+2.4(8.4%)	-2.1(3.1%)	-0.6(1.4%)
Momentum roughness length 1 x 10^{-5}	+0.3(1.1%)	-0.4(0.6%)	+ 0.2(0.4%)
$z_0=z_{0e}=z_{0h}$	+54.8(186%)	-19.8(28.5%)	- 3.3(7.8%)
z_{0h}=0.0001	+6.8(23.4%)	-3.5(5.1%)	+0.3(5.9%)
Stability correction: Högström (1988)	-0.3 (1.1%)	+3.5(5.0%)	-0.1(0.3%)
Stability correction: Businger *et al.* (1971)	-1.5(5.3%)	+2.7(3.9%)	- 1.2(2.9%)
Stability correction: Beljaars and Holtslag (1991)	-0.9(3.0%)	+0.8(1.2%)	-0.2(0.6%)
Air temperature (+ 0.2 ºC)	-0.7(2.3%)	+3.9(5.7%)	-2.3(5.4%)
Relative humidity (+ 2 %)	-1.7(6.1%)	+1.5(2.1%)	- 0.4(0.9%)
Wind speed (+ 0.2 m s^{-1})	+0.9(3.0%)	-0.6(0.9%)	+0.1(0.3%)

At the debris-covered ice site, the most important parameter is shown to be the thermal conductivity. Changes in this parameter resulted in a large increase in ablation beneath the debris. Changes to other parameters only altered the proportion of sublimation/melt of the snow on the surface.

As with the bare ice, at the debris-covered ice site the roughness lengths of momentum, vapour, and heat are important. Changes in these lengths resulted in changes in sublimation of up to 10% (Table 3.9).

Conductivities used to test the sensitivity were 3.06, and 0.76 W m^{-1} K^{-1}, (double and half the value used to run the model). These values were also approximately the maximum and minimum values reported and used in the literature for rock and debris (Section 3.3.2). When conductivity was set to 3.06 W m^{-1} K^{-1} the melting beneath the ice was calculated as 369 mm w.e. compared with 0 mm w.e.. However, when this change was made the associated calculated temperatures at 0.15 and 0.30 m deep were much higher (> 5ºC) than that recorded during the measurements (not shown) indicating that such a high thermal conductivity is likely to be unrealistic. When the thermal

conductivity of the debris was set to 0.75 W m^{-1} K^{-1}, no melt occurred beneath the debris.

Increasing the air temperature was shown not to lead to dramatic increases in melting beneath the debris. An increase of 0.2 ºC did not result in any subsurface melting and an increase of 1.0 ºC melted only 16 mm w.e. beneath the debris (Table 3.9). Given that at the bare ice site a 0.2 ºC increase in temperature resulted in a 5.7% increase in mass loss (Table 3.8) this result helps support the concept that the layer of debris is providing the underlying ice with some degree of insulation.

Table 3.9. Change in surface mass balance components over the period Day 299, 2003 - Day 16, 2004 over debris-covered ice with regard to the reference sublimation of 168.3 mm w.e., snowmelt of 94.0 mm w.e. and subsurface ice melt 0.0 mm w.e. Note: the default stability correction used was that of Businger et al. (1971) and the method of calculating roughness lengths of heat and vapour were those by Andreas (1987).

Parameter adjustment	**Change in sublimation (mm w.e.)**	**Change in snow melt (mm w.e.)**	**Change in subsurface melt (mm w.e.)**
Momentum roughness length 1 x 10^{-1}	+10.6(6.3%)	+2.5(2.6%)	0
Momentum roughness length 1 x 10^{-3}	-2.2(1.3%)	+0.5(0.5%)	0
Roughness length of heat z_{0h}=0.0001	+32.5(19.3%)	-1.7(1.8%)	0
Stability correction: Dyer (1974)	+14.7(8.7%)	+2.1(2.2%)	0
Stability correction: Högström (1988)	+12.1(7.2%)	+1.0(1.1%)	0
Stability correction: Beljaars and Holtslag (1991)	+12.1(7.2%)	+0.7(0.7%)	0
Debris thermal conductivity: 3.06	-4.1(2.4%)	+0.2(0.2%)	369.3
Debris thermal conductivity: 0.75	-16.5(9.8%)	+2.5(2.6%)	0
Air temperature (+ 0.2 ºC)	+0.4(0.2%)	+1.1(1.2%)	0
Air temperature (+ 1.0 ºC)	+3.0(1.8%)	-1.2(1.3%)	16.1
Air temperature (+ 2.0 ºC)	+6.0(3.6%)	+1.1(1.2%)	71.9
Relative humidity (+ 2 %)	-1.5(0.9%)	+1.7 (1.8%)	0
Wind speed (+ 0.2 m s^{-1})	+2.8(1.6%)	+0.9(0.9%)	0

In summary, the model is shown to be most sensitive to the momentum roughness lengths. For bare ice, the model is also shown to be sensitive to air temperature, while for debris-covered ice, the debris thermal conductivity is important.

3.6 Bare ice site surface energy and surface mass balance

The surface energy balance varied considerably over the modelling period (Figure 3.17). Net radiation was the largest gain to the system, and most energy was directed into the subsurface (Table 3.10). Available energy was also directed into sublimation/evaporation. As discussed in chapter two, the net radiation for the period investigated was dominated by the influx of short-wave radiation, and was consistently positive.

Table 3.10.Mean atmospheric conditions and mean heat fluxes for the period of observations from Day 341, 2004 – Day 22, 2005 at the bare ice site.

Air temperature (ºC)	-2.3
Wind speed (m s^{-1})	3.8
Relative humidity (%)	80
Net radiation (W m^{-2})	50
Sensible heat flux (W m^{-2})	-6
Latent heat flux (W m^{-2})	-19
Total subsurface flux (W m^{-2})	-25

3.6.1 Turbulent fluxes

The sensible heat flux (Q_H) fluctuated between being a source and a sink of energy throughout the period (Figure 3.16), with a small mean loss of energy (-5.6 W m^{-2}). The temperature gradient between the surface and the air was minimal for most of the measurement period (mean 1 ºC) resulting in low sensible heat flux (maximum gain of 27.6 W m^{-2} and loss of –28.3 W m^{-2}). Consequently, the calculated sensible heat flux value was often less than the standard deviation and needs to be interpreted with caution. However, during the measurement period, some sensible heat fluxes were sufficiently large that conclusions as to their importance may be drawn.

It is clear that there are episodes when the sensible heat flux became an important source of energy (Figure 3.17). Notably, the sensible heat gain was considerable on Day 343, 2004 (24.4 W m^{-2}) and was also large between Days 5 and 8, 2004 (~ 25.0 W m^{-2}). This gain occurred when Type A synoptic conditions prevailed, as discussed in section 3.6.4. Sensible heat flux also varied with wind speed with large positive values occurring during periods of high wind speed (Figure 2.21, 3.17). Around day 354, 2004, the

sensible heat flux suddenly became a significant sink of energy (-28.3 W m^{-2}). This change in direction coincided with a very small amount precipitation received (0.3 mm w.e.) on day 353 which caused an increase in albedo and associated decrease in net radiation (Figure 2.22), as well as an overall drop in air temperature (Figure 2.21).

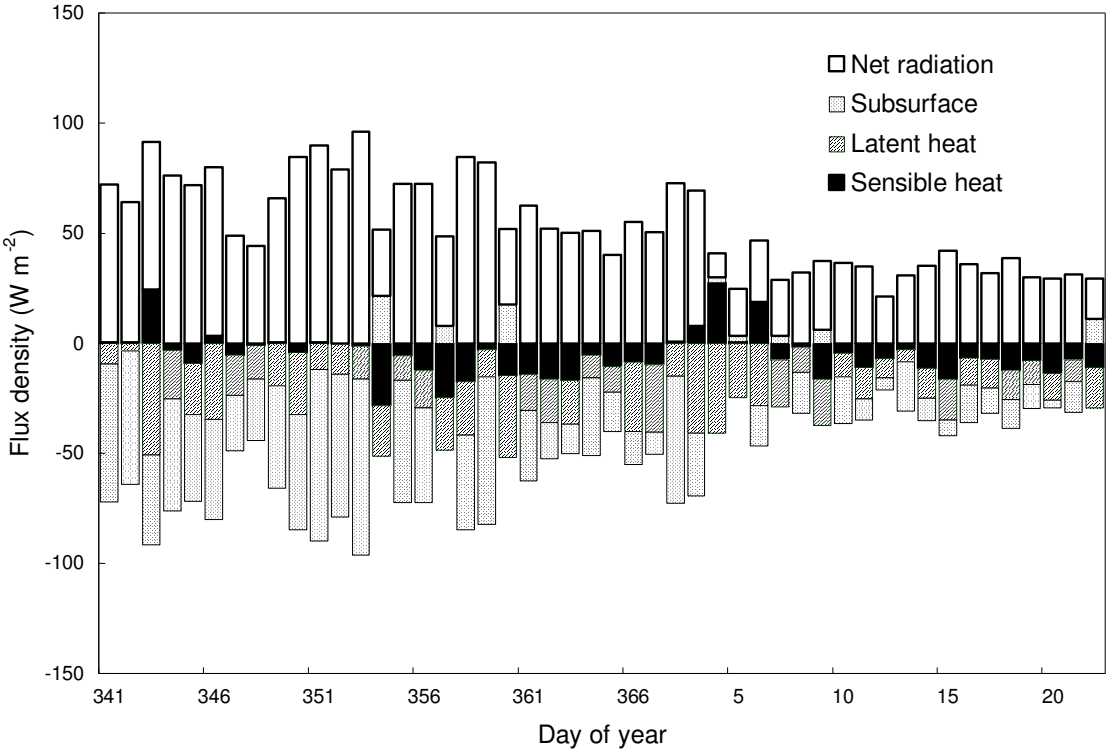

Figure 3.17 Time series of surface energy balance components at the bare ice site for the period Day 341, 2004 – Day 22, 2005. Positive fluxes represent a gain to the surface.

Although latent heat flux (Q_E) is subject to relatively high uncertainty (Section 3.4.1) it remained negative for the entire measurement period showing that sublimation plays a significant role. On average, latent heat flux was a net sink of energy at –19.2 W m^{-2}, but ranged considerably, from –3.3 to –50.6 W m^{-2} for daily means (Figure 3.17). The smallest mass losses due to latent heat flux occurred near the end of the measurement period when the ice had snow on the surface, and the surface temperature was decreasing rapidly (Figure 2.21). Latent heat flux loss was substantial at times during the modelling period (up to –50 W m^{-2}) especially near the beginning of the measurement period (Day 343, 2004) and when the surface temperature was below zero, indicating that sublimation was prevalent (Figure 3.17). The latent heat flux loss was also

considerable (~ -36 W m^{-2}) between Days 3 and 6, 2005, almost offsetting the energy gained from sensible heat (Figure 3.17).

3.6.2 Subsurface energy flux

The amount of energy directed downwards into the ice was equivalent to that directed into the combined turbulent fluxes (Table 3.10). This energy was used both to warm the subsurface and for melting. The total subsurface flux started out large (~ 60 W m^{-2}), and reduced considerably by the end of the measurements (~15 W m^{-2}). It had a maximum of 79.9 W m^{-2} and the daily mean had occasional positive values (up to 21.6 W m^{-2}), this was when heat directed from the subsurface to the surface (Figure 3.17).

3.6.3 Surface mass balance

Over the modelling period at the bare ice site (Day 341, 2004 – Day 22, 2005) surface mass balance components varied considerably (Figure 3.18) and there was a net loss of mass at the surface of 43.0 mm w.e. During the period a total of 55.7 mm w.e. was received as precipitation (prescribed). Total ablation was 98 mm w.e., with melting accounting for 69.3 mm w.e. (70%) and sublimation 29.2 mm w.e. (30%).

Melting at the bare ice site occurred primarily in the first half of the measurement period (Figure 3.18) with most occurring between Day, 349 - 359, 2004, with a loss rate of up to 11 mm w.e./day. This maximum melt period coincided with the highest net radiation recorded for the site (Figure 2.22), which occurred during Type B synoptic conditions (discussed in section 3.6.4).

Sublimation occurred throughout the entire measurement period (Figure 3.18), with a maximum loss of 1.5 mm w.e. day^{-1}. Sublimation was enhanced during periods of high winds (Day 343, 2004, and Days 4-5, 2005). The overall quantity of sublimation was reducing through the modelling period when air and surface temperatures were also reducing (Figure 2.21). From Day 5, 2005 sublimation became the dominant loss of mass from the surface at the bare ice site.

Almost all the precipitation received was ablated by the end of the period, which was evident in a small amount of snow on the surface (~0.02 m) when the site was revisited at the end of the measurement period.

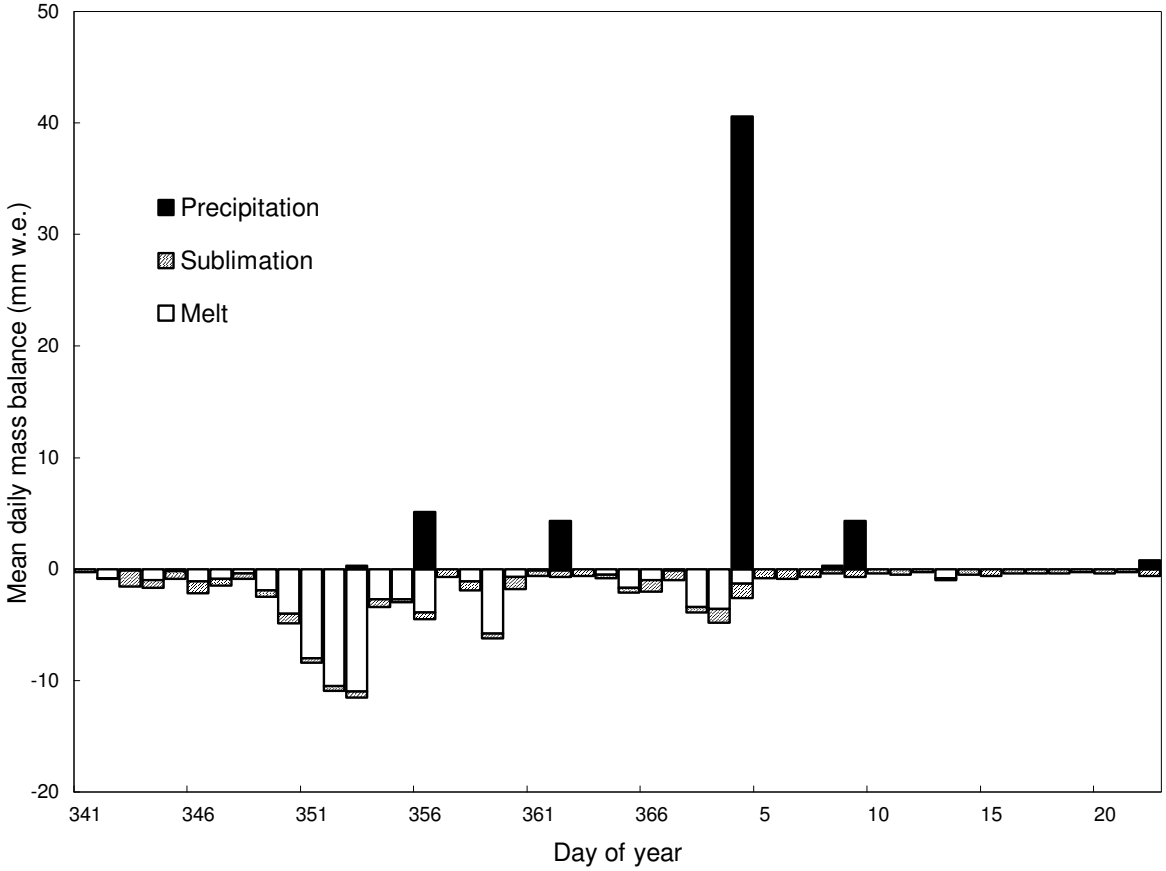

Figure 3.18 Time series of surface mass balance components at the bare ice site for the period Day 341, 2004 – Day 22, 2005. Positive fluxes represent a gain to the surface.

3.6.4 Synoptic conditions

Using the synoptic types defined in chapter two (Section 2.4) surface energy and surface mass balance data can be compared for the different types (Figure 3.19, 3.20). Significance testing on each of the components during different synoptic types (Appendix D) shows that over bare ice, all the energy balance components for Types A and B are significantly different. Type A and C are significantly different for the turbulent fluxes but not the subsurface flux. Type B and C can only be distinguished by their sensible and subsurface fluxes. Only sublimation can be considered a significantly different mass balance component (Appendix D).

During type A conditions, sensible heat flux was a significant source of energy (21.6 W m^{-2}) to the bare ice surface, being over half the mean net radiation (Figure 3.19). Sensible heat flux was enhanced due to the air mass being relatively warm and

turbulence being increased (Section 2.7.1). During these periods, there was also a large negative latent heat (-34.7 W m^{-2}) which partly offset the gain through sensible heat flux (Figure 3.19). As net radiation was relatively low during type A conditions (40.6 W m^{-2}) the corresponding total subsurface flux was low (-27.5 W m^{-2}). Energy conducted into the ice and snow was sufficient to allow melt (and subsequent runoff) to occur (Figure 3.20). This melt rate was higher than the rate of sublimation, with a mean daily rate of 1.8 mm w.e. and 1.0 mm w.e. respectively. During type A conditions there was also considerable precipitation recorded (5.0 mm w.e.) although the precipitation was highly variable (Figure 3.20). Overall, during Type A conditions there was net accumulation.

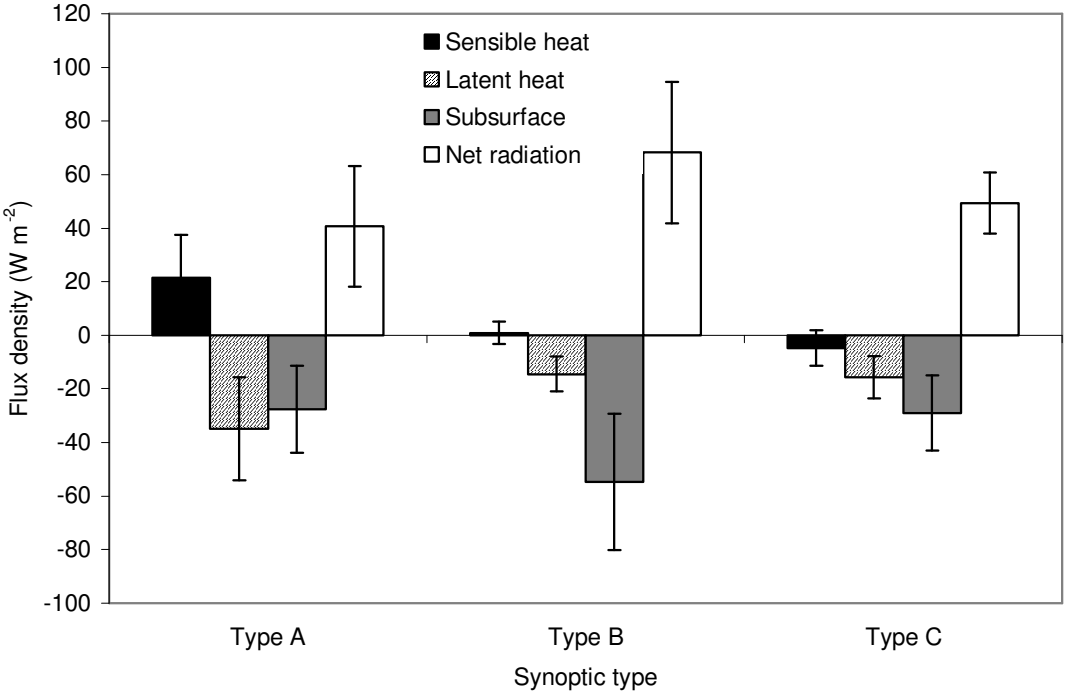

Figure 3.19 Mean energy balance terms at the bare ice for each of the synoptic types a) low pressure system residing in the Ross Sea Embayment, b) anticyclonic conditions across region, c) low pressure system extending into the Ross Sea Embayment. Error bars show standard deviation.

During type B conditions turbulent fluxes were small due to low wind speeds (Figures 3.19 and 2.21). Sensible heat flux was very small and positive (0.9 W m^{-2}) and latent heat low (14.4 W m^{-2}). During these conditions the net radiation was relatively high (mean 68.2 W m^{-2}). Since the turbulent fluxes were low, this gain of energy was mostly

directed towards subsurface (54.6 W m^{-2}). The result of this energy gain was considerable melting (-5.4 mm w.e.), and minimal sublimation/evaporation (-0.44 mm w.e.). As trace precipitation was recorded for the days classed as type B during the model run (Day 341, 2004 – Day 22, 2005), the net daily mean surface mass balance was the largest for the three synoptic types, at -5.4 mm w.e.

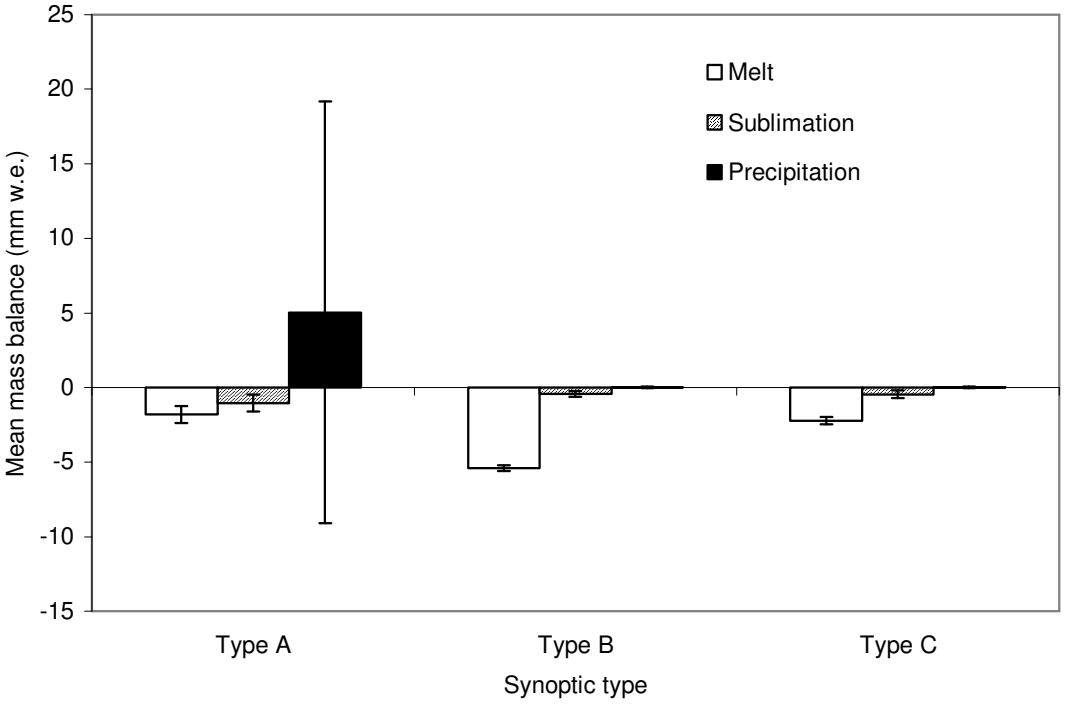

Figure 3.20 Mean daily surface mass balance terms at the bare ice for each of the synoptic types a) low pressure system residing in the Ross Sea Embayment, b) anticyclonic conditions across region, c) low pressure system extending into the Ross Sea Embayment. Error bars show standard deviation.

During type C conditions sensible heat flux was small and negative (-4.7 W m^{-2}), latent heat flux during these conditions was also negative and relatively low (-15.6 W m^{-2}). During these conditions the net radiation was intermediate between the other two types (mean 49.4 W m^{-2}). Type C conditions lost mass by both melt and sublimation with the majority by melt (-2.2 mm w.e.). Mass loss by sublimation was a similar value as during type B conditions (0.45 mm we.). Also similar to type B conditions, trace precipitation was recorded for the days classed as type C during the model run (Day 341, 2004 – Day 22, 2005). Overall Type C conditions represented a mean net surface mass balance loss at –2.65 mm w.e..

3.7 Debris-covered ice site surface energy and surface mass balance

In order to capture as much variability as possible the surface energy and surface mass balance of the debris-covered ice site is examined for the two periods: Day 299, 2003 – Day 16, 2004 and Day 317 – 339, 2004. Although these periods were different to the bare-ice site period (discussed in the previous section), as synoptic systems are considered, they can be compared and contrasted.

Similar to the bare ice site the surface energy balance varied considerably over the measurement period (Figure 3.21). The direction and magnitude of the fluxes were similar during both model periods (Table 3.11). Therefore, only the longer-term period is presented graphically.

Net radiation was the largest gain to the system (mean 118 W m^{-2}) and latent heat, the largest loss (mean –59 W m^{-2}). Available energy was apportioned into sublimation/evaporation, sensible heat flux, as well as being directed into the debris subsurface (Table 3.11). As discussed in chapter two, because of a low albedo of debris-covered ice, net radiation was much larger at this site than for the bare ice site (mean difference of 63 W m^{-2}).

Table 3.11 Mean atmospheric conditions and mean heat fluxes for the period of observations at the debris-covered ice site.

Variable	Day 299, 2003 - Day 16, 2004	Day 317- Day 339, 2004
Air temperature (ºC)	-3.8	-4.0
Wind speed m s^{-1}	3.5	3.9
Relative humidity%	63	57
Net Radiation (W m^{-2})	118	144
Sensible heat flux (W m^{-2})	-35	-39
Latent heat flux (W m^{-2})	-59	-80
Total subsurface flux (W m^{-2})	-28	-25

3.7.1 Turbulent fluxes

Sensible heat flux was an overall loss to the system (-34.9 W m^{-2}), indicative of warm surface temperatures (Figure 3.21). At the beginning of the period, when the surface was covered in snow, the sensible heat flux values were small (mean -20 W m^{-2}). After ~ Day 344, 2004, when the debris surface became snow free, the temperatures were higher and the sensible heat flux remained a large net loss to the system (mean –93 W m^{-2}) (Figure 3.21). However, sensible heat flux did fluctuate throughout the period with a maximum and minimum of 47.3 and –95.9 W m^{-2} respectively (Figure 3.21).

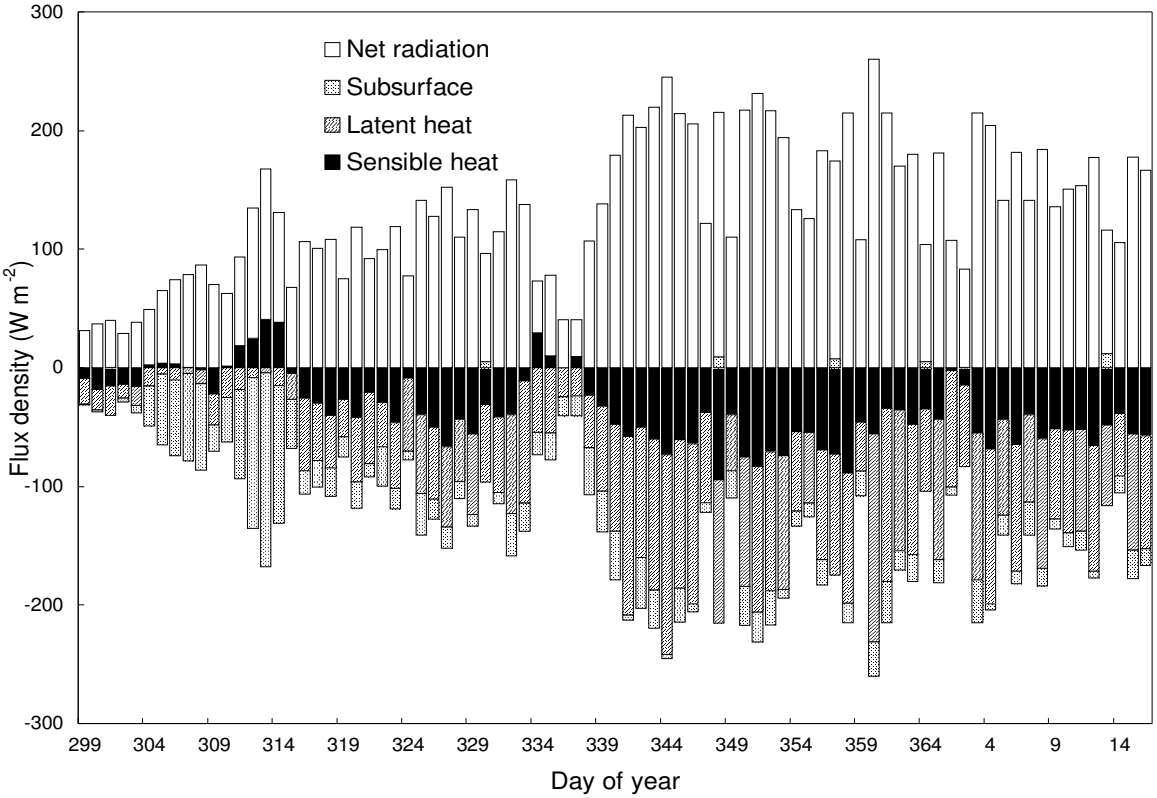

Figure 3.21 Time series of Surface energy balance components at the debris-covered ice site for the period Day 299, 2003 - Day 16, 2004. Positive fluxes represent a gain to the surface.

The calculated latent heat flux was always negative and increased slightly over the period (Figure 3.20). Latent heat flux was shown to be smallest at the beginning of the modelling period (Prior to day 330, 2003) when the surface was covered in snow. During the period Day 331 – 336, 2003 there was an increased rate of latent heat loss (~ -70 W m^{-2}) which was associated with strong wind speeds (Figure 2.17) and positive sensible heat flux (Figure 3.21). When the debris became snow free (~ Day 344, 2003) the latent heat flux remained reasonably high (Figure 3.21). The fact that the latent heat

flux was so large after the snow had disappeared may be a result of the debris being considered saturated with respect to its surface temperature, suggesting that the values were likely to be overestimated. As stated above (Section 3.4.3) any latent heat flux losses from the ice at the debris-ice interface are likely to be negligible.

3.7.2 Subsurface energy flux

Over the modelling period, energy was transferred from the atmosphere to the subsurface with a mean rate of –28 W m^{-2}. This total includes short-wave radiation penetrating into the snow layer, melt energy, and energy that was conducted downwards.

At the very beginning of the measurement period, the total subsurface fluxes were low (< -25 W m^{-2}). At around Day 313, 2003, there are gains to the surface from both sensible heat (up to 41 W m^{-2}) and net radiation (~ 127 W m^{-2}). During this period only a small amount of energy was directed into latent heat flux, and as a result of this the majority of the energy is directed to the subsurface (Figure 3.21). While a proportion of this energy was conducted downwards into the snow and underlying debris a large amount was used to melt the snow (Section 3.7.3). After Day 316, 2003, sensible heat flux became a net loss and total energy directed into the subsurface was dramatically reduced (Figure 3.21). For the rest of the modelling period the subsurface flux remained low in comparison, occasionally becoming a small source (maximum 12 W m^{-2}) of energy (Figure 3.21) when the underlying debris was warmer than the surface.

3.7.3 Surface mass balance

Surface mass balance at the debris-covered ice site was calculated at two points. Firstly, the accumulation and ablation of snow on the surface of the debris was determined and secondly, the ablation of ice at the debris-ice interface.

All of the 0.30 m of old snow on the surface (~120 mm w.e.) and all additional snowfall (18.9 mm w.e.) was removed during the modelling period (Figure 3.22). The initial snow was ablated by both sublimation and melting with the majority (93.9 mm w.e.) being removed by melting and runoff between Day 305 and 316, 2003 (Figure 3.22). The remainder was ablated by sublimation. Based on albedo the debris surface is assumed to become snow free from approximately Day 344, 2003 onwards with only the occasional precipitation event changing this condition.

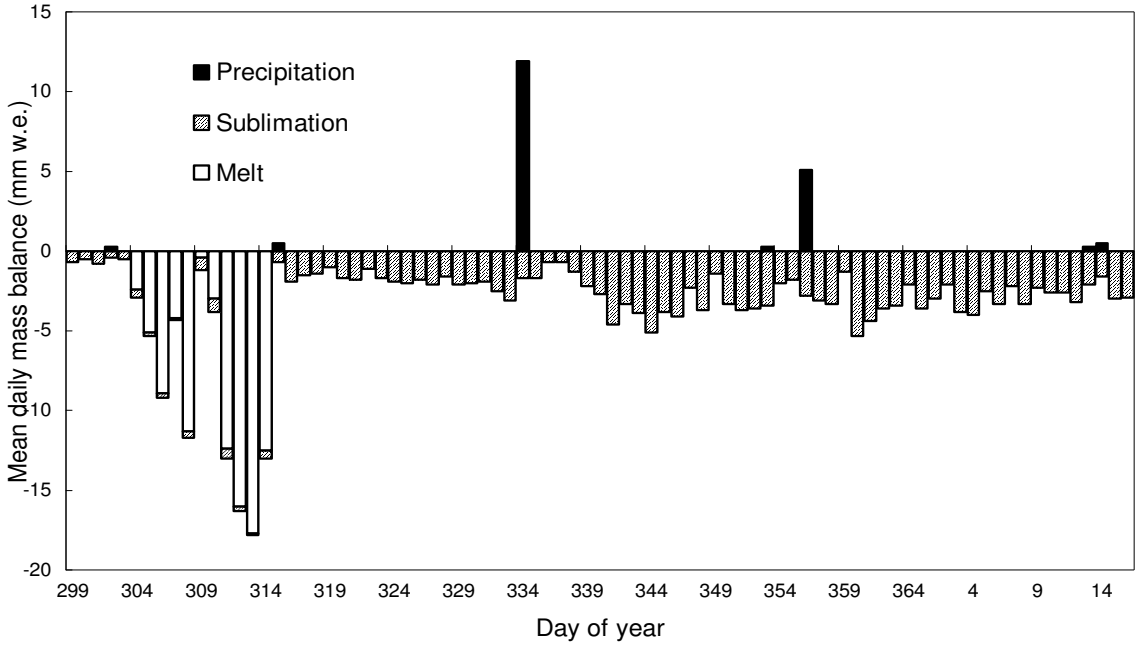

Figure 3.22 Time series of surface mass balance components at the debris-covered ice site for the period Day 299, 2003 - Day 16, 2004. Positive fluxes represent a gain to the surface.

As discussed in section 3.4.4 the amount of energy reaching the debris-ice interface did not increase the temperature to melt point during the modelling period and it is inferred on this basis that no loss of mass occurred at the debris-ice interface. Furthermore, the sensitivity testing (Section 3.5) showed that a considerable increase in temperature would only cause a small quantity of melting to occur at the debris-ice interface. Therefore it is suggested that, in this case, the debris is insulating the underlying ice from significant ablation. This supports the findings of researchers who have found that ablation was significantly reduced under thick debris (Purdie and Fitzharris, 1999; Pelto, 2000; Kayastha *et al.*, 2000; Nicholson and Benn, 2006).

3.7.4 Synoptic conditions

In contrast to the bare ice site the surface energy balance during the three different synoptic types are similar (Figures 3.23, 3.24). During the model run for the debris-covered ice site (Day 299, 2003 – Day 16, 2004) only type A and B could be considered significantly different from each other, and only then for the turbulent fluxes and net radiation (Appendix E).

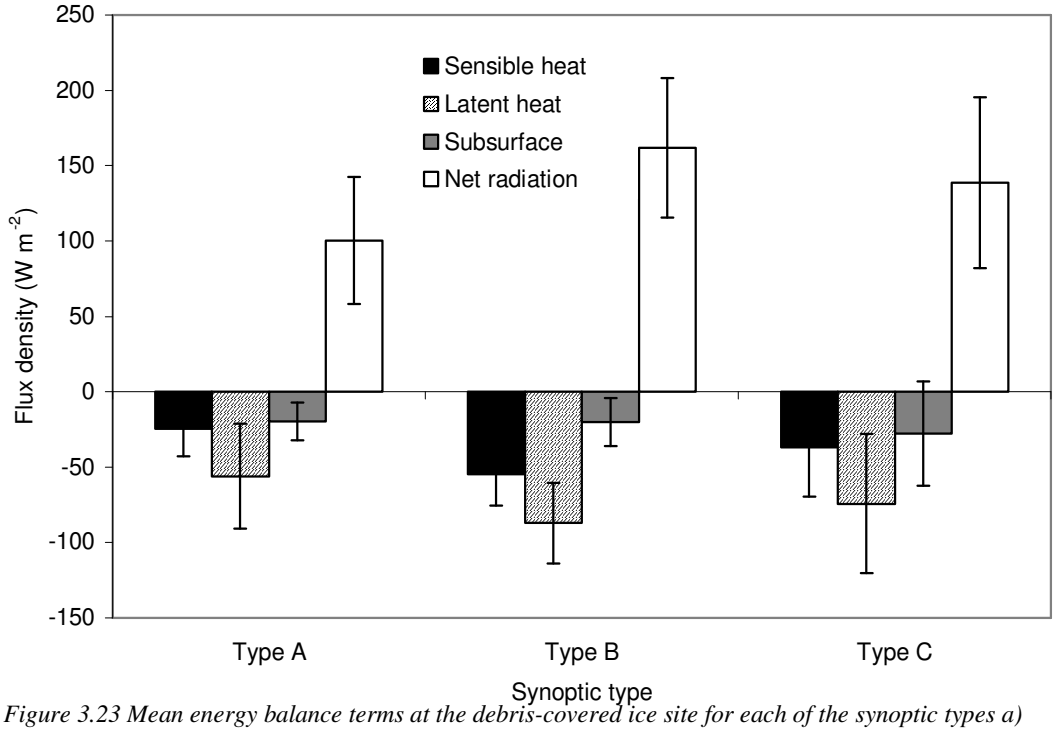

Figure 3.23 Mean energy balance terms at the debris-covered ice site for each of the synoptic types a) low pressure system residing in the Ross Sea Embayment, b) anticyclonic conditions across region, c) low pressure system extending into the Ross Sea Embayment. Error bars show standard deviation.

In all three synoptic types, net radiation was the predominant source of energy with turbulent fluxes and subsurface flux representing a net loss of energy (Figure 3.23). Similarly, the largest sink was latent heat flux, followed by sensible heat flux, then subsurface flux. During type B conditions, the net radiation was appreciably higher (161.8 W m^{-2}) compared to the other types (100.3 and 138.6 W m^{-2}). As a result, during type B conditions the sinks were all increased (Figure 3.23).

As it was determined that no melting occurred at the debris-ice interface (Section 3.7.3) the mean daily net surface mass balance values for the debris-covered ice refer to the active surface only (debris, or snow-on-debris). In contrast to the bare ice site, during the modelling period, precipitation was only recorded during type B and C conditions (Figure 3.24). Both melting and sublimation ablated the snow on the surface, with melting only occurring during type A and C conditions (Figure 3.24). As the latent heat flux is subject to high uncertainty - especially after the snow has ablated (Section 3.4.4)

- it is difficult to draws conclusions from the sublimation reported for the whole period, as it is determined from the latent heat flux.

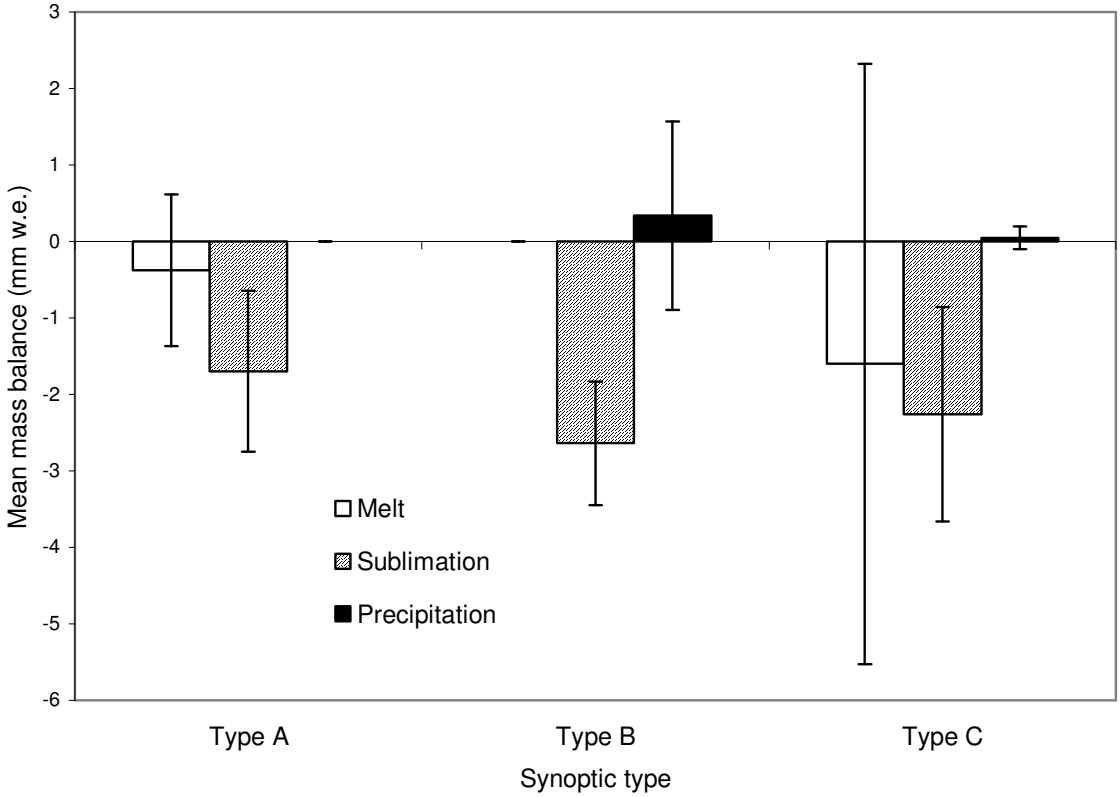

Figure 3.24 Mean daily surface mass balance terms at the debris-covered ice site for each of the synoptic types a) low pressure system residing in the Ross Sea Embayment, b) anticyclonic conditions across region, c) low pressure system extending into the Ross Sea Embayment. Error bars show standard deviation.

3.8 Comparison with other research

Comparison with several other studies is possible because most previous work has been for summer periods. For the bare ice site, net radiation is similar to that of Bintanja (2000) although larger than for other sites (Table 3.12). This similarity is likely due to the type of surface. Most energy balance studies performed in the Antarctic have been over snow surfaces with high albedos, and, consequently low net radiation (Table 3.12), whereas the work by Bintanja is over a "blue ice area".

In agreement with results from several other researchers, this work showed periods where the turbulent fluxes have opposing signs (Konzelmann and Braithwaite, 1995; Schneider, 1999; Braun and Hock, 2004). Results in this study also agreed with with Braun and Hock (2004), who found that sensible heat flux can be an important source of energy. The latent heat flux loss is reported here is larger than for most studies on snow and ice, while less that that reported by Bintanja (2000). This inconsistency is possibly due to the fact that surface melting is occurring at the bare ice site used in this study.

To the author's knowledge there are no other studies showing the influence of debris on energy transfers at high latitude sites. Similar studies at lower latitudes show the influence of different radiation, temperature and humidity environments. For example, Takeuchi *et al*. (2000) found that for the debris surface of the Khumbu Glacier in Nepal, net radiation was high, and both turbulent fluxes were negative. High net radiation and similar flux directions were also found in this research for the debirs-covered ice site (Table 3.12). Conversely, the results in this study are in contrast with recent work from Nicholson and Benn (2006) who report positive values of sensible heat flux at Larsbreen, Svalbard and Ghiacciaio del Belvedere, Italian Alps. Nicholson and Benn (2006) do, however, report negative flux values if the debris surface is considered dry.

With respect to the influence of synoptic systems on the surface energy and surface mass balance the comparison is encouraging. This work supports that of Braun *et al.* (2001) who found distinctive characteristics in the surface energy balance in relation to synoptic types, especially during conditions that have an influx of warm, moist air. This work also supports the conclusions of Riejmer and Oerlemanns (2002) who state that the energy balance of ice shelves close to the coast are strongly influenced by synoptic weather systems.

Table 3.12 Summertime energy balance components from observations in this research and other similar environments reported in the literature. Surface types are: D, debris-covered ice; I, bare ice; S, snow.

Location	Latitude/Longitude	Elevation (m.a.s.l.)	Time period of observations	Surface type	Q^* (W m^{-2})	Q_H (W m^{-2})	Q_E (W m^{-2})	Q_G (W m^{-2})	Reference
McMurdo Ice Shelf	78º00' S 165º32' E	~30	12th November – 5th December 2004	D	144	-39	-80	-25	This research
	78º00' S 165º05' E	~30	25th October 2003- 16th January 2004	D	118	-30	-59	-28	
	78º00' S 165º05' E	~30	6th December – 22nd January 2005	I	50	-5	-19	-25	
Khumbu Glacier, Nepal	28.00 N 86.83 E	5360	22nd May – 1st June 1999	I	190	10	-	-200†	Takeuchi *et al.*, 2000
	28.00 N 86.83 E	5360	22nd May – 1st June 1999	D	180	-30	-90	-60	
Antarctic Peninsula	68º08' S 67º06' W	~120	20th December – 21st February 1995	S	9	35	-25	-	Schneider, 1999
King George Ice Cap	62º10' S 58º40' W	85	2nd December 1997 – 12th January 1998	S	22	9	-1	-	Braun *et al.*, 2001
	62º08' S 58º37' W	255	2nd December 1997 – 12th January 1998	S	20	1	-3	-	
	62º08' S 58º30' W	385	6th December – 17th December 1997	S	16	-3	-2	-	
	62º08' S 58º20' W	619	19th December – 11th January 1998	S	3	-2	-3	-	
Dronning Maud Land	74º35ºS 11º13'W	1180	1st January – 10th February 1993	I	42	-7	-29	-6	Bintanja, 2000
	74º35'S 11º13'W	1120	28th December 1997 – 2nd February 1998	I	50	0.4	-34	-16	
Dronning Maud Land	72º45' S 15º29'W	34	1st - 30th November, 1998, 1999	S	0	4	-2	-4	Reijmer and Oerlemanns, 2002
			1st – 31st December, 1998, 1999	S	7	5	-3	-5	
			1st January – 31st January, 1998,1990,2000	S	0	4	-6	-4	
			1st February – 28th February, 1998,1999	S	-3	5	-4	-1	
			1998	S	-2	3	-1	-0.2	
			1999	S	-1	2	-1	0.1	
Larsbreen Svalbard, Norway*	78º11' N 15º33' E	200	9th – 20th July 2002	D	90	100	-200	-25	Nicholson and Benn, 2006
Ghiacciaio del Belvedere, Italy*	45º57' N 4º34' E;	2000	6th – 10th August 2003	D	175	0	-75	-60	Nicholson and Benn, 2006

†*Calculated energy used for melting, * for saturated debris 0.4 m deep, approximate*

3.9 Summary

An adapted energy balance model was used to model surface energy and surface mass balance on the McMurdo Ice Shelf for two different surface types. The turbulent fluxes were modelled reasonably well, with a slight underestimation of sensible heat flux and overestimation of latent heat flux. Mean daily surface and subsurface temperatures were captured well within the model suggesting that the subsurface processes are modelled correctly. It is considered that the model performs well enough to use in assessing the surface energy and surface mass balance of two sites on the McMurdo Ice Shelf.

At the bare ice site the main source of energy was net radiation, but sensible heat becomes important at times. Half of the available energy was channelled into subsurface processes and half into turbulent fluxes. Ablation at the bare ice site was by both sublimation and melting. The melting occurred in the first half of the measurement period and accounted for the majority (70%) of the mass loss at the surface. Sublimation occurred continuously throughout the period.

For the debris-covered ice site net radiation was also the dominant energy source. The magnitude of energy available at the surface was approximately three times larger than that measured at the bare ice site. The snow that was on the debris-covered ice at the beginning of the measurement period was all ablated by sublimation (~22%) and melt (~78%). Results suggest that the debris at this site is sufficiently thick to protect the ice underlying the debris from significant ablation.

At the bare ice site the surface energy and surface mass balance was distinct for different synoptic situations. During Type A conditions sensible heat becomes a source of energy and precipitation is increased resulting in an overall net gain at the surface during these conditions. During Type B conditions net radiation was high and most of this was directed towards the subsurface resulting in a high melt rate. Type C conditions were intermediary between A and B with an overall net mass loss.

At the debris-covered ice site surface energy and surface mass balance was not significantly affected by synoptic scale atmospheric conditions, inferring that the debris insulates the ice from the atmosphere.

The surface energy balance for the bare ice site in this research was similar to that the Blue Ice Areas of Dronning Maud Land, but it has considerable melting, whereas the Blue Ice Areas are not reported as melting. Although little work is available for comparison, the debris-covered ice surface energy balance appears similar to that determined for a debris-covered glacier in Nepal.

4 Detecting distributed surface characteristics

4.1 Introduction

In order to evaluate the spatial pattern of summertime surface mass balance of the McMurdo Ice Shelf, chapter five will use a distributed surface mass balance model. To initiate the model, it is necessary to know the existing distribution of surface type and albedo. Validation of the model requires direct measurements of surface mass balance which can also be used to identify broad trends. This chapter describes how these data were generated.

The primary aim of this chapter is to detect the surface characteristics used to initiate and validate the model in chapter five. This is achieved through addressing the following specific objectives:

- Illustrate the general trend of summertime surface mass balance using stake measurements.
- Determine the spatial distribution of surface types and albedo of the McMurdo Ice Shelf using remote sensing.

In order to address the chapter objectives, a combination of field based measurements and optical remotely sensed imagery were used. Several image processing techniques were applied including Principal Components Analysis (PCA), supervised classification, and narrow to broadband conversion. Results were compiled and presented using GIS software.

This chapter begins with a brief summary on the remote sensing of glacier surfaces, followed by a description of the data acquired and methods used. The methods section describes the processes involved in stake measurement processing, using remote sensing to find transient snow lines, differentiating the debris-covered ice, creating a mean surface type distribution image, and how an approximate albedo distribution image was created. The results are presented and discussed, and then the chapter concludes with a summary of the major findings.

4.2 Remote sensing of glacier surfaces

Satellite remote sensing provides an excellent platform to enable the determination of the spatial distribution of glacier albedo (Gao and Liu, 2001; Kargel *et al.,* 2005; Massom and Lubin, 2006). However, albedo alone cannot necessarily be used to distinguish between different surface types. For example, as the albedo of snow and ice, dirty ice and debris-covered ice are on a continuum, separating these by just albedo may not be possible without extensive ground based knowledge. It is therefore beneficial to use more than just albedo when differentiating surface types. Much of the research using remote sensing of glacier surfaces has focussed on two distinct themes, that of distinguishing between surfaces found on glaciers using remotely sensed signatures of snow, ice and debris-cover, and that considering short-wave albedo specifically.

The accumulation and ablation areas of typical gravity-driven glaciers are separated by the equilibrium line, where the annual net accumulation is zero (Paterson, 1994). Traditionally, the location of the annual equilibrium line is determined with stake measurements over a mass balance year, but this is laborious and logistically intensive. To counter this, various studies have attempted to determine the transient snowline using remote sensing techniques. These techniques rely on the fact that as snow ablates throughout the summer the transient snowline retreats and its position at the end of the season can be used as a proxy for the annual equilibrium line (Chinn, 1999; Gao and Liu, 2001; Konig *et al.*, 2001; Massom and Lubin, 2006). Ice shelves do not have an equilibrium line as such, but surface accumulation/ablation boundaries can be located using similar methods as those used to identify transient snow lines. These methods are based on the spectral properties of snow and ice.

Spectral signatures of the surfaces found on an ice masses are distinctive (Figure 4.1), enabling them to be identified by means of remote sensing. Studies have performed comparisons of field and satellite-derived glacier surface spectral signatures with success (Warren *et al*., 1986; Hall *et al*., 1990; Winther, 1994; Boresjö Bronge and Bronge, 1999). Therefore, the use of multi-spectral sensors with adequate bandwidth makes discrimination of glacier surfaces from remote sensing platforms feasible.

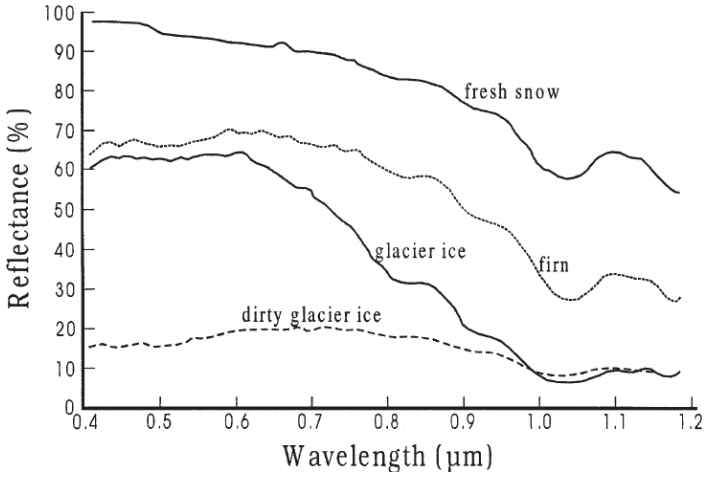

Figure 4.1 Spectral reflectance curves between 0.4 and 1.2 μm for fresh snow, firn, glacier ice, and dirty glacier ice.

Source: Gao and Liu, 2001 p.522.

Both optical and radar imagery (Table 4.1) have been used for the detection of glacier surface types and transient snow lines, although radar imagery has been most commonly used. Recently, the use of optical imagery has been brought to focus since the launch of the Terra Satellite and the provision of Advanced Spaceborne Thermal Emission and Reflection Radiometer (ASTER) images. ASTER imagery is easily obtained, of high resolution, available at a small cost, and has standardised processed products (Kargel *et al.,* 2005).

ASTER provides a new optical data source that has yet to be exploited fully for glacier research (Kargel *et al.*, 2005). Arigony-Neto *et al.* (2006) created an algorithm based on a thresholded TM band 4/band 5 ratio image using ASTER's equivalent bands 3 and 4 to determine glacial areas on the Antarctic Peninsula. Using ASTER band 3 and band 1/band 3 Peru's Cordillera Blanca was classified into snow and ice, dirty ice, lakes, moraine, rock, and vegetation (Kargel *et al.*, 2005).

A large number of studies have used other sources of optical imagery to distinguish between different surfaces, with band ratio methods often employed. For example Williams *et al.* (1991) used Landsat Thematic Mapper (TM) band 4/band 5 ratio to differentiate ice from snow on Brúarjökull, Iceland. A transition area between the ice and

snow was also found and defined as the slush area (Williams *et al.,* 1991). The normalised difference snow index (NDSI) is a ratio based tool and is used in the standard snow map product produced by NASA's Earth Observing System (EOS) using the Moderate-Resolution Imaging Spectrometer (MODIS) instrument (Hall *et al.*, 2002); it was originally based on the bands TM band 2 and TM band 5 and is calculated as follows:

$$NDSI = \frac{TM_{band2} - TM_{band5}}{TM_{band2} + TM_{band5}} \qquad 4.1$$

NDSI combined with the band ratio TM band 4/band 5 were successfully used by Sidjak and Wheate (1999) to discriminate between different glacier surface types in British Columbia, Canada. Boresjö Bronge and Bronge (1999) found that the TM band 3/band 4 ratio was better than TM band 4/band 5 at discriminating between blue ice and snow with various characteristics in the Vestfold Hills, East Antarctica.

Table 4.1 Remote sensing platforms used in detection of surface characteristics of glacier surfaces.

Abbreviation	Name	Type	Resolution
ASTER	Advanced Spaceborne Thermal Emission and Reflection Radiometer	Optical	15 m
LANDSAT	Land Satellite	Optical	30 m
MODIS	Moderate Resolution Imaging Spectroradiometer	Optical	250 – 1000 m
SSM/I	Special Sensor Microwave/Imager	SAR	25 km
AVHRR	Advanced Very High Resolution Radiometer	Optical	1100 m
ERS	European Remote Sensing Satellite	SAR	30 m

Microwave remote sensing provides an excellent data source due to its relative ability to penetrate cloud cover. Synthetic aperture radar (SAR) imagery has frequently been used to distinguish between glacier surfaces and to locate transient snow lines (Massom and Lubin, 2006). SAR imagery is sensitive to liquid water, thus enabling the distinction between areas of wet and dry snow (Lillesand and Kieffer, 1994). Brown *et al.* (1999) concluded that the firn line could be located to an accuracy of ± 20 – 40 m on Icelandic ice caps using images from the European Remote Sensing Satellite (ERS) SAR. In Antarctica, Braun *et al.* (2000) successfully used SAR images to map the ablation area on the King George Ice Cap. Furthermore, Special Sensor Microwave Image (SSM/I) data has been used to determine both the extent and the timing of the onset of melt in high latitudes (Fahnestock *et al.*, 2002; Liu and Wang, 2006).

Few direct comparisons between the use of optical imagery and SAR for detecting glacier surface features have been published (De Ruyter de Wildt and Oerlemanns, 2003; Arigony-Neto *et al.*, 2006). De Ruyter de Wildt and Oerlemans (2003) compared the use of albedo derived from AVHRR (Advanced Very High Resolution Radiometer) images with SAR images. Albedo images were used to detect the firn and transient snowlines on Vatnajökull, Iceland. Although there were difficulties in finding ideal imagery, it was found that the optical reflectance imagery was more useful than SAR in finding inter-annual variations (De Ruyter de Wildt and Oerlemans, 2003). Arigony-Neto *et al.* (2006) proposed a technique to determine glacier areas using both radar and optical imagery and by using a glacier centreline approach in order to remove the need for use of a Digital Elevation Model (DEM) to correct for topographical effects although the results are yet to be published.

Supraglacial debris introduces a number of problems into image processing. Because of high heterogeneity of debris found on glaciers, misclassification can occur. If the debris dominates the pixel it is difficult to detect ice using multispectral classification (Bishop *et al.,* 1995; Paul *et al.,* 2004). Furthermore, debris-covered ice is often spectrally similar to surrounding land. Several attempts have been made to overcome these issues including using Thermal Infrared (TIR) bandwidths but these were not successful (Taschner and Ranzi, 2002). Paul *et al.* (2004) had some success by combining multispectral classification and slope derived from a DEM.

Research concerning remote sensing of short-wave albedo of glaciers has generally been focussed on narrow to broadband conversion and its validation (e.g. Knap *et al.*, 1999; Reijmer *et al.,* 2001). This is because the albedo used in energy balance studies includes the wavelengths 0.3-3.0 μm, whilst the measurements made on remote sensing platforms are for multiple narrow bands (Liang, 2001). Some research, however, has been performed using albedo to detect surface features, for example, Greuell and Knap (2000) used Landsat derived albedo to detect the slush line of the Greenland Ice Sheet.

Overall, remote sensing has proved a useful tool for detecting different glacier surface types. Both microwave and optical imagery have been used with success, with SAR been the most commonly used. Difficulties have arisen due to mixed pixels, topographic effects,

debris cover, and image availability. This research combines the use of remotely sensed data with ground based measurements in order to eliminate as many of these types of issues as possible.

4.3 Data and Methods

The objectives of this chapter are addressed by using a combination of ground based measurements and remote sensing techniques. Ground based data collection included stake and albedo measurements. ASTER imagery was acquired for the remote sensing component.

In order to identify spatial patterns of surface mass balance, stake data from this research and from the literature were digitised and presented. A surface type distribution image was created using a succession of processing techniques. Firstly transient snowlines were detected for the ASTER images available. Next, using ASTER imagery the debris-covered ice was differentiated from the surrounding bare ice. Finally, the mean surface type distribution image was produced by combining these results and by extrapolating the surfaces types to areas that were not covered by remote sensing imagery. Each of these stages is described in this methods section. After the surface type image was created, an approximate albedo distribution image was created for use in chapter five. This image was produced using remotely sensed imagery and narrowband to broadband conversion.

Before creating these distribution images, it was first necessary to demarcate the ice shelf from its surroundings. The ice front digitised by Lawson *et al.* (*submitted*) was used for this study as no significant calving events had occurred since the SAR image they used for digitising was obtained. Land based boundaries, including the Koettlitz Glacier grounding line were obtained in digital format from SCAR (1993). The results from this chapter are combined in ESRI® ArcMap™ 9.0, geocoded using a Universal Transverse Mercator (UTM) projection, area 58 south, and datum WGS 1984.

4.3.1 Mass balance stake measurements

A network of mass balance stakes was set out across the northern part of the ice shelf in November 2003 (Figure 4.2). The stakes consisted of hollow white PVC poles that were drilled into the ice shelf. The stakes were revisited and measured in December 2003, January 2004, November 2004, and January 2005, providing two summers and one winter of data. Several extra stakes were used in the 2004-2005 summer to increase the coverage (Figure 4.2). The change in surface height was measured at each stake and then the mm w.e. was calculated using an assumed density of 917 kg m^{-3} at ice sites and measured

density at snow sites. As the stake measurements were made on different dates, and in order to make reasonable comparisons, a daily surface mass balance rate was determined for each stake.

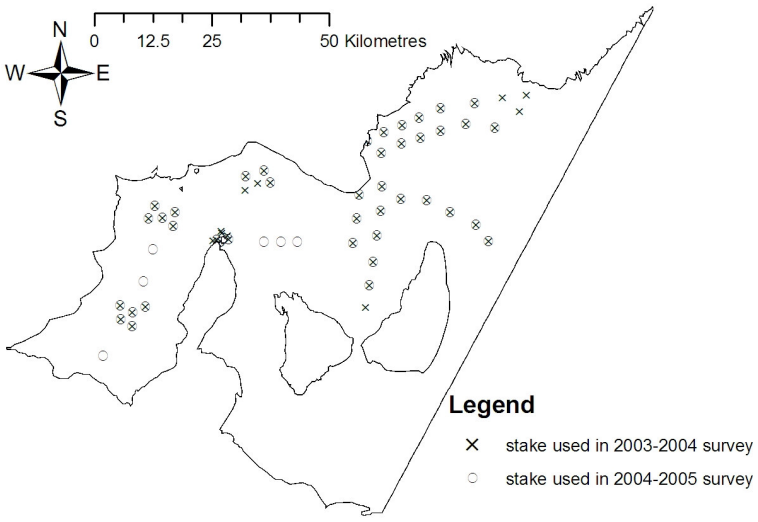

Figure 4.2 Stake locations on the McMurdo Ice Shelf for the 2003-2004 and 2004-2005 summer field campaigns.

Historical stake data for the McMurdo Ice Shelf from 1964-1984 was compiled by MacCrae (1984). Most of these stakes were in the accumulation area of the McMurdo Ice Shelf; however, a few were further to the west and were recorded as ablating. Based on these data, McCrae (1984) estimated the line of mean zero accumulation and this was manually digitised for comparative use in this study. Stuart and Bull (1963) published the location of a transition area between accumulation and ablation for the ice shelf for 1959-1960, which was also used for comparison. Furthermore, a zone of transition between ablation and accumulation for the summer of 1966-1967 was reported by Paige (1968).

4.3.2 Remote sensing data

ASTER provides data as different levels: L1A, L1B, and L2. L1A data is unprocessed data whereas L1B imagery has been corrected for striping and band-to-band co-registration. The L2 surface reflectance data product (AST07) contains surface reflectance for each of the nine VNIR and SWIR bands with atmospheric corrections pre-applied. These corrections remove effects due to satellite-sun geometry and atmospheric conditions. The

absolute accuracy for the AST07 product is ~7% for reflectances over 0.15 (Abrams and Hook, 2001). Further details and a description of the correction algorithms are outlined in Abrams and Hook (2001).

Each data granule provided by ASTER covers 60 x 60 km. Due to the extent of the McMurdo Ice Shelf, it was necessary to find two images that were acquired sequentially over the ice shelf to get maximum coverage. It was also necessary to find images that have minimal or no cloud cover. The NASA Earth Observing System Data Gateway (EDG) database was searched for imagery meeting these requirements from 2001-2006. Two pairs of data granules that satisfied these criteria were located, one pair was obtained on the 3rd February 2003 20:57 UTC and another pair on the 10th December 2004 at 20:30 UTC. This second pair also coincided with ground-based measurements at the AWS (see section 2.5.2).

The L2 surface reflectance AST07 product was obtained for both pairs of data granules. Mosaic images of the pairs of data granules were created for all bands using triangulation with nearest neighbour interpolation in Research Systems Inc. (RSI) ENVI 4.2 image processing software. The ice shelf coverage afforded by the two mosaics is shown in Figure 4.3. To aid extrapolation beyond the area covered by the AST07 image pairs, a L1B clear-sky image from 20th October 2001 was also acquired. Table 4.2 outlines all ASTER data granules used in this research.

Table 4.2 ASTER data granules obtained from the NASA Earth Observing System Data Gateway.

Date, time	ASTER data granule name	Level
20th October 2001, 20:55	AST_L1B.003:2006255987	ASTER L1B Registered radiance at the sensor V003
3rd February 2003, 20:57	AST_L1A.003:2011376230	ASTER L2 Surface Reflectance
3rd February 2003, 20:57	AST_L1A.003:2011376267	ASTER L2 Surface Reflectance
10th December 2004, 20:30	AST_L1B.003:2027023214	ASTER L2 Surface Reflectance
10th December 2004, 20:30	AST_L1B.003:2027023299	ASTER L2 Surface Reflectance

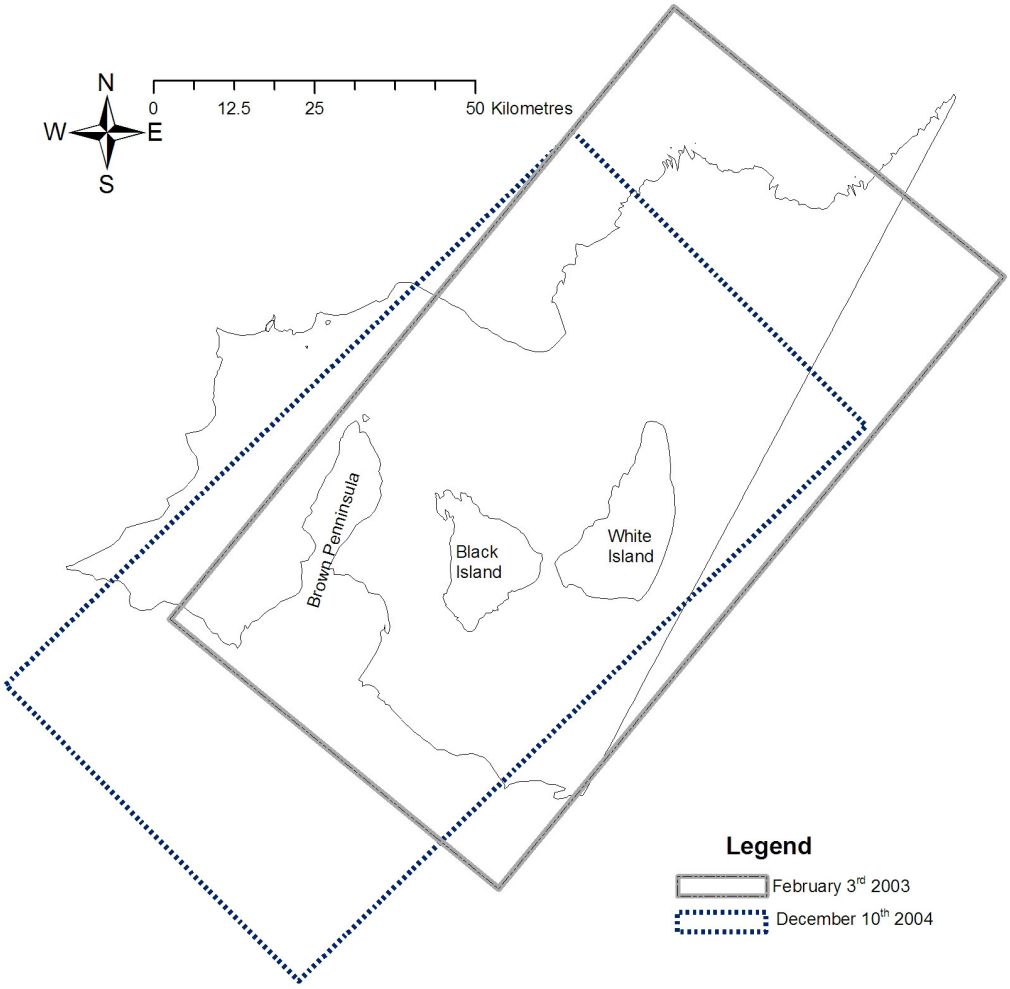

Figure 4.3 McMurdo Ice Shelf outline, showing location of the ASTER imagery used for analysis.

Two of the data granules used had minor imperfections. An area of cloud is detectable in the 3rd February 2003 image, in the north part of the northernmost image. This is not considered to be a problem for this application as it is mostly over land, only covers a very small area of the ice shelf, and is not an area focussed on in this study. Within the northernmost data granules acquired on the 10th December 2004 a region of distorted data across the middle of the image (Figure 4.4) is evident. The distortion is present in all bands except 3B (the backward facing sensor). The region of distortion is slightly offset for each band. It is suggested that this is related to the timing of the various band acquisitions, implying that some form interference occurred while the satellite was recording the nadir imagery. The region of distorted data has not affected the overall image projection. Thus it was decided to continue to use the image, and interpret the results accordingly.

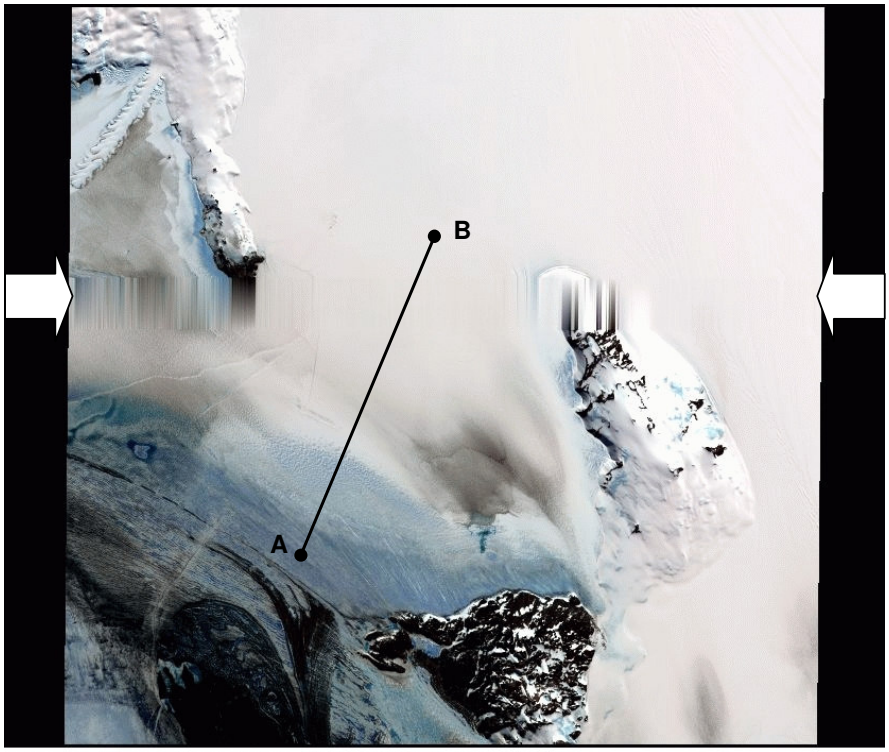

Figure 4.4 ASTER L1B data granule obtained on 10th December 2004, showing region of distortion denoted by arrows.

4.3.3 Transient snowline

Based on ground measurements Boresjö Bronge and Bronge (1999) determined that the best separation between blue ice and snow spectral response is in the near-IR, at approximately 0.841 µm. This supports other researchers who report that Landsat TM band 4 is good for distinguishing grain sizes (Williams *et al.*, 1991; Konig *et al.*, 2001). 0.841 µm corresponds to the ASTER band 3 which is 0.780 - 0.860 µm. Therefore, in this research, in order to allow future comparisons between remote sensing platforms, a band ratio image was created using the equivalent ASTER band 2/band 3 for both the 10th December 2004 and 3rd February 2003 mosaics.

The location of the transient snowline on each of the band ratio images was determined by examining values from the A-B transect that encompasses both accumulation and ablation areas (Figure 4.4). This southwest-northeast transect shows a distinct change between bare ice and fresh snow as a drop in values (Figure 4.5). The transect showed three distinct divisions. These divisions are inferred to be 1) bare ice, 2) a transitional area incorporating any percolation zone, wet-snow, and superimposed ice; and 3) dry snow. The threshold

value that separated 2) from 3) was then used as a means to depict an approximate transient snow line. This threshold had an ASTER band 2/band 3 ratio value of approximately 1.07. When the images were resampled using this threshold, relatively distinct boundaries could be seen (Figure 4.6).

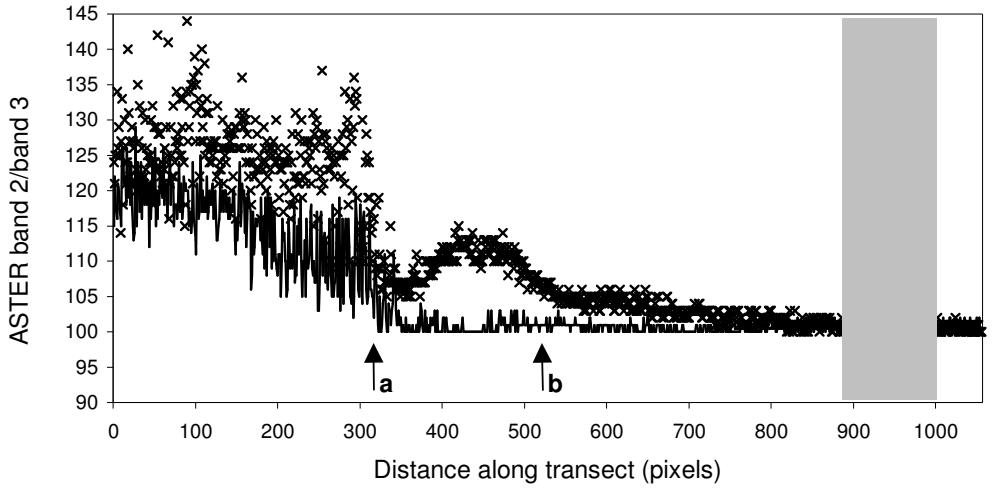

Figure 4.5 Transect A-B (Figure 4.4) of ASTER band 2/band 3 ratio image of the McMurdo Ice Shelf (southwest to northeast). Solid line is 3rd February 2003, x's are for 10th December 2004. Approximate location of the transient snow line arrows for a) 3rd February 2003, and b) 10th December 2004. Grey area represents area of distortion on original 10th December 2004 imagery.

Unfortunately the band ratio imagery was found to be unsatisfactory at differentiating the debris-covered ice from the rest of the ablation area. It was therefore necessary to treat the identification of debris-covered ice extent separately (Section 4.3.4).

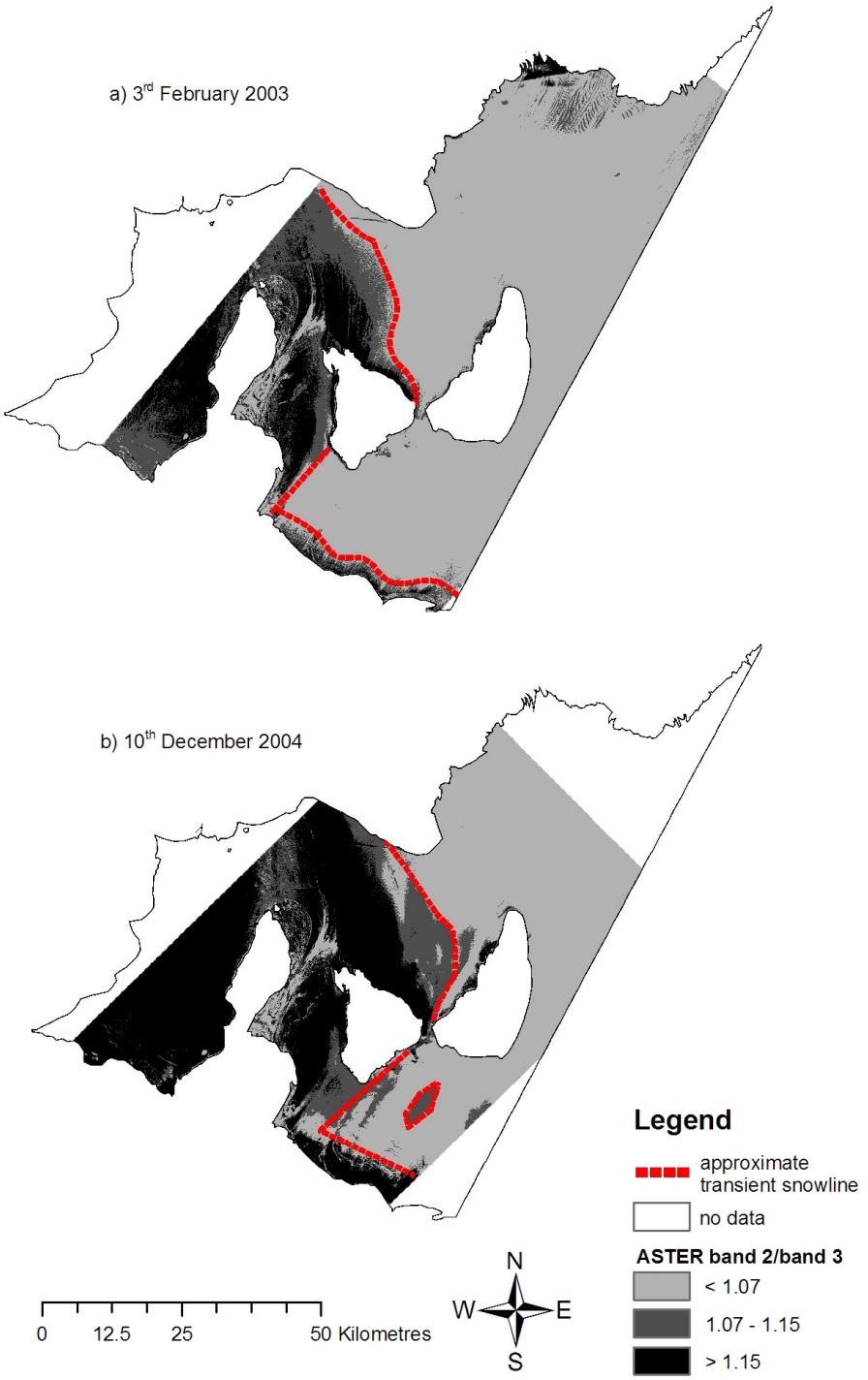

Figure 4.6 ASTER band2/band 3 ratio image of the McMurdo Ice Shelf showing the approximate location of the transient snow line (dashed line) for a) 3rd February 2003, and b) 10th December 2004.

4.3.4 Debris-covered ice extent

In order to differentiate debris-covered ice from bare ice, Principal Components Analysis (PCA) was performed on ASTER surface reflectance AST07 VNIR bands. The mosaics from 3rd February 2003 and 10th December 2004 were used for this. The two most significant principal components, PC1 and PC2, were then used in a supervised classification in RSI ENVI 4.2. Supervised classification is used to cluster pixels in an image into classes corresponding to user-defined training sets. Training sets for the classification were areas of bare ice, debris-covered ice, and snow, which were geolocated using differential GPS during fieldwork in December 2004 (Figure 4.7). Spectral signatures of the training sites are presented as both ASTER VNIR bands and principal components 1 through 3 (Figure 4.8). It is clear that applying PCA emphasises the differences between the surface types, which augments the classification.

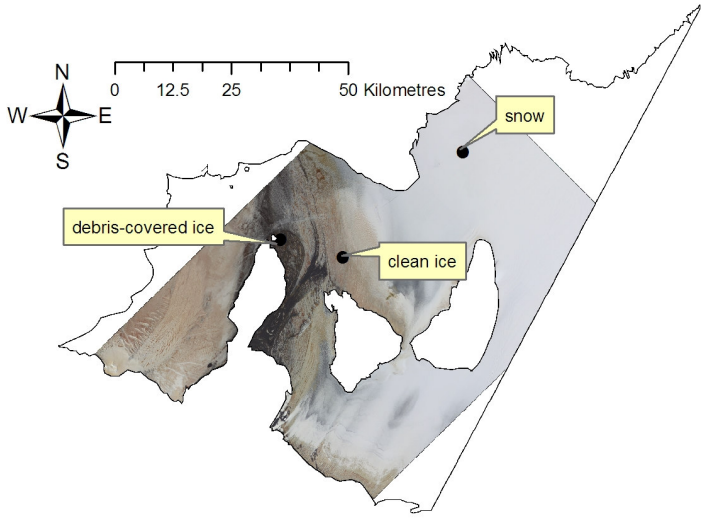

Figure 4.7 Training sites used for supervised classification of the McMurdo Ice Shelf. Sites were located during fieldwork in November 2004, and geolocated with differential GPS. Background image is VNIR ASTER image from 10th December 2004.

Although supervised maximum likelihood classification has been used by many researchers for glacier surface type differentiation (Bishop *et al*., 1995; Sidjak and Wheate, 1999; and Paul *et al.,* 2004), the minimum distance method was used here. The minimum distance method was preferable for this work as computational requirements were reduced. Further, the maximum likelihood method is based on the assumption that the data is distributed normally. Here the distribution is unknown so it was best to apply a method that

doesn't rely on normally distributed data. RSI ENVI 4.2's clumping and sifting procedures (using default parameters) were then applied to the classified images to delineate contiguous groups of pixels.

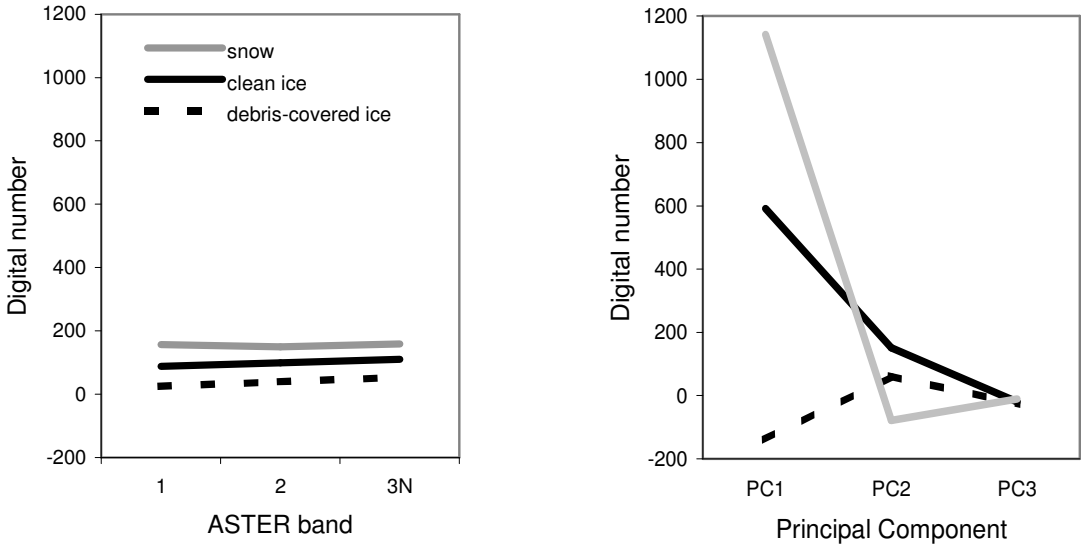

Figure 4.8 Mean spectral signatures of clean ice, debris-covered ice and snow used as training sets for classification a) ASTER VNIR bands b) Principal Components based on the VNIR bands.

A change detection map was also produced using the 3rd February 2003 and 10th December 2004 images to determine whether there were significant changes in extent of debris-covered ice. This change detection image was interpreted with caution as overlying snow may cause misclassification.

A relatively small change is apparent in the debris-covered ice extent between 3rd February 2003 and 10th December 2004 (Figure 4.9) with 46% of the change a loss, and 54% a gain in debris. Thus, although supra-glacial debris movement is controlled by ice movement, for this study period it can be considered as relatively static and the debris-covered ice area defined in the classification image for 10th December 2004 was assumed to represent the debris-covered ice area for the rest of this research.

As the entire ice shelf was not covered by the ASTER swath (Figure 4.3), the debris-cover defined above needed to be extended to the ice shelf boundaries. The remaining area was determined using the 20th October 2001 L1B clear-sky image, using PCA and unsupervised

isodata classification on PC1. The two debris-cover images were then combined and the result is used to represent debris-covered ice for the rest of this research.

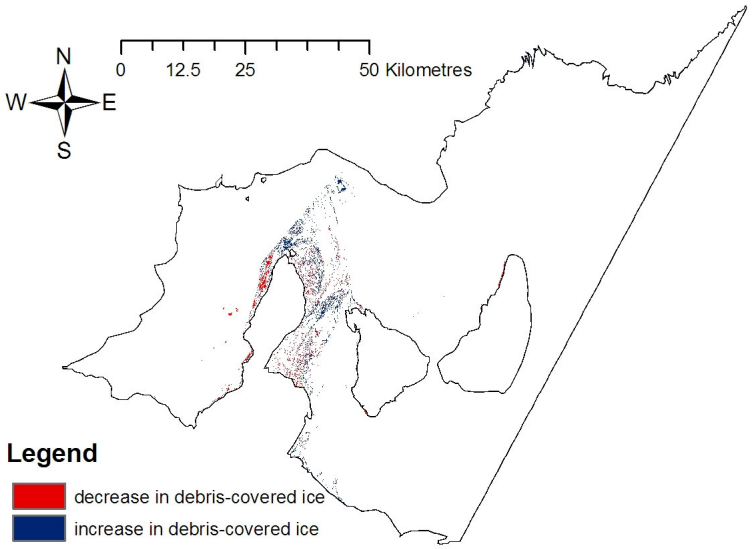

Figure 4.9 Change in extent of area classified as debris-covered ice of the McMurdo Ice Shelf between 3rd February 2003 and 10th December 2004

The absolute accuracy of the debris-covered ice extent is also difficult to determine, as, in the type of image processing used here, misclassification can occur often as the result of mixed pixels (Cracknell, 1998). Mixed pixels, also known as mixels, occur as a result of surface heterogeneity, specifically where the features on the ground are small relative to the pixel dimensions. The radiance measured at the instrument is a result of the combination of these surface types and produces erroneous values. Mixels commonly occur at the perimeter of a feature (Cracknell, 1998). There is scope for mixels to occur at the ice and debris margins, as a result of ponds within the debris-covered ice area, from snow on debris-covered ice, and from patches of debris on bare ice. This misclassification will be somewhat limited due to the fact that the pixel size of ASTER imagery is 15 m. The occurrence of Mixels should be further reduced by the use of three wavelength bands, and PCA.

The debris-covered ice accounts for approximately 6% of the McMurdo Ice Shelf, and is concentrated around Brown Peninsula, extending to the edge of the ice shelf (Figure 4.10).

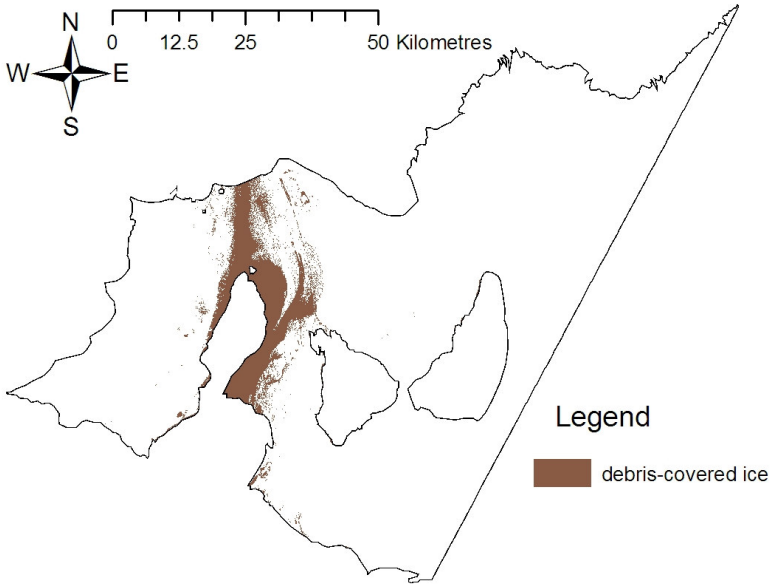

Figure 4.10 Distribution of debris-covered ice on the McMurdo Ice Shelf as determined from ASTER image acquired on 10th December 2004.

4.3.5 Surface type distribution

In order to produce a surface type distribution image to represent the beginning of the modelling period (Chapter five) it is preferable to have an image that was acquired as close as possible to the beginning of the summer. The most suitable image available was acquired on the 10th December 2004 (Section 4.3.2).

Three surface types are accounted for in the modelling: snow, bare ice, and debris-covered ice. The surface type distribution image for the whole ice shelf was firstly created using the surface transient snowline image for the 10th December 2004 (Section 4.3.3). Pixels with values below the snowline threshold were defined as ice, and those above the threshold, defined as snow. This image was then overlain with the final debris-covered ice image (Section 4.3.4).

As the ASTER swath did not cover the whole ice shelf (Figure 4.3) the pixels to the west (not defined as debris-covered ice) were assumed to be bare ice, while the pixels to the north were defined as snow. The final surface type distribution image was exported to ASCII format to be used to initiate the model developed in chapter five.

4.3.6 Distribution of albedo

During November 2004, a Licor pyranometer (LI-200SZ) was used to perform manual measurements of albedo at several of the stake sites. The sensor spectral response is 0.4-1.1 μm with an error of <5%. Observations were made at approximately 1 m above the surface. Between 5 and 20 measurements were taken at each site depending on conditions and logistical constraints. Furthermore, when the AWS was positioned at the bare ice (Section 2.5.1), albedo was measured with a Kipp & Zonen CNR1, which has a spectral sensitivity between 0.305-2.800 μm, and accuracy of 2%.

An albedo distribution image of the McMurdo Ice Shelf was produced (using the ASTER AST07 obtained on the 10th December 2004) using the following approach. Firstly, VNIR bands 1 through 3 were resampled to 30 m using nearest neighbour interpolation. Next, a narrowband to broadband conversion was applied, using the formula proposed by Liang (2001):

$$\alpha_{Short} = 0.484\alpha_{band1} + 0.335\alpha_{band3} + 0.324\alpha_{band5} + 0.551\alpha_{band6} + 0.305\alpha_{band8} + 0.367\alpha_{band9} - 0.0015 \qquad 4.2$$

Snow and ice reflect radiation anisotropically (Knap and Reijmer, 1998). However, as no specific bidirectional reflectance function (BRDF) algorithm for snow and ice and the ASTER platform was available, an assumption of isotropic reflectance is made here.

The albedo image may also be subject to mixels or misclassification (Section 4.3.4). For example, fresh snowfall can cause albedo and other surface properties to be altered. However, new snow did not cause misclassification with the 10th December 2004 imagery, as this date coincided with fieldwork, which confirmed that no significant snowfall had occurred in the region for at least several days.

The A-B transect (Figure 4.3) across the albedo image for the 10th December (Figure 4.11) shows a distinct increase at the same distance along the transect as in the band ratio image that was used to determine the transient snowline (Figure 4.12 cf. Figure 4.5). This

agreement gives some confidence in using the threshold detailed above to define the transient snowline (Section 4.3.3). However, without extensive fieldwork it is difficult to assess the absolute validity of using these divisions.

Comparisons between ground based and remotely sensed albedo were made by resampling the albedo image to a resolution of 200 m using nearest neighbour interpolation (Figure 4.11) and comparing the pixel value with the value obtained with the field-based measurements. This comparison is discussed in section 4.6.

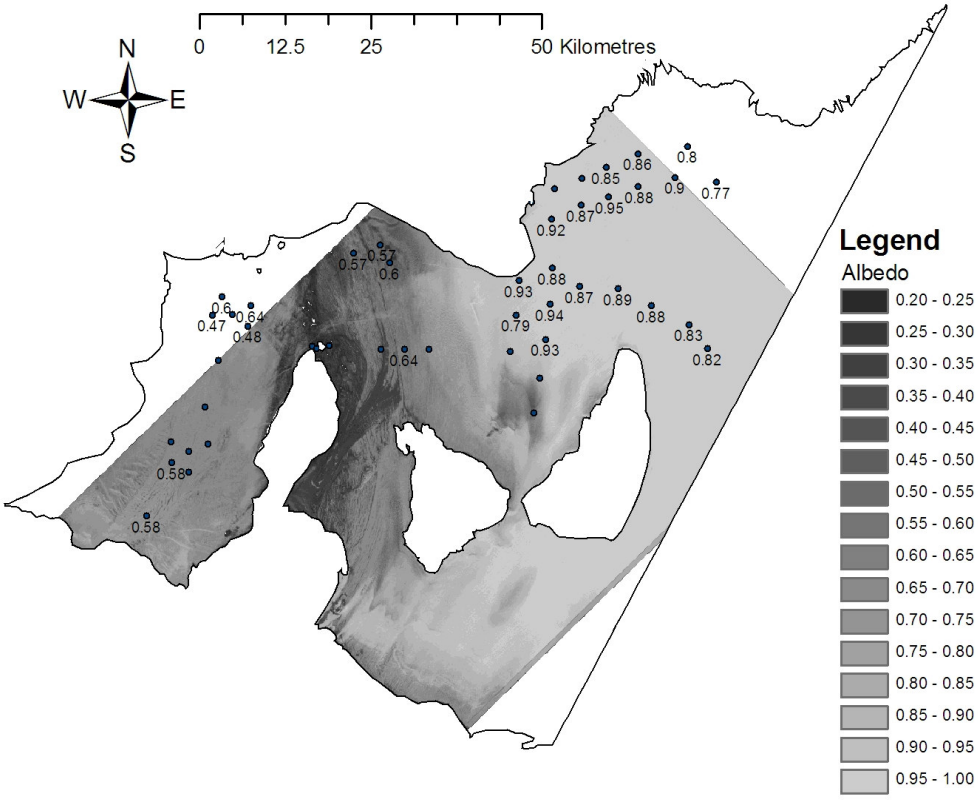

Figure 4.11 Distribution of shortwave albedo across McMurdo Ice Shelf, point values are from fieldwork conducted throughout November 2004, distributed values were determined using narrow to broadband conversion on ASTER image from 10th December 2004.

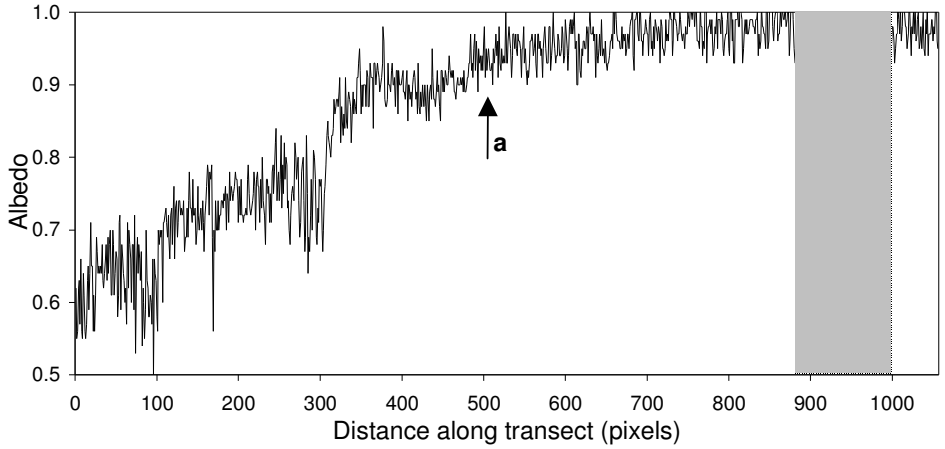

Figure 4.12 ASTER derived albedo along transect A-B for (Figure 4.4) 10th December 2004. Arrow shows the location of the boundary as detected using the band ratio image. The greyed area represents the area of distortion on the original ASTER data granule.

4.4 Surface mass balance trends

The surface mass balance pattern reported in the literature, of increased ablation towards the west and accumulation to the east (see chapter one, and Figure 1.3), is also shown in historical stake measurements (Figure 4.13). Stake data for the 2003-2004 and 2004-2005 summer also show this trend (Figure 4.14).

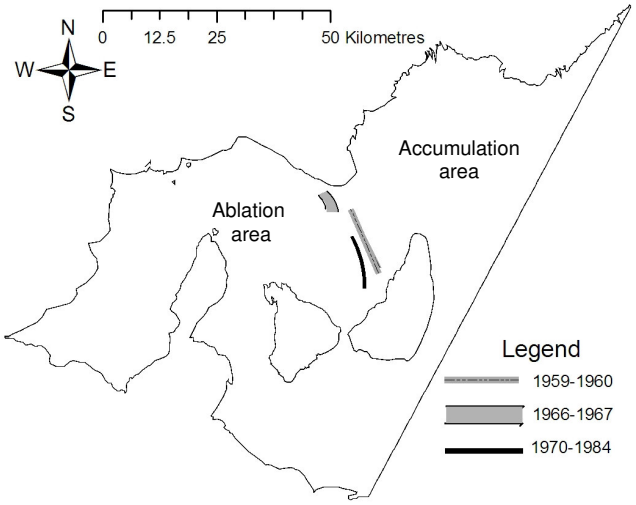

Figure 4.13 Digitised historical accumulation/ablation area boundaries based on stake measurements for 1959-1960 (Stuart and Bull, 1963), 1966-1967 (Paige, 1968) and the mean for 1970-1984 (McCrae, 1984).

A boundary separating accumulation and ablation for the two summers can be inferred (Figure 4.14). These boundaries are not representative of the actual accumulation/ablation boundary, as the stake data does not cover the entire summer period. However, as the two datasets are similar, and they cover the middle of the summer period, general comparisons may be made. The area of net ablation in the 2004-2005 summer is larger than that in 2003-2004 summer. The approximate accumulation/ablation boundaries are separated by roughly 12 km and lie to either side of the historic annual surface accumulation/ablation boundaries (Figure 4.13). The large lateral shifts are most likely to be a manifestation of the low gradient of the ice shelf.

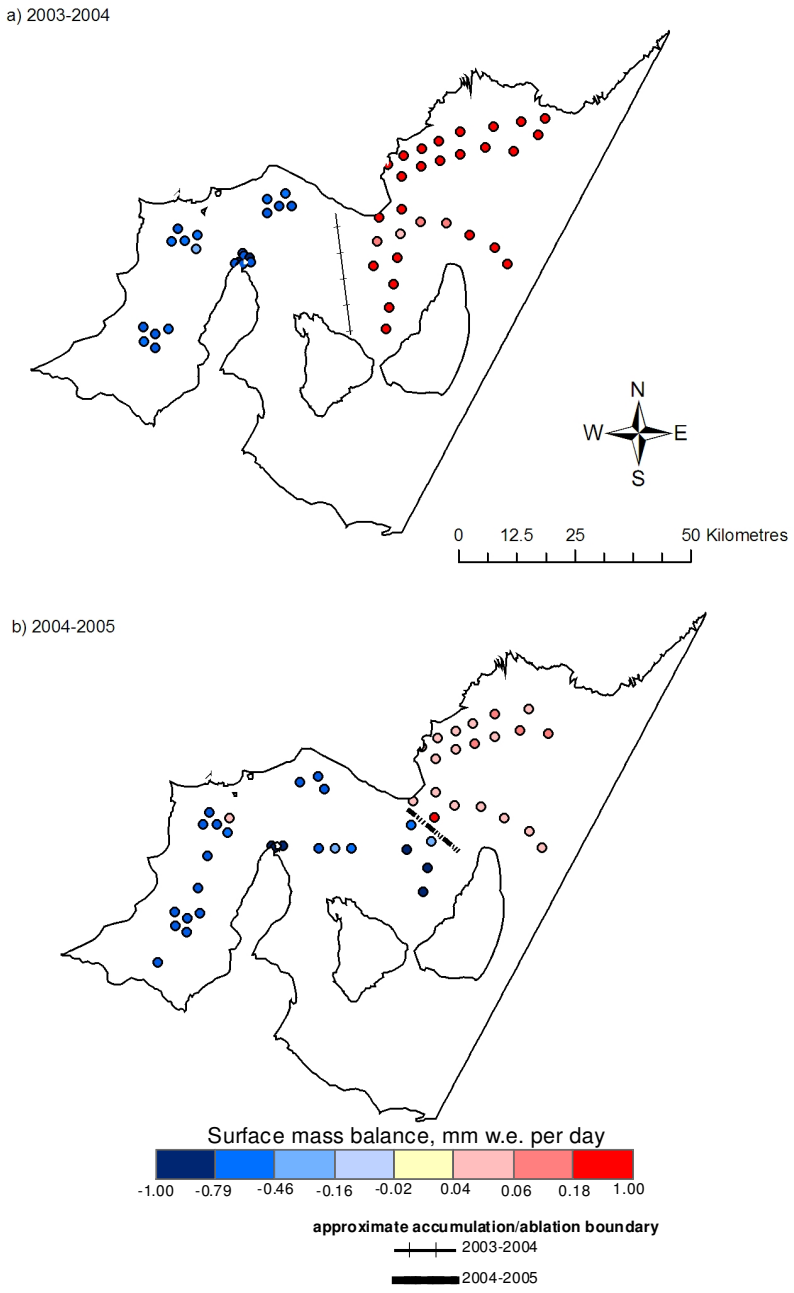

Figure 4.14 Mean daily mass balance stake data for the summer field campaigns a) 2003-2004, and b) 2004-2005.

4.5 Surface type distribution

The distribution of surface types (Figure 4.15) that will be used as input for the model in chapter five is a combination of several images, as discussed in 4.3.5. Although the images are not from the beginning of either of the two summers that will be modelled in chapter five, the distribution is based on the most suitable image available (10th December 2004) and thus was considered a reasonable approximation.

Just over half (55 %) of the entire surface area of the McMurdo Ice shelf area was be defined as snow, 39 % as bare ice and 6% as debris-covered ice. In general, the western half of the ice shelf is ice, and the eastern half snow, with two anomalies. These anomalies were areas defined as ice in the eastern half of the ice shelf. One area was adjacent to Minna Bluff, and a small patch in the middle of the southern part of the ice shelf (Figure 4.15). It is suggested that these areas may be similar to blue ice areas which are generally located in the lee of Nunataks, mountains or rock outcrops Bintanja (1999).

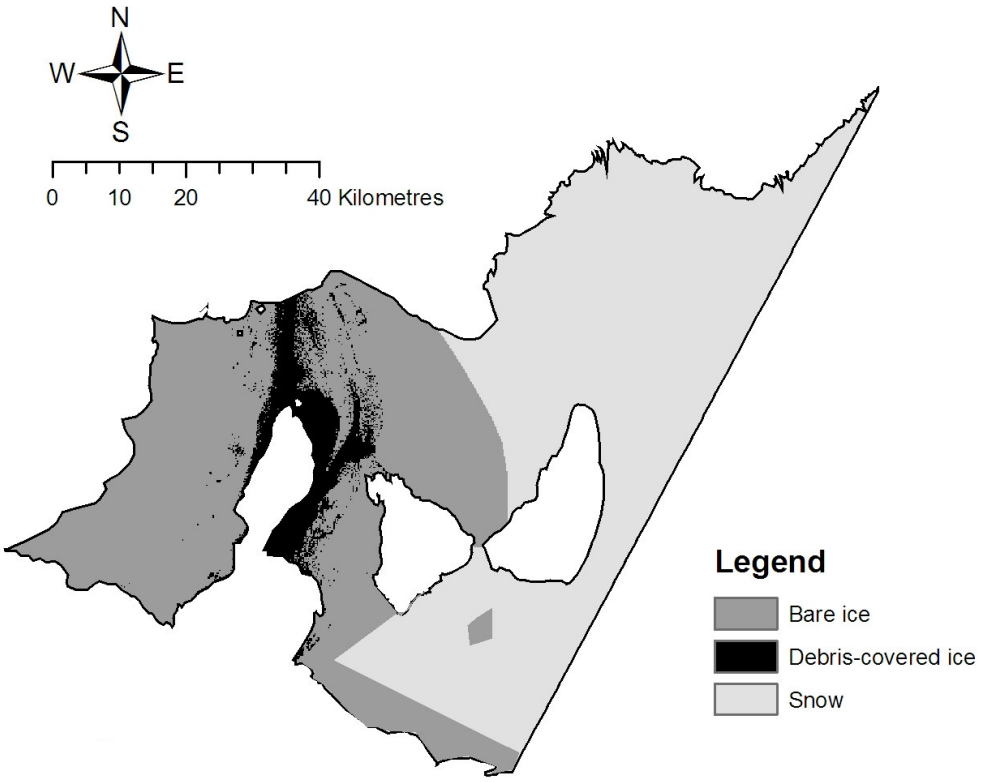

Figure 4.15 Distributed surface type conditions used as initiating conditions for the model developed in chapter five.

4.6 Albedo distribution

The final distribution of albedo used to represent the beginning of the summer is shown in figure 4.16. The debris-covered ice is apparent in the spatially distributed albedo image (Figure 4.16). The spatial heterogeneity of the bare ice albedo is also evident, with decreasing albedo towards the west and towards the Ross Sea (Figure 4.16). Large patches of low albedo ice are clearly visible both to the north and south of Black and White Islands. The relationship between the ground based and ASTER derived albedo was strong; though unfortunately the ground based measurements were concentrated in the higher range (Figure 4.17). The albedo derived from the ASTER image ranges from 0.20 to 0.99, with the bare ice being 0.55-0.65, snow 0.90-0.99 and debris-covered ice approximately 0.23.

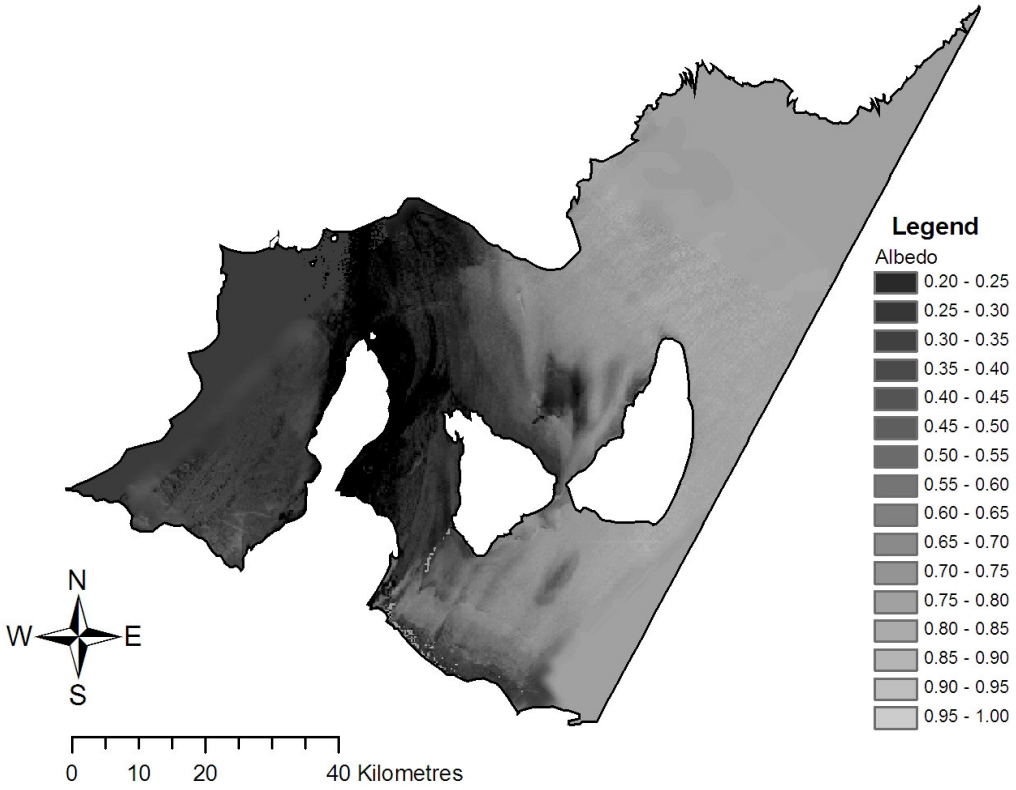

Figure 4.16 Distributed albedo used to initiate the model developed in chapter five.

The correlation between ground based and ASTER derived albedo (Figure 4.16) was unexpectedly high (correlation coefficient of 0.94) given that there were many sources of uncertainty introduced in both measurements. These include the differing azimuth and

zenith angles due to the timing, spectral sensitivities of equipment, narrowband to broadband conversion, and the assumption of isotropic reflection. Albedo at the AWS over bare ice was determined to be 0.56 at the time the ASTER imagery was obtained. The corresponding pixel (resampled to 200 m) was 0.55. The mean albedo for the debris-covered site when it was snow free during the 2003-2004 instrumentation period was 0.12 (Section 2.6) but the debris-covered ice values from the ASTER derived albedo image were approximately 0.23. Overall, the ASTER derived albedo tended to overestimate the values, possibly a result of pixel saturation or overlying snow.

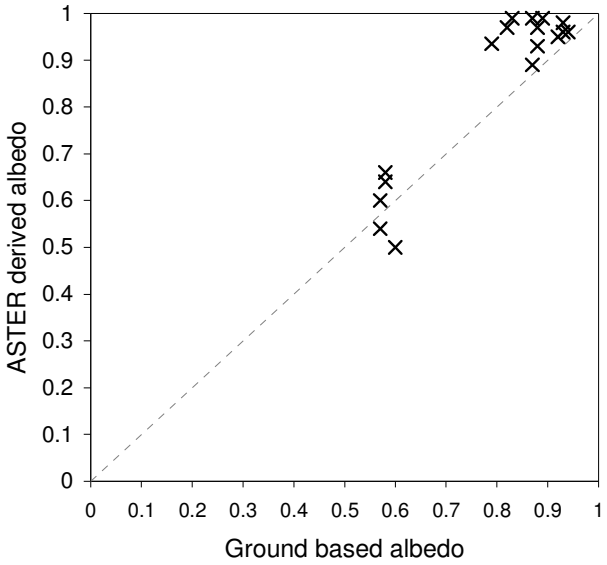

Figure 4.17 Albedo derived from ground based measurements compared with ASTER derived values. Note the albedos were measured during November 2004 while the satellite image was obtained on December 10th 2004.

The area of low albedo between White and Black Islands is indicative of low snow accumulation, possibly where the channelling of wind between the Islands would discourage the deposition of snow.

The general trend of decreasing albedo from east to west and towards the Ross Sea in the ASTER derived albedo imagery coincides with a similarly oriented surface mass balance pattern (Section 4.4). Although these albedo values must be used with caution due to the issues outlined above, the objective here was to be able to provide a more comprehensive distribution of albedo to the model rather than the singular value or gradient with altitude as is often used (Hock, 2005). Thus, the ASTER derived albedo is taken to be indicative of the initial surface albedo state and suitable for use as input into the model in chapter five.

4.7 Summary

Trends in surface mass balance for the 2003-2004 and 2004-2005 summers were shown to be similar to those reported in previous studies in the area and showed a pattern of ablation in the west and accumulation to the east. The stakes also revealed that the approximate boundary between accumulation and ablation was displaced considerably between the summers.

Approximate surface type distribution was determined using ASTER multi-spectral imagery. The extent of debris-covered ice was relatively unchanged between 3rd February 2003 and 10th December 2004, occupying approximately 6% of the total ice shelf. Approximately 55% of the ice shelf was defined as snow and 39% as bare ice.

Albedo varied considerably across the ice shelf, displaying an overall increasing trend from west to east, interrupted by large patches of low albedo. Products of this chapter will be used for initiation and validation of the distributed model developed and applied in chapter five.

5 Synthesis: distributed summer surface mass balance

5.1 Introduction

Chapters two and three investigated the climate and surface energy balance at two sites on the McMurdo Ice shelf. While these chapters enabled a detailed examination of the surface energy and surface mass balance, such work is only relevant for a point and is limited to periods when an AWS with appropriate components is available. Now that regional climate models and thus distributed datasets are becoming increasingly reliable and accessible it makes sense to develop a distributed SEB surface mass balance model that can be forced with such datasets.

This chapter synthesises the findings of the previous three chapters by using them to help develop a spatial model to examine patterns of ice shelf surface mass balance. Specific objectives of this chapter are:

- Develop a realistic distributed model to determine the spatial pattern of summertime surface mass balance of an ice shelf.
- Examine spatial patterns of the summertime surface mass balance of the McMurdo Ice Shelf and their relationship to atmospheric processes.

A distributed model is developed based on the SOMARS model used in chapter three, and is forced using distributed climate variables from a regional climate model. The distributed model also uses surface type and albedo information (from chapter four) for initial boundary conditions.

This chapter describes the process that was undertaken to develop and validate the distributed model. The patterns of summertime surface mass balance are then presented and discussed for the two summers of interest. The chapter concludes with a summary.

5.2 Developing and validating a distributed model

Developing the distributed model involved several steps. It was first necessary to ensure that the climate model data was suitable to use to force the energy balance model. To do this validation, the point based SOMARS, presented in chapter three, was forced using regional climate model data that covered the bare ice site. The results of this model run were validated by comparing it against components measured by the AWS situated at the bare ice site. A distributed version of SOMARS was then developed to use spatially distributed climate variables as input, as well as to incorporate spatial variations of both albedo and topographical parameters. Additionally, the performance of the distributed model was evaluated against direct ablation stake measurements presented in chapter four. The following sections describe these steps in order.

5.2.1 Forcing SOMARS with regional climate model data

The Antarctic MM5 Meso-scale Prediction System (AMPS) was established in October 2000 as a result of the dependence on weather for support of the New Zealand and United States Antarctic field operations (Monaghan *et al.,* 2005). This system is a physically based numerical weather prediction model, adapted for polar regions that uses the Polar MM5 (Fifth-generation Mesoscale Model) model with a 3.3 km resolution domain (Figure 5.1). AMPS at 3.3 km is only available for the McMurdo region and was developed to provide a functional forecast for the McMurdo aircraft operations. This prediction system is

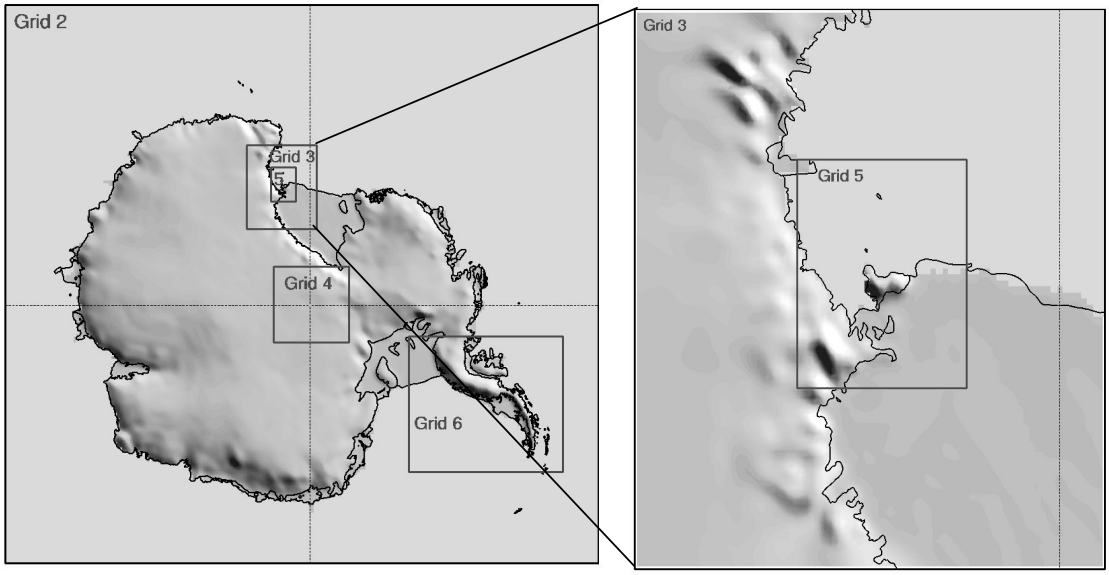

Figure 5.1 The Antarctic MM5 Meso-scale Prediction System (AMPS) domains. Focused on the whole of Antarctica (Grid 2) and the McMurdo Region (Grid 5).

considered adequate to assess the climatology of the McMurdo Region at a high resolution (Monaghan *et al.,* 2005). Output from AMPS is available for 6 hour intervals and includes the necessary variables required to force the SOMARS model.

The format of AMPS output is arranged by data type, time, and then grid location. A program was developed (AMPS2FORCE) to extract the relevant AMPS data and create forcing files for each 3.3 km grid point (Figure 5.2). This component was kept separate from the distributed SOMARS so that it can be adjusted to use with different climate model data. Within this program, the variables were also converted to the appropriate units. To run the point based SOMARS, only the forcing file that covered the bare ice site was used as input.

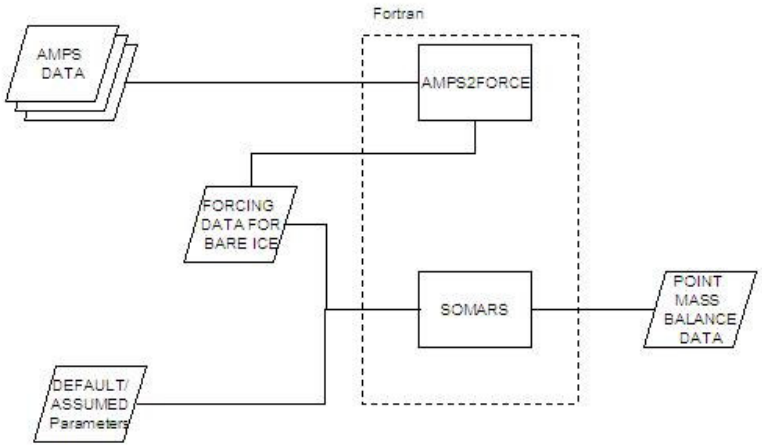

Figure 5.2 Processes and datasets involved in the procedure to check that the AMPS data was suitable for running the SOMARS model.

The forcing file contained AMPS values of temperature, relative humidity, wind speed, precipitation, global radiation, incoming long-wave radiation, cloud cover and precipitation. Although MM5 provides reflected radiation and emitted long-wave radiation, these were not used here, as it was more desirable to have SOMARS internally calculate the albedo and surface temperatures.

When not supplied to SOMARS, reflected solar radiation (K↑) is calculated as a function of albedo (α).

$$K\uparrow = K\downarrow \alpha \qquad 5.1$$

Albedo of snow is decreased exponentially from high to low prescribed values according to a time-scaled decay function and surface wetness (Greuell and Genthon, 2003). Conversely, it is increased as a function of the depth of fresh snow. The albedo of ice is an assumed constant, unless the model has calculated that there is a layer of water on the surface, in which case albedo is decreased according to depth of the water layer (Greuell and Konzelmann, 1994).

Using the mean albedo from measured data at the bare ice site (Section 2.7) the initial albedo of bare ice was set to 0.57. Snow albedo is defined as 0.80, and old snow 0.60, while the decay time scale is taken to be the same as Zuo and Oerlemans (1996) at 20 days (Table 5.1).

When outgoing long-wave radiation (L↑) is not prescribed in the forcing files, it is approximated as a function of the surface temperature according to the Stefan-Boltzmann Law (Eq. 1.2) and an assumed emissivity of 1.0. Surface temperature (T_0) is calculated as a function of the sub-surface component of the model (Section 3.2.2).

Table 5.1 Specific input parameters for the McMurdo Ice shelf used in running SOMARS forced with AMPS data.

Parameter	Value
Albedo of fresh snow α	0.80
Albedo of old snow	0.60
Albedo of ice	0.57
Albedo of superimposed ice	0.50
Time decay for snow albedo	20 days
Height of wind measurement	10 m
Height of temperature measurements	2 m

5.2.2 Validation of point based run forced with AMPS data

The model was run for the period Day 341, 2004 – Day 22, 2005, with a time step of 30 minutes to allow comparison with directly measured variables from the AWS. Here, daily

modelled surface temperature, surface mass balance, and radiative fluxes were compared with those recorded at the AWS.

Modelled surface temperature had a reasonable agreement with that measured at the bare ice site (Figure 5.3) with a correlation coefficient of 0.62 and an index of agreement of 0.70. Overall, there is a slight underestimation of the surface temperature (Figures 5.3, 5.4) with a mean difference of 1.0ºC.

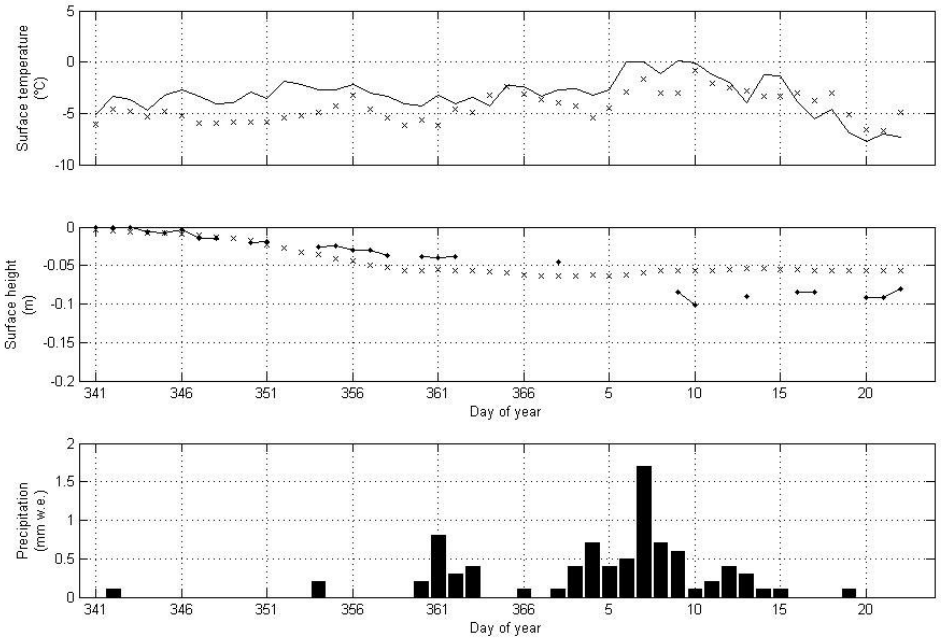

Figure 5.3 Time series of modelled results with variables directly measured at the bare ice site (Day 341, 2004 – Day 22, 2005). Measured variables are shown by a solid line, modelled with x *'s. The precipitation record is directly from the AMPS data while the surface temperature and height change are calculated within SOMARS.*

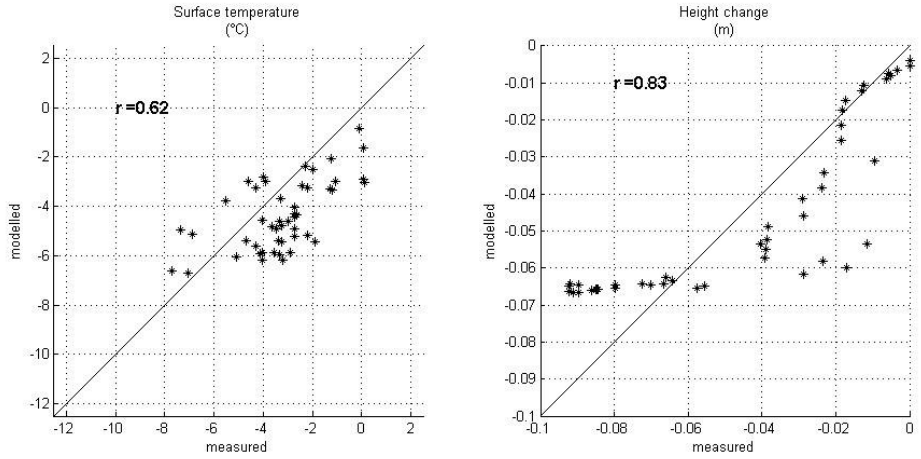

Figure 5.4 Surface temperature and surface mass balance results from the SOMARS model run using AMPS data for a point (Day 341, 2004 – Day 22, 2005).

Net surface height change was predicted well (Table 5.2). Measured ablation at stakes in the same area of the ice shelf as the AWS were also comparable to that predicted by the model (Table 5.2). While the model does not capture the rapid lowering in the first ten days of 2005, the overall surface mass balance trend is evident (Figure 5.3b). This result appears to have overcome some of the issues discussed in chapter three (Section 3.4.1) with regards to precipitation derived from McMurdo Station, giving a smoother surface mass balance change, more in line with that recorded at the AWS (cf. Figure 5.3, 3.5). However the surface is still higher at the end of the period than that measured by the sonic ranger (Figure 5.3).

Table 5.2 Modelled and measured total height change of bare ice on the McMurdo Ice Shelf ablation area, from Day 341, 2004 to Day 22, 2005.

Source	**Height change (m)**
Modelled	- 0.057
Mean stake	-0.053
Stake 90	- 0.020
Stake 91	- 0.041
Stake 92	- 0.100
Sonic ranger (mode)	- 0.081

The model was found to reproduce the radiative fluxes very well (Table 5.3). As modeled incoming radiative fluxes were derived from AMPS data, the low modeled incoming short-wave radiation value (Table 5.3) is most likely due to a discrepancy in the AMPS data, especially given that the long-wave radiation was closer to the measured value. Albedo was reasonably well modeled (Figure 5.5), although there is a slight overestimate overall (Table 5.3). Given that the combined uncertainties are accumulated in the net radiation, the modeled net radiation is acceptable, with correlation coefficient of 0.68 (Table 5.3).

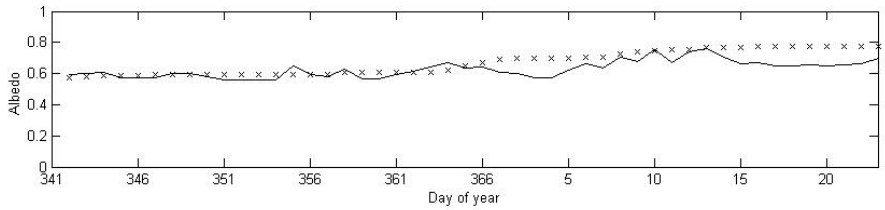

Figure 5.5 Time series of modelled albedo compared with that measured at the bare ice site (Day 341, 2004 – Day 22, 2005). Measured variables are shown by a solid line, modelled with x*'s.*

Overall, the ability of model to calculate the daily surface temperatures, the radiation budget, and surface mass balance for a single point using climate variables derived from the AMPS database is shown to be realistic (Table 5.3). Therefore, it was decided to further develop the model to create spatially distributed surface mass balance.

Table 5.3 Comparison of point based SOMARS modelled results (driven using AMPS) with variables directly measured at the bare ice site. Variables are daily means for the period the model was run (Day 341, 2004 – Day 22, 2005). Standard deviation is shown in brackets.

	Mean Surface Temperature (ºC)	Mean Incoming short-wave radiation (W m^{-2})	Mean Albedo	Mean Incoming long-wave radiation (W m^{-2})	Mean Outgoing long-wave radiation (W m^{-2})	Mean Net Radiation (W m^{-2})	Total Height change (m)
Observed	-3.23(1.79)	295.7(91.4)	0.62(0.05)	245.3(29.9)	304.1(6.2)	53.9(21.7)	-0.08(0.03)
Modelled	-4.27(1.42)	250.8(74.0)	0.66(0.07)	248.1(24.7)	305.3(5.8)	34.2(18.2)	-0.06(0.02)
Correlation coefficient	0.65	0.80	0.74	0.82	0.87	0.68	0.83
Root mean squared error	1.69	70.7	0.06	17.3	3.3	25.5	0.02
Index of Agreement	0.7	0.82	0.74	0.89	0.92	0.68	0.86

5.2.3 Distributed model

Developing the distributed model involved changes in inputs and processing of SOMARS, as well as the treatment of the outputs (Figure 5.6). The Fortran programming language was used in all but the presentation of the final surface mass balance maps, for which a GIS was used.

For the distributed model, AMPS data covering the whole ice shelf were used as input. Forcing files were created as above with AMPS2FORCE (Section 5.2.1). Because of the relatively low spatial resolution used in AMPS (3.3 x 3.3 km) compared with the resolution used internally to the model, it appears as if there are abrupt changes in data (Figure 5.7). Because of these resolution differences, atmospheric forcings are determined by using the closest geographic coordinates of each AMPS grid point being processed. In order to ensure that original data were used throughout the process, the AMPS data was not resampled or smoothed prior to being used in the distributed model. It is therefore expected that the abrupt changes will also be apparent in the results. The “diamond” shapes of the

individual grids are due to different map projections used by AMPS and that used for this research in the GIS.

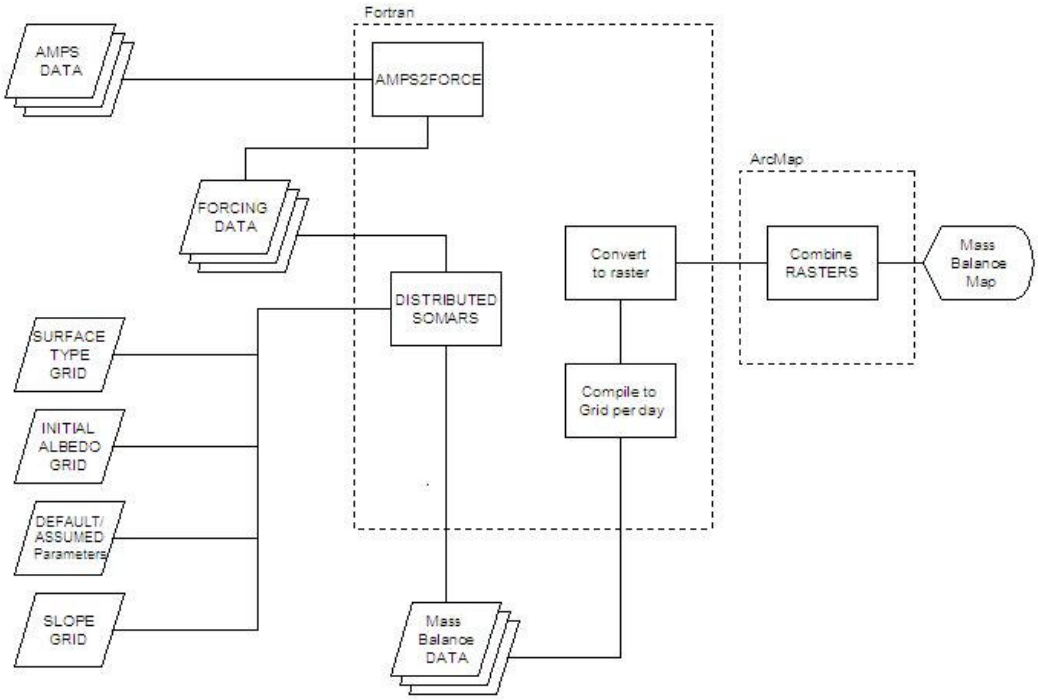

Figure 5.6 Procedure showing inputs and outputs for the final distributed model used to assess summertime surface mass balance of the McMurdo Ice Shelf.

To account for spatial variability the model was also modified to allow the input of the initial surface type, albedo, aspect and slope for each point on the ice shelf surface. The initial surface type and albedo were assigned to each grid point based on results from chapter four (Figure 4.16).

Elevation, slope and aspect were calculated for each grid point, using the 200 x 200 m Antarctic Digital Elevation Model (DEM) from RADARSAT Antarctic Mapping Project (Alaska Satellite Facility, 2003). An assumption of no shading was made for the entire ice shelf. Given its topography, the McMurdo Ice Shelf represents a situation where this assumption is reasonable for the majority of the shelf. Other parameters were held the same for the initial run (Section 5.2.1) and shown in Table 5.1 and 3.3.

The model was adapted to allow for multiple grid points, and the model was run for every single grid point. Each grid point is initialized with albedo, surface type and temperature, after that these variables are internally generated. If a grid point is characterised as debris-covered ice, the grid point is not processed as ablation is considered negligible (Section 3.7.3).

Outputs for the distributed model were similar to the original SOMARS, but include variables for each 200 x 200 m grid point. Model output was imported into ESRI® ArcMap™ 9.0 GIS to construct raster images of total surface mass balance and of the surface mass balance components.

5.2.4 Distributed model: validation

The distributed SOMARS model was further validated using ablation stake measurements taken at various times throughout the summers of 2003-2004 and 2004-2005. As these stake measurements were made on different dates, the model was run several times, once for each group of stakes. This processing was undertaken a total of thirteen times, covering both the 2003-2004 and 2004-2005 field periods (Table 5.4).

For each model run, the relevant grid point value was extracted from the GIS and then compared with the measured stake value. It is important to note that for all these runs the initial boundary conditions were set to the same which will introduce some error into the final results. Trial runs with excessive initial surface temperatures showed that realistic values of surface temperature were obtained after seven days. Thus, it is defined that the model has a spin up period of approximately ten days. As all the runs in Table 5.4 are longer than the spin up period, any errors resulting from initial boundary conditions will be reduced. The following validation does not include the areas within the debris (stakes 52, 55,57) as these stakes were on small patches of bare ice surrounded by thick debris and would be excessively influenced by the debris.

Table 5.4 Distributed model runs used to enable a comparison with ablation stake measurements.

Run no.	Summer	Group name	Stakes covered	Dates
1	2003-2004	North Koettlitz	70-74	Day 331, 2003 – Day 10, 2004
2		South Pole Road	31-35	Day 320, 2003 – Day 3, 2004
3		South Koettlitz	80-84	Day 334, 2003 – Day 9, 2004
4		Windless Bight	1-15	Day 317, 2003 – Day 5, 2004
5		North Bratina	60-64	Day 328, 2003 – Day 13, 2004
6		White Straight	20-25,28,29	Day 329, 2003 – Day 2, 2004
7	2004-2005	East Bratina	90-92	Day 341, 2004 – Day 22 2005.
8		North Koettlitz	70-75	Day 322, 2004 – Day 27, 2005
9		South Pole Road	31-35	Day 328, 2004 – Day 31, 2005
10		South Koettlitz	76,80-86	Day 325, 2004 – Day 26, 2005
11		Windless Bight	1-6,10-15	Day 327, 2004 – Day 30, 2005
12		North Bratina	61-63	Day 320, 2004 – Day 25, 2005
13		White Straight	23,24,28-30	Day 333, 2004 – Day 28, 2005

The modeled surface mass balance has a positive correlation with the stake measurements during both summers (Figure 5.8, 5.9), with the results from the 2004-2005 period the most encouraging.

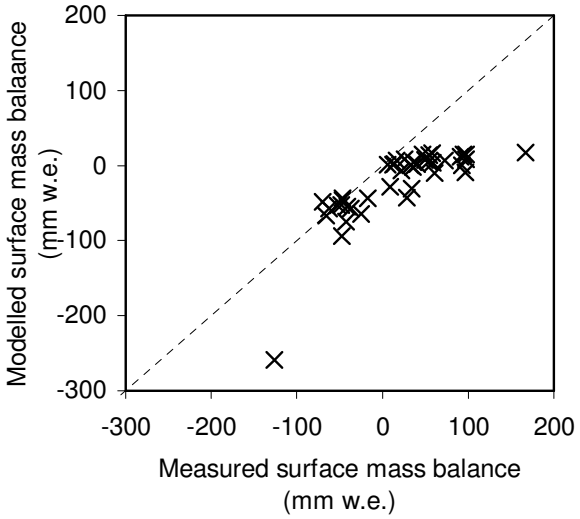

Figure 5.8 Comparison between stake measurements of surface mass balance, and the distributed model output for the 2003-2004 field campaign.

During the 2003-2004 field campaign, modelled surface mass balance using distributed climate variables shows good agreement with that measured at the stakes (Figure 5.8). In this summer, the correlation coefficient is 0.78, the index of agreement is 0.76, and RMSE is 56 mm w.e. There is a slight overestimate of the ablation and a distinct underestimate of

total accumulation (Figure 5.8). Underestimation of the accumulation may be due to snow redistribution. The comparison is considered reasonable given that, as above, the initial boundary conditions are only truly valid for Day 345, 2004.

For the 2004-2005 field measurement period agreement is not as good with a correlation coefficient is 0.65 (Figure 5.9a). However, examining the results, there is an anomaly, at stake 21, where a large amount of accumulation was recorded at the stake (449 mm w.e.) while the model reported a considerably lower value (3 mm w.e.). This particular stake measurement is also anomalous when compared with the other stakes in the area (maximum of 116 mm w.e., with a mean gain of 44 mm w.e.). Such an anomaly could be caused by many factors including, localized wind loading, recording error, or snow redistribution. Thus, it is considered reasonable to remove this outlier and reassess the model performance without the data for stake 21. With stake 21 removed from the dataset, the performance of the distributed model during the 2004-2005 field campaign improves considerably, with a correlation coefficient of 0.89, an index of agreement of 0.91 and a reduced RMSE (33 mm w.e.). These results are considered very good given that the initial boundary conditions only really hold true for day 345, 2004. Sites of accumulation during the 2004-2005 summer were better modeled than those for the 2003-2004 summer (Figure 5.8, 5.9b). Possible explanations for the differences between the two seasons include: initial conditions; different synoptic conditions; snow redistribution conditions; the AMPS dataset; and precipitation variability (much higher in 2003-2004).

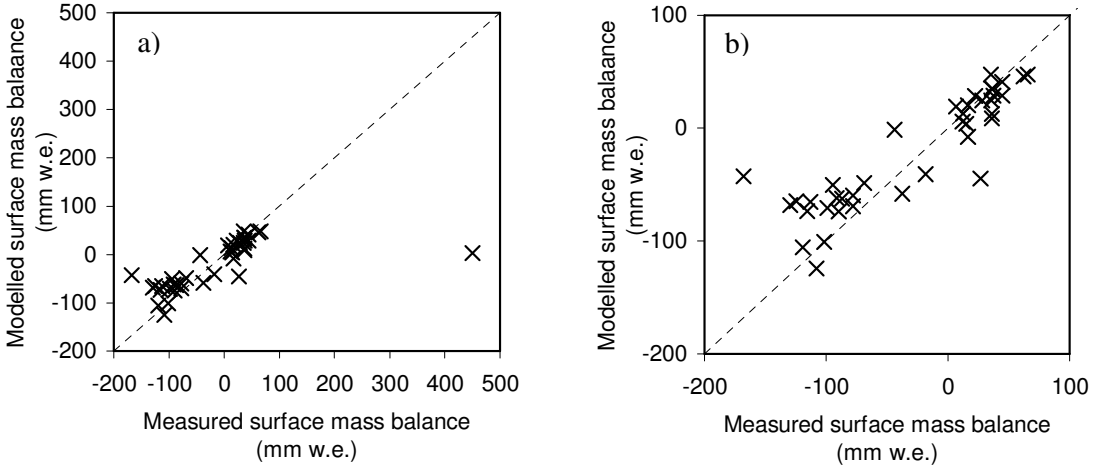

Figure 5.9 Comparison between stake measurements of surface mass balance, and the distributed model output for the 2004-2005 field campaign. a) all data, b) mass balance data with the outlier remove – see text for explanation.

While a there is room for improvement in these results, they are encouraging given that a large amount of discrepancy can be attributed to initial boundary conditions. The following may improve the results:

- Use of alternative satellite imagery to determine initial surface conditions.
- More detailed initial field survey including ice shelf temperature.
- Development and inclusion of a snow redistribution model.

Despite these factors, it is considered that the distributed model produced realistic results and can be used to assess overall patterns of surface mass balance.

5.3 Patterns of summertime surface mass balance

In order to assess the surface mass balance pattern, the distributed model was run for the four month period November – February for both 2003-2004 and 2004-2005. Initial boundary conditions were those used above (Section 5.2.3). It is considered that a spin up period of 10 days allows the 120 day run to produce realistic results. The following sections present and describe the surface mass balance and surface mass balance components, then discusses their significance.

5.3.1 Surface mass balance pattern

For both 2003-2004 and 2004-2005 summers (Figure 5.10), the overall pattern of surface mass balance predicted by the model is consistent with the well known surface mass balance pattern of the McMurdo Ice Shelf. The pattern is ablation in the west and accumulation in the east (Section 1.5.2, 4.4). Additionally the southern area of the McMurdo Ice Shelf is shown to be part of the ablation area (Figure 5.10).

Ablation is spatially irregular for both summers, with a number of areas clearly subject to higher ablation than others. Largest net ablation values occurred towards the southwestern boundary of the ice shelf. This ablation is made up of two parts, an area immediately to the north of Minna Bluff (Figure 5.10) and an area further to the west, where the ice shelf is fed by the Koettlitz Glacier (Figure 5.10). In the immediate vicinity of Brown Peninsula, there is also an area of slightly enhanced ablation (Figure 5.10). This area of increased ablation extends beyond Brown Peninsula and the debris-covered ice and north towards the ice edge in the Ross Sea.

A small anomalous area of ablation is identified in the northeastern part of the ice shelf (Figure 5.10). This is a relatively narrow area where the ice shelf is bounded by Ross Ice Shelf to the east and Ross Island to the north. This is in the area usually defined as accumulating.

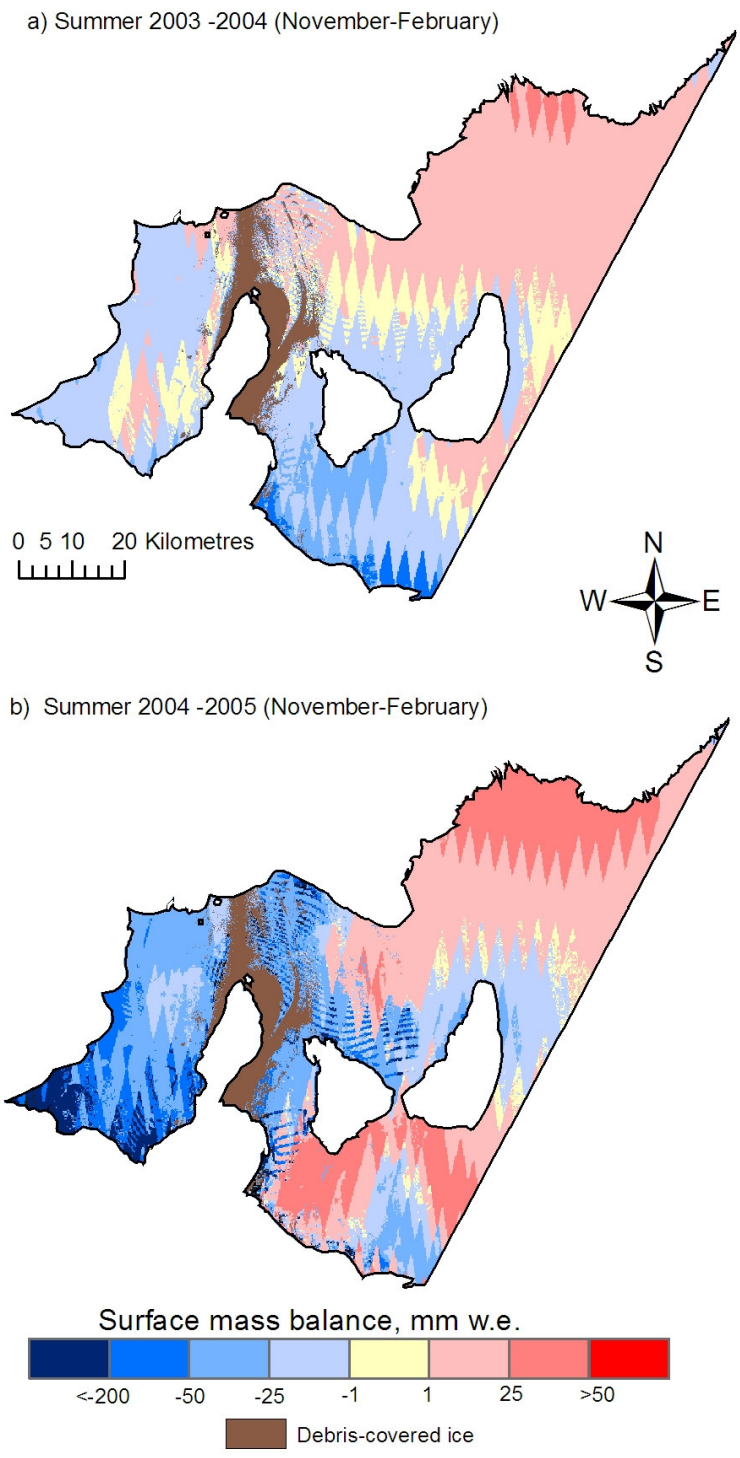

Figure 5.10 Modelled distribution of total net surface mass balance of McMurdo Ice Shelf for summers of a) 2003-2004 and b) 2004-2005 where summer is defined as November – February inclusive.

Although the overall pattern of summertime surface mass balance was similar for both the summer periods investigated, some differences are apparent. The most intense area of ablation for both summers is along the southwestern boundary of the ice shelf. For the 2004-2005 summer, the quantity of ablation is much greater (Figure 5.10b). The greatest surface mass balance loss in 2003-2004 is just to the north of Minna Bluff, whereas in 2004-2005 it is further west, at the terminus of the Koettlitz Glacier (Figure 5.10). While both summers have a small amount of ablation modelled in the northeastern tip of the ice shelf, this is more extensive for the 2003-2004 summer (Figure 5.10a).

The area of near-equilibrium surface mass balance was much larger for the 2003-2004 summer, (Figure 5.10a). This illustrates a gradual transition from positive to negative surface mass balance across the ice shelf. Within the accumulation area for 2004-2005 there is an area of enhanced accumulation to the north in the Windless Bight region, including up to 50 mm w.e (Figure 5.10b). The area of enhanced accumulation is smaller for the 2003-2004 summer (Figure 5.10a).

The surface mass balance images show distinct patterns of east-west linear features, especially for 2004-2005 (Figure 5.10). This lineation is an artifact of using the RADARSAT digital elevation model to derive slope and aspect within the GIS. It is considered that the true surface mass balance would be more even.

Overall, mean values for the entire ice shelf show an increase in surface mass loss in 2004-2005 (Table 5.5). Importantly, the distributed model was able to illustrate that the amount of change in surface mass balance across the ice shelf was increased during the 2004-2005 summer compared with 2003-2004 (Figure 5.10).

Table 5.5 Mean surface mass balance and components of McMurdo Ice Shelf. Standard deviation shown in brackets.

Summer period	Surface mass balance	Precipitation	Sublimation	Melt
2003-2004	-2.5(15.6)	6.9(5.4)	-8.8(12.3)	-0.7(2.8)
2004-2005	-6.7(39.7)	31.4(33.3)	-34.6(37.2)	-3.4(14.1)

5.3.2 Surface mass balance components

For the 2003-2004 summer, precipitation was widespread across the ice shelf (Figure 5.11a) with a mean of 6.9 mm w.e. (Table 5.5). There was, however, an increased amount in the Windless Bight area (Figure 5.11a), which reached a maximum of 26.8 mm w.e. Sublimation also occurred extensively, with an area of negligible sublimation occurring in the Windless Bight area (Figure 5.11b). A small area at the northwest tip shows enhanced sublimation also. Maximum losses due to sublimation occurred in the southern section of the ice shelf (Figure 5.11b).

Over the whole 2003-2004 summer, melting is shown to occur primarily in the western area of the ice shelf (Figure 5.11c), with maximum loss of 10.4 mm w.e.. There is also a patch of enhanced melt reported to occur between Black and White Islands (Figure 5.11c).

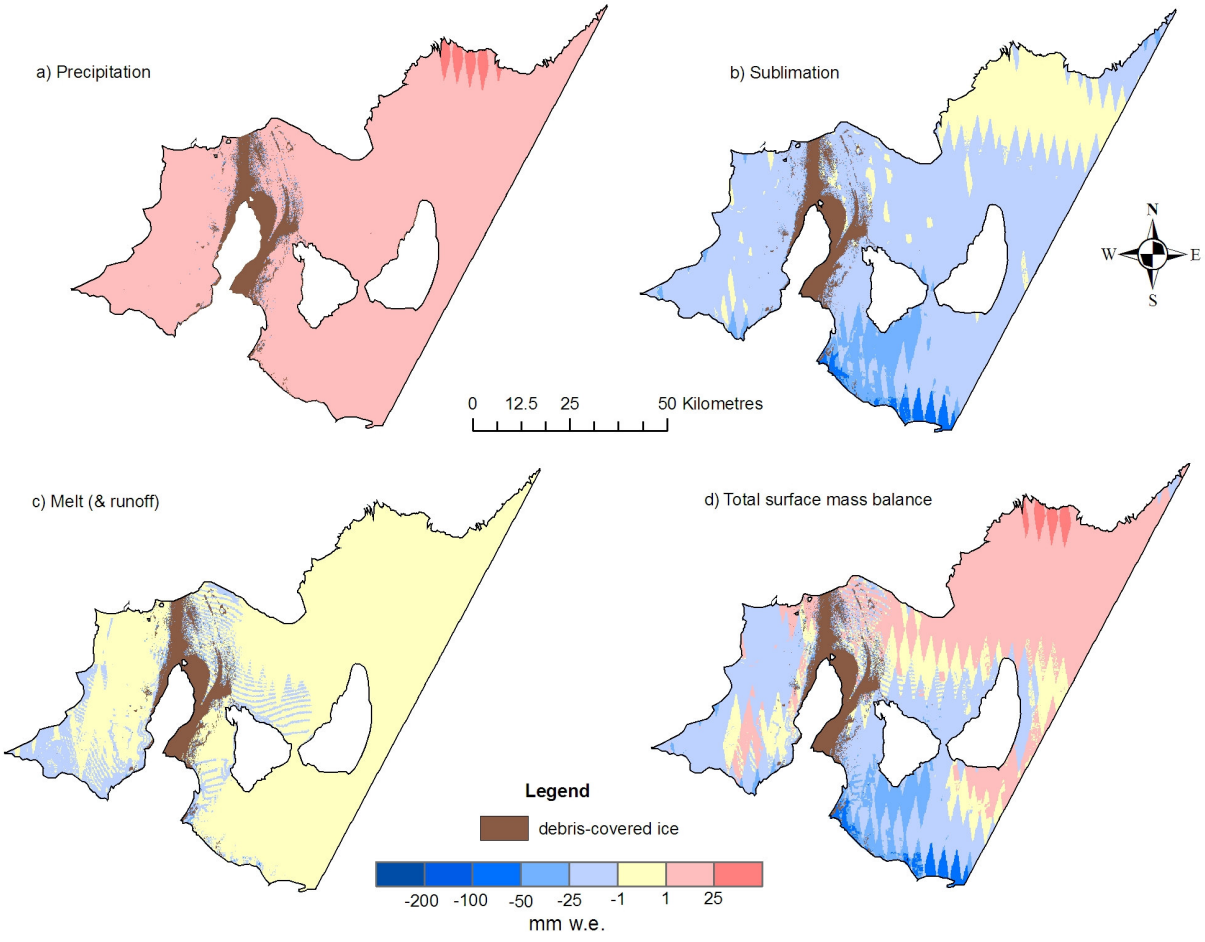

Figure 5.11 Modelled distribution of McMurdo Ice Shelf surface mass balance components for the summer of 2003-2004 (considered here as November – February inclusive).

Surface mass balance components of the summer of 2004-2005 display a distinctively different picture to that of 2003-2004. Precipitation, sublimation and melting are all greater during the second summer (Figure 5.12). Over the summer there is mean precipitation of 31 mm w.e. with a maximum of 190 mm w.e.. While precipitation is widespread there are higher values reported in the Windless Bight area, the middle of the ice shelf, and to the northwest edge of the ice shelf (Figure 5.12a).

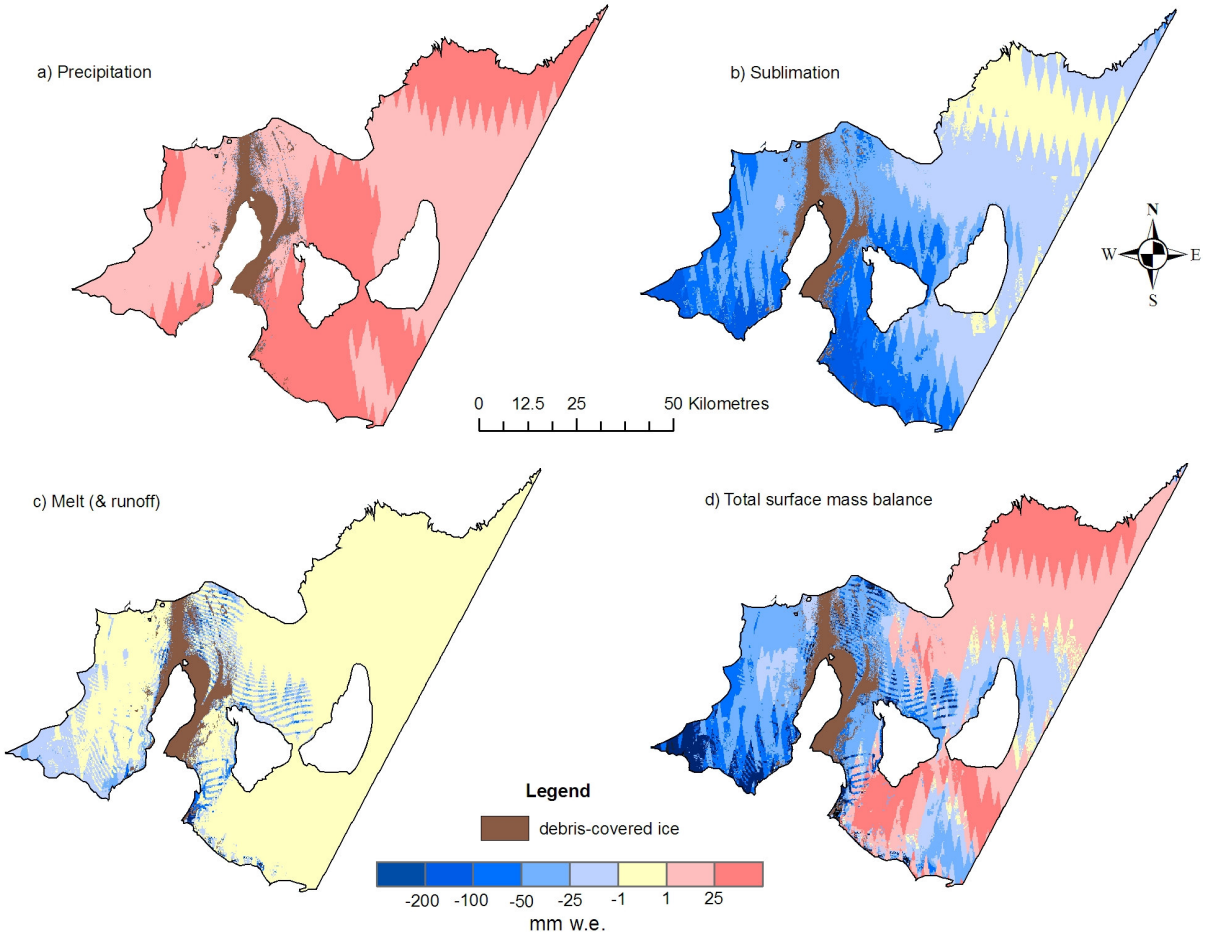

Figure 5.12 Modelled distribution of McMurdo Ice Shelf surface mass balance components for the summer of 2004-2005 (considered here as November – February inclusive.

Sublimation during 2004-2005 (Figure 5.12b) is of greater magnitude than for 2003-2004 (Figure 5.11b), but it has a similar pattern. Large losses were recorded for the southern part

of the ice shelf on both sides of Brown Peninsula. The same regions were subject to melt during both summers, however melting was greater during 2004-2005 (Figure 5.12c), with a maximum value of –220 mm w.e. High values of melting only occurred over small areas. Most of the melting occurred in the vicinity of Brown Peninsula (Figure 5.12c).

5.3.3 Interpretation of surface mass balance patterns

It was reported in chapter two that the 2004-2005 summer was warmer, windier and had higher precipitation than during the 2003-2004 summer (Section 2.3). The surface mass balance pattern for the two summers reflects these statistics, with precipitation sublimation and melt all high in 2004-2005. Larger amounts of sublimation can be accounted for by the higher mean winds (Table 2.1) while the increased and more widespread melting may be influenced by the warmer temperatures (Table 2.1).

During the summer of 2004-2005 there were reported to be more Type A conditions (Section 2.4, Table 2.4). Type A conditions result in both higher precipitation and sublimation rates (Section 3.6.4). As expected, the modeled distributed surface mass balance also exhibited these enhanced conditions in 2004-2005. While type C conditions nearly doubled during the 2004-2005 summer (Table 2.4), the impact of these conditions is less pronounced as the precipitation and sublimation conditions are similar to type B (Figure 3.20). Thus, the overall pattern can be attributed to the larger proportion of Type A conditions during 2004-2005.

Conversely, although it was shown that Type B conditions were likely to cause increased melting (Section 3.6.4), the summer of 2003-2004, which had more Type B conditions (Section 2.4, Table 2.4), did not have more melting compared with 2004-2005 (Figure 5.11c). This discrepancy may be due to initial boundary conditions, or be influenced more strongly by air temperature than is indicated in chapter three (Section 3.6.4).

The overall pattern of surface mass balance of the McMurdo Ice Shelf is clearly not controlled by elevation, with almost all ablation and accumulation occurring over a vertical range of 30m. However, it is suggested that the surrounding topography has a strong control through its influence on local climate. For example, the area of low albedo between

White and Black Islands (Figure 4.16) is indicative of low snow accumulation and/or high sublimation, possibly where the channelling of wind between the Islands would discourage the deposition of snow and enhance turbulence. In contrast, Windless Bight is an area of positive surface mass balance for both the summers. Low wind speeds in the area (O'Connor and Bromwich, 1988) result in less turbulence and thus less sublimation compared to other areas of the ice shelf (Figure 5.11, 5.12). Additionally, more net accumulation is likely in low wind speed areas like Windless Bight, as the snow at the surface is more likely to be deposited by wind redistribution processes than removed.

Surface conditions are also shown to play an important role. For example, in the area surrounding Brown Peninsula there is a lowered albedo due to dust particles and small patches of debris. This lowered albedo results in higher net radiation compared with areas of higher albedo. The larger amount of net radiation results in more energy available for ablation.

The area of enhanced melt and sublimation between Black and White Islands is also an area of lower albedo than its surroundings (Figure 4.16). Consequently this area is also subject to increased ablation during times when net radiation is dominant. However, the cause of lowered albedo was not determined. This area (along with the area north of Minna Bluff and the section of the ice shelf immediately to the north of Black Island) has parallels with Blue Ice Areas (BIA) as described by Bintanja (1999). BIAs are generally located in the lee of nunataks, mountains or rock outcrops. These topographic features induce greater turbulence and local warming, and thus enhanced sublimation. According to Bintanja (1999), these areas are primarily subject to sublimation, and not to melt. However Liston *et al.* (1999) have suggested that BIAs are areas of subsurface melt, but not necessarily runoff. It is suggested that this area is likely to be subject to sub-surface melt.

Other areas of enhanced sublimation and melt on the ice shelf, such as near the Koettlitz Glacier in the southwest, and the area in the northeast corner of the ice shelf do not have substantially different albedo compared with the rest of the ablation area (Figure 4.16). Enhanced ablation in these areas may be the result of localised climatic controls or an artifact of the boundary conditions or AMPS dataset. The area of enhanced ablation in the

northeastern tip of the iceshelf could be caused by accelerated wind flow near Cape Crozier (near the east end of Ross Island).

Overall, it is shown that the surface mass balance of the McMurdo Ice Shelf has a distinct pattern that changes to some extent inter-annually. The pattern is formed by a unique combination of synoptic conditions, topography and surface characteristics.

5.4 Summary

It has been shown that a point based surface mass balance model using regional climate model data as input can produce a realistic summertime surface mass balance. When the model was extended to a distributed version, covering an entire ice shelf, the model continued to produce realistic results. The major limiting factors are the initial inputs to the model. Such factors could be improved with increased fieldwork, or better remote sensing coverage at the beginning of the model runs.

Using the distributed model, it was possible to examine the patterns of surface mass balance for the summers of 2003-2004 and 2004-2005 for the McMurdo Ice Shelf. The pattern of surface mass balance of the McMurdo Ice Shelf is controlled by a combination of surface characteristics, topography, and synoptic conditions. During both summers, the surface mass balance followed the basic trend seen in ablation stake studies, that trend being accumulation in the east, and ablation in the west. This research has also revealed additional detail about the spatial variability of surface mass balance that cannot be obtained with stake-based studies.

The east-west pattern of surface mass balance on the McMurdo Ice Shelf is formed by a unique combination of topography and surface characteristics with wind and synoptic systems likely to be an influence. Within the ablation area several zones subject to enhanced ablation were identified. These were around Brown Peninsula, a section between Black and White Islands, an area in the north-eastern tip, and two areas on the southwestern boundary of the ice shelf. Some of these can be explained by a lowered albedo, while others are likely due to localised climatic controls.

The extent of the modelled ablation area was slightly larger for the 2003-2004 summer than for 2004-2005. However, the intensity of ablation and accumulation was greater in 2004-2005. This disparity resulted in a greater amount of change in surface mass balance across the ice shelf during the 2004-2005 summer compared with 2003-2004. This difference in surface mass balance change is attributed to the relative frequency of Type A synoptic systems during the summer of 2004-2005.

6 Conclusions

6.1 Introduction

To improve current understanding of ice-atmosphere linkages, the overall aim of this research was to demonstrate the relationship between variations in summertime surface mass balance of the McMurdo Ice Shelf and atmospheric processes. The specific objectives of this research were to:

- Characterize the McMurdo Ice Shelf climate for the summers of 2003-2004 and 2004-2005.
- Identify distinct synoptic situations that occur during the summer.
- Determine surface energy and surface mass balance of two key surfaces of the McMurdo Ice Shelf and link these with the distinct synoptic types.
- Detect surface characteristics used for distributed surface mass balance modelling.
- Determine the pattern of summertime surface energy and surface mass balance over the entire McMurdo Ice Shelf and associate this with climate characteristics.

These objectives have been achieved throughout the thesis. This chapter outlines the main findings in the context of these objectives, and then discusses their implications with regards to the key themes identified in chapter one. Future research directions are then recommended and the chapter finishes with a concluding statement.

6.2 Summary of main findings

The findings of this research are now outlined with respect to the specific objectives above, with an additional section describing methodological findings. The two key surfaces investigated were bare ice and debris-covered ice.

Summer characteristics

- The summers investigated for this research had similar meteorological conditions to the long term mean.
- The 2003-2004 summer was slightly cooler than the long term mean and had higher than normal pressure.
- The summer of 2004-2005 was warmer than usual.

Distinct summer synoptic situations

- Three distinct synoptic types were found to occur during summer, these were:
    a. Type A: Low pressure system residing in the Ross Sea Embayment.
    b. Type B: Anticyclonic conditions across region.
    c. Type C: A trough of low pressure extending into the Ross Sea Embayment.
- During the 2003-2004 summer, Type B conditions were common.
- Type A conditions were most frequent in the summer of 2004-2005 causing high wind speeds and precipitation.
- During 2004-2005 Type C conditions also occurred more frequently than in 2003-2004 which resulted in increased cloudiness and wind speeds.

Surface energy and surface mass balance of two key surfaces

- The microclimate of the McMurdo Ice Shelf is strongly affected by the surface type in summer.
- Bare ice site characteristics:
    a. The main source of energy was net radiation, but sensible heat becomes important at times.
    b. Ablation was by both melting (70%) and sublimation (30%).
    c. Sublimation occurred continuously throughout the period.
    d. Type A conditions resulted in an overall net gain at the surface.
    e. Type B conditions had a high melt rate and most mass lost.

f. Type C conditions were intermediate between A and B with an overall net mass loss.

- Debris-covered ice site characteristics:
    a. Net radiation was the dominant energy source,
    b. The snow that was on the debris-covered ice at the beginning of the measurement period was all ablated by melt (~78%) and sublimation (~22%),
    c. It is inferred that the debris at this site is sufficiently thick to protect the ice underlying the debris from significant ablation,
    d. During Type A conditions at the debris-covered ice site temperature is reduced,
    e. Surface energy and surface mass balance was not significantly affected by synoptic type.

Distributed surface characteristics

- A trend of ablation in the west and accumulation in the east was evident for both the 2003-2004 and 2004-2005 summers.
- A surface type distribution was determined and had the following characteristics:
    - Debris-covered ice 6%
    - Snow 55%
    - Bare ice 39%
- Albedo varied from 0.20 to 0.99 across the ice shelf surface.

Summertime surface mass balance patterns and climate characteristics

- During both summers, the surface mass balance pattern followed the basic trend seen in ablation stake studies.
- Several zones subject to enhanced ablation were identified. Some of these can be explained by a lowered albedo, while others are likely due to localised climatic controls.
- The extent of the modelled ablation area was slightly larger for the 2003-2004 summer than for 2004-2005.
- Amount of change in surface mass balance across the ice shelf was larger during the 2004-2005 summer compared with 2003-2004 this attributed to more type A conditions in that summer.

- Although more type B conditions occurred in 2003-2004 melting was not shown to be more dominant during this summer.

Methodological findings

- The debris-covered ice subsurface component developed here was very good at modeling surface and subsurface debris temperatures but needs further validation, particularly against ablation, before it can be used with confidence.
- The distributed energy balance model was adept at predicting the broad scale patterns of surface mass balance.
- Narrow to broadband conversion of ASTER data to determine albedo was found to perform well in a polar environment with a slight overestimation.

6.3 Implications

The following sections discuss the implications of this research with respect to the three key research themes introduced in chapter one.

6.3.1 Surface energy and surface mass balance

By providing detailed surface energy and surface mass balance of a bare ice and debris-covered ice surface this work has added to the limited number of surfaces investigated in polar environments. While the energy balance of the bare ice site has been shown to be similar to that of the blue ice areas, contrary to these, it has been shown that melting occurs in this environment, and that these areas should be treated differently in future modeling.

The importance of using a distributed surface mass balance model rather than traditional stake or single point studies has been highlighted. By using the distributed model the surface mass balance allows one to see where the ablation is occurring and by what form. The modelling process has helped identify anomalous areas of low albedo and high ablation that warrant further investigation.

For the 48 day period of measurements during the 2004-2005 summer, the bare ice site had a total ablation of -98 mm w.e., but using the distributed model has shown that this is not necessarily representative of the entire ice shelf ablation area. At other points across the ablation area, the relative importance of melting is reduced. The mean summertime ablation (melt and sublimation combined) across the entire ice shelf for the 2003-2004 and 2004-2005 summers were –9.5 mm w.e. and –38.0 mm w.e. respectively. This ablation almost balances the mean summertime precipitation giving a mean summertime surface mass balance across the entire ice shelf for the 2003-2004 and 2004-2005 summers of –2.5 mm w.e. and –6.7 mm w.e. respectively. These results suggest that summertime mass balance processes are not necessarily an important process in the overall mass balance of the ice shelf. Given that the area has an approximate mean annual precipitation of 184 mm w.e. (Monaghan *et al.,* 2006) it is suggested that both the precipitation and snow redistribution/blowing snow sublimation processes are important during winter. It is difficult to quantify other mass loss processes from these results as the McMurdo Ice Shelf may be maintaining equilibrium by winter sublimation, snowdrift sublimation, or basal melt.

The model adapted here has much potential for future use. The distributed model can be easily manipulated to use different distributed inputs and to be applied to different locations. However, before the model can be confidently applied to other seasons or in a predictive manner using regional climate model data, several model limitations must be addressed. Once these limitations are addressed, the model will be especially useful for other ice shelves, such along the Antarctic Peninsula, where there has been a rapid southward-progressing loss of ice shelves (Lemke *et al.*, 2007).

6.3.2 Ice-atmosphere linkages

This work has added to the limited knowledge on ice-atmospheric circulation linkages, especially in polar environments. A simple synoptic classification has identified three distinct situations that have been shown to have an impact on ice surface mass balance, and these synoptic situations can be applied to other analyses in this area.

Overall 2004-2005 was both warmer, and the net mean surface mass balance loss was increased, in comparison to the 2003-2004 summer. This study has shown that the surface mass balance change is complex and cannot be explained by the temperature difference alone. However, insights can be made by assessing the frequency of different synoptic types that occurred.

The existence of strong links between synoptic types and surface mass balance implies that models that predict atmospheric circulation rather than detailed analysis may be used for future mass balance modelling.

Predictions suggest that cyclonic systems in the Southern Hemisphere will intensify, and that the number of deep cyclones in the Ross Sea to Bellingshausen Sea sector will increase by 20 to 40% in summer and up to 63% in winter by the middle of the 21st century (Christensen *et al.*, 2007). This work has shown that surface mass balance is strongly related to the presence and positioning of cyclonic systems. Therefore, if the predictions hold true, this work implies that there will be an important effect on the mass balance of the McMurdo Ice Shelf. This effect is likely to be both an increase in precipitation and ablation but an overall increase in net surface mass loss.

Type B conditions were most frequent in the summer of 2003-2004 and although it was shown that the bare ice site had increased melting, this was not shown for other ablating areas on the ice shelf suggesting that the controls on this melt are also related strongly to surface conditions such as temperature and albedo.

6.3.3 Debris on ice

This research has developed a tool that can be used to determine the surface energy and surface mass balance of a debris-covered ice surface and should be applicable in other environments with some simple validation. The most important parameters to determine for this validation are the moisture content and thermal properties of the debris as well as ablation beneath the debris. Using this model tool, the thesis has presented one of the first surface energy and surface mass balance assessments for debris-covered ice in a polar environment.

For the debris-covered ice site, it was inferred that the debris sufficiently thick to protect the underlying ice. This finding, along with further work with the model may help aid paleoclimatic reconstructions.

6.4 Future research directions

This research has laid a foundation for future surface mass balance analyses of polar ice bodies and at a scale that incorporates synoptic effects. Further work that could be done to enhance the findings of this research should focus particularly on the following areas.

Because the study was limited to summertime, winter surface mass balance was not considered. Extending the modeling and validation period to include a full year would clearly provide more useful models for assessing surface mass balance. In conjunction with this extension, a further synoptic classification should be performed to identify any synoptic situations that occur in winter months. Once annual surface mass balance can be calculated, the model could be used in a predictive manner. This model could potentially be coupled with flow and subsurface mass balance models to assess the overall mass balance of the ice shelf.

This work was somewhat limited by the quality of the initial data. Although spin up time was allowed for, it is considered that if more suitable remote sensing imagery were available, the model performance would improve considerably. This issue may be overcome by extending the model run length as above, as the model could be initiated on the day that the best remote sensing imagery was available.

Further validation of the model would also help to make it more robust. In particular, inclusion of AWS measurements over a snow surface would be most beneficial. Ideally this AWS would include precipitation measurements, although, if the AWS was in place for a longer period, sonic ranger data could be more easily interpreted and precipitation data extracted. This research has also identified several areas of interest where more data should be obtained, ideally with an AWS as well as stakes, these areas are:

- North of Minna Bluff.
- Between Black and White Island.
- In the northeastern tip of the ice shelf.
- Near the Koettlitz Glacier.

The debris subsurface component also needs to be validated using moisture content and thermal properties of the debris as well as ablation beneath the debris. It would also be desirable to make such measurements in debris of varying depth.

In addition to better quality input and further validation the model used in this research is likely to be improved by inclusion of other processes. For example, an investigation into how incorporation of snowdrift sublimation into the energy balance component of the model effects performance would be desirable. It is also suggested that if this model had a snow transport model incorporated somehow, the performance may be improved. Further, once the debris subsurface component is fully validated, the model could be simply adapted to incorporate a debris thickness map.

6.5 Concluding comment

By providing an insight into the patterns of surface energy and surface mass balance of an ice shelf and their linkages with atmospheric processes, this research has improved the understanding of how the atmosphere interacts with polar surfaces. Several tools that will aid continued understanding of these interactions were produced, thus contributing towards more accurate predictions of mass balance in response to climate change.

Appendices

Appendix A: Significance testing on the temperatures at Scott Base.

In order to determine if the temperature during the summers of 2003-2005 and 2004-2005 was statistically distinct, a Welch t-test was applied for each month and for the four-month summer (Table A.1). The Welch test was used here as the variance of each data set cannot be assumed the same. The threshold of statistical significance for the t-test was set to 0.05.

Table A.1 Pairs of months showing significant differences in temperature recorded at Scott Base at 2100 (UTC) from 1964 – 2005. Bold pairs are significantly different.

Period	Level of significance	Dataset pairs
November	<0.05	**2003 & 2004**
	not significant	2003 & long-term, 2004 & long-term
December	<0.05	**2004 & long-term**
	not significant	2003 & 2004, 2003 & long-term
January	<0.05	**2004 &2005, 2004 & long-term**
	not significant	2005 & long-term
February	not significant	2004 & 2005, 2004 & long-term, 2005 – long-term
Summer	<0.05	**2003-2004 & 2004-2005, 2004-2005 & long-term**
	not significant	2003-2004 & long-term

Appendix B: Debris properties

Table B.1. Published properties of debris over ice used in determination of ablation of underlying ice.

Location	Lat/long	Elevation (m.a.s.l.)	k Thermal conductivity ($W\ m^{-1}\ K^{-1}$)	κ Thermal diffusivity ($mm^2\ s^{-1}$)	φ Porosity	Reference
Djankuat glacier, Central Caucasus	43°12'N 42°46'E	2700 -3900	2.8	-	0.43	Bozhinskiy *et al.,* 1986
Beacon valley, Dry Valleys, Antarctica	77 49 S, 160 38 E,	1200	-	-	0.1 – 0.2	Hindmarsh *et al*., 1998
Tasman Glacier, New Zealand	43 67 S 170 19 E	760 (terminus)	1.8	-	-	Purdie and Fitzharris, 1999
Base Camp, Khumbu Glacier, Nepal	28.00 N 86.83 E	5360	0.83	0.6 ± 0.1	0.3	Conway and Rasmussen, 2000
Lobuche, Khumbu Glacier, Nepal	28.00 N 86.83 E	4960	1.28	0.9 ± 0.1		
Larsbreen Svalbard, Norway (dry)	78º11' N, 15º33' E	200	0.585 ± 0.12	0.30 ± 0.05	0.2	Nicholson and Benn, 2006
Larsbreen (wet)			1.669 ± 0.35			
Ghiacciaio del Belvedere, Italian Alps (dry)	45º57' N, 4º34' E;	2000	0.637 ± 0.07	0.38 ± 0.02	0.3	
Ghiacciaio (wet)			1.776 ± 0.19			

Appendix C: Forcing the SOMARS model with reduced precipitation.

When validating the SOMARS model against the measured records at the bare ice site (Day 341, 2004 – Day 22, 2005) it was found that there was no clear record of precipitation at the bare ice during the Type A conditions. Type A conditions were prevalent during Day 3 – 8, 2005. At McMurdo Station 40 mm w.e. precipitation was recorded on Day 4, 2005. It is proposed that there was some precipitation at the bare ice site, but that it may less than the large amount recorded at McMurdo Station. In order to see how a change of this nature might affect the surface and mass balance components, an extra model run was made with half the amount of McMurdo Station precipitation for Day 4, 2004 (with all other conditions kept identical).

In the model run with half the precipitation net mass loss increased by 33%. Despite this, the turbulent fluxes and the ablation components were not altered significantly (Table E.1) with a maximum change of –11% for sensible heat flux. As there were no measurements of precipitation at the bare ice site, and there is and no scientific basis for altering the precipitation in this manner, it was decided to keep the precipitation the same as what was recorded at McMurdo Station.

Table C.1 SOMARS model run results for the bare ice site for the model run Day 341, 2004 – Day 22, 2005. Precipitation reduced run refers to reducing the value of precipitation on Day 4, 2005 from 40 to 20 mm w.e.

Variable	McMurdo Station precipitation run	Reduced precipitation run	Proportion change
Sensible heat flux (W m^{-2})	6	5	-11%
Latent heat flux (W m^{-2})	19	18	-5%
Precipitation (mm w.e.)	55	35	-36%
Melt (mm w.e.)	-69	-71	+3%
Sublimation (mm w.e.)	-29	-27	-7%
Total mass balance (mm w.e.)	-43	-64	+33%

Appendix D: Significance of surface energy and mass balance components at the bare ice site by synoptic type.

In order to determine if the surface energy and mass balance components observed at the bare ice site for each synoptic type defined was statistically distinct, a Welch t-test was applied between each climate variable for each synoptic type (Table D.1). The Welch test was used here as the variance of each data set cannot be assumed the same. The threshold of statistical significance for the t-test was set to 0.05.

Table D.1 Pairs of synoptic types showing significant differences in surface energy and mass balance components for the bare ice site. Bold pairs are significantly different.

Variable	Level of significance	Synoptic type pairs
Sensible heat flux	<0.05	**A & B, A & C, B & C**
	not significant	
Latent heat flux	<0.05	**A & B, A & C**
	not significant	B & C
Subsurface heat flux	<0.05	**A & B, B & C**
	not significant	A & C
Net radiation	< 0.05	**A & B, B & C**
	not significant	A & C
Melt	not significant	A & B, A & C, B & C
Sublimation	<0.05	**A & B, A & C**
	not significant	B & C

Appendix E: Significance of surface energy and mass balance components at the debris-covered ice site by synoptic type.

In order to determine if the surface energy and mass balance components observed at the debris-covered ice site for each synoptic type defined was statistically distinct, a Welch t-test was applied between each climate variable for each synoptic type (Table E.1). The Welch test was used here as the variance of each data set cannot be assumed the same. The threshold of statistical significance for the t-test was set to 0.05.

Table E.1 Pairs of synoptic types showing significant differences in surface energy and mass balance components for the debris-covered ice site. Bold pairs are significantly different.

Variable	Level of significance	Synoptic type pairs
Sensible heat flux	<0.05	**A & B, A & C**
	not significant	B & C
Latent heat flux	<0.05	**A & B**
	not significant	B & C, A & C
Subsurface heat flux	not significant	**A & B, A & C, B & C**
Net radiation	< 0.05	**A & B**
	not significant	A & C, B & C
Melt	not significant	A & B, A & C, B & C
Sublimation	<0.05	**A & B**
	not significant	B & C, A & C

References

Abrams, M. and Hook, S., 2001. *ASTER User Handbook*. The Jet Propulsion Laboratory, California Institute of Technology, Los Angeles.

Alaska Satellite Facility (ASF), 2003. Radarsat-1 Scansar Geocoded (Polar Stereographic) Image (Full Resolution). Product: R141102673P3S005. Pixel size: 50m. 19th September 2003.

Alt, B.T., 1987. Developing synoptic analogs for extreme mass balance conditions on Queen Elizabeth Island Ice Caps. *Journal of Climate and Applied Meteorology,* vol. 26(12), 1605-1623.

Anderson, P.S., 1994. A method for rescaling humidity sensors at temperatures well below freezing. *Journal of Atmospheric and Oceanic Technology*, vol.11, 1388-1391.

Anderson, P.S., 1996. Reply to "Comments on 'A method for rescaling humidity sensors at well below freezing'". *Journal of Atmospheric and Oceanic Technology*, vol.13, 913-914.

Andreas E.L., 1987. A theory for the scalar roughness and the scalar transfer coefficients over snow and sea ice. *Boundary-Layer Meteorology*, vol.38, 159-184.

Andreas, E. L. 2002. Parameterizing Scalar Transfer over Snow and Ice: A Review. *Journal of Hydrometeorology*, vol. 3 (4), 417-432.

Andreassen, L.M., van den Broeke, M.R., Giesen, R.H., Oerlemans, J., 2008. A 5 year record of surface energy and mass balance from the ablation zone of Storbreen, Norway. *Journal of Glaciology*, vol. 54(185), 245-258.

Arendt, A., 1999. Approaches to modelling the surface albedo of a high arctic glacier. *Geografiska Annaler* vol.81(A), 477-487.

Arigony-Neto, J., Saurer, H., Jana, R., and Rau, F., 2006. Monitoring snow parameters on the Antarctic Peninsula using satellite data: a new methodological approach. *EARSeL eProceedings,* vol.5(1), 100-110.

Arnold, N.S., Rees, W.G., Hodson, A.J. and Kohler, J., 2006. Topographic controls on the energy balance of a high Arctic glacier. *Journal of Geophysical Research*, vol.111 F02011, doi:10.1029/2005JF000426.

Arnold, N.S., Willis, I.C., Sharp, M.J., Richards, K.S., Lawson, W.J., 1996. A distributed surface energy-balance model for a small valley glacier. I. Development and testing for Haut Glacier d'Arolla, Valais, Switzerland. *Journal of Glaciology*, vol.42(140), 77-89.

Barry, R.G. and Carleton, A.M., 2001. *Synoptic and Dynamic Climatology*. Routledge, New York, 620p.

Beljaars, A.C.M., and A.A.M., Holtslag, 1991. Flux parameterization over land surfaces for atmospheric models. *Journal of Applied Meteorology*, vol.30, 327-341.

Bintanja, R. and Reijmer, C.H., 2001. A simple parameterization for snowdrift sublimation over Antarctic snow surfaces. *Journal of Geophysical Research,* vol.106, 31,739-31,748.

Bintanja, R. and Van den Broeke, M.R., 1995. The surface energy balance of Antarctic snow and Blue Ice. *Journal of Applied Meteorology,* vol.34, 902-926.

Bintanja, R., 1995. The local surface energy balance of the Ecology Glacier, King George Island, Antarctica. *Journal of Glaciology*, vol.33(115), 1-6.

Bintanja, R., 1999. On the glaciological, meteorological, and climatological significance of Antarctic blue ice areas. *Reviews of Geophysics*, vol.37(3), 337-59.

Bintanja, R., 2000. Surface heat budget of Antarctic snow and blue ice: Interpretation of spatial and temporal variability. *Journal of Geophysical Research,* vol.105(D19), 24387-24407.

Bintanja, R., 2004. The mass balance of a dry snow surface during a snowstorm. *Annals of Glaciology*, vol.38, 79-83.

Bintanja, R., and Reijmer, C., 2001. Meteorological conditions over Antarctic blue-ice areas and their influence on the local surface mass balance. *Journal of Glaciology,* vol.47(156), 37-50.

Bintanja, R., Jonsson, S. and Knap, W.H., 1997. The annual cycle of the surface energy balance of Antarctic blue ice. *Journal of Geophysical Research,* vol.102(D2), 1867-1881.

Bintanja, R., Reijmer, C. H., and Hulscher S.J.M.H., 2001. Detailed observations of the rippled surface of Antarctic blue ice areas. *Journal of Glaciology,* vol.47(158), 387-396.

Bishop, M.P., Shroder, J.F., and Ward, J.L., 1995. SPOT Multispectral analysis for producing supraglacial debris-load estimates for Batura Glacier, Pakistan. *Geocarto International,* vol.10(4), 81-90.

Bishop, M.P., Shroder, J.F., Hickman, B.L., and Copland, L., 1998. Scale-dependent analysis of satellite imagery for characterization of glacier surfaces in the Karakoram Himalaya. *Geomorphology,* vol.21, 217-232.

Boresjö Bronge, L. and Bronge, C., 1999. Ice and snow-type classification in the Vestfold Hills, East Antarctica, using Landsat-TM data and ground radiometer measurements. *International Journal of Remote Sensing,* vol.20(2), 225-240.

Bougamont, M. and Bamber, J.L., and Greuell, W., 2005. A surface mass balance model for the Greenland Ice Sheet. Journal of Geophysical Research, vol.110(F4), F04018, doi:10.1029/2005JF000348.

Box, J.E., 2001. *Surface water vapour exchanges on the Greenland ice sheet derived from automated weather station data*. A thesis submitted to the faculty of the graduate school of the University of Colorado in partial fulfilment of the requirements for the degree of Doctor of Philosophy, Department of Geography, University of Colorado, 160p.

Box, J.E., and Steffen, K., 2001. Sublimation on the Greenland Ice Sheet from automated weather station observations. *Journal of Geophysical Research D: Atmospheres,* vol.106(24), 33965-33981.

Box, J.E., D. H. Bromwich, L-S Bai., 2004. Greenland ice sheet surface mass balance for 1991-2000: application of Polar MM5 mesoscale model and in-situ data, *Journal of*

Geophysical Research D: Atmospheres, vol.109(D16), D16105, 10.1029/2003JD004451.

Bozhinsky, A.N., Krass, M.S, and Popovnin, V.V., 1986. Role of debris cover in the thermal physics of glaciers, *Journal of Glaciology,* vol.32(11), 255-266.

Braithwaite, R. J., 1995. Aerodynamic stability and turbulent sensible-heat flux over a melting ice surface, the Greenland ice-sheet. *Journal of Glaciology,* vol.41(139), 562-571.

Braithwaite, R.J., 2002. Glacier mass balance: the first 50 years of international monitoring. *Progress in Physical Geography,* vol.26(1), 76-95.

Braithwaite, R.J., and Olesen, O.B. 1989. Calculation of glacier ablation from air temperature, West Greenland, *in* Oerlemans, J.(ed.), *Glacier fluctuations and climatic change*. Dordrecht, Kluwer Academic Publishers, 219-233.

Brandt, R.E. and Warren, S.G., 1993. Solar-heating rates and temperature profiles in Antarctic snow and ice. *Journal of Glaciology,* vol.39(131), 99-110.

Braun, M., and Hock, R., 2004. Spatially distributed surface energy balance and ablation modelling on the ice cap of King George Island (Antarctica). *Global and Planetary Change,* vol.42, 45-58.

Braun, M., Rau, F., Saurer, H., and Gobmann, H., 2000. Development of radar glacier zones on the King George Island Ice Cap, Antarctica, during austral summer 1996/97 as observed in ERS-2 SAR data. *Annals of Glaciology*, vol.31, 357-363.

Braun, M., Saurer, H., Vogt, S., Simões J.C and Gobmann, H., 2001. The influence of large-scale atmospheric circulation on the surface energy balance of the King George Island Ice Cap. *International Journal of Climatology*, vol.21, 21-36.

Brock, B. W. and Arnold, N.S., 2000. Technical communication: a spreadsheet-based (Microsoft Excel) point surface energy balance model for glacier and snow melt studies. *Earth Surface Processes and Landforms*, vol.25, 649-658.

Brock, B.W., Willis, I.C., Sharp, M.J., 2000a. Measurement and parameterization of albedo variations at Haut Glacier d'Arolla, Switzerland. *Journal of Glaciology*, vol.46(155), 675-688.

Brock, B.W., Willis, I.C., Sharp, M.J., Arnold, N.S., 2000b. Modelling seasonal and spatial variations in the surface energy balance of Haut Glacier d'Arolla, Switzerland. *Annals of Glaciology,* vol.31, 53-62.

Brock, B.W., Willis, I.C., Sharp, M.J., 2006. Measurement and parameterization of aerodynamic roughness length variations at Haut Glacier d'Arolla, Switzerland. *Journal of Glaciology*, vol.52(177), 281-297.

Bromley, A.M., 1994. The climate of Scott Base. *Natianal Institute of Water and Atmospheric Research NIWA,* Wellington, 19p.

Bromwich, D. H., 1988. Snowfall in high southern latitudes. *Review of Geophysics.*, vol.26, 149-168.

Bromwich, D.H., 1989. Subsynoptic-scale cyclone developments in the Ross Sea Sector of the Antarctic *in* Twitchell, P.F., Rasmussen, E.A., and Davidson, K.L.(*eds*.), 1989 *Polar and Arctic Lows,* Deepak Publishing, Hampton.

Bromwich, D.H., 1998. Antarctic Meteorology and Climatology. *Bulletin of the American Meteorological Society*, vol.79(5), 881-882.

Bromwich, D.H., Carrasco, J.F., and Stearns, C.R., 1992. Satellite observations of katabatic-wind propagation for great distances across the Ross Ice Shelf. *Monthly Weather Review,* vol.120(9), 1940-1949.

Bromwich, D.H., Monaghan, A.J., and Guo, Z., 2004. Modeling the ENSO Modulation of Antarctic Climate in the Late 1990s with the Polar MM5. *Journal of Climate*, vol.17(1), 109-129.

Bromwich, D.H., Monaghan, A.J., Manning, K.W., and Powers, J.G., 2005. Real-time forecasting for the Antarctic: An evaluation of the Antarctic Mesoscale Prediction System (AMPS). *Monthly Weather Review*, vol.133, 579-603.

Brown, I.A., Kirkbride, M.P., and Vaughan, R.A., 1999. Find the firn line! The suitability of ERS-1 and ERS-2 SAR data for the analysis of glacier facies on Icelandic icecaps. *International Journal of Remote Sensing,* vol.20(15&16), 3217-3230.

Brown, I.C. and Scambos, T.A., 2004. Satellite monitoring of blue-ice extent near Byrd Glacier, Antarctica. *Annals of Glaciology,* vol.39, 223-230.

Businger, J. A., Wyngaard, J. C., Izumi, Y., and Bradley, E. F., 1971. Flux-profile relationships in the atmospheric surface layer. *Journal of the Atmospheric Sciences,* vol.28(2), 181-189.

Calanca, P., 2001. A note on the roughness length for temperature over melting snow and ice. *Quarterly Journal of the Royal Meteorological Society,* vol.127, 255-260.

Cameron, R.E., and Conrow, H.P., 1969. Soil moisture, relative humidity, and microbial abundance in Dry Valleys of Southern Victoria Land. *Antarctic Journal of the United States,* vol.4, 23-28.

Campbell Scientific Inc., 2003a. *CNR1 net radiometer instruction manual, revision 1/03*. Campbell Scientific Inc., Logan, Utah.

Campbell Scientific Inc., 2003b. *SR50 Sonic ranging sensor operators manual, revision 3/03*. Campbell Scientific Inc., Logan, Utah.

Campbell, D.I., MacCulloch, R.J.L., and Campbell, I.B., 1997. Thermal regimes of some soils in the McMurdo Sound region, Antarctica, *in* Lyons, Howard-Williams and Hawes (eds), *Ecosystem Processes in Antarctic Ice-free Landscapes.* Balkema, Rotterdam.

Campbell, I.B., Claridge, G.C., Campbell, D.I., and Balks, M.R., 1998. The soil environment of the McMurdo Dry Valleys, Antarctica. *in* Priscu, J.C.C., (ed), Ecosystem dynamics in a polar desert: the McMurdo Dry Valleys. *Antarctic Research Series*, vol.72.

Carrasco, J.F., and Bromwich, D.H., 1992. Case studies of katabatic wind forced mesoscale cyclogenesis over the southwestern Ross Sea. *Preprint Volume, Third Conference on Polar Meteorology and Oceanography,*

Portland, Oregon, American Meteorological Society, Boston, Massachussetts, J129-J132.

Carrasco, J.F., Bromwich, D.H., and Monaghan, A.J., 2003. Distribution and characteristics of mesoscale cyclones in the Antarctic: Ross Sea eastward to the Weddell Sea. *Monthly Weather Review,* vol.131(2), 289-301.

Cavazos, T., and Hewitson, B., 2002. Relative performance of empirical predictors of daily precipitation. *Intergrated Assessment and Decision Support*, vol.2, 349-354.

Chinn, T.J., 1999. New Zealand glacier response to climate change of the past two decades. *Global and Planetary Change*, vol.22. 155-168.

Christensen, J.H., Hewitson, B. Busuioc, A., Chen, A., Gao, X., Held, I., Jones, R., Kolli, R.K., Kwon, W.-T., Laprise, R., Magaña Rueda, V., Mearns, L., Menéndez, C.G., Räisänen, J., Rinke, A., Sarr A., and Whetton, P., 2007. Regional Climate Projections. *in* Solomon, S., Qin, D., Manning, M., Chen, Z., Marquis, M., Averyt, K.B., Tignor M., and Miller H.L. (eds.), *Climate Change 2007: The Physical Science Basis. Contribution of Working Group I to the Fourth Assessment Report of the Intergovernmental Panel on Climate Chang*e. Cambridge University Press, Cambridge, United Kingdom and New York, NY, USA.

Chrysoulakis, N., 2003. Estimation of the all-wave uban surface radiation balance by use of ASTER multispectral imagery and in situ spatial data. *Journal of Geophysical Research,* vol.108(D18), 4582-4593.

Clauser, C., and Huegnes, E., 1995. Thermal conductivity of rocks and minerals. *in* Ahrens, T.J., (ed), Rock physics and phase relations: A handbook of physical constants: American Geophysical Union Reference Shelf, no.3, 105-126.

Coléou, C., and Lesaffre, B., 1998. Irreducible water saturation in snow: experimental results in a cold laboratory. *Annals of Glaciology*, vol.26, 64-68.

Conway, H., and Rasmussen, L.A., 2000. Summer temperature profiles within supraglacial debris on Khumbu Glacier, Nepal. *in* Nakawo, M., Raymond, C.F., and Fountain, A., (eds.). *Debris-covered glaciers*. IAHS Publication no.264. Wallingford, IAHS Press, 89-97.

Cracknell, A.P., 1998. Synergy in remote sensing – what's in a pixel? *International Journal of Remote Sensing,* vol.19(11), 2025-2047.

Cullen, N.J., Molg, T., Kaser, G., Steffen, K. and Hardy, D.R., 2007a. Energy-balance model validation on the top of Kilimanjaro, Tanzania, using eddy covariance data. *Annals of Glaciology*, vol.46, 227-233.

Cullen, N.J., Steffen, K., Blanken, P.D., 2007b. Nonstationarity of turbulent heat fluxes at Summit, Greenland. *Boundary-Layer Meteorology,* vol.122, 439-455.

Culter, P., and Munro, D.S., 1996. Visible and near infrared reflectivity during the ablation period on Peyto Glacier, Alberta, Canada. *Journal of Glaciology*, vol.42, 333-340.

Daly, C., 2006. Guidelines for assessing the suitability of spatial climate data sets. vol.26(6), 707-721.

Das, S.B., and Alley, R.B., 2005. Characterization and formation of melt layers in polar snow: observations and experiments from West Antarctica. *Journal of Glaciology,* vol. 51(173), 307-312.

de Mora, S. J., Lee, P.A., Gout, A., Schall, C. and Heumann, K.G., 1996. Aspects of the biogeochemistry of sulphur in glacial meltwater ponds on the McMurdo Ice Shelf, Antarctica. *Antarctic Science,* vol.8(1), 15-22.

de Mora, S. J., Whitehead, R.F., and Gregory, M., 1994. The chemical composition of glacial melt water ponds and streams on the McMurdo Ice Shelf, Antarctica. *Antarctic Science,* vol.6(1), 17-27.

De Ridder, K., and Mensink, C., 2003. Surface fluxes and atmospheric stability obtained from a surface energy balance model with parameters estimated from satellite remote sensing. *International Journal of Environment and Pollution,* vol.19(1), 22-32.

De Ruyter de Wildt, M.S., and Oerlemans, J., 2003. Satellite retrieval of mass balance: comparing SAR images with albedo images and in situ mass-balance observations. *Journal of Glaciology,* vol.49(166), 437-448.

De Ruyter de Wildt, M.S., Oerlemans, J., and Bjornsson, H., 2002. A method for monitoring glacier mass balance using satellite albedo measurements: application to Vatnajökull, Iceland. *Journal of Glaciology,* vol.48(161), 267-278.

Debenham, F., 1965. The genesis of the McMurdo Ice Shelf, Antarctica. *Journal of Glaciology,* vol.5(42), 829-832.

Denby, B., and Greuell, W., 2000. The use of bulk and profile methods for determining the surface heat fluxes in the presence of glacier winds. *Journal of Glaciology,* vol.46, 445–452.

Denby, B., and Smeets, C.J.P.P., 2000. Derivation of turbulent flux profiles and roughness lengths from Katabatic flow dynamics. *Journal of applied meteorology,* vol.39, 1601-1612.

Dery, S.J., and Yau, M.K., 2002. Large-scale mass balance effects of blowing snow and surface sublimation. *Journal of geophysical research,* vol.107(D23), D4679, doi:10.1029/2001JD001251.

Diak, G.R., Mecikalski, J.R., Anderson, M.C., Norman, J.M., Kustas, W.P., Torn, R.D., and DeWolf, R.L., 2004. Estimating Land Surface Energy Budgets From Space: Review and Current Efforts at the University of Wisconsin—Madison and USDA–ARS. *Bulletin of the American Meteorological Society*, vol.85, 65-78.

Dyer, A.J., 1974. A review of flux-profile relationships. *Boundary layer meteorology,* vol.99, 1-9.

Erath, S. 2005. Simulation of the mass and energy balance at Kongsvegen 2001-2003, *Unpublished Masters Thesis,* Department of Meteorology and Geophysics University Innsbruck.

Fahnestock, M.A., Abdalati, W., and Shuman, C.A., 2002. Long melt seasons on ice shelves of the Antarctic Peninsula: an analysis using satellite-based microwave emission measurements. *Annals of Glaciology,* vol.34, 127-133.

Farouki, O.T., 1981. *Thermal properties of soils*. CCRL Monograph 81-1, U.S. Army cold regions research and engineering Laboratory, Hanover.

Fetterer, F., and Untersteiner, N., 1998. Observations of melt ponds on Arctic sea ice. *Journal of Geophysical Research,* vol.103(C11), 24821-24835.

Finnigan, J.J., 2004. A re-evaluation of long-term flux measurement techniques Part II: Coordinate systems. *Boundary-Layer Meteorology,* vol.113, 1-41.

Finnigan, J.J., Clement, R., Malhi, Y., Leuning, R., and Cleugh, A., 2003. A re-evaluation of long-term flux measurement techniques Part I: Averaging and coordinate rotation. *Boundary-Layer Meteorology,* vol.107, 1-48.

Fitzharris, B.B., and Bakkehøi, S., 1986. A synoptic climatology of major avalanche winters in Norway. *Journal of Climatology,* vol.6, 431–446.

Fogt, R.L., 2005. *Trip report: McMurdo, Antarctica, 18 – 31 January 2005*. Byrd Polar Research Center, Columbus, 21p.

Fountain, A.G., Lewis, K.J., and Doran, P.T., 1999. Spatial climatic variation and its control on glacier equilibrium line altitude in Taylor Valley, Antarctica. *Global and Planetary Change,* vol.22(1-4), 1-10.

Frezzotti, M., Gandofi, S., La Marca, F., and Urbini, S., 2002. Snow dunes and glazed surfaces in Antarctica: new field and remote-sensing data. *Annals of Glaciology,* vol.34, 81-88.

Gao, J., and Liu, J., 2001. Applications of remote sensing, GIS and GPS in glaciology: a review. *Progress in Physical Geography,* vol.25(4), 520-540.

Glasser, N., Goodsell, B., Copland, L., and Lawson, W., 2006. Debris characteristics and ice-shelf dynamics in the ablation region of the McMurdo Ice Shelf, Antarctica. *Journal of Glaciology,* vol.52(177), 223-234.

Goring, D., and Pyne, A., 2003. Observations of sea-level variability in Ross Sea, Antarctica. *New Zealand Journal of Marine and Freshwater Research,* vol.37, 241-249.

Gow, A.J., Weeks, W.F., Hendrickson, G., and Rowland, R., 1965. New light on the mode of uplift of the fish and fossiliferous moraines of the McMurdo Ice Shelf, Antarctica. *Journal of Glaciology*, vol.5(42), 813-828.

Greuell, W., and Böhm, R., 1997. 2 m temperatures along melting mid-latitude glaciers, and implications for the sensitivity of the mass balance to variations in temperature. *Journal of Glaciology,* vol.44(146), 9-20.

Greuell, W., and Genthon, C., 2003. Modelling land-ice surface *in* Bamber, J.L. and Payne, A.J. (eds), *Mass balance in Mass balance of the cryosphere : observations and modelling of contemporary and future changes.* Cambridge University Press. 644pp.

Greuell, W., and Knap, W.H., 2000. Remote sensing of the albedo and detection of the slush line on the Greenland Ice Sheet. *Journal of Geophysical Research,* vol.105(D12), 15567-15576.

Greuell, W., and Konzelmann, T., 1994. Numerical modelling of the energy balance and the englacial temperature of the Greenland Ice Sheet. Calculation for the ETH-Camp location (West Greenland, 1155 m a.s.l.). *Global and Planetary Change*, vol.9, 91-114.

Greuell, W., and Oerlemans, J., 1986. Sensitivity studies with a mass balance model including temperature profile calculations inside the glacier. *Z. Gletscherkd. Glazialgeol.*, vol. 22(2), 101-124,

Greuell, W., and Smeets, P., 2001. Variations with elevation in the surface energy balance on the Pasterze (Austria). *Journal of Geophysical Research,* vol.106(D23), 31717-31727.

Hall, D.K., Bindschadler, R.A., Foster, J.L., Chang, A.T.C., and Siddalingaiah, H., 1990. Comparison of in situ and satellite derived reflectances of Forbindels Glacier, Greenland. *International Journal of Remote Sensing*, vol.11, 493-504.

Hall, D.K., Kelly, R.E.J., Riggs, G.A., Chang, A.T.C, and Foster, J.L., 2002. Assessment of the relative accuracy of hemispheric-scale snow-cover maps, Annals of Glaciology, vol.34, 24-30.

Hannah, D.M., Gurnell A.M., and McGregor, G.R., 2000. Spatio-temporal variation in microclimate,the energy balance and ablation over a cirque glacier. *International Journal of Climatology*, vol.20(7), 733-758.

Hawes, I., Smith, R., Howard-Wiliams, C. and Schwarz, A-M., 1999. Environmental conditions during freezing, and response of microbial mats in ponds of the McMurdo Ice Shelf, Antarctica. *Antarctic Science*, vol.11(2), 198-208.

Hawes, I., Smith, R., Howard-Williams, C., and Schwarz, A., 1999. Environmental conditions during freezing, and response of microbial mats in ponds of the McMurdo Ice Shelf, Antarctica. *Antarctic Science*, vol.11(2), 198-208.

Hay, J. E. and Fitzharris, B.B., 1988. A comparison of the energy-balance and bulk-aerodynamic approaches for estimating glacier melt. *Journal of Glaciology*, vol.34(117), 145-153.

Heinemann, G., and Klein, T., 2003. Simulations of topographically forced mesocyclones in the WeddelllSea and the Ross Sea region of Antarctica. *Monthly Weather Review,* vol.131(2), 302-317.

Henneken, E.A.C., Bink, N.J., Vugts, H.F., Cannemeijer, F., and Meesters, A.G.C.A., 1994. A case study of the daily energy balance near the equilibrium line on the Greenland Ice Sheet. *Global and Planetary Change,* vol.9, 69-78.

Herron, M.M., Langway Jr, C.C., 1980, Firn densification: an empirical model. *Journal of Glaciology*, vol.25(93), 373-385.

Herzfeld, U.C., 1999. Geostatistical interpolation and classification of remote sensing data from ice surfaces. *International Journal of Remote Sensing,* vol.20(2), 307-327.

Hindmarsh, R.C.A., and Jenkins, A., 2001. Centurial-millenial ice-rafted debris pulses from ablating marine ice sheets. *Geophysical Research Letters*, vol. 28(12), 2477-2480.

Hindmarsh, R.C.A., van der Wateren, F.M., and Verbers, A.L.L.M., 1998. Sublimation of ice through sediment in Beacon Valley, Antarctica, *Geografiska Annaler, Series A: Physical Geography*, vol.80(3-4), 209-219.

Hock, R., 2003. Temperature index melt modelling in mountain regions. *Journal of Hydrology*, vol.282(1-4), 104-115.

Hock, R., 2005. Glacier melt: a review of processes and their modelling. *Progress in Physical Geography,* vol.29(3), 362-391.

Hock, R., and Holmgren, B., 2005. A distributed surface energy-balance model for complex topography and its application to Storglaciären, Sweden. *Journal of Glaciology*, vol.51(172), 25-36.

Högström, U., 1988. Non-dimensional wind and temperature profiles in the atmospheric surface layer: a re-evaluation. *Boundary Layer Meteorology*, vol.42, 55-78.

Horst, T.W., 1997. A simple formula for attenuation of eddy fluxes measured with first-order response scalar sensors. *Boundary-Layer Meteorology,* vol.82, 219-233.

Horst, T.W., 2000. On frequency response corrections for eddy covariance flux measurements, *Boundary-Layer Meteorology,* vol.94, 517–520.

Humlum, O., 1998. The climatic significance of rock glaciers. *Permafrost and Periglacial Processes,* vol.9(4), 375-395.

Inoue, J., and Yoshida, M., 1980. Ablation and heat exchange over the Khumbu Glacier. *Seppyo*, vol.41, Special Issue, 26-33.

Ishikawa, N., and Kobayashi, S., 1985. On the internal melting phenomenon (puddle formation) in fast sea ice, East Antarctica. *Annals of Glaciology*, vol. 6, 138-141.

Kaab, A., 2002. Monitoring high-mountain terrain deformation from repeated air- and spaceborne optical data: examples using digital aerial imagery and ASTER data. *ISPRS Journal of Photogrammetry and Remote Sensing*, vol.57, 39-52.

Kaimal, J.C., and Finnigan, J.J., 1994. *Atmospheric boundary layer flows*. Oxford University Press, New York.

Kargel, J.S., Abrams, M.J., Bishop, M.P., Bush, A., Hamilton, G., Jiskoot, H., Kääb, A., Kieffer, H.H., Lee, E.M., Paul, F., Rau, F., Raup, B., Shroder, J.F., Soltesz, D., Stainforth, D., Stearns, L., and Wessels, R., 2005. Multispectral imaging contributions to global land ice measurements from space. *Remote Sensing of Environment,* vol.99, 187-219.

Kayastha, R.B., Takeuchi, Y., Nakawo, M., and Ageta, Y., 2000. Practical prediction of ice melting beneath various thickness of debris cover on Khumbu Glacier, Nepal, using a positive degree-day factor. *in* Nakawo, M., Raymond, C.F., and Fountain, A.,

(eds.). *Debris-covered glaciers*. IAHS Publication no.264. Wallingford, IAHS Press, 71-81.

Kellogg, D. E., and Kellogg, T. B. 1987. Reworking of biotic and sedimentary debris on the McMurdo Ice Shelf. *Antarctic Journal,* vol.10, 118-119.

Khalsa, S.J.S., Dyrurgerov, M.B., Khromova, T., Raup, B.H., and Barry, R.G., 2004. Space-Based Mapping of Glacier Changes Using ASTER and GIS Tools. *IEEE Transactions on Geoscience and Remote Sensing,* vol.42(10), 2177-2182.

King, J. C., and Anderson, P.S., 1994. Heat and water vapour fluxes and scalar roughness lengths over an Antarctic ice shelf. *Boundary-Layer Meteorology,* vol.69, 101-121.

King, J. C., Argentini, S. A., and Anderson, P. S., 2006. Contrasts between the summertime surface energy balance and boundary layer structure at Dome C and Halley stations, Antarctica. *Journal of Geophysical Research* vol.111, D02105, doi:10.1029/2005JD006130.

King, J. C., Jrrar, A. and Connolley, W. M., 2007. Sensitivity of modelled atmospheric circulation to the representation of stable boundary layer processes. *Geophysical Research Letters*, vol.34, L06708, doi:10.1029/2006GL028563.

King, J.C. and Turner, J., 1997. *Antarctic Meteorology and Climatology.* Cambridge University Press, Cambridge.

King, J.C., 1996. Longwave atmospheric radiation over Antarctica. *Antarctic Science,* vol.8(1), 105-109.

King, J.C., Anderson, P.S., Smith, M.C., and Mobbs, S.D., 1996. The surface energy and mass balance at Halley, Antartica during winter. *Journal of Geophysical Research*, vol.101(D14), 19119-19128.

Kirnbauer, R., Blöschl,. G., and Gutknecht, D., 1994. Entering the era of distributed snow models. *Nordic Hydrology*, vol.25, 1-24.

Klein, A.G., and Isacks, B.L., 1999. Spectral mixture analysis of Landsat thematic mapper images applied to the detection of the transient snowline on tropical Andean glaciers. *Global and Planetary Change*, vol. 22(1-4), 139-154.

Klok, E.J., and Oerlemans, J., 2002. Model study of the spatial distribution of the energy and mass balance of Morteratschgletscher, Switzerland. *Journal of Glaciology,* vol.48(163), 505-518.

Klok, E.J., Nolan, M., and van den Broeke, M.R., 2005. Analysis of meteorological data and the surface energy balance of McCall Glacier, Alaska. *Journal of Glaciology,* vol.51(174), 451-461.

Knap, W. H., and Reijmer, C. H., 1998. Anisotropy of the reflected radiation field over melting glacier ice: measurements in Landsat-TM bands 2 and 4. *Remote Sensing of Environment*, vol.65, 93-104.

Knap, W. H., Brock, B. W., Oerlemans, J, and Willis, I. C., 1999. Comparison of Landsat-TM derived and ground-based albedo of Haut Glacier d'Arolla. *International Journal of Remote Sensing*, vol.20(17), 3293-3310.

Knap, W.H., Reijmer, C.H., and Oerlemans, J., 1999. Narrowband to broadband conversion of Landsat-TM glacier albedos. *International Journal of Remote Sensing*, vol.20(10), 2091-2110.

Konig, M., Winther, J. and Isaksson, E., 2001. Measuring snow and glacier ice properties from satellite. *Reviews of Geophysiscs,* vol.39(1), 1-27.

Konya, K., Matsumoto, T., and Naruse, R., 2004. Surface Heat Balance and Spatially Distributed Ablation Modelling at Koryto Glacier, Kamchatka Peninsula, Russia. *Geografiska Annaler: Series A, Physical Geography*, vol.86(4), 337-348.

Konzelmann, T., and Braithwaite, R.J., 1995. Variations of ablation, albedo and energy balance at the margin of the Greenland ice sheet, Kronprins Christian Land, eastern North Greenland. *Journal of Glaciology,* vol.41(137), 174-182.

Konzelmann, T., van de Wal, R.S.W., Greuell, W., Bintanja, R., Henneken, H., and Abe-Ouchi, A., 1994. Radiation measurements and a parameterization of radiation for the Greenland Ice Sheet. *Global and Planetary Change*, vol.9, 143-164.

Krause, P., Boyle, D.P., and Base, F., 2005. Comparison of different efficiency criteria for hydrological model assessment. *Advances in Geosciences,* vol.5, 89-97.

Lawson, W.J., Copland, L., and Goodsell, B., *Submitted*. A century of change at the McMurdo Ice Shelf, Antarctica. *Global and Planetary Change*.

Lazzara, M.A., 2006. A McMurdo Station Climatology. UW SSEC Publication no.06.06.L1. Space Science and Engineering Center, University of Wisconsin-Madison, 10p. [Available http://amrc.ssec.wisc.edu/McMurdo-Climatology.pdf]

Leathers, D.J., Graybeal, D., Mote, T.L., Grundstein, A.J., and Robinson, D.A, 2004. The role of air mass types and surface energy fluxes in snow cover ablation in the central Appalachians. *Journal of Applied Meteorology*, vol.43, 1887-1898.

Lefebre, F., Gallee, H., van Ypersele, J.-P., and Huybrechts, P., 2002. Modelling of large-scale melt parameters with a regional climate model in South-Greenland during the 1991 melt season. *Annals of Glaciology*, vol.35, 391-397.

Lemke, P., Ren, J., Alley, R.B., Allison, I., Carrasco, J., Flato, G., Fujii, Y., Kaser, G., Mote, P., Thomas, R.H., and Zhang, T., 2007. Observations: Changes in Snow, Ice and Frozen Ground. *in* Solomon, S., Qin, D., Manning, M., Chen, Z., Marquis, M., Averyt, K.B., Tignor M., and Miller H.L. (eds.), *Climate Change 2007: The Physical Science Basis. Contribution of Working Group I to the Fourth Assessment Report of the Intergovernmental Panel on Climate Chang*e. Cambridge University Press, Cambridge, United Kingdom and New York, NY, USA.

Lettau, H., 1969. Note on aerodynamic roughness-parameter estimation on the basis of roughness-element description. *Applied Meteorology*, vol. 8, 828-832

Lewis, K. J., Fountain, A.G., and Dana, G.L., 1998. Surface energy balance and meltwater production for a Dry Valley Glacier, Taylor Valley, Antarctica. *Annals of Glaciology*, vol.27, 603-609.

Liang, S., 2001. Narrowband to broadband conversions of land surface albedo I: Algorithms. *Remote Sensing of Environment*, vol.76(2), 213-238.

Liang, S., Shuey, C.J., Russ, A.J., Fang, H., Chen, M., Walthall, C.L., Daughtry, C.S.T. and Hunt, R., 2003. Narrowband to broadband conversions of land surface albedo: II. Validation. *Remote Sensing of Environment*, vol.84(1), 25-41.

Lillesand, T.M., and Keiffer, R.W., 1994. *Remote Sensing and Image Interpretation.* John Wiley, New York.

Liston, G. E., Bruland, O., Winther, J-G., Elvehøy, H., and Sand, K., 1999. Meltwater production in Antarctic blue-ice areas: sensitivity to changes in atmospheric forcing. *Polar Research*, vol.18(2), 283-290.

Liston, G. E., Bruland, O., Winther, J-G., Elvehøy, H., and Sand, K., 2000. Snow and blue-ice distribution patterns on the coastal Antarctic ice sheet. *Antarctic Science,* vol.12(1), 69-79.

Liston, G.E., 2004. Representing subgrid snow cover heterogeneities in regional and global models. *Journal of Climate,* vol.17(6), 1381-1387.

Liston, G.E., and Winther, J., 2005. Antarctic surface and subsurface snow and ice melt fluxes. *Journal of Climate,* vol.18(10), 1469-1482.

Liston, G.E., Winther, J., Bruland, O., Elvehøy, H., and Sand, K., 1999. Below-surface ice melt on the coastal Antarctic ice sheet. *Journal of Glaciology,* vol.45(150), 273-285.

Liu, H., and Wang, L., 2006. Spatiotemporal variations of snowmelt in Antarctica derived form satellite scanning multichannel microwave radiometer and Special Sensor Microwave Imager data (1978-2004). *Journal of Geophysical Research,* vol.111, F01003, doi:10.1029/2005JF000318, 20p.

Liu, H., Peters, G., and Foken, T., 2001. New equations for sonic temperature variance and buoyancy heat flux with an omnidirectional sonic anemometer. *Boundary-Layer Meteorology*, vol.100, 459–468.

Lowe, P.R., 1977. An approximating polynomial for the computation of saturation vapor pressure. *Journal of Applied Meteorology*, vol.16(1), 100-103.

Massman, W.J., 2000. A simple method for estimating frequency response corrections for eddy covariance systems. *Agricultural and Forest Meteorology*, vol.104, 185–198.

Massman, W.J., and Lee, X., 2002. Eddy covariance flux corrections and uncertainties in long-term studies of carbon and energy exchanges. *Agricultural and Forest Meteorology,* vol.113, 121–144.

Massman, W.J., Fox, D.G., Zeller, K.F., Lukens, D., 1990. Verifying eddy correlation measurements of dry deposition: a study of the energy balance components of the Pawnee Grasslands. *United States Department of Agriculture, Forest Service Research Paper RM-288,* Fort Collins.

Massom, R., and Lubin, D., 2006. *Polar Remote Sensing, volume II: Ice Sheets*. Springer Praxis, Chichester.

Mauder, M., Oncley, S.P, Vogt, R., Weidinger, T., Ribeiro, L., Bernhofer, C., Foken, T., Kohsiek, W., De Bruin, H.A.R., and Liu, H., 2007. The energy balance experiment EBEX-2000. Part II: Intercomparison of eddy-covariance sensors and post-field data processing methods. *Boundary-Layer Meteorology,* vol. 123, 29–54.

McCrae, I. R., 1984. *A summary of glaciological measurements made between 1960 and 1984 on the McMurdo Ice Shelf, Antarctica*: a report submitted to the Antarctic Division of D.S.I.R. Auckland, N.Z., Dept. of Theoretical and Applied Mechanics University of Auckland.

McKay, C.P., Mellon, M.T., and Friedmann, E.I., 1998. Soil temperatures and stability of ice-cemented ground in the McMurdo Dry Valleys, Antarctica. *Antarctic Science,* vol.10(1), 31-38.

Mellor, M. and Swithinbank, C., 1989. *Airfields on Antarctic glacier ice*, U.S. Army Corps of Engineers, Cold Regions Research & Engineering Laboratory.

Meyers, T.P., and R.F., Dale, 1983. Predicting daily insolation with hourly cloud height and coverage. *Journal of Climate and Applied Meteorology*, vol.2, 537-545.

Monaghan, A.J., Bromwich, D.H., and Wang, S.H., 2006. Recent trends in Antarctic snow accumulation from Polar MM5. *Philosophical Transactions of the Royal Society A*, vol.364, 1683-1708.

Monaghan, A.J., Bromwich, D.H., Powers, J.G. and Manning, K.W., 2005. The climate of the McMurdo, Antarctica region as represented by one year of forecasts from the Antarctic Mesoscale Prediction System. *Journal of Climate,* vol.18,1174-1189.

Monaghan, A.J., Bromwich, D.H., Wei, H.L., Cayette, A.M., Powers, J.G., Kuo, Y.H., and Lazzara, M.A., 2003. Performances of weather forecasts models in the rescue of Dr. Ronald Shemelski from the South Pole in April 2001. *Weather and Forecasting*, vol.18(2), 142-160.

Monteith, J., and Unsworth, M., 1990. *Principles of Environmental Physics*. Edward Arnold, London.

Moore, C.J., 1986. Frequency response corrections for eddy correlation systems. *Boundary-Layer Meteorology,* vol.37, 17–35.

Morassutti, M.P., and Ledrew, E.F., 1996. Albedo and depth of melt ponds on sea-ice. *International Journal of Climatology*, vol.16, 817-838.

Motta, L., and Motta, M., 2004. Distribution and pattern of shallow melting at hte local glacier of Terra Nova Bay (Antarctica) coast. *Annals of Glaciology,* vol.39, 483-489.

Munn, R.E., 1966. *Descriptive Micrometeorology*. Academic, San Diego.

Munro, D.S., 1989. Surface roughness and bulk heat transfer on a glacier: comparison with eddy correlation. *Journal of Glaciology,* vol.35(121), 343-348.

Nakawo, M., and Rana, B., 1999. Estimate of ablation rate of glacier ice under a supragalcial debris layer. *Geografiska Annaler,* vol.81(A), 695-701.

Nakawo, M., and Takahashi, S., 1982. A simplified model for estimating glacier ablation under a debris layer. *Hydrological Aspects of Alpine and High Mountain Areas* (Proceedings of the Exeter Symposium, July 1982). IAHS Publication. no. 138. IAHS Press, Wallingford.

Nakawo, M., and Young, G. J., 1981. Field experiments to determine the effect of a debris layer on ablation of glacier ice. *Annals of Glaciology,* vol 2, 85-91.

Nakawo, M., and Young, G. J., 1982. Estimate of glacier ablation under a debris layer from surface temperature and meteorological variables. *Journal of Glaciology*, vol.28(98), 29-34.

Nakawo, M., Raymond, C.F. and Fountain, A., 2000. *Debris Covered Glaciers.* IAHS publication no.264, IAHS Press, Wallingford.

Neale, S.M., and Fitzharris, B.B., 1997. Energy balance and synoptic climatology of a melting snowpack in the Southern Alps, NZ. *International Journal of Climatology*, vol.17, 1595-1607.

Nicholson, L., 2005. Modelling melt beneath supraglacial debris: implications for the climatic response of debris-covered glaciers, *Unpublished PhD Thesis*, School of Geography and Geosciences, University of St. Andrews.

Nicholson, L., and Benn, D.I., 2006. Calculating ice melt beneath a debris layer using meteorological data. *Journal of Glaciology,* vol.52(178), 463-470.

O'Connor, W. P. and Bromwich, D. H., 1988. Surface air-flow around Windless Bight, Ross Island. *Quarterly Journal of the Royal Meteorological Society*, vol.114, 917-938.

Oerlemanns, J., 1992. Climate sensitivity of glaciers in southern Norway: application of an energy balance model to Nigardsbren, Hellstugubreen and Alfotbreen. *Journal of Glaciology*, vol.38, 223-232.

Oke, T.R., 1987. *Boundary Layer Climates*. Routledge, London.

Oliphant, A. J., Grimmond, C. S. B., Zutter, H. N., Schmid, H. P., Su, H. B., Scott, S., Offerle, L.B., Randolph, J. C. and Ehman, J. L., 2004. Heat storage and energy balance fluxes for a temperate deciduous forest. *Agricultural and Forest Meteorology,* vol.126, 185–201.

Oncley, S.P., Foken, T., Vogt, R., Kohsiek, W., DeBruin, H.A.R., Bernhofer, C., Christen, A., van Gorsel, E., Grantz, D., Feigenwinter, C., Lehner, I., Liebethal, C., Liu, H., Mauder, M., Pitacco, A., Ribeiro, L., and Weidinger, T., 2007. The Energy Balance Experiment EBEX-2000. Part I: overview and energy balance. *Boundary-Layer Meteorology,* vol.123, 1–28.

Paige, R.A., 1968. Sub-surface melt pools in the McMurdo Ice Shelf, Antarctica. *Journal of Glaciology*, vol.7(51), 511-516.

Parish, T.R., and Bromwich, D.H., 1998. A Case Study of Antarctic Katabatic Wind Interaction with Large-Scale Forcing. *Monthly Weather Review*, vol.126, 199-209.

Pasricha, P.K., Singh, R., Sarkar, S.K., Dutta, H.N., and Reddy, B.M., 1991. Characteristics of atmospheric turbulence in the surface layer over Antarctica. *Boundary-Layer Meteorology,* vol.57, p.207-217.

Paterson, W. S. B., 1994. *The Physics of Glaciers*. Butterworth Heinemann, Oxford.

Paul, F., Huggel, C., and Kääb, A., 2004. Combining satellite multispectral image data and a digital elevation model for mapping debris-covered glaciers. *Remote sensing of the Environment,* vol.89, 510-518.

Pelto, M.S., 2000. Mass balance of adjacent debris-covered and clean glacier ice in the North Cascades, Washington. *in* Nakawo, M., Raymond, C.F., and Fountain, A., (eds.). *Debris-covered glaciers*. IAHS Publication no.264. Wallingford, IAHS Press, 35-42.

Périard, C., and Pettré, P., 1993. Some aspects of the climatology of Dumont d'Urville, Adélie Land, Antarctica. *International Journal of Climatology*, vol.13, 313-327

Petrone, R.M. and Rouse, W.R., 2000. Synoptic controls on the surface energy and water budgets in sub-arctic regions of Canada. *International Journal of Climatology*, vol.20, 1149-1165.

Phillips, H.A., 1998. Surface meltstreams on the Amery Ice Shelf, East Antarctica. *Annals of Glaciology,* vol.27, 177-181.

Pirazzini, R., 2004. Surface albedo measurements over Antarctic sites in summer *Journal of Geophysical Research, vol.*109(D20), D20118.

Pomeroy, J.W., and Essery, R.L.H., 1999. Turbulent fluxes during blowing snow: field tests of model sublimation predictions. *Hydrological Processes,* vol.13, 2963-2975.

Powers, J.G., Monaghan, A.J., Cayette, A.M., Bromwich, D.H., Kuo, Y-H., and Manning, K.W., 2003. Real-time mesoscale modelling over Antarctica: The Antarctic Mesoscale Prediction System. *Bulletin of the American Meteorological Society.* Vol.84(11), 1533-1545.

Pridmore, R.D., Vant, W.N., and Cummings, V.J., 1995. Factors affecting the water clarity of ponds on the McMurdo Ice Shelf, Antarctica. *Antarctic Science*, vol.7(2), 145-148.

Prosek, P., and Brazdil, R., 1994. Energy balance of the tundra at the Spitsbergen island (Svalbard) in the summer seasons of 1988 and 1990. *Scripta Fac. Sci. Nat. Univ. Masaryk. Brun.,* vol.24. 43-60.

Purdie, J. and Fitzharris, B., 1999. Processes and rates of ice loss at the terminus of Tasman Glacier, New Zealand. *Global and Planetary Change,* vol.22, 79-91.

Reeh, N., Mohr, J. J., Krabill, W. B., Thomas, R., Oerter, H., Gundestrup, N., and Bøggild, C. E., 2002. Glacier specific ablation rate derived by remote sensing measurements. *Geophysical Research Letters,* vol.29(16), 10.1029/2002GL015307.

Rees, W.G., 2006. *Remote sensing of snow and ice.* Taylor and Francis Group, Boca Raton.

Reijmer, C.H., and Oerlemans, J., 2002. Temporal and spatial variability of the surface energy balance in droning Maud Land, East Antarctica. *Journal of Geophysical Research,* vol.107(D24), D4759, doi:10.1029/2000JD000110.

Reijmer, C.H., Bintanja,R., and Greuell, W., 2001. Surface albedo measurements over snow and blue ice in thematic mapper bands 2 and 4 in Dronning Maud Land, Antarctica. *Journal of Geophysical Research*, vol.106(D9), 9661-9672.

Reithmaier, L., Göckede, M., Markkanen, T., Knohl, A., Churkina, G., Rebmann, C., Buchmann, N., and Foken, T., 2005. Use of remotely sensed land use classification for a better evaluation of micrometeorological flux measurement sites. *Theoretical and Applied Climatology*, vol.84(4), 219-233.

Rigor, I.G., Colony, R.L., and Martin, S., 2000. Variations in Surface Air Temperature Observations in the Arctic, 1979–97. *Journal of Climate,* vol.13, 896-914.

Roth, M., and Oke, T.R., 1995. Relative efficiencies of turbulent transfer of heat, mass, and momentum over a patchy urban surface. *Journal of the Atmospheric Sciences,* vol.52(11), 1863-1874.

Sakai, A., Fujita, K., and Kubota, J., 2004. Evaporation and percolation effect on melting at debris-covered Lirung Glacier, Nepal Himalayas, 1996. *Bulletin of Glaciological Research,* vol.21, 9-15.

Sansom, J., 1989. Antarctic surface temperature time series. *Journal of Climate,* vol.2, 1164-1172.

Scambos, T., Raup, B. and Bohlander, J. (compilers), 2004. *Images of Antarctic Ice Shelves, March 2004.* Boulder, National Snow and Ice Data Center. Digital media.

Scambos, T.A., Hulbe, C., Fahnestock, M., and Bohlander, J., 2000. The link between climate warming and break-up of ice shelves in the Antarctic Peninsula. *Journal of Glaciology*, vol.46(154), 516-530.

Schmid, H.P., 1994. Source areas for scalars and scalar fluxes. *Boundary-Layer Meteorology*, vol.67, 293-318.

Schneider, C., 1999, Energy balance estimates during the summer season of glaciers of the Antarctic Peninsula. *Global and Planetary Change,* vol.22, 117-130.

Schotanus, P., Nieuwstadt, F.T.M., and De Bruin, H.A.R., 1983. Temperature measurement with a sonic anemometer and its application to heat and moisture fluxes. *Boundary-Layer Meteorology*, vol.26, 81-93

Schwerdtfeger, W., 1984. *Weather and Climate of the Antarctic.* Elsevier, Amsterdam.

Scientific Committee for Antarctic Research, 1993. *Antarctic Digital Database version 3.0 on CD-ROM.* Scott Polar Research Institute, Cambridge, England.

Scientific Committee for Antarctic Research, 2000. *Antarctic Digital Database Verion 3.0 Manual and Bibliography*. Scott Polar Research Institute, Cambridge, England.

Seefeldt M.W., Tripoli, G.J. and Stearns, C.R., 2003. A high-resolution numerical simulation of the wind flow in the Ross Island region, Antarctica. *Monthly Weather Review*, vol.131(2), 435-458.

Sheridan, S.C., 2002. The redevelopment of a weather-type classification scheme for North America. *International Journal of Climatology,* vol.21, 51–68.

Sidjak, R.W., and Wheate, R.D., 1999. Glacier mapping of the Illecillewaet Icefield, British Columbia, Canada, using Landsat TM and digital elevation data. *International Journal of Remote Sensing,* vol.20(2), 273-284.

Simmonds, I., Keay, K., and Lim, E., 2003. Synoptic activity in the seas around Antarctica. *Monthly Weahter Review,* vol.131(2), 272-292.

Sinclair, M.R., 1988. Local topographic influence on low-level wind at Scott Base, Antarctica. *New Zealand Journal of Geology and Geophysics,* vol.31, 237-245.

Spronken-Smith, R., Kossmann, M., and Zawar-Reza, P., 2006. Where does all the energy go? Surface energy partitioning in suburban Christchurch under stable wintertime conditions. *Theoretical and Applied Climatology,* vol.84(1-3), 137-149.

Stearns, C.R., 1997. Ross Island area wind field. *Antarctic Journal - Review 1997,* 181-182.

Stearns, C.R., and Weidner, G.A., 1993. Sensible and latent heat flux estimates in Antarctica. *Antarctic Meteorology and Climatology*, vol. 61, 109-138.

Stroeve, J., Box, J.E., Gao, F., Liang, S., Nolin, A. and Schaaf, C., 2005. Accuracy assessment of the MODIS 16-day albedo product for snow: comparisons with Greenland in situ measurements. *Remote Sensing of Environment*, vol. 94(1), 46-60.

Stuart, A.W., and Bull, C., 1963. Glaciological observations on the Ross Ice Shelf near Scott Base, Antarctica. *Journal of Glaciology*, vol.4(34), 399-414.

Stull, R., 1988. *An introduction to boundary layer meteorology.* Kluwer Academic Publishers, Dordrecht.

Sturm, M., Holmgren, J., and Perovich, D., 2001. Spatial Variations in the Winter Heat Flux at SHEBA: Estimates from Snow-ice Interface Temperatures. *Annals of Glaciology*, vol.33, 213-220.

Sturman, A., 2001. Synoptic controls on the on the weather *In* Sturman, A. and Spronken-Smith, R. (eds.). *The physical environment: a New Zealand Perspective*. Oxford University Press, Melborne. 76-93.

Sun, J., 1999. Diurnal variations of thermal roughness height over a grassland. *Boundary Layer Meteorology*, vol.92, 407-427.

Swithinbank, C., 1970. Ice Movement in the McMurdo Sound area of Antarctica. *International Symposium on Antarctic Glaciological Exploration, Dartmouth College, 1968*. International Association of Scientific Hydrology vol.86, 472-487.

Takeuchi, Y., Kayastha, R.B. and Nakawo, M., 2000. Characteristics of ablation and heat balance in debris-fee and debris-covered areas on Khumbu Glacier, Nepal Himalayas, in the pre-monsoon season. *in* Nakawo, M., Raymond, C.F., and Fountain, A., (eds.). *Debris-covered glaciers*. IAHS Publication no.264. Wallingford, IAHS Press, 53-61.

Takeuchi, Y., Naruse, R., Satow, K. and Ishikawa, N., 1999. Comparison of heat balance characteristics at five glaciers in the Southern Hemisphere. *Global and Planetary Change,* vol.22, 201-208.

Tanner, B.D., and Greene, J.P., 1989. Measurements of sensible heat and water vapour fluxes using eddy correlation methods. Final Report to US Army Dugway Proving Grounds.

Taschner, S., and Ranzi, R., 2002. Comparing the Opportunities of LANDSAT ETM+ and ASTER Data for Monitoring a Debris Covered Glacier in the Italian Alps within the GLIMS project. *Proceedings of IGARSS'02 Symposium, Toronto*.

Theiler, J., Lavenier, D.D., Harvey, N.R., Perkins, S.J., and Szymanski, J.J., 2000. Using blocks of skewers for faster computation of pixel purity index. *Proceedings of SPIE*, vol.4132, 61–71.

Tsengdar, J.L., and Pielke, R.A., 1992. Estimating the soil surface specific humidity. *Journal of applied Meteorology,* vol.31, 480-484.

van As, D., van den Broeke, M., and Van de Wal, R., 2005a. Daily cycle of the surface layer and energy balance on high Antarctic Plateau. *Antarctic Science,* vol.17(1), 121-133.

van As, D., van den Broeke, M., Reijmer, C., and Van de Wal, R., 2005b. The summer surface energy balance of the high Antarctic Plateau. *Boundary-Layer Meteorology,* vol.115, 289-317.

van de Wal, R.S.W., Greuell, W., van den Broeke, M.R., Reijmer, C.H., and Oerlemans, J. 2005. Surface mass-balance observations and automatic weather station data along a transect near Kangerlussuaq, West Greenland. *Annals of Glaciology*, vol.42, 311-316.

van den Broeke, M.R., 1997. Spatial and temporal variation of sublimation on Antarctica: results of a high-resolution general circulation model. *Journal of Geophysical Research*, vol.102(D25), 29765-29777.

van den Broeke, M.R., Reijmer, C.H., and van de Wal, R.S.W., 2004a. A study of the surface mass balance in Dronning Maud Land, Antarctica, using automatic weather stations. *Journal of Glaciology,* vol.50(171), 565-582.

van den Broeke, M.R., Reijmer, C.H., and van de Wal, R.S.W., 2004b. Surface radiation balance in Antarctica as measured with automatic weather stations. *Journal of Geophysical Research*, vol.109(D9), D09103, doi:10.1029/2003JD004394.

van der Veen, C.J., 2002. Polar ice sheets and global sea level: how well can we predict the future? *Global and Planetary Change,* vol.32, 165-194.

van Dijk, D., and Law, J., 2003. The rate of grain release by pore-ice sublimation in cold-aeolian environments. *Geografiska Annaler, Series A: Physical Geography,* vol.85(1), 99-113.

Vaughan, D.G., 2006. Recent trends in melting conditions on the Antarctic Peninsula and their implications for ice-sheet mass balance and sea level. *Arctic, Antarctic and Alpine Research,* vol.38(1), 147-152.

Vaughan, D.G., and Doake, C.S.M., 1996. Recent atmospheric warming and retreat of ice shelves on the Antarctic Peninsula. *Nature,* vol.379, 328-330.

Vaughan, D.G., Bamber, J. L., Giovinetto, M., Russell, J., and Cooper, A.P.R., 1999. Reassessment of Net Surface Mass Balance in Antarctica. *Journal of Climate*, vol.12, 933-946.

Warren, S.G., Grenfell, T.C., and Mullen, P.C., 1986. Optical properties of Antarctic snow. *Antarctic Journal of the United States*, vol.21, 247-248.

Waterhouse, E.J., 2001. *Ross Sea Region 2001: A State of the Environment Report for the Ross Sea Region of Antarctica.* New Zealand Antarctic Institute, Christchurch.

Webb, E.K., Pearman, G.I., and Leuning, R., 1980. Correction of flux measurements for density effects due to heat and water vapor transfer. *Quarterly Journal of the Royal Meteorological Society,* vol.106, 85-100.

Whitehead, R.F., 1989. *Aqueous geochemistry of meltwater on the McMurdo Ice Shelf and the Alph River, Antarctica.* Thesis submitted in partial fulfillment of the requirements for the degree of Master of Science in Geography in the University of Canterbury.

Whiteman, C.D., 2000. *Mountain meteorology: fundamentals and applications.* Oxford University Press, New York.

Williams, K.S., and Taboton, D.G., 1999. The ABC's of snowmelt: a topographically factorized energy component snowmelt model. *Hydrological Processes,* vol.13, 1905-1920.

Williams, P.J., and Smith, M.W., 1989. *The frozen earth: fundamentals of geocryology.* Cambridge University Press, Cambridge.

Williams, R.S., Hall, D.K., and Benson, C.S., 1991. Analysis of glacier facies using satellite techniques. *Journal of Glaciology,* vol.37(12), 120-128.

Willmott, C.J., 1981. On the validation of models, *Physical Geography,* vol.2, 184-194.

Willmott, C.J., 1982. Some comments on the evaluation of model performance. *Bulletin of the American Meteorological Society*, vol.63, 1309-1313.

Winther, J., 1994. Spectral bi-directional reflectance of snow and glacier ice measured in Dronning Maud Land, Antarctica. *Journal of Glaciology*. Vol.42(141), 271-278.

Winther, J., Jespersen, M.N., and Liston, G.E., 2001. Blue-ice areas in Antarctica derived from NOAA AVHRR satellite data. *Journal of Glaciology,* vol.47(157), 325-334.

WMO, 2000. General Meteorological Standards and Recommended Practices, WMO-NO 49, Vol I App. A.

Wolken, G.J., 2006. High-resolution multispectral techniques for mapping former Little Ice Age terrestrial ice cover in the Canadian High Arctic. *Remote Sensing of the Environment,* vol.101, 104-114.

Wuttke, S., Seckmeyer, G., and König-Langlo, G., 2006. Measurements of spectral snow albedo at Neumayer, Antarctica. *Annales Geophysicae*, vol.24, 7-21.

Yague, C., Maqueda, G., and Rees, J.M., 2001. Characteristics of turbulence in the lower atmosphere at Halley IV station, Antarctica. *Dynamics of atmospheres and oceans,* vol.34, 205-223.

Yarnal, B., 1984. Synoptic-Scale Atmospheric Circulation over British Columbia in Relation to the Mass Balance of Sentinel Glacier. *Annals of the Association of American Geographers*, vol.74(3), 375-392.

Yarnal, B., Comrie, A.C., Frakes, B., and Brown, D.P., 2001. Developments and prospects in synoptic climatology. *International Journal of Climatology*, vol.21, 1887-1914.

Zuo, Z., and Oerlemans, J., 1996. Modelling albedo and specific balance of the Greenland Ice Sheet: Calculations for the Sondre Stromfjord transect. *Journal of Glaciology*, vol.42(141), 305-317.

Zwally, H.J., and Fiegles, S., 1994. Extent and duration of Antarctic surface melting. *Journal of Glaciology*, vol.40(136), 463-476.